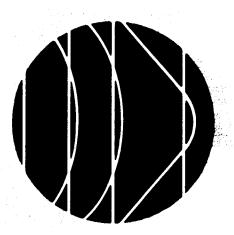
SE 8/8-/8
REPORT NO. F694

PART B3 ALTERNATIVES, ANALYSES, SELECTION



VOLUME II CAPSULE BUS SYSTEM

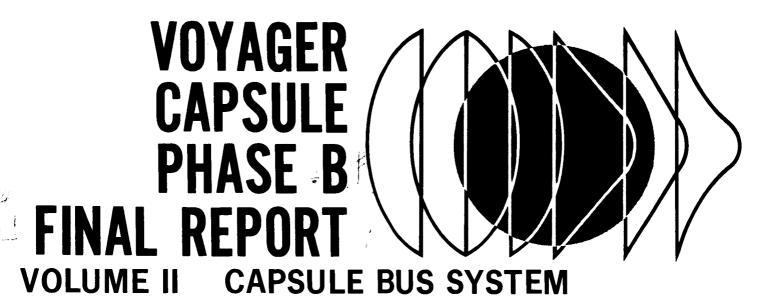
		602	- N67 - 4004	6
GPO PRICE \$		- Y	(ACCESSION NUMBER)	(THRU)
CFSTI PRICE(S) \$		FACILIT	(PAGES) (NASÁ CR OR TMX OR AD NUMBER)	(CATEGORY)
Hard copy (HC)	9 00	j		,

Hard copy (HC) 3-00

Microfiche (MF) 65

ff 653 July 65

PART B3 ALTERNATIVES, ANALYSES, SELECTION



PREPARED FOR:
CALIFORNIA INSTITUTE OF TECHNOLOGY
JET PROPULSION LABORATORY
PASADENA, CALIFORNIA
CONTRACT NUMBER 952000

REPORT ORGANIZATION

VOYAGER PHASE B FINAL REPORT

The results of the Phase B Voyager Flight Capsule study are organized into several volumes. These are:

Volume I Summary
Volume II Capsule Bus System

Volume III Surface Laboratory System

Volume IV Entry Science Package

Volume V System Interfaces

Volume VI Implementation

This volume, Volume II, describes the McDonnell Douglas preferred design for the Capsule Bus System. It is arranged in 5 parts, A through E, and bound in 11 separate documents, as noted below.

Part A	Preferred Design Concept	2 documents, Parts A_1 and A_2
Part B	Alternatives, Analyses, Selection	5 documents, Parts B_1 ,
		B_2 , B_3 , B_4 and B_5
Part C	Subsystem Functional Descriptions	2 documents, Parts ${ t C}_1$
		and C_2
Part D	Operational Support Equipment	1 document
Part E	Reliability	1 document

In order to assist the reader in finding specific material relating to the Capsule Bus System, Figure 1 cross indexes broadly selected subject matter, at the system and subsystem level, through all volumes.

VOLUME II CROSS REFERENCE INDEX

/		PARTA	PART B	PART C	PART D	PART E
/	VOLUME II PARTS +	DESCRIPTION OF	A! TERNATIVES	DETAIL FD DE-	OPERATIONAL SUP-	RELIABILITY CON-
/		PREFERRED SYS.	ANALYSIS AND	SCRIPTION OF		STRAINTS, ANALY-
′		TEM OBJECTIVES,	SELECTION -	SUBSYSTEM	- SYSTEM, SUBSYS-	SIS, RESULTS, PRO-
	/	MISSION, DESIGN,	METHODS TRADE	FUNCTIONS	TEM, LAUNCH COM-	GRAM TESTING,
	/	SUBSYSTEMS,	STUDIES, OPTIMI-		PLEX, MISSION,	CONTROL
SYSTEM/S	SYSTEM/SUBSYSTEM	OPERATIONS, SUP- PORTING FUNC-	ZATION STUDIES RESULTS		HANDLING, SOFT. WARE	
	4	TIONS				
CAP	CAPSULE BUS SYSTEM				-	1
	Objectives	1.1—Summary	2-Analysis	N/A	1-General	1-Constraints
Mission	Profile	1.2—Summary	2—Analysis 2.4—Selection	N/A	N/A	3.1.1—Analysis
	Operations	4-Description by	2.3-Analysis	N/A	4.4-LCE Description 3-Estimates	3-Estimates
	_	Phase	2.3.7—Landing Site Select		4.5-MDE Descript ion	
	General	2-Criteria Summary	1-Study Approach	A/A		4-Program Require-
		3.1—Configuration	3-Functional Re-		ıry	ments
		,	quirements			5—Component Reli- ability
Design	Standardization/Growth	2.5-Summary	(See Specific Sub-	N/A		N/A
		==	system Below)		4.4.8-LCE Growth 4.5.8-MDE	
	Weight	3.1.2.4-Summary	(See Specific Sub-	N/A	N/A	2.3.2-Reliability vs
		5-Breakdown	system Below)			Weight
Interfaces	Interfaces (See Also Vol. V)	3.1—Summary 9.0—Operational	(See Volume V)	N/A	4.2.1,4.3.5,4.4.5, 4.5.5	N/A
Implemento	Implementation (See Also Vol. VI)	10-Schedule 8 11-OSE	(See Volume VI)	N/A	(See Specific Sub- system Below)	N/A
Planetary (Planetary Quarantine	7-General	(See Volume VI, C,7	N/A	None Required	V/ V
) S E (Sa	OSE (See Also Part D)	8_General	(See D2.5-Selection	(See D5-Subsystem	Complete OSE	(See D4.3.6-STC
3		(See Also-D1,D2,	Criteria, D9-Analy-	Level Test Equip-	Description	D4.4.6-LCE
		D3,D4)	sis, DIO - Alterna- tives)	ment, See Also D4, D6, D7)		D4.5.6-MDE)
	LW2			11	61526153	/See Part C Sections
Sterilization	Sterilization Canister	3.2.1.1-Description	5. I-Andlysis	- -	6.1.5.6	1.1.1.7
		7.1.5			6.1.5.8-AHSE	1.1.2.7
			-		6.2.15-Servicing	1.1.3.7)
Adapter		3.2.1.2-Description	5.2-Analysis	1.2	None Required	(See Part C, 1.2.7)
		3.1.2—30mmary				/C. 1 2 7)

Figure 1

Aeroshell	3.2.173-Description	Coloningorarron		- soughou giou.	
). 1.2-30mmary	4.6-Separation			
		5.3.1-Structure 5.3.2-Heat Shield			
Lander	3.2.1.4—Description 3.1.2—Summary	4.2—Configuration Selection 5.4—Analysis	1.4	6.1.5.9Fixture	(See Part C, 1.4.7)
Telecommunications	3.2.2.1—Description	4.9-In-Flight Monitoring toring 5.5-Analysis	2-Telemetry 3-Radio 4-Antenna 5-Data Storage 6-Command	4.3.9.1—STC Console (See Part C, 5.7—Test Set 3.1.7, 2.2.7, 3.2.7, 3.2.7, 5.2.7, 6.2.7)	(See Part C, Sections 2.1.7, 2.2.7, 2.3.7, 3.1.7, 3.2.7, 4.5, 5.1.7, 5.2.7, 6.1.7, 6.2.7)
Power	3.2.2.2-Description	5.6—Analysis	7	4.3.9.1-STC Console 5.3-Test Set	(See Part C, Sect. 7.7)
Sequencing and Timing	3.2.2.3—Description	5.7-Analysis	8	4.3.9.1_STC Console 5.4_Test Set	(See Part C Sections 8.1.7, 8.2.7)
Guidance and Control	3.2.2.4—Description	4.7-De-orbit Atti- tube Reqm*t. 5.8-Analysis	6	4.3.9.1-STC Console 5.5-Test Set	(See Part C, 9.7)
Radar	3.2.2.5-Description	5.9-Analysis	10	4.3.9.1-STC Console 5.6-Test Set	(See Part C, Sections 10.1.7, 10.2.7)
Aerodynamic Decelerator	3.2.3—Description	4.4—Selection 5.10—Analysis	11	None Required	(See Part C, 11.7)
Pyrotechnics	3.2.4—Description	5.11-Analysis	12	4.3.9.1—STC Console 5.9—Test Set	(See Part C, 12.7.1)
Thermal Control	3.2.5-Description	5.12—Analysis	13	4.3.9.1-STC Console 5.8-Test Set	(See Part C, 13.6)
De-orbit Propulsion	3.2.6.1-Description	5.13.1—Analysis	14	5.10-Test Set 6.1.5.10-AHSE	(See Part B, 5.13.4.5) (See Part C, 14.7)
Reaction Control	3.2.6.2-Description	5.13.2-Analysis	15	5.10-Test Set 6.2-Servicing	See Part B, 5.13.4.5) (See Part C, 15.7)
Terminal Propulsion	3.2.6.3—Description	4.3-Configuration Selection 4.5-Terminal Deceleration 5.13.3-Analysis	16	onsole	See Part B, 5.13.4.5) See Part C, 16.7)
Packaging and Cabling	3.2.7.Description	5. 14—Analysis	17	4.3.9.8—Special Purpose Complex Equipment	Not Required

Note: Parentheses Refer Reader to Volumes/Parts Outside of the Respective Notation

TABLE OF CONTENTS

		Page
SECTION 5	SUBSYSTEM ANALYSIS	5-1
5.1 Ste	erilization Canister	5.1-1
5.1.1	Configuration Selection Summary	5.1-1
5.1.2	Canister Structure	5.1-6
5.1.3	Separation Studies	5.1-28
5.1.4	Pressurization and Venting Studies	5.1-46
5.1.5	Canister Electrical Optimization Studies	5.1-65
5.2 Ada	apter	5.2-1
5.2.1	Design Constraints and Requirements	5.2-1
5.2.2	Alternative Design Approaches	5.2-2
5.2.3	Evaluation and Selection	5.2-2
5.2.4	Preferred Approach	5.2-9
5.2.5	Structural Analysis of Preferred Truss Adapter	5.2-11
5.2.6	Adapter Dynamic Analysis	5.2-11
5.2.7	Capsule Separation	5.2-15
5.3 Aer	oshell	5.3-1
5.3.1	Structure	5.3-3
5.3.2	Heat Shield	5.3-100
5.4 Lan	der	5.4-1
5.4.1	General Stability Studies of Legged Systems	5.4-2
5.4.2	Preferred Concept	5.4-3

This Document Consists of the Following Pages:

Title Page i through iii 5-1 and 5-2 5.1-1 through 5.1-73 5.2-1 through 5.2-17 5.3-1 through 5.3-229 5.4-1 through 5.4-29

SECTION 5

SUBSYSTEM ANALYSIS

Subsystem analysis has been a major element of our preferred design selection. In addition to the subsystem analysis to support the major trade studies described in Section 4, there have been two types of studies of the subsystems themselves. First, trade studies to determine the preferred subsystem approach from among several candidates were conducted. Second, analyses to size and optimize the subsystem were performed. The preferred subsystem configuration is the one that yields an optimum Capsule Bus System. To assure consistent judgement at every step of the analysis, the system-oriented analytical procedures of trade studies described in Section 4 have been carried over to the subsystem analyses. The selection criteria of Section 1 were used:

- a. Probability of Mission Success
- b. System Performance
- c. Development Risk
- d. Versatility
- e. Cost

In our Phase B effort, the selection from alternate concepts, subsystems, and components has been conducted within technical disciplines but with extensive interdisciplinary coordination. As examples, the landing radar subsystem is greatly affected by the pitch angles of the Aeroshell during the radar search and track modes; the type of structure used in the Aeroshell is affected by its heat protection subsystem; and the deployable aerodynamic decelerator is designed to improve thrust initiation conditions of the terminal propulsion subsystem.

The following sections describe problems anticipated in the design, development, and use of the subsystems; the alternative solutions for the problems; and the selection of the preferred design. In one case - that of the Independent Data Package (IDP) - the entire concept was rejected. (See Section 4.8 for the trade study). However, before this conclusion was reached, the subsystem was thoroughly studied and many alternative implementations were weighed and a preferred IDP configuration chosen (Section 5.15).

The subsystems are discussed by functional groups. The structure elements - canister, adapter, Aeroshell, and lander - are presented in Sections 5.1 through 5.4.

The electronic subsystems are then discussed in Sections 5.5 through 5.9. They include telecommunications (with separate dissertations on multipath, blackout

ionization, interleaving, and data compression, power, sequencers and timers for event control, guidance and control electronics, and radar.

The third group of subsystem discussions, Sections 5.10 through 5.15, includes the deployable aerodynamic decelerators, pyrotechnic devices, thermal control, the three propulsion subsystems (de-orbit, reaction control, and terminal), packaging and cabling, and the IDP description. These analyses allowed us to evaluate concepts and evolve designs of subsystems which perform better as a combination than the sum of their individual capabilities would indicate. Critical items have been subjected to tests that verified feasibility.

5.1 <u>STERILIZATION CANISTER</u> - Prior to terminal heat sterilization the Flight Capsule will be placed in a Sterilization Canister that then functions as a biological barrier. Recontamination is prevented by keeping the canister sealed until the Capsule release point in the Mars Orbit.

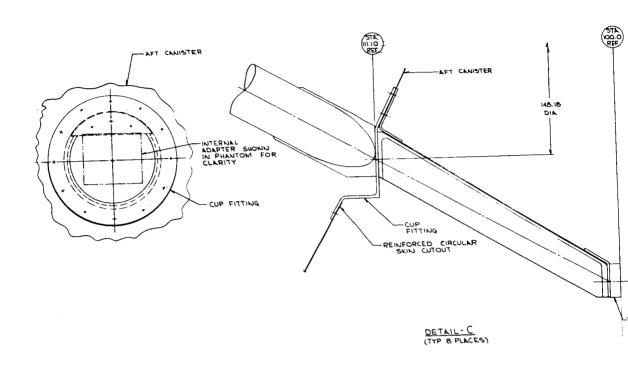
A study was conducted to design a Sterilization Canister capable of reliably performing its function at a minimum weight penalty to the overall Capsule Bus system. The study approach used, the selection criteria employed, and the preferred approach selected are presented in this Section.

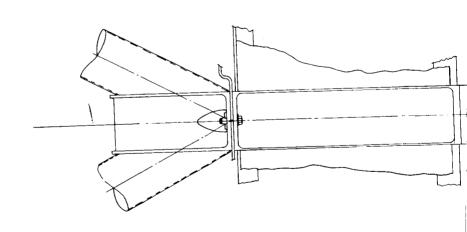
Section A2 presents the spectrum of mission/environmental/structural requirements imposed on the VOYAGER Capsule Bus system. Studies showed that those most significantly affecting the canister design are:

- a. Maximum allowable envelope for the Flight Capsule
- b. Maximum diameter of the Aeroshell (19 ft.) and resulting dynamic envelope.
- c. Pressure resulting from temperature changes after sealing and sterilization.
- d. Requirement for serving as a physical and biological barrier.
- 5.1.1 <u>Configuration Selection Summary</u> Conceptual designs studies were:
 - a. Two-piece, rigid shell canister, forward piece ejected, presented in the preferred approach, Figure 5.1-1.
 - b. Two-piece, with double forward canister to maintain clean inner assembly forward pieces (2) jettisoned. This concept is illustrated in Figure 5.1-2.
 - c. Rigid aft canister, flexible forward canister, forward piece ejected. This concept is similar to the one illustrated in Figure 5.1-2 except that only the outer piece of the two forward pieces is used.
 - d. Hinged canister, two-piece forward clamshell, forward pieces retaived, as illustrated conceptually in Figure 5.1-3.
 - e. Canister separated from Spacecraft in closed condition. This approach could be used with any of the above by addition of a separation system at the Canister/Spacecraft interface, estimated to weight 20 pounds (eight explosive bolts plus initiation and associated harness).

The last was eliminated as no requirement exists to establish the need and criteria for this type.

Of the remainder, the first was shown to be simplest and lightest in weight by about 40 pounds, except for the flexible canister which is judged to be prone to handling damage and resultant recontamination. On this basis, the first was





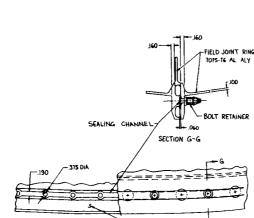
A

5,1-2-1

REPORT F694 • VOLUME II • PART B • 31 AUGUST 1967

160.0 BC

EXTOLITE INSULATION PAD



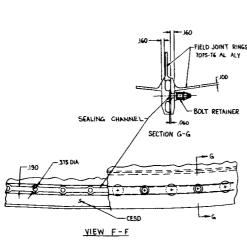
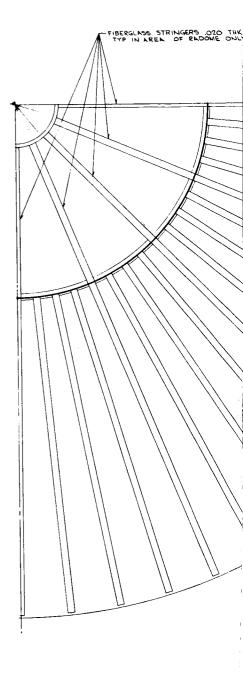
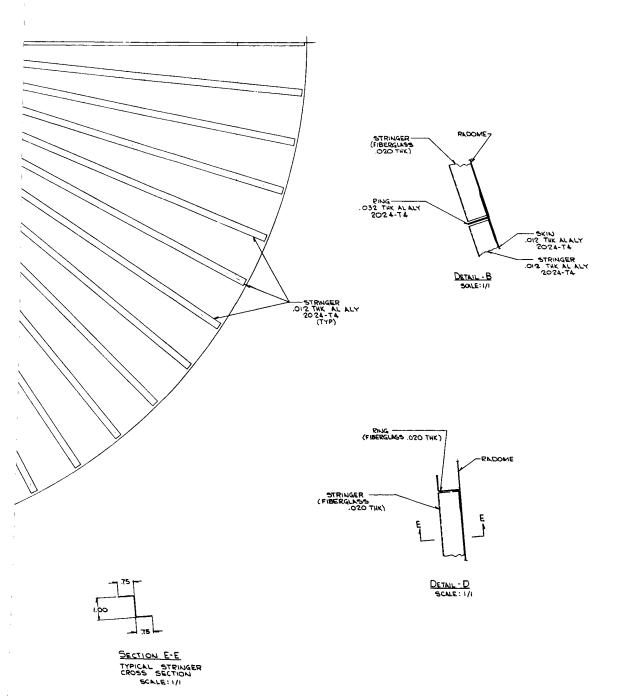
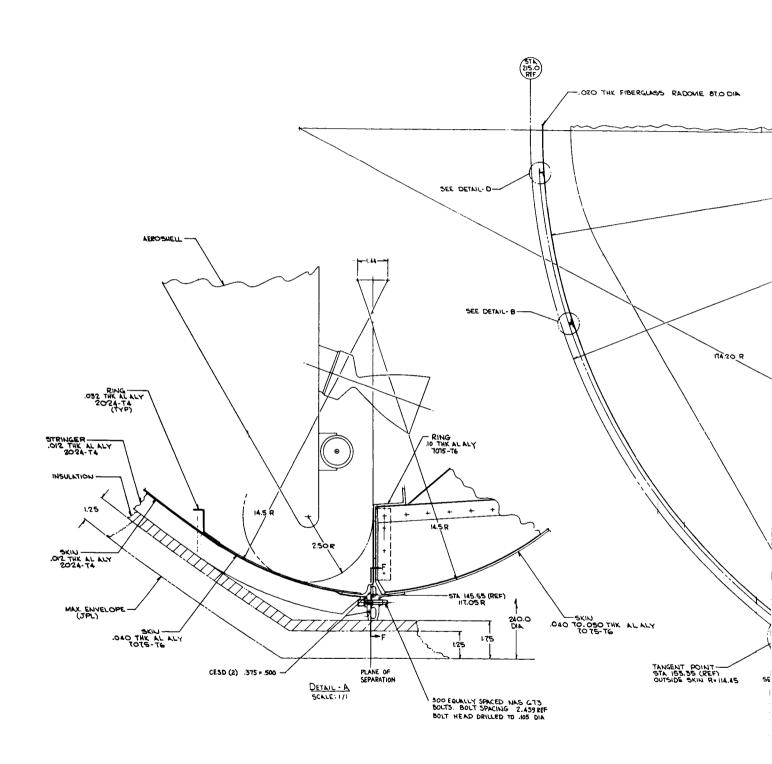


Figure 5.1-1





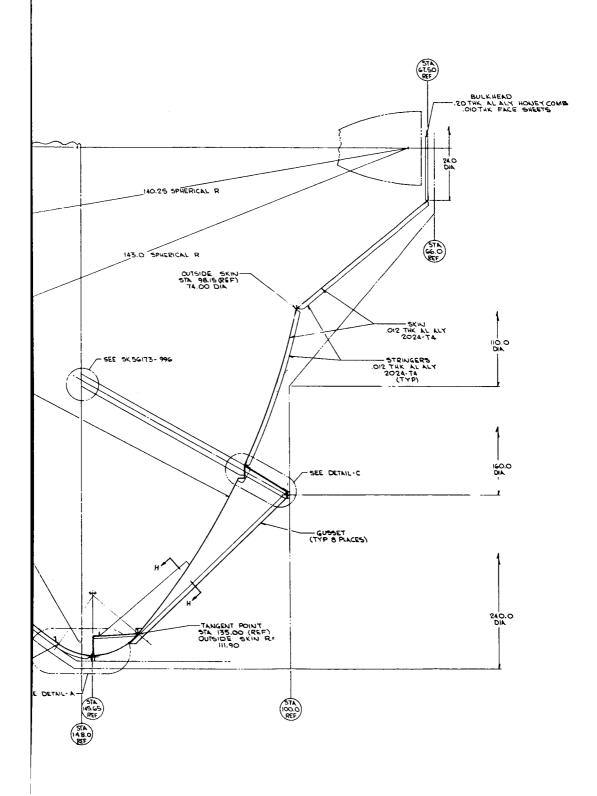
B



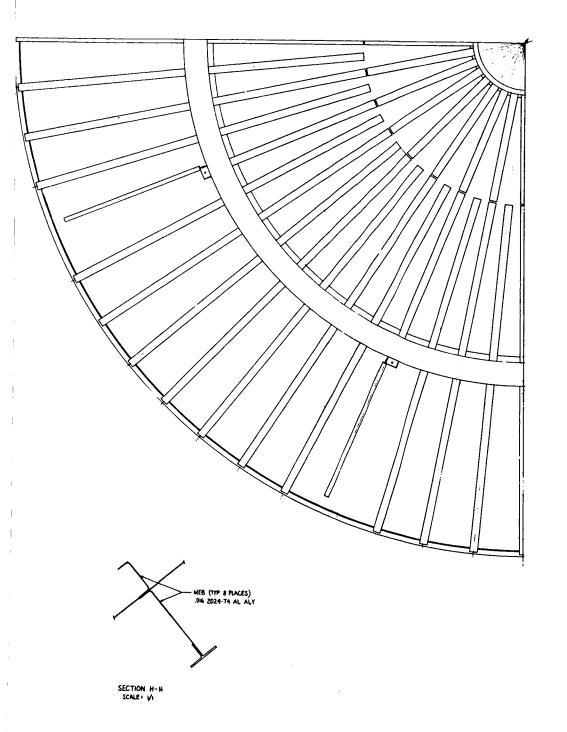
A

Figure 5.1-1 (Continued)

5.1-3-(



3.1-3-2



B

CANISTER, STERILIZED - DOUBLE FORWARD

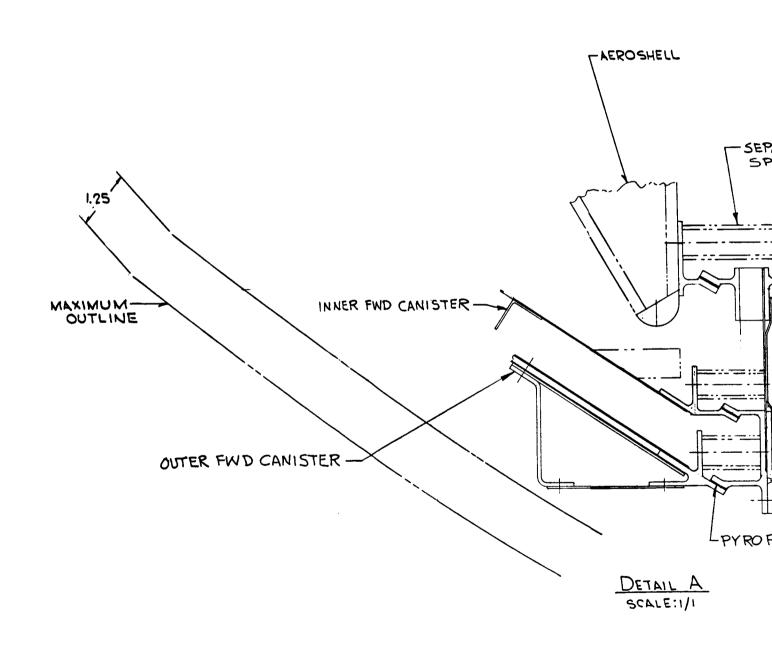
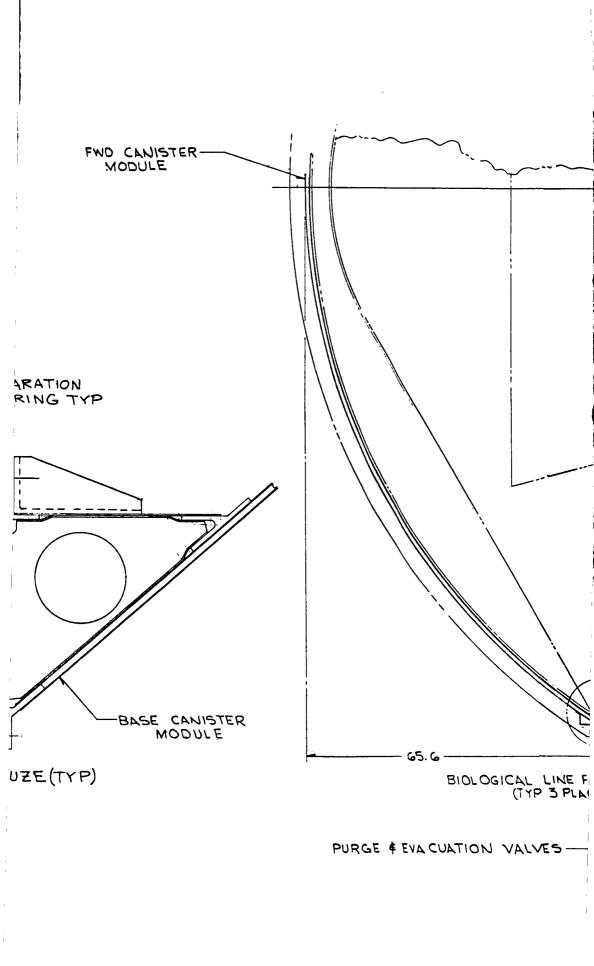
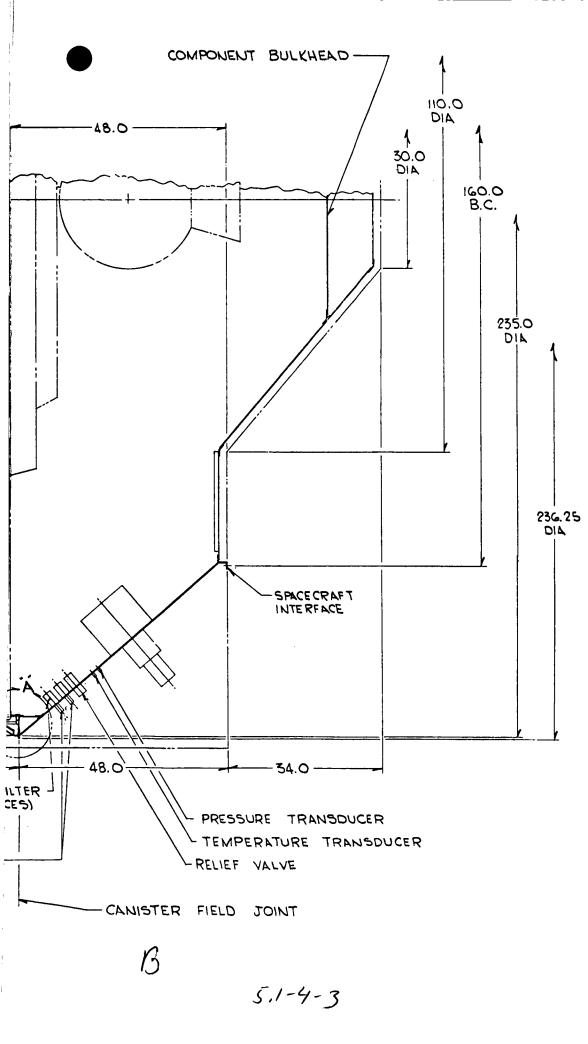


Figure 5.1-2 5.1-4-)

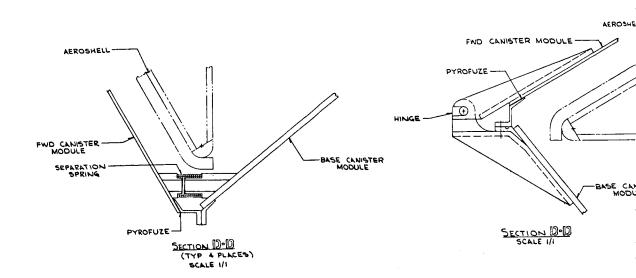
A

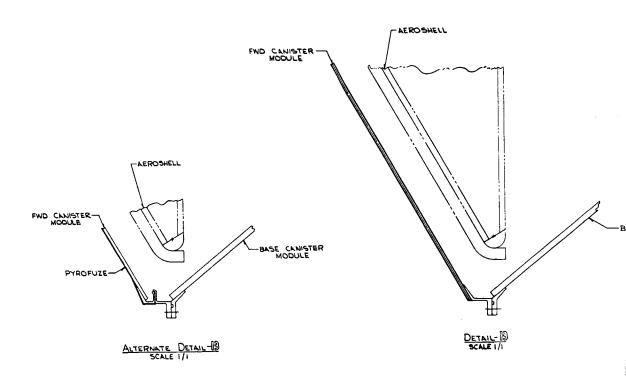
REPORT F694 • VOLUME II • PART B • 31 AUGUST 1967





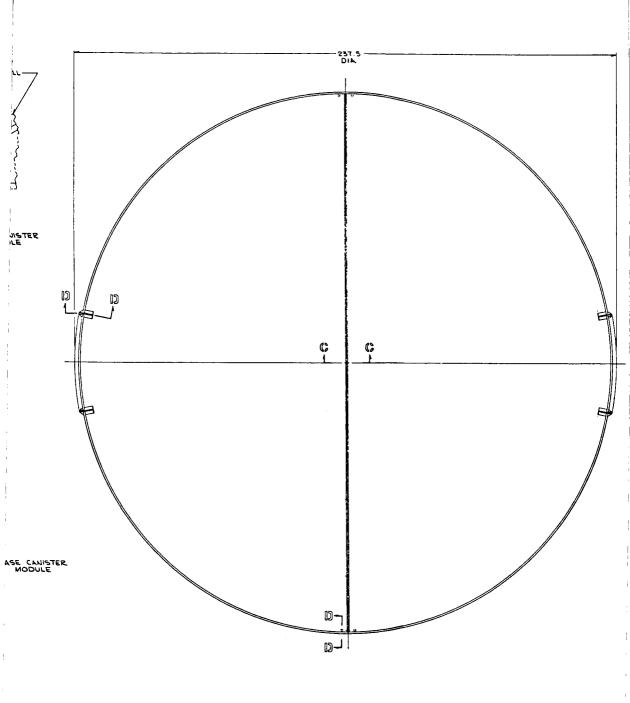
HINGED CANISTER CONCEPT





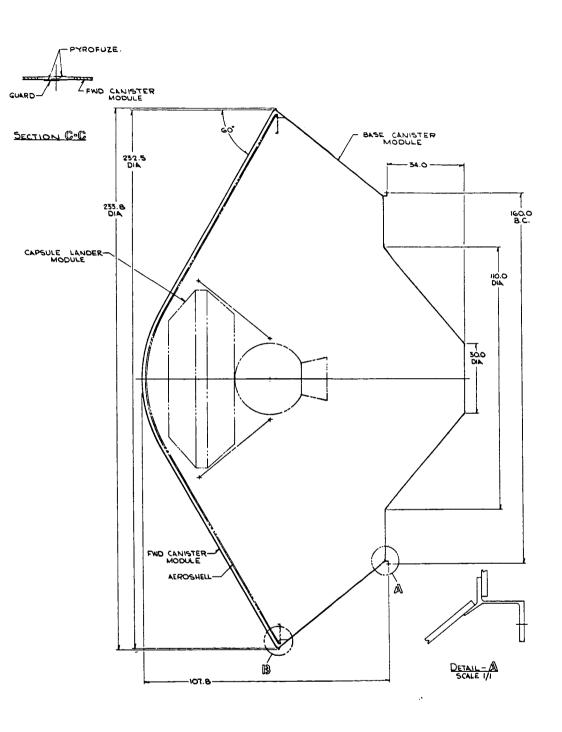
5.1-5-1 A

REPORT F694 • VOLUME II • PART B • 31 AUGUST 1967



gure 5.1-3

5,1-5-2



selected for the preferred approach and the other concepts were discarded. A hinged canister which does not jettison pieces of structure in the vicinity of Mars would appear to be a very attractive candidate from the planetary quarantine standpoint. However, the entire canister (700-800 lbs.) would remain on the spacecraft.

- 5.1.2 <u>Canister Structure</u> The tradeoff analyses and design of the structure were primarily concerned with the following areas:
 - a. Study of the pressure level to be used.
 - b. Determination of the shape of the forward canister (conical or spherical)
 - c. Definition of the material and type of construction
 - d. Evaluation of a canister which acts to support the capsule by attachment near the maximum diameter of the Aeroshell.
 - e. Definition of the field joint for installation of the capsule
 - f. Sealing of the field joint and the canister structural joints
 - g. Definition of the means and penalties of providing protection against meteoroid penetration

An aluminum semi-monocoque canister, having a 3.75 psi burst pressure and a spherical forward canister shape was selected. The field joint, located at the maximum diameter of the canister, also contains the Confined Explosive Separation Device (CESD). The joint is sealed by an injection groove sealing technique derived from that used for integral fuel tanks. A separate adapter was choosen for the preferred design (see Section 5.2). Meteoroid protection to a probability of no penetration of .995 (NASA LRC Criteria) would require an addition of approximately 150 pounds to the canister as well as a reduction of volume available for the capsule.

5.1.2.1 Interface Constraints - A critical condition in the design studies and analyses is the allowable static and dynamic envelopes specified for the capsule in the launch system flight shroud. The envelope specified is a 240-inch diameter cylinder with the fore end capped with a 143-inch spherical radius (Figure 3.1.4.8-1 of Reference 5.1-1). The canister lateral dynamic excursion was estimated, pending dynamic analysis of the complete launch vehicle, to be 1.25 inches toward both the 240-inch envelope and the 228-inch diameter capsule. The capsule dynamic excursion was also estimated at 1.25 inches. This leaves the maximum allowable structural envelope of the canister, including the insulation, in the plane of the capsule base diameter to be 2.25 inches. This limit is required because the capsule can move independently of the canister motion under the design

approach of a separate canister and Capsule Adapter. If the adapter were integral with the canister, the canister structural envelope could be a maximum of 4.75 inches thick including insulation, as shown in Figure 5.1-4.

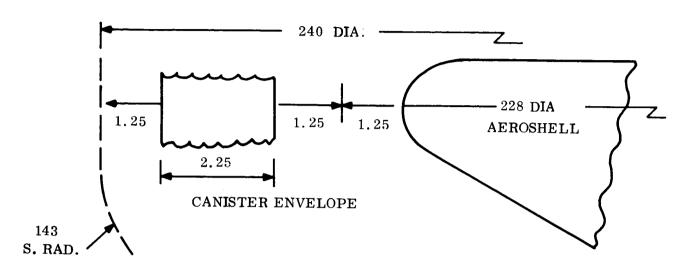
The geometry constraints of the 240-inch diameter dynamic envelope, the 228-inch diameter capsule, and the 1.25-inch maximum dynamic displacement further limit the design latitude for the separate canister and adapter approach. The section modulus and resulting weight of the field joint structure for the separate adapter design increase as the lateral loads due to skin tension increase with the slope of the shell at the field joint ring. Ideally, a 0° shell slope will prevent the laterial loading under shell tension loading but the geometry constraints prevent construction of a near-ellipsoidal forebody shape to attain this slope. The maximum radius of shell curvature possible in the corner of the 143-inch spherical cap and the 240-inch diameter cylinder is a 14.5-inch radius with a slope of 5 degrees to the forward and aft section interface plane.

The canister aft section closure structure isolating the capsule from the spacecraft is also affected by dimensional constraints. If no capsule equipment projects past the capsule to spacecraft interface plane (48 inches from the Capsule base diameter) the closure can be a stiffened diaphragm. If the maximum available volume to the Capsule System is utilized as now planned for the capsule de-orbit motor, then a discontinuous shaped closure is required to go from the assembly station into the 34-inch deep recess of the spacecraft.

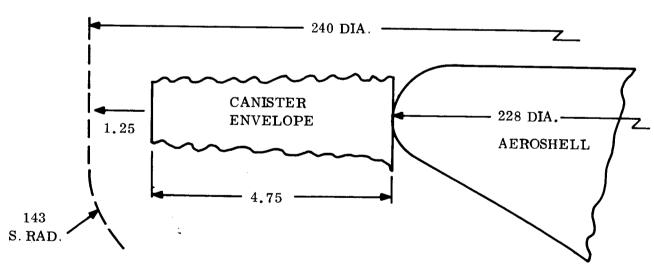
- 5.1.2.2 <u>Structural Tradeoffs and Analyses</u> The principal trade studies are discussed below. These led to the selection of the preferred design presented in the next section which is supported by the analysis in greater depth in the later sections.
- 5.1.2.2.1 <u>Pressurization Level</u> The strength analyses showed that the inertial loading during powered flight, with an assumed 1.20 dynamic factor, can be satisfied with less than the minimum sheet gages. The principal design load condition was the differenctial pressure action on the canister shell.

The design pressure level was selected by considering the variation in shell weight with internal pressure, the weight and complexity of the pressurization and venting control equipment, and the amount of makeup gas and the pressure control required in the 14 to 90 day period between terminal sterilization and launch. Pressure control is required because the internal pressure of the canister will fluctuate due to ambient temperature changes. Selecting a 0.5 psi gage as the minimum desirable pressure from planetary quarantine considerations, the pressure rises to 5 psi gage as the temperature increases from 20° to 160° F.

AVAILABLE CANISTER STRUCTURE ENVELOPE



ALLOWABLE CANISTER ENVELOPE FOR INDEPENDENT MOVEMENT OF AEROSHELL AND CANISTER FOR 1.25 CLEARANCE.



ALLOWABLE CANISTER ENVELOPE FOR CANISTER WITH CAPSULE AND CANISTER AFT BODY CONNECTED FOR 1.25 CLEARANCE.

Figure 5.1-4

A completely leak-proof canister could maintain a minimum 0.5 psi pressure without makeup gas within the temperature range of 20° F to 160° F if the structure is designed for a 5 psi limit pressure. Minimum realistic sheet thickness could satify a 6.25 psi burst design pressure level (based on 5 psi and a 1.25 factor for ground loads) for canister forebody designs in a hemispherical shape, with slightly heavier gages required for conical shape forebodies (e.g., .012 for hemisphere and .016 for a conical shape using aluminum). Structural reinforement at the field joint, however, varied almost linearly with pressure. Further study in the tradeoff in structural weight and pressure control determined that a 3.75 psi burst pressure (2.25 psi limit x 1.67 factor) design was preferred because of reduced weight in the structure. This preference is primarily because of the lateral components of skin tension loads at the field joint. For this limit pressure (2.25 psi), temperature variations must be limited to 50°F to 110°F or relief valve venting and a large makeup supply of sterile gas would be required. 5.1.2.2.2 Forward Canister Shape - The studies on the shape led to the following conclusions.

- o The spherical is at least 40 pounds lighter because skin tension kick loads imposed on the field joint ring area are less than for the conical.
- o The sperical has the maximum internal volume (within the specified envelope) and provides for maximum growth of capsule or canister equipment.
- o The spherical has much higher rigidity (see dynamic analysis below) and can more easily withstand the vibration environment.
- o The spherical is more expensive and requires a longer development cycle because of the compound curvature skin and curved stringer.

<u>Dynamic Analysis</u> - The dynamic characteristics of conical and hemispherical shells were analyzed for a comparison of the stiffness characteristics. The natural frequency with respect to each harmonic for the 2 shell shapes is given in Figure 5.1-5 and shows that the hemispherical shell is more than 4 times stiffer than the conical. For example, the lowest natural frequency is 188 cps and 44 cps, for the hemispherical and conical, respectively.

The dynamic model for analysis of hemispherical honeycomb and semimonocoque shells is shown in Figure 5.1-6. The transient response of the free hemispherical shell was analyzed for an impulse applied at the edge causing rigid body separation at a rate of 1 ft/sec. The results indicate that the induced elastic displacements are small and that no interference with the Aeroshell or the aft canister shell is expected during the separation event.

NATURAL FREQUENCY OF CANISTER

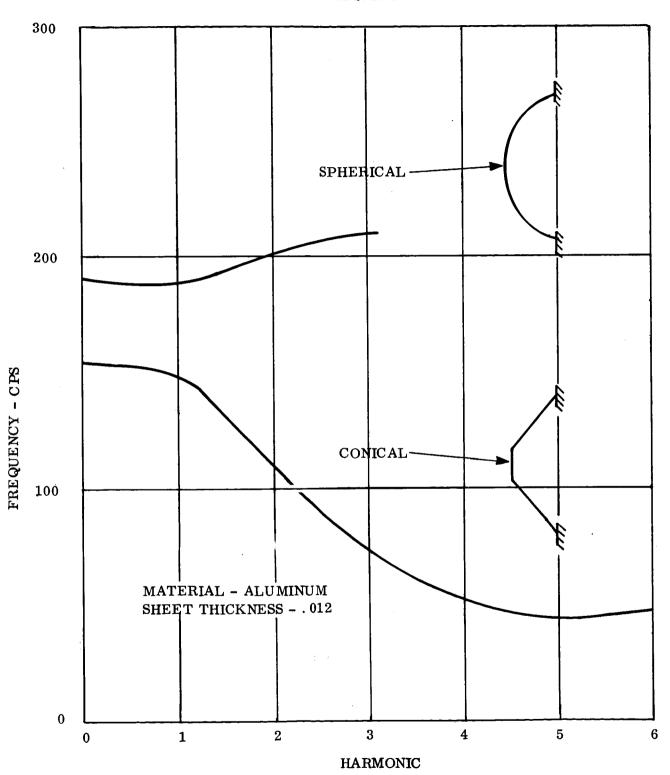


Figure 5.1-5

5.1-10

DYNAMIC MODEL FOR STUDY CANISTER

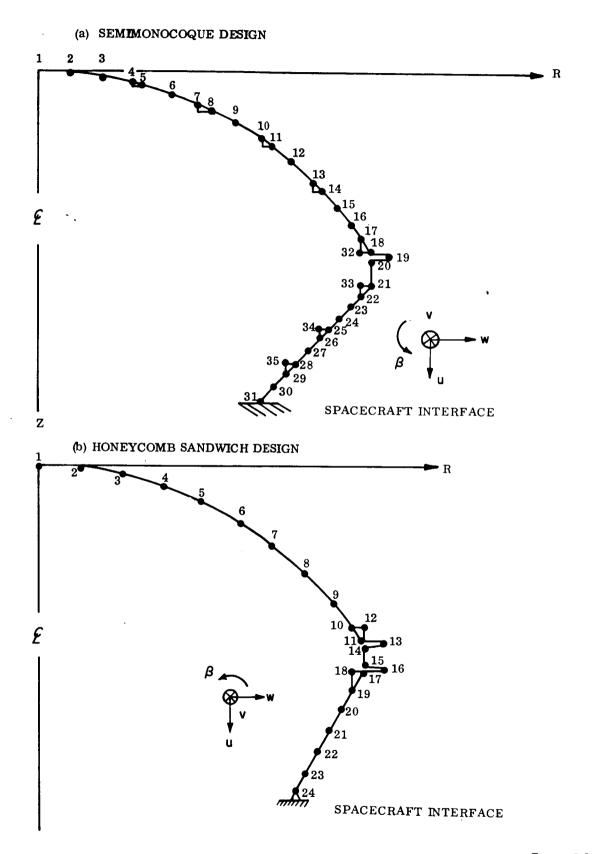


Figure 5.1-6

5.1.2.2.3 <u>Material and Type of Construction</u> - Stress and structural optimization analyses were performed on canisters of hemispherical and conical shapes in monocoque, semi-monocoque, corrugation - stiffened, and honeycomb construction in aluminum, magnesium, beryllium, titanium, steel, and fiberglass materials. The material characteristics of tensile and compressive strength, stiffness and weight properties, and the minimum manufacturing gages realistic for fabrication and handling are given in Figure 5.1-7. The influence of minimum practical gage on the minimum weight of tension structures is shown by the product of material density and minimum gage. The order of increasing weight is magnesium, aluminum, titanium, and beryllium. The ratio of modulus to density, an index for stiffness, shows that beryllium is outstanding, followed by a close grouping of aluminum, titanium, magnesium, and steel.

The eight constructions analyzed ranged from single sheet shells to reinforced, two sheet design. Sketches of the configurations studies are shown in Figure 5.1-8. The unit weight of each construction type in minimum gage sheet is shown in Figure 5.1-9, which shows the further influence of construction on minimum gage/weight design and shows aluminum in monocoque and in reinforced monocoque shells to be the minimum weight approach.

The trade studies performed on the different combinations of shape, design, material, and load distribution were based on the inertial loads of flight and on a range of shell internal pressures from 0 to 15 psi. It was further determined that handling loads, inadvertently applied to the shells during fabrication and assembly, will have to be limited because the skins and stiffeners required to resist such loads are heavier than the design based on the critical pressurization loads. For example, semi-monocoque shells, stiffened in panel sizes of 30 x 25 inches with sheet sized for a 10 psi burst pressure (.022 inch for spherical and .040 inch for conical in aluminum alloy) are limited to concentrated handling loads of 30 pounds on the .022 inch and 95 pounds on the .040 inch aluminum. Internal loads analyses were performed on shells designed to be independent of the Capsule Adapter and integral with the adapter. The analysis showed that the critical loading for design is governed by the internal shell pressure. The inertial loads of powered flight are balanced but are ultimately passed when pressure increases above 1 psi. A 0 to 15 psi range of design pressures was analyzed. A summary of the shell forces for each design is given in Figure 5.1-10.

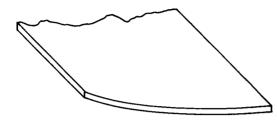
The required skin thicknesses, weights, and the locations of reinforceing members required were determined for the inertial loads and for a pressure

MATERIAL CHARACTERISTICS

Material Material	Alum	ninum	Titanium	Beryllium	Magnesium	Phenolic	Stainless	
Specification	2024-74	7075-76	6A 4V	Cross-Rolled Sheet	HK31A-H24	Fiberglass	Steel PH 15-7 MO	Lock Alloy
Material Density (lb/in. ³)	. 100	.101	.160	.067	.065	.066	.277	.076
Minimum Skin Thickness (in.)	.012	.012	.008	.020	.016	.030	.008	.020
Minimum Face Thickness (Sandwich Construction) (in.)	.010	Ω 10	.005	.010	.010	.010	.005	.010
Ultimate Tensile Strength (1b/in ² x 10 ³)	62	76	134	70	34	40	223	60
Elastic Modulus (lb/in ² x 10 ⁶)	10.5	10.3	16	42	6.5	2.82	2.9	18.5
U.T.S./density (in. x 10 ³)	620	753	838	1045	523	606	805	790
Modulus/density (in. x 10 ⁶)	105	102	100	627	100	38	105	375

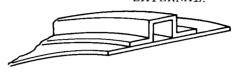
STRUCTURAL CONFIGURATIONS

1. MONOCOQUE.

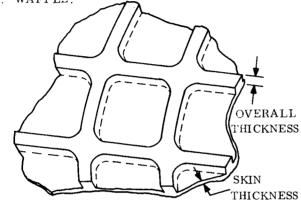


2. RING STIFFENED.

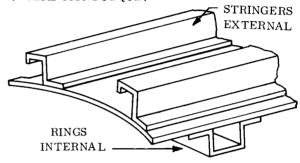
RING STIFFENERS EXTERNAL.



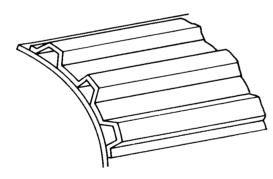
3. WAFFLE.



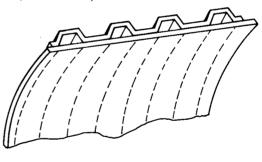
4. SEMI-MONOCOQUE.



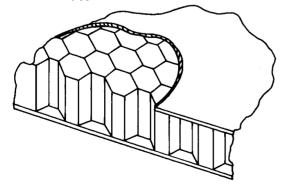
5. AXIAL CORRUGATION. (EXTERNAL)



6. CIRCUMFERENTIAL CORRUGATION (EXTERNAL)



7. HONEYCOMB SANDWICH



8. CORRUGATION SANDWICH

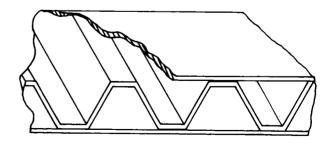


Figure 5.1-8

WEIGHT PER SQUARE FOOT - MINIMUM GAGES

	8	88	94	46	<i>L</i>		66	82	
	.2408	.2928	.3694	.2346	.3177		69/9	.4129	
SS	.3342	.4075	.5142	.8550	.5427		.9424	.7525	
PFG	.2993	.3813	.4811	.2037	.2648		.8818	.3586	laterials.
₩	.1572	.2003	.2527	.2006	.2781	-	.4632	.3532	r all metallic m
88	.2026	.2581	.3256	.2068	.2853		.5968	.3640	thickness is 0.125 and minimum skin thickness is 0.0125 for all metallic materials.
i	. 1936	.2465	.3110	.4938	.3321		.5701	.4347	vimum skin thic
AI 7075	.1830	.2334	.2945	.3117	.4077		.5398	.5488	s is 0.125 and min
AI 2024	.1814	.2311	.2916	.3087	.4041		.5344	.5433	overall thickness
F _b Fabrication Factor Included	1.05	1.20	1.20	1.4	1.25		1.20	1.20	*NOTES: 1. For waffle construction, minimum overall
Material/Alloy Construction	Monocoque	Ring Stiffened	Semi- Monocoque	Waffle	Honeycomb Sandwich	Axialar or Circumferential	Single-Face Corrugated	Double-Face Corrugated Sandwich	*NOTES: 1. For wafi

Figure 5.1-9

2. Minimum thickness for stiffeners-rings, stringers and corrugations – are taken to be same as skin thickness.

SUMMARY - SHELL FORCE RESULTANTS

TOTAL CAPSULE/CANISTER WT. = 5000 LB. $X_{cg} = 26 in$. (AFT OF CANISTER NOSE TIP)

Case Pint. PSI	NXBEG. Lb/In.	NXEND. Lb/In.	N⊕BEG. Lb/In.	N∂END. Lb/In.	P Lb.
FWD. CANISTER	Total Surface Area = 2	270 ft. ²			
For a cone:		$R_{F} = 10.$	$R_A = 118.$	X = 64.	$SCA = 66^{\circ}$
0	0	-5.68	0	0	P = -4148 lb.
1.	10.06	114.3	20.	236.	
5.	50.06	586.3	100.	1180.	
10.	100.1	1176.	200.	2360.	
15.	150.1	1766.	300.	3540.	
AFT CANISTER	(INTEGRAL ADAPTER) Total Surface Area = 2	60 ft. ²		
For a cone:		$R_{F} = 118.$	$R_A = 80.$	X = 48.	$SCA = 43^{O}$
0	-54.80	- 105.4	.0	0	P = -52,980 lb.
1.	38.51	-50.72	161.3	109.4	, i
5.	361.2	226.5	806.7	546.9	
10.	764.6	500.	1613.	1094.	
15.	1168.	773.5	2420.	1641.	
AFT CANISTER	(for Separate Adapter)				
0	-3.78	-11.65	0	1 0	P = -5854 lb.
1	77.43	47.16	161.3	109.4	
5	400.1	265.9	806.7	546.9	
10	803.5	540.4	1613.	1094	
15	1206.9	813.9	2420	1641	
ADAPTER Total	 Surface Area = 276 ft ²				
	sule Wt. = 4400 lb X _{cg} =				
For a Cone:		R _F = 45.	$R_A = 80.$	H = 90.	SCA = 21 ⁰
-	-75.9	-73.37	0.	0.	

X = Axial direction,

BEG = Fwd. face of shell,

 θ = Meridional direction,

F = Fwd.

A = Aft face of shell

END = Aft of shell

Figure 5.1-10

ranging up to 15 psi. The unit weight of construction for each shell design approach in magnesium, aluminum, titanium, and beryllium is given in Figures 5.1-11 through 5.1-14.

5.1.2.2.4 Combined Adapter/Canister - In one design concept, the aft section which contains the capsule release and separation apparatus also serves as the structural transition from the capsule to the spacecraft. In such a design approach, the Capsule Adapter is an integral part of the canister, supporting the capsule near the 19-foot base diameter and providing the maximum usable volume between the capsule and the spacecraft. The field joint rings of the fore and aft canister sections are of minimal weight under the lateral loading component of the skin pressure induced tension because the Capsule structure provides a ring stabilizing effect. Another design approach analyzed, in various combinations of material, construction and shapes, was based on separate canister and adapter structures. Superior structural and dynamic response is obtained under powered flight conditions by providing capsule support inboard rather than by supporting the capsule near the maximum diameter of the Aeroshell. Temperature control of the capsule is more favorable using the separate interior adapter. A third advantage of this separate adapter design over the canister with an integral adapter design is that it facilitates the assembly and inertial platform alignment of the capsule to the spacecraft. These approaches are more fully discussed in Section 5.2 of this volume.

5.1.2.2.5 <u>Field Joint and Canister Sealing</u> - The field joint for installation of the Flight Capsule can be combined with the device used for in-flight separation or could be entirely separate. Maximum leak-tightness must be an over-riding criteria in either case. The use of 0-ring and other elastomeric seals and metallic seals was considered.

The selected approach is to use a field joint which incorporates the separation device (CESD) in grooves in one of the matching rings of the bolted joint. This leads to minimum weight since the bolts and rings function both as the field joint and as functional parts of the CESD. For gas-tight sealing of the joint an approach was selected which has been used successfully on integral fuel tank designs. Details F-F and G-G of Figure 5.1-1 show a channel sealing technique wherein after joint assembly a sealant is injected into the channel groove through holes in the ring flanges. A room temperature curing compound (RTV-560) was selected as the sealant because of operational flexibility. The channel is placed on the interface bolt centerline where gaps and mismatches are minimized by the

STRUCTURAL DENSITY - MAGNESIUM

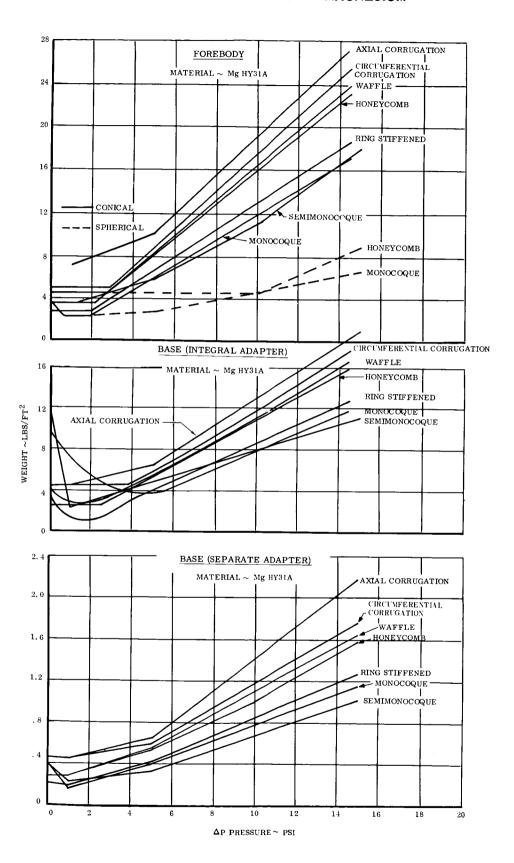


Figure 5.1-11

STRUCTURAL DENSITY - ALUMINUM

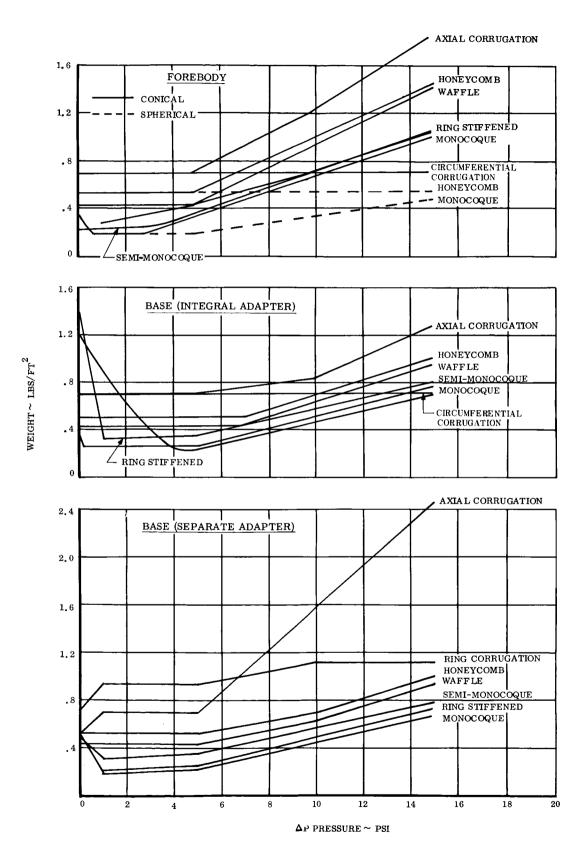


Figure 5.1-12 5.1-19

STRUCTURAL DENSITY - TITANIUM

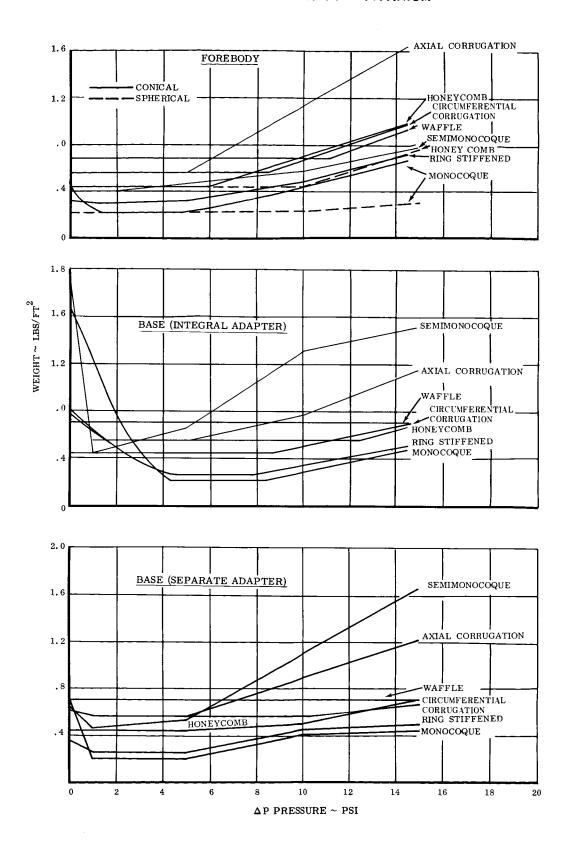
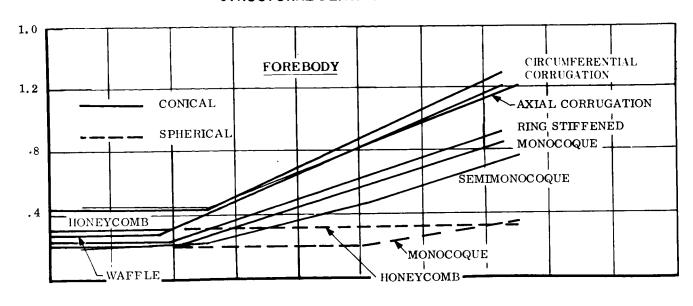
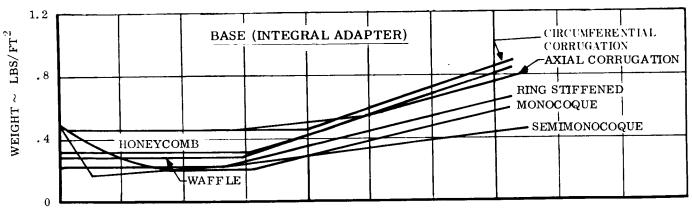
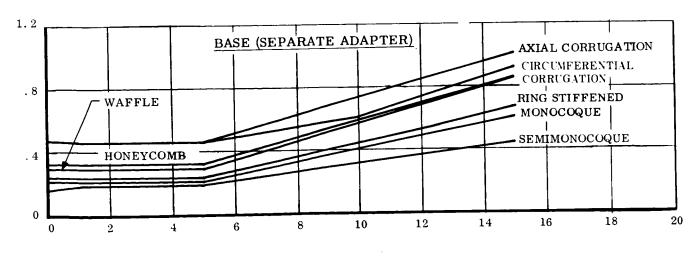


Figure 5.1-13

STRUCTURAL DENSITY - BERYLLIUM







 ΔP PRESSURE \sim PSI

Figure 5.1-14

bolt preload. This method provides a reliable and reproducible seal and minimizes fabrication costs by not requiring abnormally high tolerances on groove dimensions. Field joint bolts have been spaced at a 2.5 inch pitch to avoid excessive gapping between bolts of the mating flanges under the internal pressure.

All of the other joints and penetrations in the canister wall will also be sealed with RTV-560 to obtain a completely sealed enclosure with maximum reliability and retention of gas-tight integrity.

5.1.2.3 <u>Preferred Canister Design</u> - Based on the results of tradeoffs and detailed design studies of the canister and adapter, a canister independent of the adapter and constructed of modified-hemispherical forward and aft section shells was selected as the preferred design for the 1973 Mars mission.

The forward and aft sections of the canister are as hemispherical in shape as possible within the envelope constraints and are made of 2024-T4 aluminum with zee section meridional stiffeners to provide for inertial loads and general ground handling requirements. No rings are required for the design load of internal pressure. Eliminating rings relieves the stiffeners of the additional thickness required to carry the bending induced by the constraint of the rings. The canister is designed for a burst pressure of 3.75 psi with the pressurization and venting equipment limiting the pressure during phases in the ground environment, launch operations and powered flight to less than 2.25 psi. Details of the design are given in Figure 5.1-1.

A torus segment is used on both sides of the field joint ring to provide a smooth transition of load between the two large radius hemispheres. The stresses in this section are a direct function of the two radii being joined, with the lower stress occurring as the radius of the torus is increased. Therefore, this radius was made as large as possible consistent with the space envelope available. The resulting slopes of the skins at the attachment of the torus to the field joint ring, which creates the components of radial compressive loading, establish the requirements for this field joint ring. Modification of the aft section contour was required in order to enclose the de-orbit rocket. A conical structure with an aft enclosure made of honeycomb was used due to the tight space envelope near the de-orbit rocket nozzle. An ellipsoidal shape was investigated for both forward and aft sections but it could not be confined within the available space envelope for the forward section.

5.1.2.4 <u>Strength Analysis</u> - The ultimate design loads used in this analysis are based on inertia load factors of 7.35 axial and .98 lateral including a 1.20

assumed dynamic factor, pressure differential load of 0 to 3.75 psi, and thermal loads from cold soak at -150°F to sterilization at +256°F. Ground handling and transportation loads were considered in the overall design concept; however, the effect of these loads can be minimized by precaution during fabrication and checkout so that they will not penalize the structure.

The pressure loads are resisted by the membrane action of the thin sheet material. Since this loading always induces tensile stresses in the hemispherical sheets, local wrinkling problems caused by the manufacturing processes or thermal effects are self-relieving and, hence, of secondary importance. Inertial loads on the canister, caused by its own weight, were transformed into equivalent pressure loads and found to be negligible in comparison to the 2.25 psi limit pressure. A check made on the buckling capability of the .012 aluminum shell stabilized by the stiffeners, for an axial load of 7.35 g's and no internal pressure, showed the structure to be adequate. Ground loads are resisted by the stiffeners of the semi-monocoque structure stabilized by the sheet and by handling OSE.

Current analytical techniques were utilized to provide gross structural verification of the preferred canister design. Emphasis has been placed on those items comprising a significant portion of the total weight (outer shell, rings, stiffeners) with limited analysis covering the remaining items (guessets, fittings, and fasteners).

Skin Thickness - Skin stresses in the canister structure were determined using the MULTISHELL computer program. This program computes stresses, loads, and deflections in any structure of revolution composed of shells (disks, cones, cylinders, toroidal), rings, flange joints, and other elastic systems under the influence of axi-symmetric loads, neglecting the longeron effects.

The results of this program, using the geometry of Figure 5.1-1 and an internal pressure of 3.75 psi, are shown in Figure 5.1-15. A minimum gage (.012 inch) sheet of 2024-T4 aluminum is adequate for the computed meridional and hoop stresses shown in Figure 5.1-15.

An elastic buckling check of the torus section (Figure 5.1-1) of the canister showed that it is stable under the circumferential compressive stresses of 42,000 psi, shown in Figure 5.1-15. This was analyzed, using the method of Reference 5.1-2, with the aid of a computer program at the Army Mechanics and Materials Research Agency, Watertown, Massachusetts.

Field Joint/Separation Ring - The separation ring was designed locally to withstand the bolt breaking load. This load in turn was established consistent with

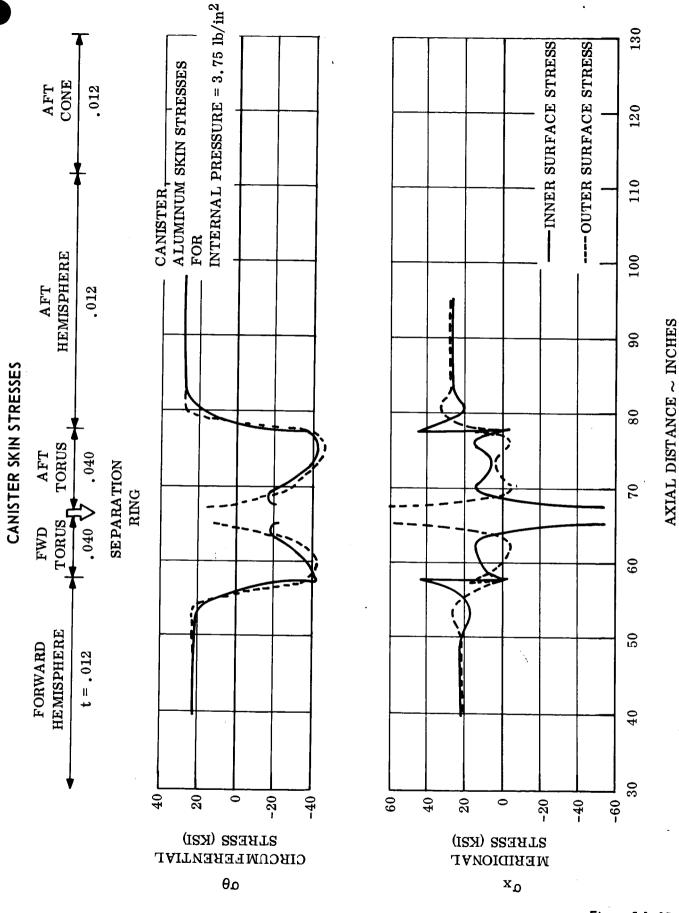


Figure 5.1-15 5.1-24

pressure requirements and bolt spacing which was set at 2.50 inches to minimize defelctions and gaps between bolts to ensure reliable sealing. A practical lower limit of 1000 pounds per bolt was established based on a similar type application on the Gemini Program. Based on a clip effective width of 1.5 inches, the thickness required in the 7075-T6 ring flanges is .15 inches.

The required radial depth of the separation ring is established by overall ring stability requirements. A uniform radial ultimate load occurs from two sources, first, a 40 pound/inch load due to the entry angle from the torus to the ring, and second, a 35 pound/inch load from the discontinuity of the ring and torus. The general stability expression for a ring loaded with a radial load is:

$$P_{cr} = \frac{3EI}{R3}$$

where: EI = Flexural rigidity, 1b-in²

R = Radius of ring, in.

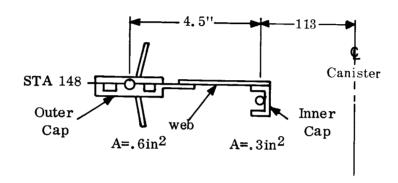
The ring is shown on Figure 5.1-16. It has an EI of 42×10^6 lb-in² and a radius (R) of 115 inches. With these properties, P_{cr} is 82.7 lb/in. which is adequate to carry the 75 lb/in applied. The hoop stress due to the radially applied load is 4800 psi, well below the allowable stress of the 7075 of the 7075-T6 ring.

With this low value and the support afforded the inner cap member due to the eight meridional gussets, inner cap lateral instability is not critical.

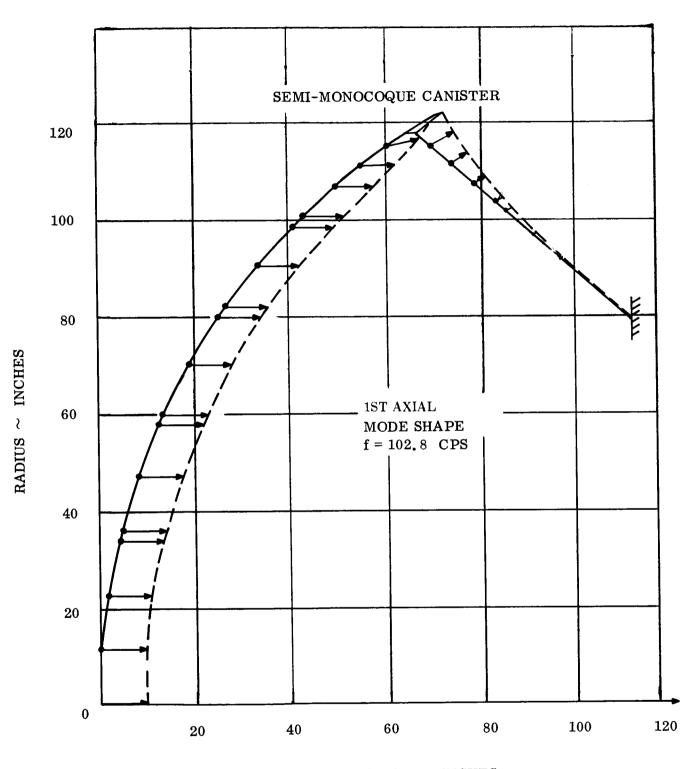
Dynamic Analysis - The natural frequencies of the hemispherical, semimonocoque canister forward and aft shell assemblies in the launch configuration are sufficiently high as to be uncoupled from the estimated booster frequencies ranging from 0 to 50 cps. The minimum natural frequency of the canister assembly is 64 cps occurring in the first harmonic. Figure 5.1-17 describes the mode shape at the fundamental frequencies of the preferred canister configuration for axial and lateral conditions.

5.1.2.5 <u>Meteoroid Protection Studies</u> - It is not possible at this time to define the probability of recontamination associated with meteoroid puncture. Pending more definitive requirements in this area, the canister has been designed on the basis of providing a physical barrier to recontamination on the ground and during flight through the Earth's atmosphere, as well as the conventional requirements of flight and ground loading. The penalties in weight and complexity of providing protection against meteoroid penetration have been assessed in this study and are presented below. As the planetary quarantine allocation by system become better

SEPARATION RING CROSS-SECTION



CANISTER NATURAL FREQUENCY

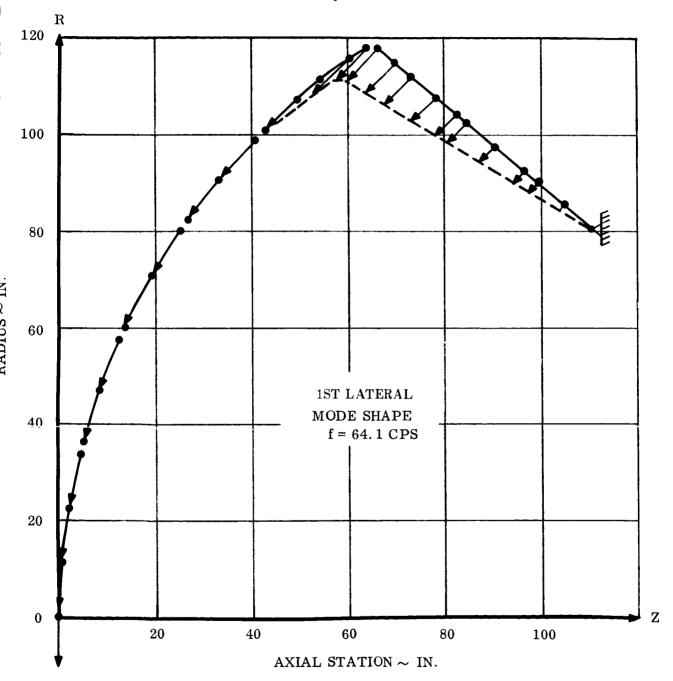


AXIAL STATION ~ INCHES

Figure 5.1-17 5.1-27 ~ \

CANISTER NATURAL FREQUENCIES

SEMI-MONOCOQUE CANISTER



defined and the contribution of meteoroid penetration to recontamination is evaluated, the need for meteoroid protection will be reviewed.

Development of Techniques for Analysis of Two-Sheet Meteoroid Resistant Structures – It is obvious that an analytical solution of the meteoroid/two-sheet structure impact problem, in its full generality, is not possible. Therefore, in order to obtain a solution which is useful for design purposes, it is necessary to use simplified analytical models. Some work has been done in this direction by Maiden, McMillan, and Sennett (Reference 5.1-3) and by Madden (Reference 5.1-4). Madden derived the following approximate formula for the ballistic limit velocity, $V_p, \text{ of a two-sheet structural configuration, both sheets being the same material:} V_p = 4\pi \left(\frac{\sigma_{\text{cr}}}{E} \sqrt{\frac{\sqrt{(1-\mu)}}{3(1+\mu)}} \right) \frac{S^2 d^2 m_1 m_2}{m_2 2} \tag{1}$

Here σ_{cr} is a critical fracture stress, E is Young's modulus, c is the sonic velocity in the target material, and μ is Poisson's ratio of the material of the second sheet. The particle diameter and mass are denoted by d and m_p , respectively. S is the spacing between the two sheets and m_1 and m_2 are the mass per unit area of the first and second sheet, respectively. Maiden, employing a slightly more simplified model, also found the dependence of the ballistic limit velocity on S^2 . A suggestion made by Madden, since the critical fracture stress is not known, was that the entire bracketed quantity in Equation 1 could be considered as a single factor to be determined experimentally. Based on test data from Reference 5.1.5, the quantity in the brackets is 4.95 m/sec for aluminum.

Using this method, the weight of meteoroid protection for non-filled, two-sheet aluminum construction was found. Figure 5.1-18 shows the variation of probability of no penetration with canister weight as a function of spacing and the gage of sheet used. The probability of no penetrations for a structure of .012 in. sheet spaced 3 inches apart is .995. Figure 5.1-19 gives the design details of such a canister construction that satisfies all of the established mission requirements in addition to providing high resistance to penetration at a minimum weight expenditure. This design with meteoroid defense protection weighs 150 1b more than the selected canister design of Figure 5.1-1. In addition, the Aeroshell must be moved approximately four inches aft to obtain the same clearance from the specified envelope.

5.1.3 <u>Separation Studies</u> - The separation of the forward section of the canister requires devices and networks that initiate, release, and eject the forward canister section. The preferred separation technique, shown in Figure 5.1-20, uses

METEORITE CANISTER - WEIGHT FOR PROBABILITY OF NO PENETRATIONS

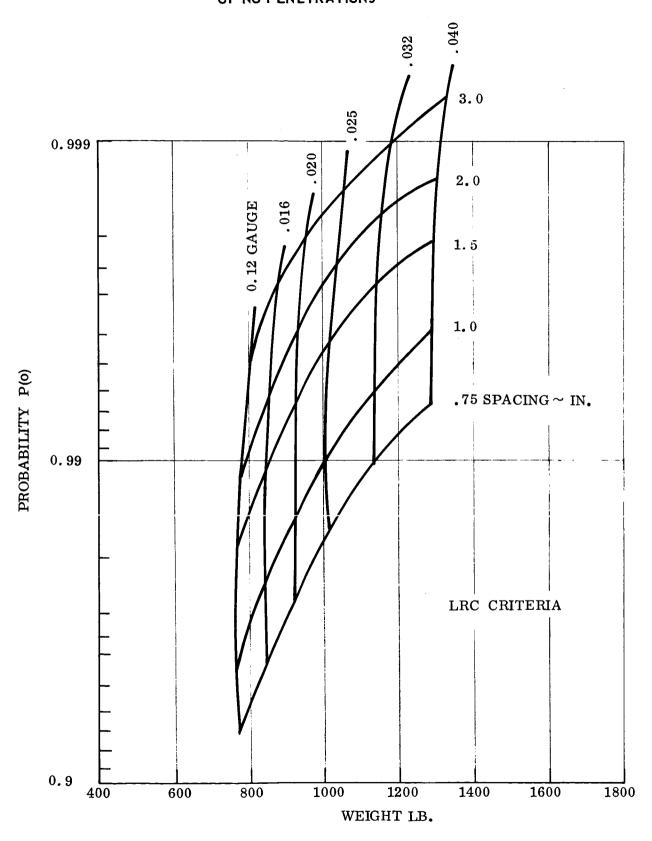
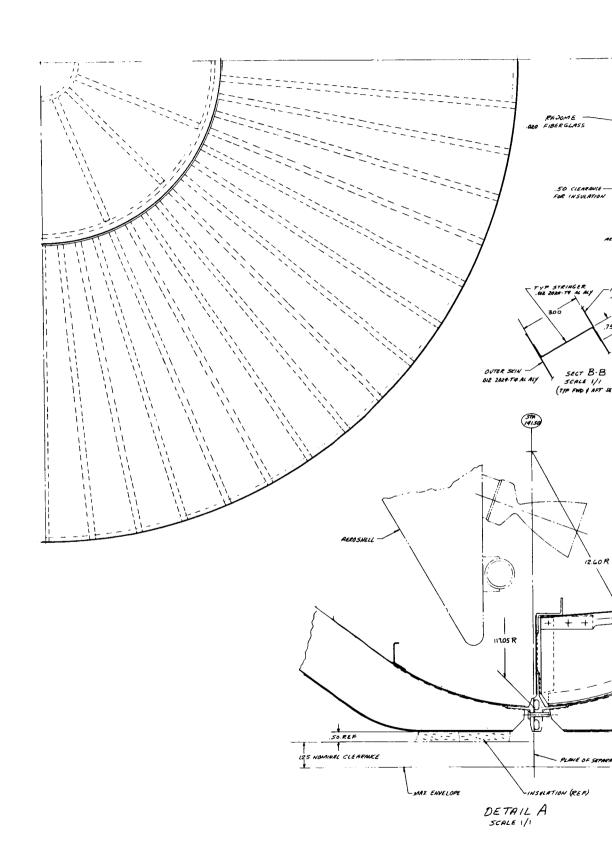


Figure 5.1-18 5.1-29

METEOROID RESISTANT CANISTER STRUCTURE



311-30-1

REPORT F694 • VOLUME II • PART B • 31 AUGUST 1967

MCDONNELL ASTRONAUTICS

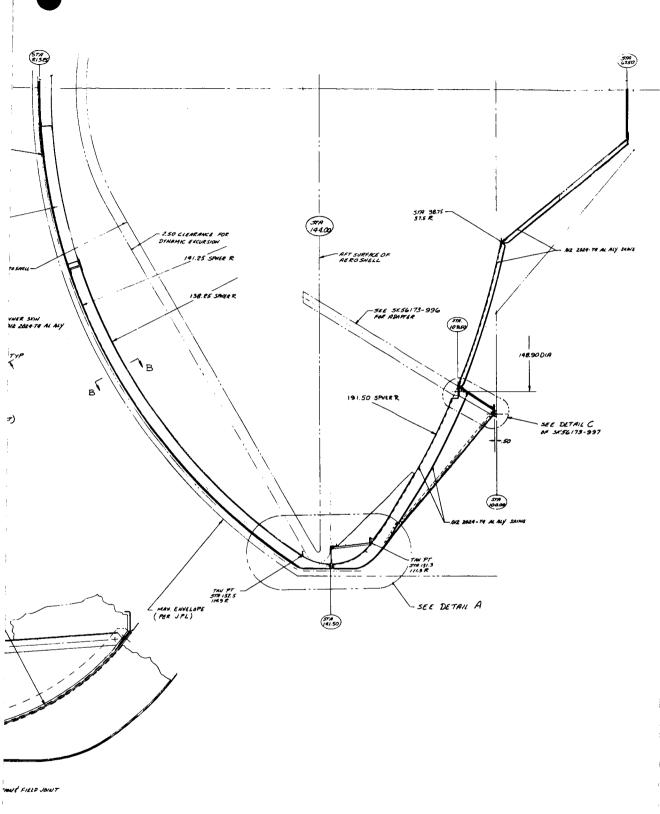
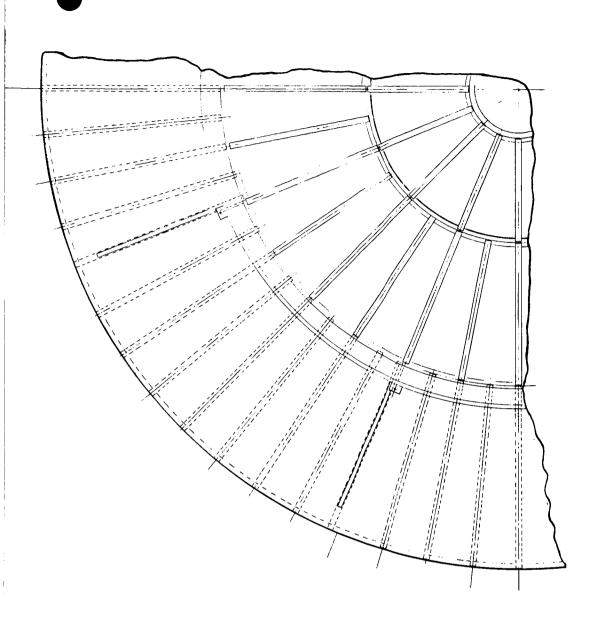


Figure 5.1-19



NOTE; THIS DWG SIMILING TO SKSG173-997 EXCEPT AS SHN

B

CONFINED EXPLOSIVE SEPARATION DEVICE

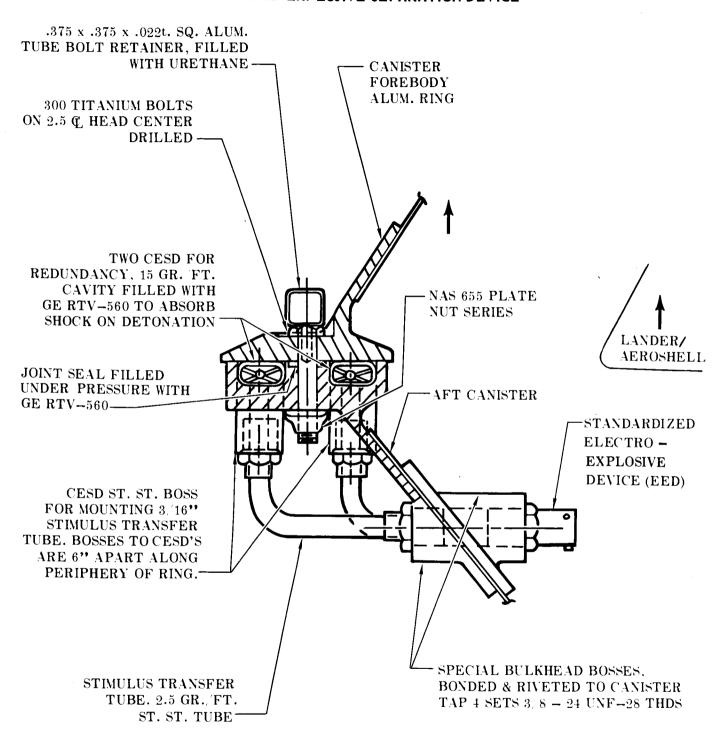


Figure 5.1-20

a dual installation of confined explosive separation device (CESD) which, when detonated, breaks the titanium bolts in tension and ejects the canister forebody. Test data on simulated masses, shows that each CESD is capable of rupturing the bolts and ejecting the forward canister section with a separation velocity from 4 to 6 ft/sec. A system similar to the canister release system, also studied for release of the Capsule Bus supported by an integral adapter (see Section 5.2), required springs to add ejection impulse because of its larger mass.

- 5.1.3.1 <u>Separation Requirements</u> The following criteria were most significant in selecting the design of the release and ejection device:
 - o Continuous load carrying and pressure tight joint for 2.25 psi internal pressure with a safety factor of 1.67. When at 160° F, the ultimate tension load in the separation area and field joint is 225 lbs/linear inch.
 - o No debris or recontamination during or after separation.
 - o System sterilization of $+300^{\circ}$ F for three cycles of 24.5 hrs each.
 - o Use of ETO for decontamination of subassemblies.
 - o Cold soak at -150° F for 380 consecutive days (based on estimated 1979 trip time) including probable non-linear temperature gradient in the canister separation joint, varying from -150° F to $+70^{\circ}$ F.
 - o Electro-explosive devices and firing circuitry shall conform to Reference 5.1.6.

The first three criteria exceed the state-of-the-art of any flight tested separation system: therefore, heavy emphasis was placed on evaluating and finding techniques that could meet these design requirements.

5.1.3.2 <u>Alternate Approaches</u> - The ten release techniques studied during Phase "B" are:

0	Confined Explosive Separation Device (CESD)	Fig. 5.1-20
0	Pyrofuse Sheet Release	Fig. 5.1-21
0	Flat Sheet chemical heat pad	Fig. 5.1-22
0	Cold gas collet release	Fig. 5.1-23
0	Shoe lace "hot wire" release	Fig. 5.1-24
0	Subliming system - Benzoic Acid C ₆ H ₅ COOH	Fig. 5.1-25

- o Continuous linear 360° Electron Beam Separation
- o Continuous Plasma Hot and Cold Torch Separation
- o Traveling Laser Beam
- o Ultrasonic Desoldering Separator

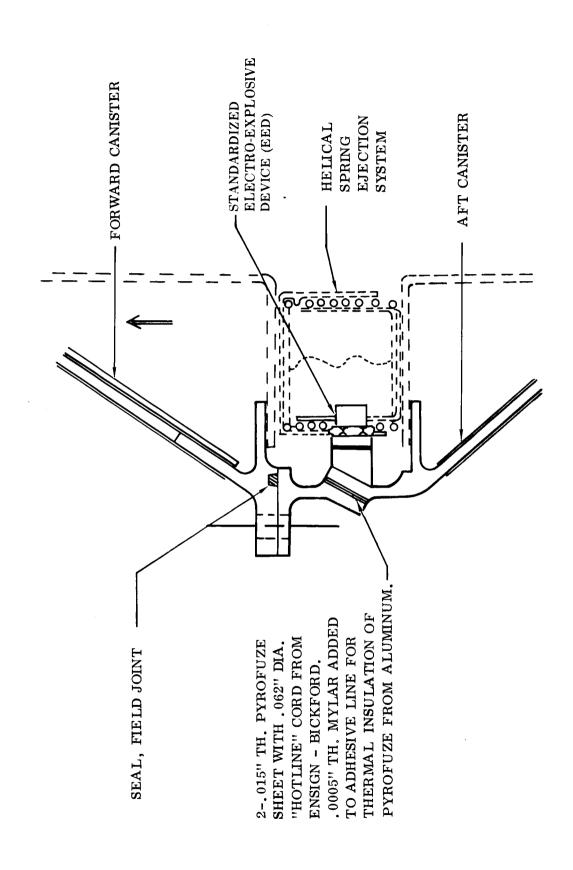


Figure 5.1-21

5.1-33

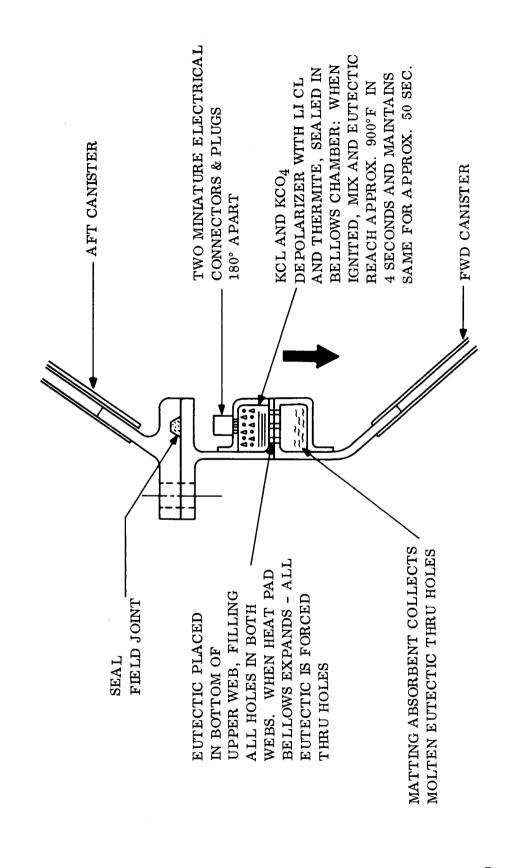


Figure 5.1-22

COLD GAS COLLECT RELEASE

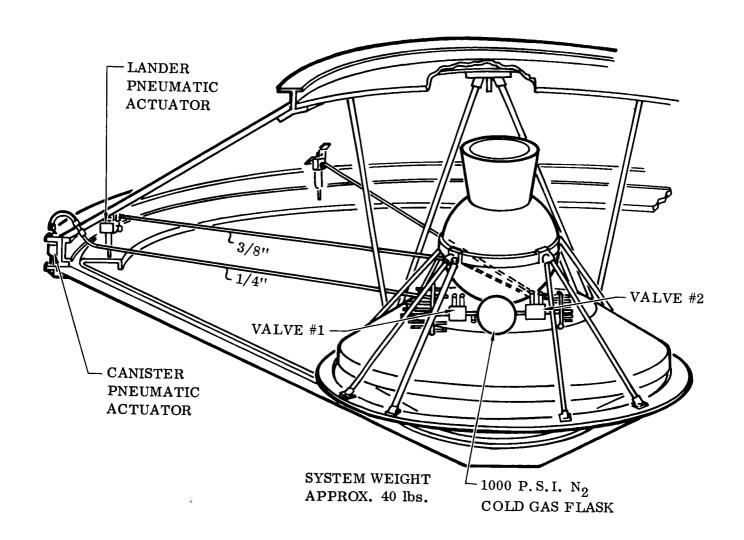


Figure 5.1-23

SHOE LACE "HOT WIRE" RELEASE

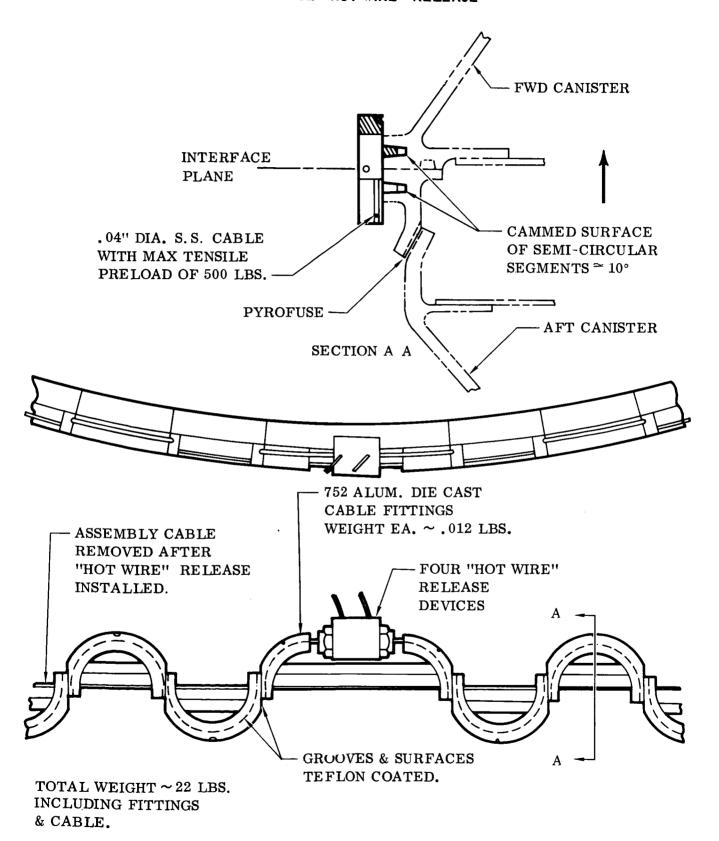
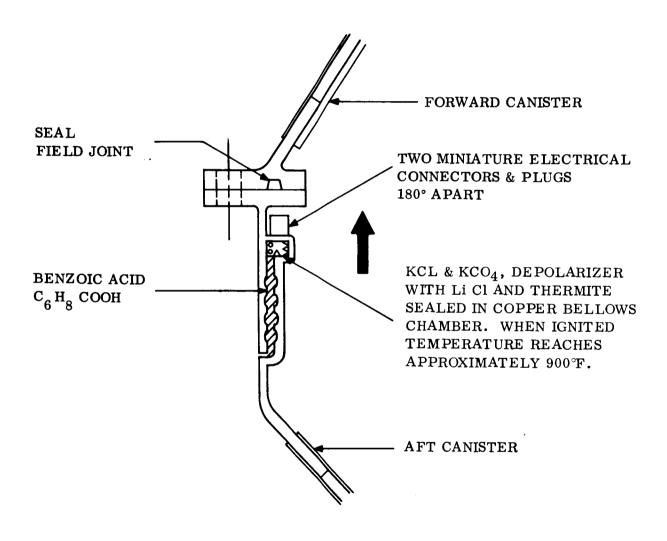


Figure 5.1-24

5.1 - 36

SUBLIMATION RELEASE



The last 4 release systems are not described herein since they were disqualified because of the large electrical power required.

The five ejection techniques considered were:

- o Helical springs ejector
- o Negator spring-ramp Fig. 5.1-26
- o Magnetic ejection Fig. 5.1-27
- o Cold Gas-Pancake Bag ejector Fig. 5.1-28
- o Spring Magnetic dashpot ejector

The low temperature requirement may lead to an advance in the state-of-theart of separation techniques. General Electric is now engaged in test and evaluation of the pyrofuse sheet and chemical heat pad release method and the magnetic ejection device.

A tradeoff analysis was conducted to determine the most suitable separation system from the ten release techniques and five ejection techniques. From this evaluation, the major factors were collated in a weighted numberical selection as covered below.

Canister Separation Analysis - The time-dependent geometry of the forward canister section and the remainder of the Planetary Vehicle determines the maximum angular rate that may be imparted and still preclude collision. The imparted and still preclude collision. The imparted angular rates result from: (1) residual moments in the planetary vehicle; (2) non-uniform release of separation energy; and (3) hinge effect resulting from separation elements.

Figure 5.1-29 illustrates the configuration. The relationship between angular rate and separation velocity is plotted in Figure 5.1-30.

A conservative analysis was performed by assuming no roll moment or rate imparted to the canister and using a ΔV of only 22 inch/sec. For these conditions (with I = 210 slug-ft²) the c.g. offset could be 15 inches before collision occurs. Inasmuch as there is no possibility of such offset, it is concluded that collision probability may be discounted at this time.

5.1.3.3 <u>Selection Characteristics and Evaluation</u> - Figure 5.1-31 tabulates the parameters and operational factors utilized for comparison and ranking of the candidate concepts. Figure 5.1-32 is a numberical rating based on the parameters and factors from Figure 5.1-31. The table shows the relative weights among the approaches finally considered as possible design concepts for the separation.

NEGATOR SPRING - CAM EJECTOR

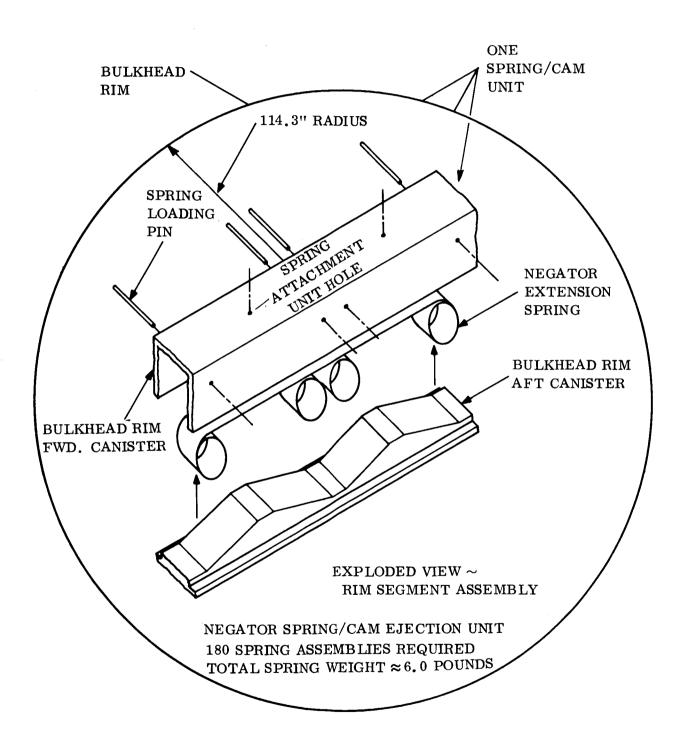


Figure 5.1-26

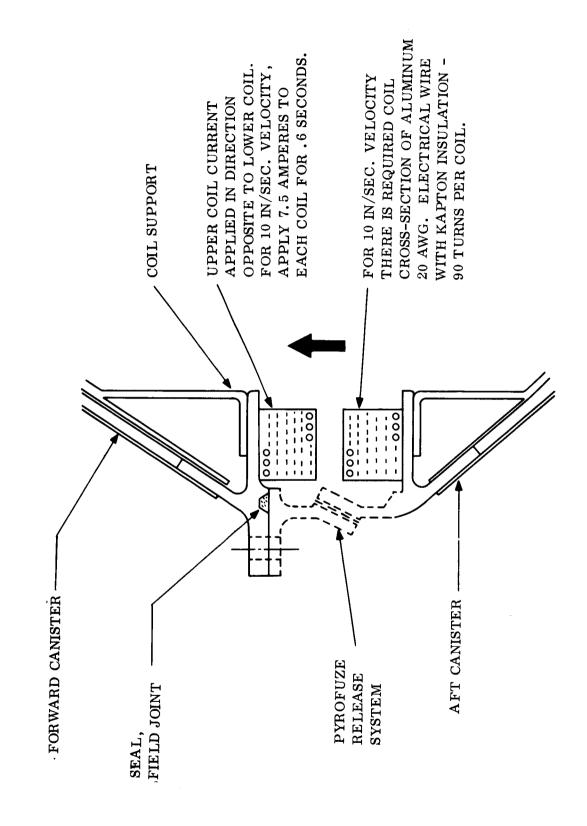


Figure 5.1-27

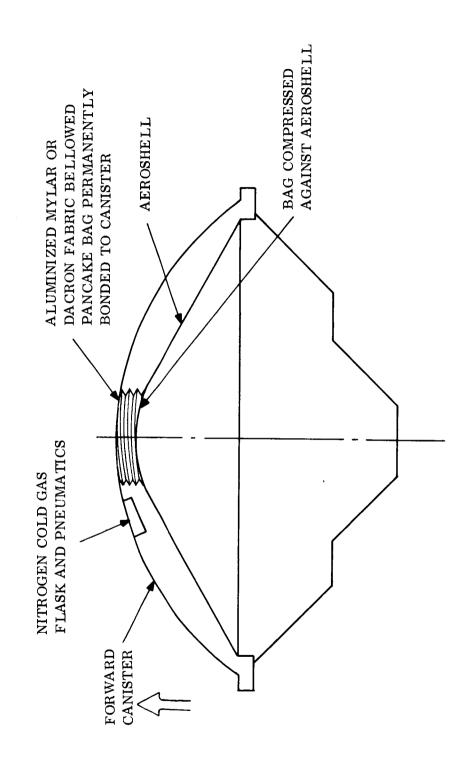


Figure 5.1-28

CANISTER CONFIGURATION SEPARATION STUDY

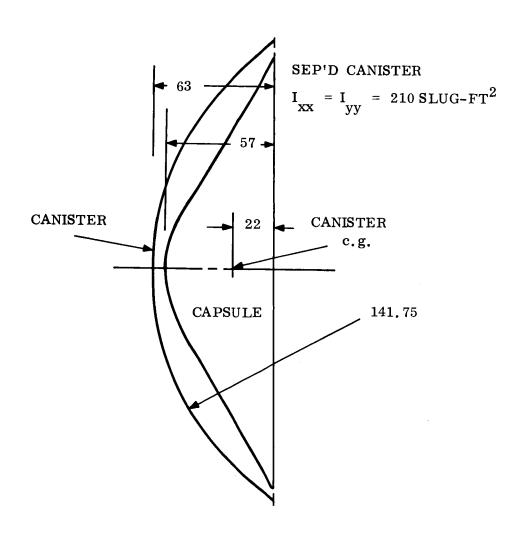


Figure 5.1-29

ACCEPTABLE SEPARATION CRITERIA

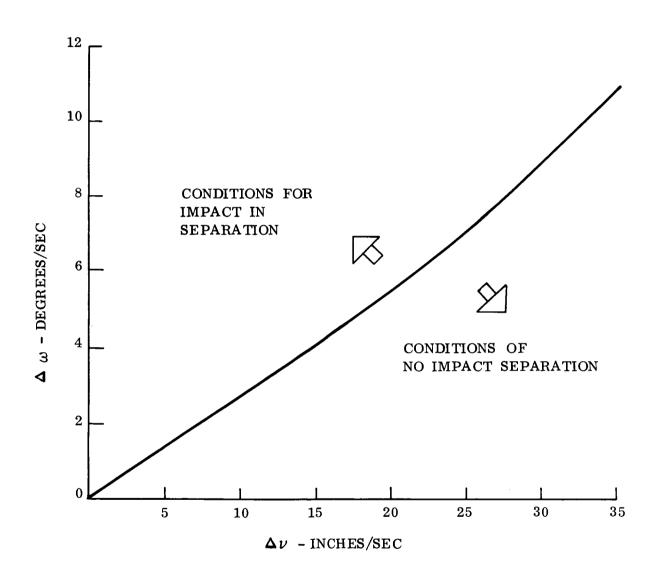


Figure 5.1-30

CHARACTERISTICS AND FACTORS

L_	SOSTEMACASO		REI FASE TECHNIOUES		EJECTION T	EJECTION TECHNIQUES
	ר אואשבו בויט	CESD - BOLTS	PYROFUSE SHEET (CHEMICAL HEAT PAD	HELICAL SPRINGS	MAGNETIC
<u> </u>	WEIGHT (Relative): Weight of prime material; Weight added by required S/S interface; Structural support weight; weight penalty due to	113 pounds with structure interface only.	68 pounds with structure interface only.	90 pounds with structure interface only.	5 pounds — weight of optimum spring system — springs alone.	25 pounds — weight of complete system excluding structure interface.
	redundant configurations. POWER (Electrical): Type of power required; duty cycle; load profile; source; is redundancy required; system size (black boxes).	Redundant ignitors 4.5 amps, for 10 ms each.	Squib Ignition/Redundant. 4.5 amps, for 10 ms.	Squib Ignition/Redundant. 4.5 amps, for 10 ms.	No electrical power required. Energy stored via spring compression.	2.5 kw; use of Squib Ignition. 4.5 amps, 10 ms. Thermal Batteries in redundant configuration activated for ≈ 1 second.
	REDUNDANCY: Require two independent systems; Real time or on board programmed; electrical; mechanical; weight and volume penalty; reliability of operation.	Two CESD units provide complete redundancy. Electrical initiation redundancy.	Two pyrofuse sheets with hot-line cord for redundancy. Electrical initiation redundancy.	Electrical initiation redundancy. Requires two individual joints for physical redundancy.	The use of springs in parallel.	Initiate alternate N-turns for use as a back-up coil. Electrical initiation redundancy.
	SAFETY: During Manufacturing; During assembly; transport; test, both qualification and development; launch-pre-launch check-out; toxic material, sterilization; electrical shock; pyro.	Pyrotechnic/Electro explosives utilized. Require AFETRM 127-1 compliance. Facilities, handling, transportation, etc. require adequate specifications.	Pyrofuse sheet itself not considered as an explosive/pyrotechnic; if used with hot line cord – requires safety handling procedure. AFETRM 127-1.	EED Initiation. Safety required. Tests – high heat at separation joint. (+9000F – R.T.)	Normal safety practices during assembly and test. (Design includes spring limiter.)	Normal safety practices during test.
	CONTAMINATION: Risk during test; risk upon actual separation; risk during handling; risk at final prelaunch check-out/assembly.	Care must be exercised on assembly.	Possibility for contamination exists. Small detached particles result of deflagration.	Possibility for contamination exists. Solder debris may exist if complete joint separation has not taken place.	None	None
	MATERIALS/PROCESSES: New Developments; Vendor dependability; schedule effects; in-house capability; future growth — useful life.	Investigate low temperature cold soak. Probable new sealing technique. Bolt torque at low temperature.	Probable new bonding technique. Investigate low temperature cold soak.	Prevention of cold welding, Investigate low temperature cold soak.	Prevention of cold welding and creep.	Investigate low temperature cold soak. Insulation techniques.
Eiguro 5 1	RELIABILITY: MTBF; Figure of Merit; separation/jettison; electrical apportionment; instrumentation apportionment.	Previous use/test data indicates good reliability at room temperature.	Reliability—a function of configuration. Available test data indicates good reliability at temperature higher than expected environment.	New system. Not previously used. Requires develop- ment.	Reliable, Actual reliability — a function of system configuration.	New System. Not previously used. Requires develop- ment/test.
21	FUTURE GROWTH: Will design meet future more stringent planetary requirements; Increased cleanliness; Adaptable to change of separation point; effect of advanced sterilization procedures.	Excellent for future growth, requires minimum weight penalty.	Mechanical properties and configuration provides limitations. Possible problems with new sterilization techniques.	High weight penalty and fabrication problems for increased load capability.	Adaptable for larger system requirements with relatively low weight penalty.	Not too adaptable for quick growth. Growth in functional capability means weight and power penalty.

Figure 5.1-31

5.1-44 - (

B

Good Good Good Good Good Good Good Good	Good Good Good Good Good Good Good Requires test Good Good	Possible problem area Good Configuration dependent Good Good Good Requires test Requires test Good	Requires test Good Good Good Good Requires test Good	A. Non-operating 1. Sterilization — ETO effects and high temperature 2. Effect of MM 3. Transportation (Vibration) 4. Acoustic 5. Humidity 6. Pressure 7. Lift-off (Launch combined environment effects). B. Operating Low Temperature Deep Space Vacuum
† 4 4 0	res test res test res test	ble problem guration ident ires test	ies ies	MPATIBILL I Y: TO effects and Vibration) combined environment
	res test res test res test	ble problem guration ident ires test	res	PATIBILITY: **Deffects and ibration) Ombined environment
	res test res test	ble problem guration ident	les S	O effects and bration)
	res test res test	ble problem guration ident	ēs	ATIBILLIY:) effects and mation)
	res test	ble problem guration ident	res	ATIBILLIY:) effects and ration)
	res test	oroblem	res	ATIBILIT: Deffects and mation)
	ies test	oroblem	res	ATIBILLIY:) effects and
	ires test	ble problem guration	res	ATIBILITY: Deffects and
	res test	ble problem	res	ATIBILITY: Deffects and
		Possible problem		ATIBILITY: O effects and
				ATIBILITY:
				ATIBILI1Y:
יכלחו כווכון וו לנוי	be problem.			
weight penalty; power requirement high.	Electrical interface. Cold welding may	present problems on bonding.	sterilization and humidity capability.	
lems. Electrical coil	der, aluminum, etc.	sterilization may	design enhances	
		quirements. ETO	quirements. Shielded	final sterilization; vent and pressurization.
<i>V</i> :		trical interface re-	trical interface re-	thermal; testing; structure; instrumentation;
Minimum interface Structure and electrical	face is	Structure and elec-	Structural and elec-	SYSTEM COMPATIBILITY: Electrical;
		Numerous release techniques.	systems-shroud ejection.	compatible with design requirements.
Utilization verified on No data available.	Concept used in Utili Utili Utili	Previous use in time-delay elements.	Mercury; Gemini; (MAC) ballistic	PRIOR USE/TEST RESULTS: Use on previous programs; resultant test/flight data;
		fication tests.	+160 °F. only.)	
prime qualification devices; test chamber area. instrumentation.	Soluer material and prime heat producing area.	ification. Multiple	tiple final assembly tests. (-65°F. to	600
	4	Release without	Piece part qualifi-	QUALIFICATION: Material; vendor; com- ponents: subsystem: environmental tests:
	new system-develop- ment costs.		Range Safety after installation.	
Majority of costs in qualification test.		dualification costs.	sterilization. Special Range Safety after	
minimum cost for the first complete new functional capability. system-development costs.		Manufacture and	Major cost in manu- facture test and	development, test, materials; tools, facilities, transportation; test equipment; sterilization
Minimum coet for		High cost.	T	TOTAL COST: Design; manufacture;
	multiple test speci- mens required. Large chamber – final test	mens required. Large chamber – final test.	mens required. Large chamber – final test.	
		ation/reliability.		
ţ.	plexity is repetitive cree tests to verify oper-	plexity is repetitive tests to verify oper-	plexity is repetitive tests to verify oper-	racinties, special materials; special test equipment; schedule commitments.
<u>-</u>		Prime area of com-		TEST COMPLEXITY: System compatibility;
cy and reliability.		reliability.	bility.	:
parallel system redun- dancy and reliability		program - critical verify redundancy	onments. Test for redundancy and relia-	
		configuration. Test	figuration and envir-	results; research; analysis.
effort. Adapt prev ous test to verify analysis; results to a large con-	sis; test to verify effor	data results to a large load carrying	cepts to the new con-	confidence in test
Minimum development Prove theory; analysis;	<u>-</u>	Adapt all previous	Adapt all previous	DEVELOPMENT REQUIRED: Amount of Engineering design effort: tooling manufacture
in sections — electrically interconnected.	.condens.		turing problems.	
		problem due to thin		requirements; handling, maintenance.
Previous program exper- tolerance-winding, insula- ience. May be some tion, sealing: large assem-	Assembly technique Prev A difficult one. Large ienc	problems. Close tolerances will be a	except for large con-	cesses; meet schedule commitments; safety
A producible system. Large coil winding; Close		Bonding and assembly	A producible system.	PRODUCIBILITY OF SYSTEM: Special skills required: problems created due to new pro-

CRITERIA/SELECTION FACTORS

				RELEASE TECHNIQUES		EJEC TECHN	TION IQUES
			SMDC-Bolts	Pyrofuse Sheet	Chemical Heat Pad	Helical Springs	Magnetic
A. Probability of Mission Success (.35)							
Subsystem Reliability Meet Planetary Quarantine Requirement Vehicle Recontamination Inadequate Subsystem Performance		(.14) (.07)	.120 .070	.100 .060	.084 .056	.112 .067	.098 .070
System Compatibility Return of Engineering Data on S/S Performa No effects on data performance No effects on data transmission	nce	(.035)	.030	.028	.024	.034	.028
Environmental Compatibility Vulnerability to Environment Uncertainty High Confidence in Complete Sterilization		(.035)	.032	.030	.027	.032	.030
5) Contamination of Mars		(.07)	.070	.060	.049	.067	.070
	TOTAL	(.35)	(.322)	(.278)	(.240)	(.312)	(.296)
B. Subsystem Performance (.20) 1) Weight 2) Power 3) System Compatibility		(.06) (.04) (.08)	.045 .030 .067	.060 .030 .060	.042 .036 .056	.06 .04 .072	.036 .032 .064
Demonstration of Meeting Confidence in Test Results Quality of Data							
4) Environmental Compatibility	TOT44	(.02)	.018	.015	.016	.016	.018
C. Development Risk (.20)	TOTAL	(.20)	(.160)	(.165)	(.150)	(.188)	(.150)
Engineering Design/Test Complexity Schedules Transportation Facilities		(.06)	.048	.040	.036	.046	.045
Number of in-series tests 2) Special Materials/Processes/Tools Need for State of Art		(.02)	.016	.016	.012	.016	.016
 3) Duration of Development Cycle 4) Future Application 5) Effects on Other Subsystems 6) Confidence in Results 		(.02) (.02) (.02) (.02)	.018 .020 .020 .019	.016 .018 .018 .016	.014 .016 .016 .016	.016 .018 .020 .020	.016 .016 .012 .016
Reliance on Design Analysis/Test Results 7) Safety Risk of handling/assembly Risk of test		(.04)	.028	.038	.036	.034	.037
Hazards of nature/accident	TOTAL	(.20)	(.169)	(.162)	(.146)	(.170)	(.158)
D. Versatility (.15) 1) System Compatibility	,0,,,,	(.05)	.043	.041	.035	.045	.04
Future Growth Heavier Payloads Compatible with Future Advanced Techniqu a) Material	es	(.025)	.024	.022	.017	.022	.02
b) Sterifization Procedure 3) Flexible Design for Quick Change 4) Accessibility		(.05) (.025)	.042 .021	.042 .020	.035 .017	.042 .021	.034 .017
	TOTAL	(.15)	(.130)	(.125)	(.104)	(.130)	(.110)
E. Cost (.10)							
1) Material Fabrication 2) Safety Launch, Manufacturing, etc. 3) Facilities 4) Redundancy 5) Special Handling Tools 6) Test Complexity 7) OSE 8) Design, Qualification, Produceability		(.01) (.01) (.01) (.02) (.005) (.02) (.005) (.02)	.004 .003 .003 .015 .002 .011 .002	.006 .009 .007 .013 .0026 .015 .0024	.007 .008 .006 .011 .002 .015 .002	.008 .008 .006 .0185 .0024 .016 .0027	.007 .009 .006 .014 .0023 .017 .0027
	TOTAL	(.10)	(.050)	(.073)	(.061)	(.08)	(.076)
	TOTAL RATING		.831	.803	.701	.880	.790

Figure 5.1-32

5.1.3.4 <u>Preferred Approach</u> - The most suitable separation device proved to be the dual CESD that, when detonated, breaks a line of titanium bolts at the field joint, which releases and ejects the canister at more than the required velocity of 1.75 ft/sec. (See Section 2.3.2.5).

CESD has been used to break drilled titanium bolts by McDonnell and was qualified for use on the Mercury-Capsule escape hatches and on the Gemini recovery parachute separation ring. Selection of the explosives is based on their use in over 250 stimulus transfer tubes on each F-111 crew module. In these installations the CESD has been qualified between $-65^{\circ}F$ and $+425^{\circ}F$. There is no physical or chemical reason to believe that with proper selection of explosives for the MDC and the detonator that the CESD will not detonate satisfactorily after a 380 day (for 1979 mission) cold soak at $-150^{\circ}F$.

Qualification tests will be required, but more experience has been acquired with the CESD technique than with any of the other systems evaluated. This system provides both release from the aft canister and a more than sufficient velocity to the forward canister.

The alternate separation technique recommended for parallel development because of potential weight and flexibility gains is the pyrofuse release system shown in Figure 5.1-21. Pyrofuse is a fused bimetal (Palladium-Aluminum-Palladium) which has been evaluated and tested as a release mechanism between the temperature extremes of -250°F to $+300^{\circ}\text{F}$. The test data is published in Reference 5.1-7. In addition to meeting the design and environment criteria, pyrofuse offers the following advantages:

- o It is approximately 40 lb lighter on the study configuration.
- o It imparts no shock to system on deflagration.
- o Its manufacturing tolerances and test complexity are less stringent.

Pyrofuse has not had the flight proven experience of CESD. Therefore, it is considered to involve a greater development risk before a qualified release system is developed. General Electric is presently testing Pyrofuse as a release technique and will evaluate its performance and ability to meet the VOYAGER complete environment criteria.

5.1.4 <u>Pressurization and Venting Studies</u> - The function of the pressurization and venting equipment of the sterilization canister is to: (1) maintain pressure control of the canister during terminal sterilization of the Flight Capsule (2) maintain a positive canister pressure of up to 2.25 psi in the period from sterilization

to launch operations; (3) vent the canister during powered flight to control structural loading to design limits; and (4) assure that the canister is not under pressure during the separation event.

The prime trade-off area is defined by Figure 5.1-33 which shows the pressure rise in a sealed container starting at .50 psi at $20^{\circ}F$ as the temperature rises to $160^{\circ}F$. This indicates 5 psi will be imposed on the canister structure if the above extremes of temperature variation must be tolerated. Hence, the trade-off is between (1) providing the structural weight to withstand a pressure of up to 5 psi limit; (2) providing the pressurization and vent (P&V) equipment weight and complexity to obtain a lower limit pressure, and (3) limiting the allowable temperature variation within the sealed canister to less than $20^{\circ}F$ to $160^{\circ}F$. Of these, a combination of the last two was selected: a design limit pressure of 2.25 psi and a temperature variation of 60° ($50^{\circ}F$ to $110^{\circ}F$).

5.1.4.1 <u>Requirements</u> - The most critical requirements in design of the P&V equipment are discussed in the following paragraphs.

Leakage - In order to maintain a positive internal pressure, leakage must be minimized or a sterilized make-up gas supply must be provided. A maximum leakage rate was determined based on a .50 psi differential inside the canister and an estimated 14 day period without need of make-up gas. Using the perfect gas law and a starting pressure of 15.2 psia, a tolerable leakage rate was determined for reducing the differential pressure to zero. At 15.2 psia the volume of gas in the canister is approximately 850 ft³; at 14.7 psia the gas would occupy 879 ft³; hence, a volume of 29 ft³ could be allowed to escape. On this basis, the maximum leakage rate has been established at .7 cc/sec. for the assumed 14 days without replenishment.

This analysis does not presume that this rate is allowable from a recontamination standpoint, or that a single leak of this rate is tolerable, both of which must be determined from a micro-biological standpoint. Rather, this rate cannot be exceeded if internal pressure is to be maintained to provide structural integrity by preventing pressure loss to a point where a minor temperature variation could cause a negative pressure.

<u>Venting During Launch</u> - During lift-off and ascent, the ambient and canister pressures change as indicated by Figure 5.1-34. The canister interior must be vented so that the pressure differential does not exceed flight limit pressures.

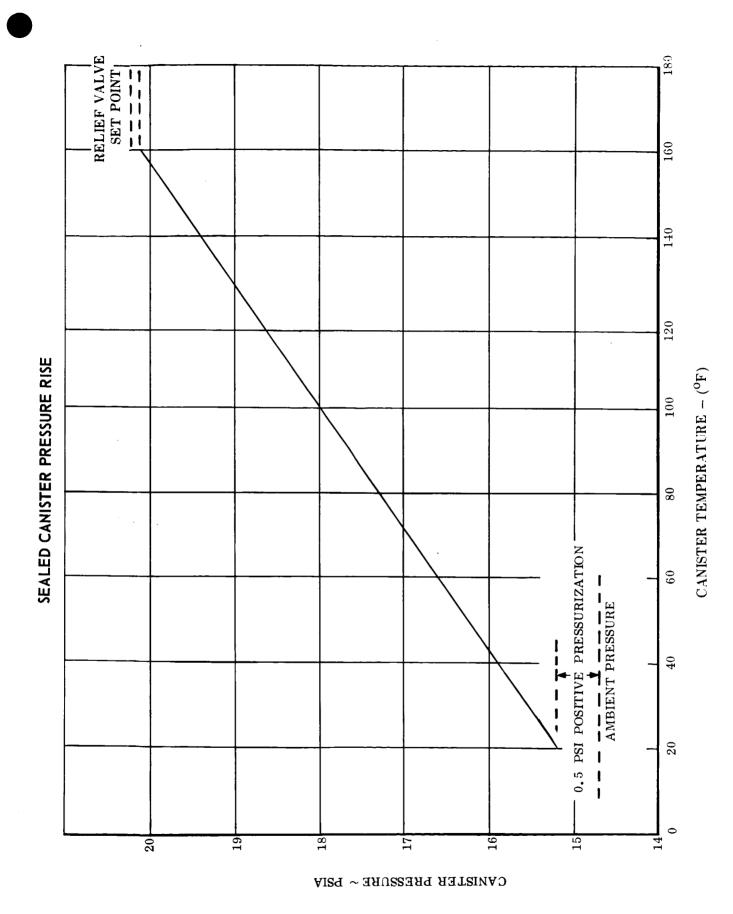
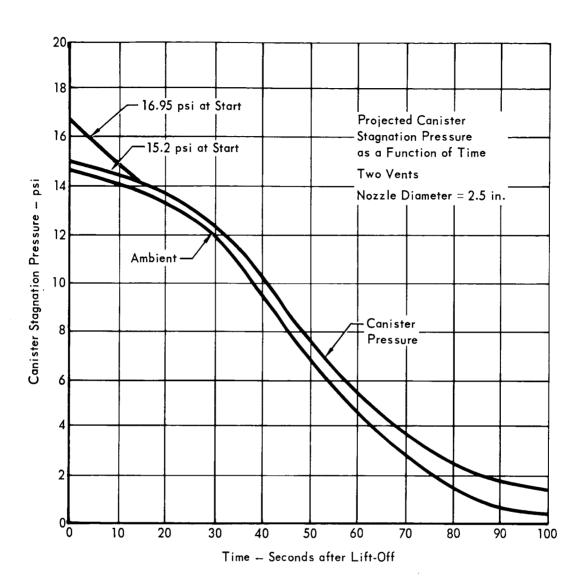


Figure 5.1-33

5.1 - 48

PRESSURE/TIME HISTORY



<u>Backflow Considerations</u> - The problem of flow separation allowing micro-organisms to propagate upstream was investigated. A convergent subsonic nozzle would inherently eliminate the possibility of flow separation. Positive ejection of the vented fluid can be assured with minimum weight penalty by a nozzle built into the vent outlet port. The positive ejection prevents recontamination since it minimizes the exposure to contaminated gas or particles of a filter upstream of the valve.

Canister designs unable to withstand the pressure variation due to temperature extremes may require an internal pressurization system or an OSE make-up supply or a combination thereof. This approach would control the cainster pressure equalization by relieving the gas expanded by a temperature buildup or by pressurizing to maintain the internal canister pressure above ambient while the gas contracted during any cooldown.

<u>Interface Definition</u> - The following interfaces of the P&V subsystem with other subsystems affect its design:

- o Canister Structure The structure provides supports and accessibility for the P&V components and is, in turn, protected from over-pressurization.
- o Electrical Programming and power as required to control the valves are provided by the electrical system.
- o Telemetry and Sensors Information on capsule pressure and valve position are provided by the telemetry subsystem.
- o OSE Interface The OSE provides gases and control for decontamination, during sterilization and for makeup before enclosing in the Launch Vehicle shroud.
- 5.1.4.2 <u>Alternative Approaches</u> A number of venting techniques were considered for the various canister designs studied. The venting design is critically influenced by the allowable operating pressure of the canister structure. Venting studies were made for canister pressures of 1, 3, 5, and 15 psi (design or limit). The factors and relevant characteristics of each technique considered are described in Figure 5.1-35. A mission profile for the preferred approach is described in Section 5.1.4.6. Figures 5.1-36 through 5.1-39 present the four approaches schematically.
- 5.1.4.3 <u>Evaluation and Selection</u> The selection criteria, weighting factors, and relevant notes are presented in Figure 5.1-40. A summation is presented in Figure 5.1-41.

PRESSURIZATION AND VENT EVALUATION

SYSTEM	DESIGN CRITERIA	SOLUTION	COMMENT
ONE PSI SYSTEM	A. To assure a positive internal gage pressure during diurnal temperature fluctuations, a makeup gas reservoir is necessary.	Evacuate or pressurize reservoirs to allow the system to breathe.	A. Size and weight of the makeup gas supply system is a function of the number and severity of temperature cycles and the maximum no-access period.
	B. Maintain adequate flow rate even though a small (one psi) difference exists across the canister wall.	2. Design components to allow desired flow to occur.	B. Large filtration and exit nozzle areas result in a reduction of confi- dence in sterilization.
		3. Install a turbine to effectively increase the back pressure.	C. Complexity and weight of auxiliary parts do not offset component miniaturization.
		4. Install an ejector to effectively reduce the exit pressure.	D. See C above.
FIVE PSI SYSTEM	C. An automatic pressure equaliza- tion system is not necessary to account for diurnal temperature fluctuations.	5. Inherent in the canister design.	E. Adequate to cope with the effect on the stagnation pressure due to the diurnal temperature fluctuations.
	D. Maintain adequate flow rate to limit internal pressure below 5 psig.	6. Design components to establish desired flow.	F. Higher operating pressure allows smaller component size which reduced the weight and improves the dynamic flow characteristics.
	E. Maintain high sterility.	7. Motor-operated port valve.	G. Light weight for this design. A solenoid valve will be traded off based on added reliability to weight increase
		8. Pyrofuse disk that prevents the microorganisms from entering the nozzle.	H. The valve cannot reseal itself to maintain canister sterilization.
		 No mechanical connections are made across the canister sterilization barrier from the sterilization cycle to liftoff. 	I. High assurance against recontamination.
THREE PSI SYSTEM	F. To assure a positive internal gage pressure during diurnal temperature fluctuations, a makeup gas reservoir is necessary.	10. If the temperature range varies more than 75° this pressure equalization system shall be used.	J. It is recommended that the shroud be air-conditioned during its on-pad time.
	G. Maintain adequate flow rate to limit the internal pressure to 3 psi.	11. Design components to maintain adequate flow.	K. Higher flow rate when compared to 5 psi system and smaller area when compared to 1 psi system reduces probability of spore entrance and further migration upstream.
	H. Maintain high sterility.	12. No mechanical connections are made across the sterilization barrier from the sterilization cycle to liftoff.	L. Insures high certainty against recontamination.
		13. Filter component design to cause a low pressure loss.	M. Weight of the subsystem will increase due to additional weight of low pressure drop filter.
FIFTEEN PSI SYSTEM	I. Vent the system.	14. Vent when a ΔP pressure indicator senses a relatively high pressure differential.	N. Sterility is guaranteed at the expense of weight.

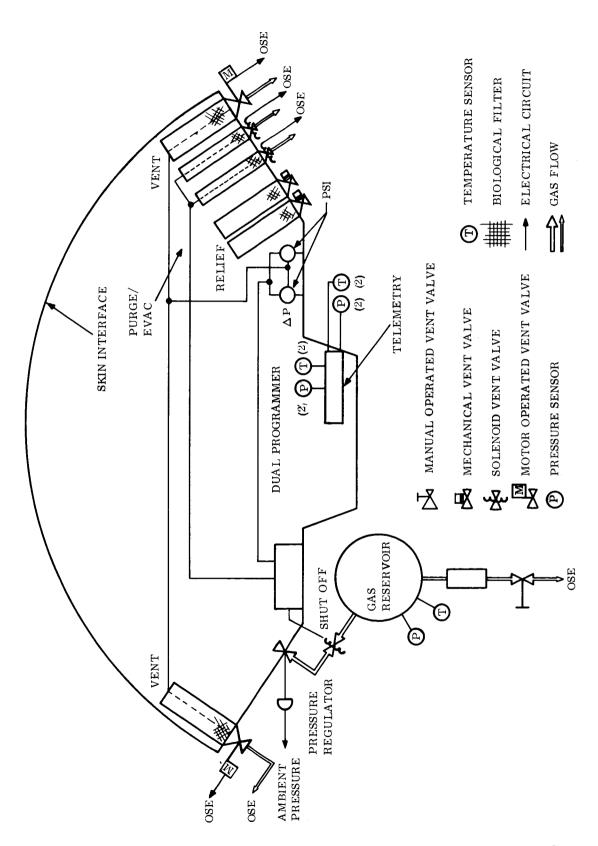


Figure 5.1-36

5.1-52

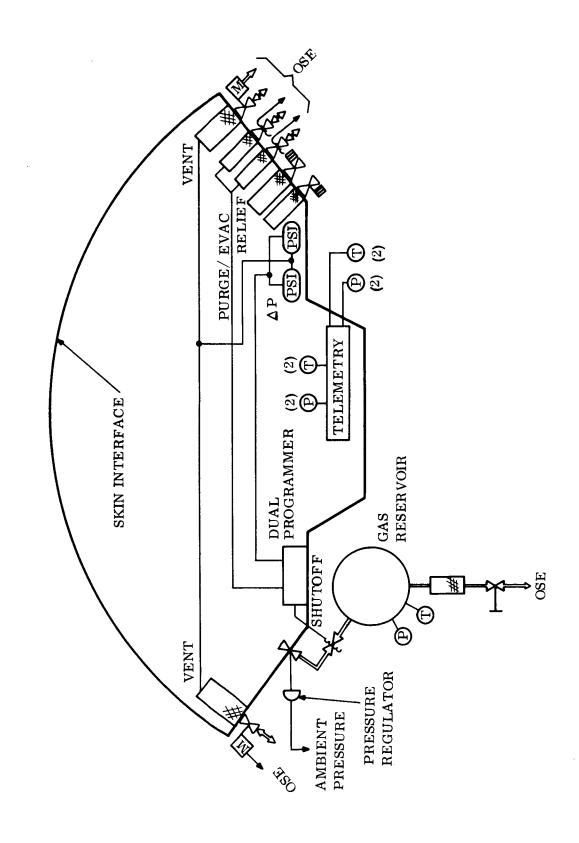


Figure 5.1-37

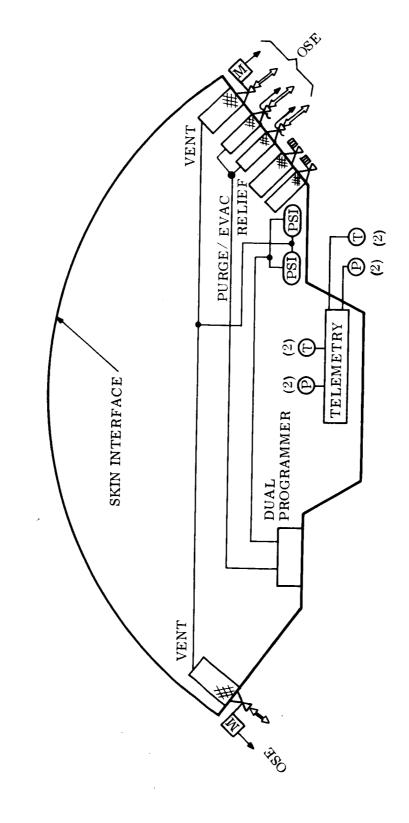


Figure 5.1-38

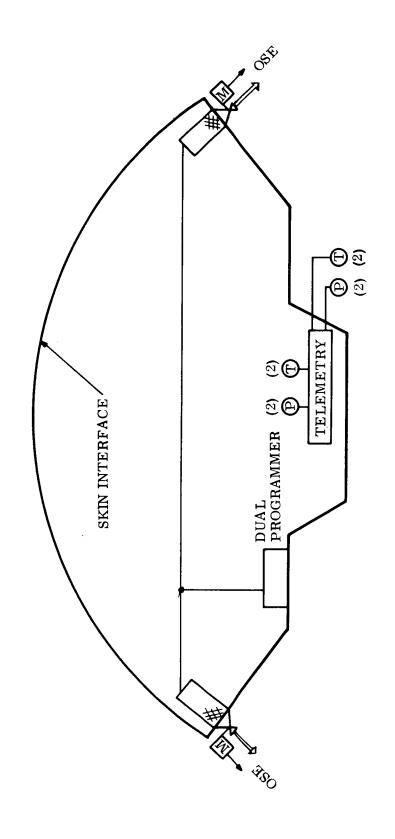


Figure 5.1-39

SELECTION CRITERIA AND WEIGHTING FACTORS

Probability of Mission Success

Comments		Not recommended due to high flow	is higher than 3 psi because no makeup gas system is required.	The 15 psi system has the most effect on other subsystems. Due to its vulnerability, its own reliability cannot be rated higher than the other subsystems.
fnio9 %	.31	.17	.17	.35
ls1oT [[]	32	17	17	39
Probability of Baringle Quarantine	4	2	2	
Possibility of Contaminating Surface	4	2	က	5
ot ytilidsienluV Environmental Uncertainties	10	2	ю	∞ .
Other S/S Reliability	2	က	က	10
Effect on 2\A 19410	2	-	က	10
Subsystem Reliability	10	4	က	ഹ
	1 PSI	3 PSI	5 PSI	IS PSI

1				
Comments	Standardization probably will be compromised.	Higher $\triangle P$ minimizes weight and improves overall operation.	Makeup gas supply or relaxation of diumal temp. is detrimental.	Standardization probably will be compromised.
fnio9 %	.33	.13	.18	.36
lstoT -	22	6	12	24
noitszibrebnst2	5	2		8
Quality of Eubsysdem Serformance	10	က	က	S
Effects on Total System Weight	ന	1	9	10
Subsystem Weight	4	ĸ	2	1
	1 PSI	3 PSI	5 PSI	15 PSI
	Weight Effects on Total System Weight Cuality of Standardization Standardization Total	Subsystem Weight Effects on Total System Weight Subsystem Performance Performance Standardization Total Standardization	Subsystem Effects on Total System Weight Ouality of Subsystem Performance Standardization Standardization Standardization Standardization Standardization	Subsystem 2 4 Weight Effects on Total System Weight Subsystem Subsystem Performance 3 1 2 5 22 Total Inordal 33 % Point

P & V Subsystem Subsystem Development Development		Total %oint	15 .29 High complexity of parts to accomplish venting.
P & V Subsystem C/S Control opment		Total System	
× 8 q		Development	1
흥 -	velopment Risk	gnpzλsfew Ь & Λ	L ISA

Figure 5.1-40

5.1-56 - 1

	Slight advantage over 3 PSI due to lesser complexity.	Greatly affect the canister and separation subsystem.	
	.17	.40	
7	6	21	
က	က	10	
	က	10	
က	က	1	
3 PSI	5 PSI	15 PSI	

		>	2
	:	=	
	-	-	
	4	Ξ	
	1.10	S	
		ă	
1		>	•

	Соттепts	Would presently advance the state-of-the-art making versatility more		Slight advantage due to ground environments. It can withstand and no makeup gas supply.	Present weight is high discouraging addition of extra weight.
ļui	ºd %	.29	.16	.14	.41
	letoT	21	12	10	30
ty to Adapt -norivon- stad la	to Ne	7	5	က	10
d) VJ i i i i	Grow	7	4	က	10
of Accommo- grignerd) g	unteb	7	က	က	10
`		1 PSI	3 PSI	5 PSI	15 PSI

Cost

	Comments	High cost due to component development	reduileu.	Does not need makeup gas system. Advantage over 3 psi	Large cost in other areas such as canister design, and separation.
	Jnio9 %	.32	.32 .19		.29
	lstoT	45	56	27	40
	Кеdundancy	3	က	က	10
	yillidissəccA	6	80	7	10
	OSE Reqmt.	8	က	က	1
	Special Skills, Mat'ls, Etc.	10	S.	4	7
	Other S/S Des. Dev. Mfg.	5	က	7	10
	Design Dev. Mfg.	10	4	က	
36		1 PSI	3 PSI	5 PSI	15 PSI

NOTE: The smaller the number, the higher the rating or ranking.

SUMMÀTION OF SELECTION CRITERIA

	ن Probability of Mission Success	System Performance	i. Development Risk	r. Versatility	.1	Totals	Preferred Order
1psi	.31	.33	.29	.29 .044	.032	.308	3
3psi	.059	.13	.14	.16	.19	.156	1
5psi	.059	.18	.17	.14	.20	.170	2
15psi	.35	.36	.40	0.41	.29	.366	4

NOTE: The number appearing above a diagonal line is a percentage summation of criteria evaluations shown on the following pages for each of the candidates. The smaller the number, the higher the rating or ranking.

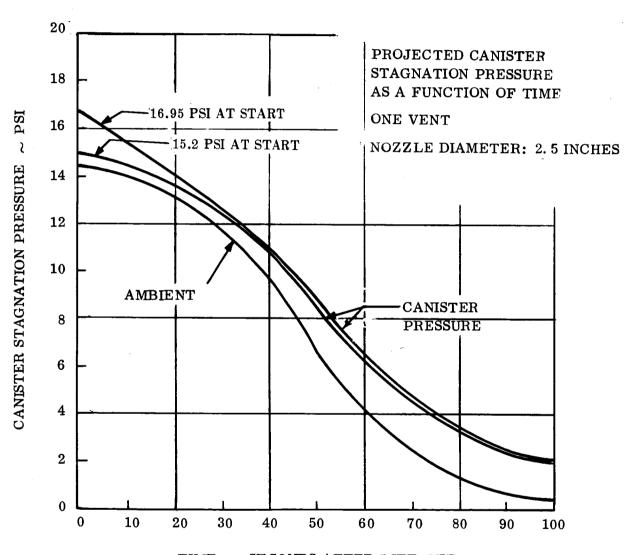
Figure 5.1-41

5.1.4.4 Preferred Approach - The approach selected is a slight variation of the 3 psi design indicated above to be near optimum. It is based on a design pressure of 2.25 psi which leads to a structural flight burst pressure of 3.75 psi. This would permit a ground limit pressure of 3.0 psi based on the 1.25 ground safety factor. However, no significant gain would be achieved by this arrangement, so pressure on the ground will be limited to 2.25 psi. Two sets of redundant components (see Figure 5.1-37) are used in order that no single component failure can result in mission failure. In addition, filters are provided upstream of all valves in order to provide a double barrier against recontamination wherever a penetration of the canister wall exists. The design pressure of 2.25 psi permits a temperature variation of approximately 60° F so a range of 50° F to 110° F can be tolerated by the sealed canister after removal of the OSE makeup gas supply. This gas supply is attached to the purge and evacuation valves to regulate internal pressure and provide circulation of gases during the terminal sterilization cycle and, hence, will also be sterilized. It will remain attached to the canister after leaving the sterilization chamber until just before the launch vehicle shroud is installed.

5.1.4.5 <u>Venting Performance</u> - At lift-off, the vent valves are opened by signal from the programmer so that the canister pressure does not exceed 2.25 psi above ambient on the preferred design. An iterative computer program was used to calculate the pressure in the canister as a function of time using the component characteristics. The program assumes the system reaches equilibrium after each iteration. The perfect gas law is used to calculate the pressure in the canister.

Since redundancy is required, two identical minimum size venting systems will be included in the pressurization and venting subsystem. The canister absolute pressure for two-valve operation is shown on Figure 5.1-34 and for one-valve operation (single failure mode) on Figure 5.1-42. The differential pressures for two-valve and one-valve operation are shown on Figures 5.1-43 and 5.1-44 respectively. Note that the initial stagnation pressure has little effect on the canister pressure through the major portion of the flight. Even with one vent inoperative, the differential pressure falls rapidly and rises again to only about 2.0 psi (Figure 5.1-44). In normal operation with both valves operating, differential pressure does not exceed 1.25 psi (Figure 5.1-43) after the first rapid drop. The anticipated mass flow after launch is presented in Figure 5.1-45 for one vent open.

PRESSURE HISTORY FOR ONE VENT OPERATION

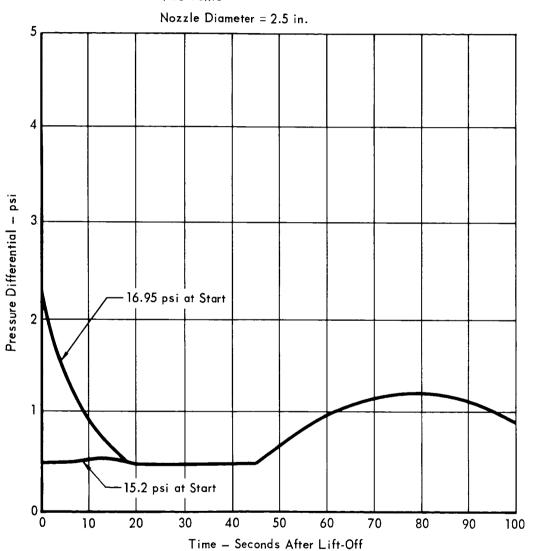


TIME ~ SECONDS AFTER LIFT-OFF

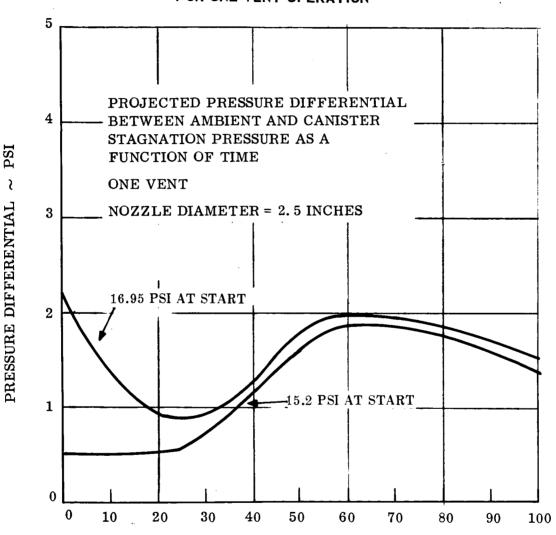
PRESSURE DIFFERENTIAL, TWO VENTS

Projected Pressure Differential Between Ambient and Canister Stagnation Pressure as a Function of Time

Two Vents



PRESSURE DIFFERENTIAL FOR ONE VENT OPERATION



TIME ~ IN SECONDS AFTER LIFT-OFF

MASS FLOW FOR ONE VENT OPERATION

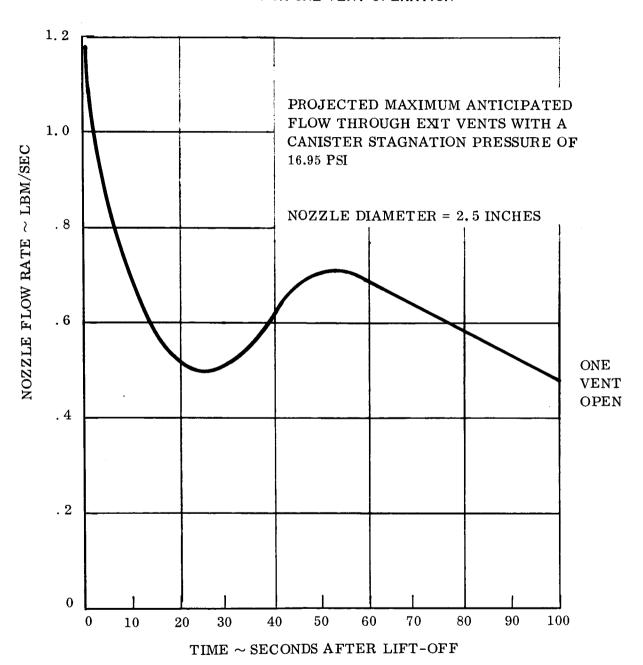


Figure 5.1-45

- 5.1.4.6 <u>Operations</u> A typical mission profile for the pressurization and venting subsystem is as follows:
 - o <u>Decontamination Cycle</u> The purge and evacuation valves are opened and the decontaminating gas enters through one valve while the other valve discharges the displaced internal canister gas. The relief valves will operate maintaining the maximum canister pressure at 2.25 -.10 psi above the ambient in the event that an abnormal condition occurs, such as, clogged filter or an inoperative valve. After the cycle is completed, the purge and evacuation valves are closed to reseal the canister.
 - o Sterilization Cycle Prior to commencing the sterilization cycle, the OSE Gas Servicing Unit is connected to the purge and evacuation valves to regulate the canister pressure and provide circulation throughout the cycle. The canister is also pressurized with sterilized gas through the purge and evacuation valves by the Gas Service Unit as the canister temperature decreases to ambient. (The canister must be positively pressurized per Figure 5.1-46 to approximately 1.1 psi at 70°F before it is removed from the sterilization chamber.
 - o <u>Transportation and Storage</u> OSE will provide a supply of make-up gas, attached and sterilized during terminal sterilization, to compensate the canister for any minor leakage which may occur during transportation and storage. This supply will be removed prior to installation of the shroud assembly.
 - o On Pad (No Access) Normal pressure variations within a temperature range of 50° F to 110° F will not exceed the canister design pressures. (It is recommended that the launch vehicle shroud be air conditioned to minimize the pressure variations and thus minimize leakage.)
 - o <u>Lift-Off and Ascent</u> At T = 0, the vent valves are enabled and venting commences. As the canister internal pressure approaches 0.5 psi, the differential pressure switch operates to close the vent valve. This preserves canister bio-integrity by preventing reverse flow in through the valves.
 - o <u>Earth Orbit</u> After exiting the Earth atmosphere, the purge and evacuation valves will be opened and the canister fully evacuated.

 Evacuation is completed prior to flight shroud separation. The purge and

SEALED CANISTER PRESSURE RISE

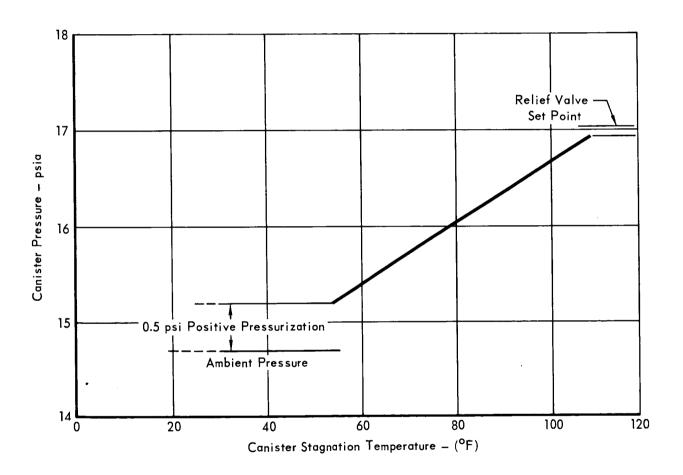


Figure 5.1-46

evacuation valves will then remain open through the interplanetary flight to vent any outgassing by the internal components and preserve the internal vacuum.

o <u>Subsystem Functions</u> - The specific functions of the pressurization and vent subsystem are listed below as a function of mission phase.

Mission Phase	Sub	system Function
Decontamination cycle	1.	Provide inlet and outlet ports
		to canister
	2.	Prevent overpressurization
Sterilization cycle	1.	Provide inlet and outlet ports
		to canister
	2.	Prevent overpressurization
	3.	Maintain sterility
	4.	Permit outgassing
Transportation & checkout to launch	1.	Provide sterile gas to replace minor
		leakage (up to shroud installation)
	2.	Maintain biologically sealed canister
	3.	Prevent overpressurization
	4.	Maintain sterility
Lift-off and ascent	1.	Open vent valves
	2.	Prevent overpressurization
	3.	Close vent valves
. •	4.	Maintain sterility
Earth orbit	1.	Open evacuation valves
	2.	Maintain Sterility
Cruise	1.	Maintain sterility
	2.	Maintain zero internal pressure

5.1.5 <u>Canister Electrical Optimization Studies</u> - Electrical equipment performance to meet the VOYAGER Capsule Bus requirements has been defined and the engineering activities carried through preliminary design. The steps used in configuration development included identifying functional performance, design constraints and sequence of operation. Electrical/electronic components were identified to support a mission objective or limiting constraint. This together with back-up or emergency mode features provides a basis for definition.

- 5.1.5.1 <u>Canister Electrical Requirements</u> The canister electrical equipment has the following functions:
 - o Sequencing of canister venting, evacuation, and separation
 - o Initiation of canister forward section and Capsule Bus separation
 - o Provide Electrical Inflight disconnects (IFD disconnects from Capsule Bus)
 - o Provide interconnecting cabling for Spacecraft, Capsule Bus, and canister equipment.
 - o Provide engineering performance data instrumentation

Definition of the canister electrical equipment has been based on the following constraints:

- o Dual command pyrotechnic firing
- o Pyrotechnic firing source isolated
- o Separation energy contained in canister
- 5.1.5.2 <u>Approaches</u> In the effort to design a canister which would meet the design requirements a initial electrical approach was configured. Variations of this approach led to a total of eleven approaches. These are:
 - o <u>Initial Approach</u> The initial canister approach consisted of self-contained programming initiated by spacecraft command, an integral power source and squib initiated spring ejection. Pressurization and venting was controlled by solenoid valves.
 - o <u>Full Capsule Bus Utilization</u> This approach depends on the Capsule Bus for all programming and power.
 - o <u>Forward Programmer Approach</u> The capsule provides all programming with canister power for the canister equipment.
 - o <u>Integral Load/Energy Storage Approach</u> Each pyrotechnic device has an integral capacitor, charged by spacecraft power, for ignitors.
 - o <u>Passive Canister Design</u> The canister is supplied all programming and power by the Spacecraft.
 - o <u>Minimum Entry Weight</u> Detailed programming and power are Spacecraft supplied. This minimizes the electrical equipment in the capsule and leaves more weight for experiments.
 - o <u>Minimum Entry Weight with Electrical Constraints</u> Programmer power regulator, and power source all mounted in the canister.
 - o <u>Synchronous A/C Power</u> The use of A/C power throughout the system permitting use of magnetic decoupling and separation.

- o <u>Enhanced Contamination Control</u> The use of electromagnetic ejection enhances the control of contamination by providing a low shock ejection at separation. Spacecraft power and programming were utilized.
- o <u>Enhanced Contamination Control with Electrical Constraints</u> This approach utilizes canister power and programming with the previous approach.
- o <u>Diametric Approach</u> Capsule power and control are used with electromagnetic coupling for firing signals across the interface.

The listed approaches have been tabulated in Figure 5.1-47. This chart includes all the configurations of the various equipment controlled.

As a result of constraint evaluation and approach synthesis two approaches were selected for detailed evaluation. These are a revised Minimum Entry Weight with Electrical Constraints, and a revised Enhanced Contamination Control with Electrical Constraints.

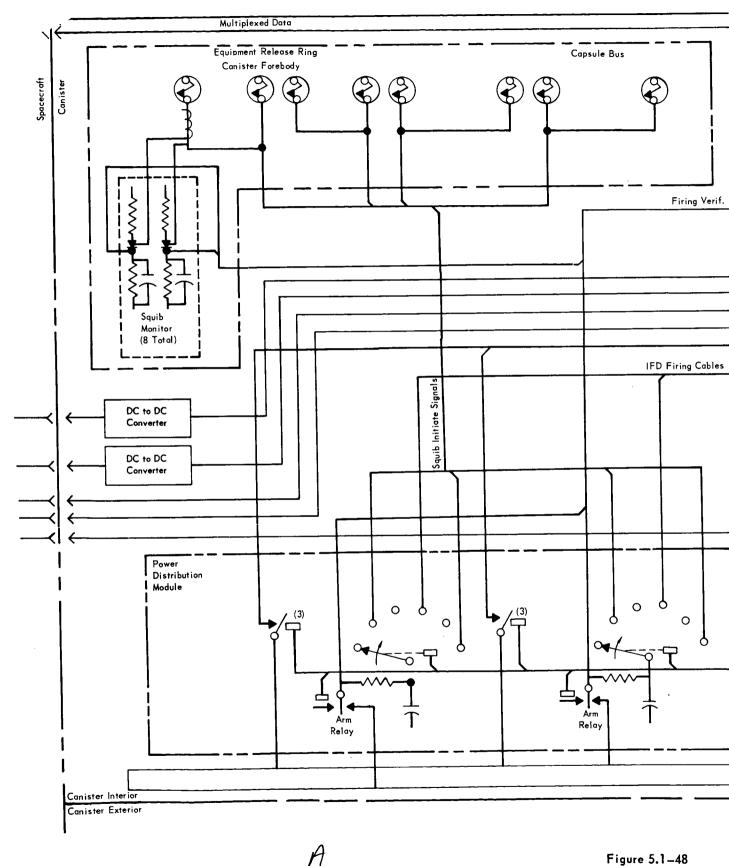
o Revised Minimum Entry Weight with Electrical Constraints - (Recommended Approach) The canister electrical design in this approach, shown in Figure 5.1-48, contains power equipment, including a battery, battery charger, power controller, and power distribution module. The battery is a sealed silver-zinc type which provides power for separation sequencing. The battery charger is a two step float charger, and maintains the battery in a fully charged condition during cruise. The Power Controller provides power and ground return switching within the canister. The Power Distribution Module contains a capacitor energy source, stepping switch, and relays for event sequencing. A command decoder is incorporated to decode the spacecraft commands for the Capsule Bus and canister equipment. pressurization and vent sequence is programmed by the dual programmer and initiation of the valves is provided by the power distribution module. The Dual Programmer also provides the separation sequence commands to the power distribution module. Sensor and event data collected from throughout the canister is commutated and then directed to the spacecraft telemetry link. Separation of the canister forebody results from the Confined Explosive Separation Device and separation of the Capsule Bus is by explosive bolts and the Capsule bus reaction control thrusters.

= INDICATES NON-COMPLIANCE TO ELECTRICAL CONSTRAINTS.

	g ch	Valve	Hi Pwr.						×					
	Venting Approach	S	Lo Pwr.	×	×	×	×	×		×	×	×	×	×
	> ¥		€anidıu	Z	z	Z	z	z	z	Z	×	z	z	×
	<u> </u>		Pneumatic						×					×
L	Ejection Method	Solenoid	Hi Vel.			×	×							
	Ē	S	Lo Vel.						-	×	×	×	×	
		ļ	Sgning2	×	×			×						
	Release Method	:	lgniter					×		×	XFMR			×
	~ ₹		sdiup2	×	×	×	×		×			×	×	
	rce		[External	FROM S/C	FROM CAP.	FROM CAN.	FROM S/C	FROM S/C						FROM CAP.
TRIX	Type of Energy Source		Capacitor	CAN.	CAN.	CAN.	CAN.							
W	<u>ਜ਼</u>		Auto Activated Batry						×	×				\times
Ä			Manual Btry			×			l		×	×	×	
CONFIGURATION DEVELOPMENT MATRIX	of urce		Regul ation	CAN.	CAP.	CAN.	S/C	2/2	S/C	CAN.	CAN.	S/C	CAN.	CAP.
EVEL	Location of Energy Source		Stored	CAN.	CAP.	CAN.	CAN.	ı	ı	1	1	ı	ı	
N D	급		- Риіл Р	S/C.	CAP.	CAN.	3/0	S/C	CAN.	CAN.	CAN.	CAN.	CAN.	CAP.
Ĕ	Power Type		a.c.								×			×
JRA			.o.b	×	×	×	×	×	×	×		×	×	
ಠ	nd- Type		Simultaneous Commanded		×		×	×	×					×
NO.	Redund- ancy Type		Sequence Commanded	×		×				×	×	×	×	
_	ler ion		Spacecraft	×		*****		×		×	×		×	
	Data Encoder Location		Sanister				×		×			×		
			Capsule		×	×								×
			Supplementary Programming	Z	Pyro	Pyro	Z	z	z	z	Pyro	z	Z	PNEU
	gu _		Spacecraft				$[\times$	$[\times$	[×			[×		
	Programming Location	-	Canister	×						×			×	
	Prog		Capsule		×	×					×			×
				Baseline Concept	Full Capsule Bus Utilization	Forward Programmed Approach	Integral Load/Energy Storage Approach	Passive Canister Design	Minimum Entry Weight System	Minimum Entry Weight Elect. Constraints	Synchronous a-c Approach	Enhanced Contamination Cont.	Enhanced Contamination Contr. W. Elect. Constraints	Diametric Approach
					~	-								

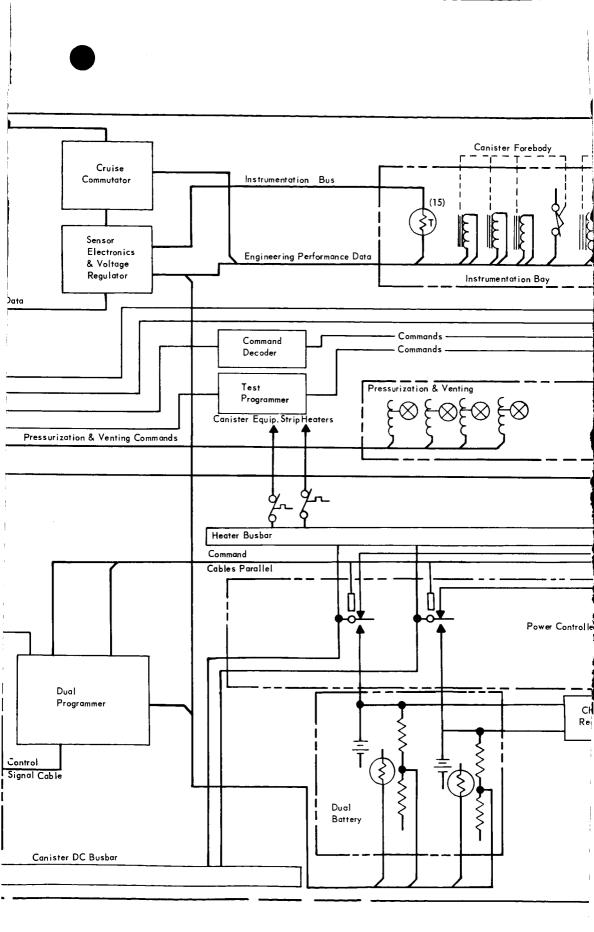
Figure 5.1-47

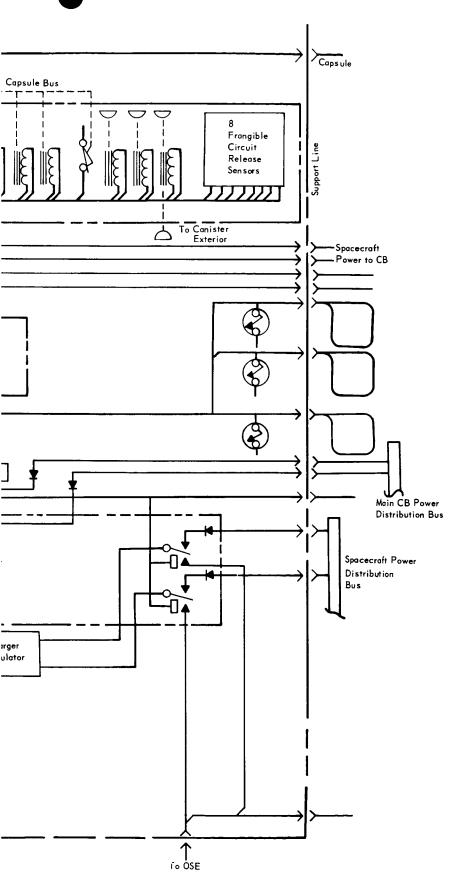
PREFERRED APPROACH VOYAGER CANISTER ELECTRICAL SYSTEM



rigure 5.1—48

5.1-69-1





B

5-1-69-3

- Revised Enhanced Containment Control with Electrical Constraints (Alternate Approach) This approach, shown in Figure 5.1-49, derives complete sequencing and primary power from the Capsule Bus except power for separation of the Capsule Bus. Power for this separation is supplied by thermal batteries in the Canister Energy Storage and Distribution Unit since CB power is removed at the inflight disconnect prior to CB physical separation. Separation of the canister forward section as well as the Capsule Bus in this approach is by electromagnetic solenoids. Capacitors in the Energy Storage and Distribution Unit, charged from the Capsuel Bus, are used for forebody and Capsule Bus release, inflight disconnect initiation, and thermal battery initiation. This unit also contains relays for pressurization and venting and heater control. Sensor and event data collection from throughout the canister is commutated and directed to the spacecraft telemetry link as in the other approach.
- 5.1.5.3 <u>Selection Factors</u> In the selection of a final approach to the canister electrical equipment the following criteria were subdivided into selection factors:
 - o Probability of mission Success
 Equipment reliability
 Effect on other subsystems
 Vulnerability to uncertain Environments
 - o System Performance Weight
 - o Development Risk Time of development Effect on other subsystem design State-of-the-art improvement Testing
 - O Versatility Ease of change Growth
 - o Cost
 Fabrication
 Handling
 Development

The overall weighting of the two approaches is summarized below, leading to selection of the Minimum Entry Weight Concept as the Preferred Design.

ALTERNATE APPROACH VOYAGER CANISTER ELECTRICAL SYSTEM

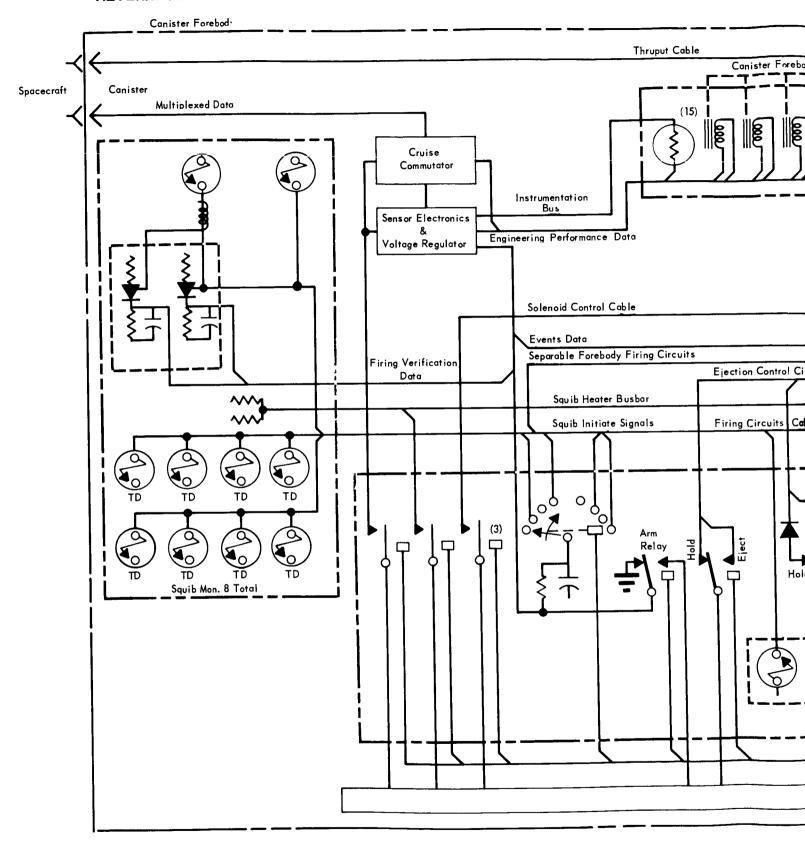
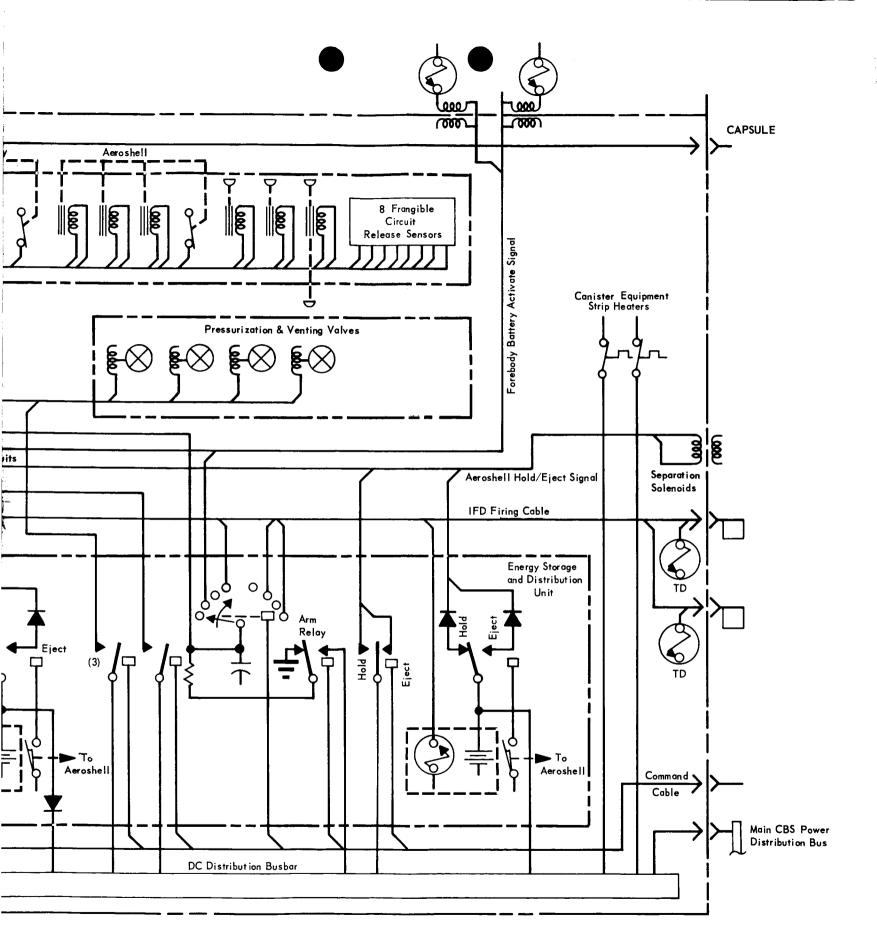


Figure 5.1-49

5.1-71 -1



Criteria	Recommended Approach	Alternative Approach
Probability of Mission Success (0.35)	0.35	0.292
System Performance (0.2)	0.20	0.167
Development Task (0.2)	0.20	0.182
Versatility (0.15)	0.15	0.110
Cost (0.1)	0.09	0.100
TOTAL	0.99	0.851

In the recommended approach, minimum interfacing is required between the canister and the Capsule Bus thereby adding to overall reliability and minimizing intersubsystem effects. The canister located programmer and power source maintained in a charged condition minimize interference with Capsule Bus functions. Vulnerability to environmental uncertainty is minimized by analyzing effects of electrical heating and adjusting heating duty cycles.

Subsystem weight is an important factor favoring the Recommended Approach. The overall weight remains the same, however it is shifted into the canister, resulting in lighter capsule bus entry weight. Development Risk and Versatility also favor the Recommended Approach. By maximizing the independence of the canister, development changes and changes in capability requirements can be accommodated with minimum interference to the Capsule Bus development. The cost of the Recommended Approach is somewhat higher because of the more complex canister. equipment, and special installation and handling procedures required for the separate batteries.

REFERENCES

- 5.1-1 Performance and Design Requirements for the 1973 VOYAGER Mission, General Specification for; SE002BB001-1B21, Jet Propulsion Laboratory, dated 1 January 1967
- 5.1-2 NASA Report CR 540
- 5.1-3 Maiden, C. J.; McMillan, A. R.; and Sennett, R. E.; <u>Thin Sheet Impact</u>; General Motors Defense Research Laboratory Report TR64-61; November 1964
- 5.1-4 Madden, R.: <u>Ballistic Limit of Double-Walled Meteoroid Bumper Systems</u>; NASA TN D-3816; dated April 1967
- 5.1-5 Nysmith; Summers; An Experimental Investigation of Impact Resistance of

 Double Sheet Structure at Velocities to 24,000 Feet per Second; NASA

 TN D-1431; dated October 1962
- 5.1-6 Air Force Eastern Test Range; Range Safety Manual I; AFETRM 127-1.
- 5.1-7 Convair Astronautics, Report FZM-4750, dated 6 January 1967

5.2 ADAPTER - The adapter is the structural transition between the Capsule Bus and the Flight Spacecraft and contains the equipment for Capsule separation. Ground handling, launch and cruise phase loads were investigated. The most severe conditions for design, including an estimated 1.20 dynamic factor, are as follows:

Condition	Longitudinal Load Factor (ultimate)	Lateral Load Factor (ultimate)
Transportation by Air	<u>+</u> 3.75	0
	0	<u>+</u> 3.75
Ground Handling Cantilevered	0	<u>+</u> 1.80
Lift Off	3.15	<u>+</u> 0.98
S-IC End Boost	7.35	<u>+</u> 0.15
S-IC Thrust Decay and Separation	-2.85	<u>+</u> 0.15

The load factor is assumed to act at the c.g. of the weight supported by the adapter. The selection of the conditions and subsequent analysis is based on the Structural Design Criteria of Part A, Section 2.3.

- 5.2.1 <u>Design Constraints and Requirements</u> The major Adapter functional requirements and design constraints in addition to the load criteria above are:
 - a. Requirement for limitation of dynamic frequencies and excursions.
 - b. Requirement for thermal isolation of Flight Spacecraft from the Flight Capsule.
 - c. Requirement for attachment of adapter to Capsule Bus prior to attachment to canister.
 - d. Requirement for interchangeability of adapter as a total assembly.

The second requirement is a constraint from Reference 5.2-1, the other requirements were self-imposed to assure ease of system assembly. The adapter design must also be compatible with the decontamination and heat sterilization cycles and support cabling.

Presented herein are the results of the trade-offs conducted to optimize the adapter configuration and structural approach. The release and separation equipment used to provide capsule separation is described in Part A, Section 3.2.1.4.

- 5.2.2 <u>Alternative Design Approaches</u> Two adapter design approaches were studied in various combinations of structural design and materials. The two approaches are adapters that are independent of, and integral with, the sterilization can-ister.
- 5.2.2.1 Integral Adapter The design approach for the integral adapter is given in Figure 5.2-1. In the integral adapter arrangement, the aft section of the canister would serve as both a pressure vessel (sealed, biological barrier) and as the Capsule Bus support. The adapter structure considered was primarily a web-stiffened angular ring with its aft end attached to the forward wall of the aft canister while its forward end was attached to the outer edge of the Aeroshell by means of a separation ring. Thermal isolation between the separation ring and the adapter was achieved by the use of thermally insulated stand-off points.

 Details A and B of Figure 5.2-1 illustrate the integral adapter configuration.

 5.2.2.2 Separate Adapter The separate adapter was considered primarily in two basic structural forms: truss, (Figure 5.2-2 and 5.2-3) and conical panel (Figure 5.2-4). It forms a direct cantilever column support for the Capsule Bus carrying its inertial loads directly to the ring at the canister/spacecraft interface.

Truss Adapter - The truss configuration which was used for comparison studies consists of 16 tubular members supporting the Capsule Bus at 8 points on a 111.0 inch diameter ring. The Capsule Bus loads are carried through these points to 8 attachment points on the periphery of a 160.0 inch diameter ring at the canister/spacecraft interface. The truss configuration was analyzed using three materials for comparison. The tube diameters and wall thicknesses shown in Figure 5.2-5 were derived on the same load basis.

<u>Conical Panel Adapter</u> - The panel adapter (Figure 5.2-4) was computer analyzed using the loads previously presented with results shown in Figure 5.2-6.

The resulting weights represent the minimum skin gages necessary to provide the column strength required. The summary table (Figure 5.2-6) considers the minimum practical material gauges as indicated.

- 5.2.2.3 <u>Weight Comparison</u> Figure 5.2-7 gives an approximate weight comparison of the various structural configurations considered, based on aluminum construction and without end fittings.
- 5.2.3 <u>Evaluation and Selection</u> The matrix of adapter types, construction configurations and materials considered are presented below:

CANISTER WITH INTEGRAL ADAPTER

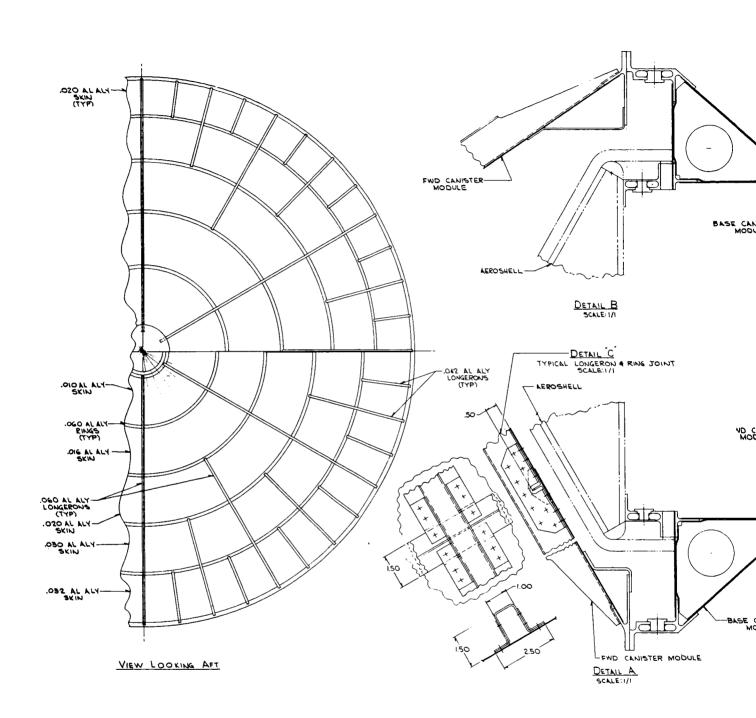
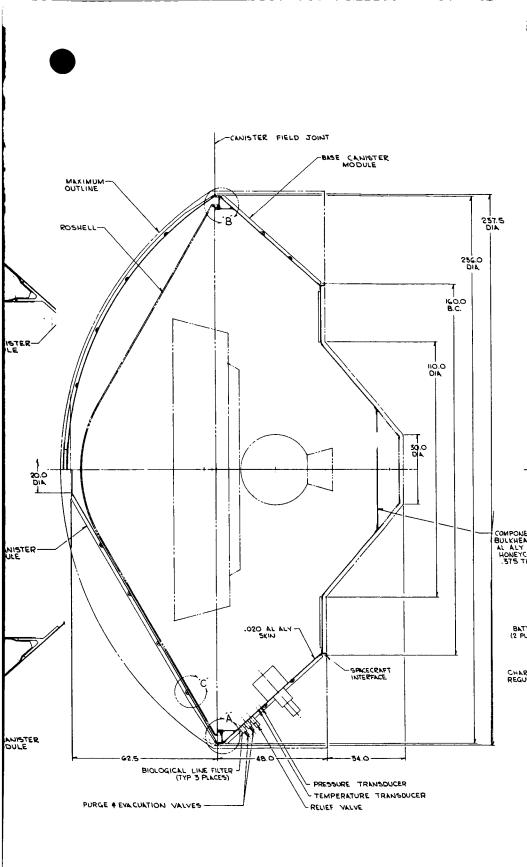
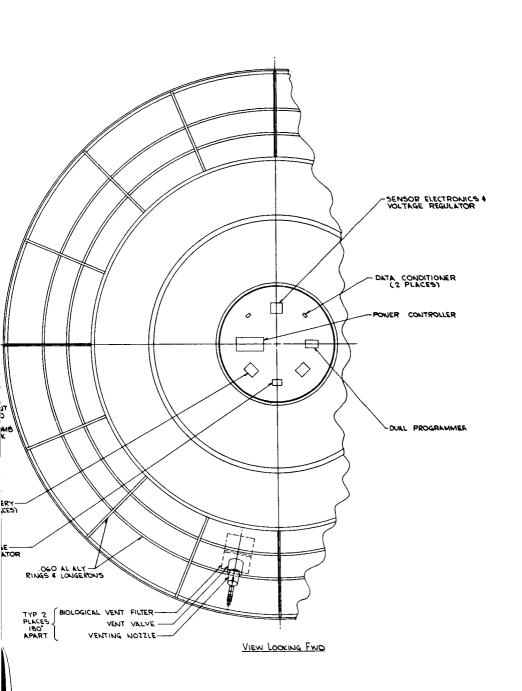


Figure 5.2-1 5.2-3-1





B

ADAPTER, TRUSS DESIGN (8 POINT)

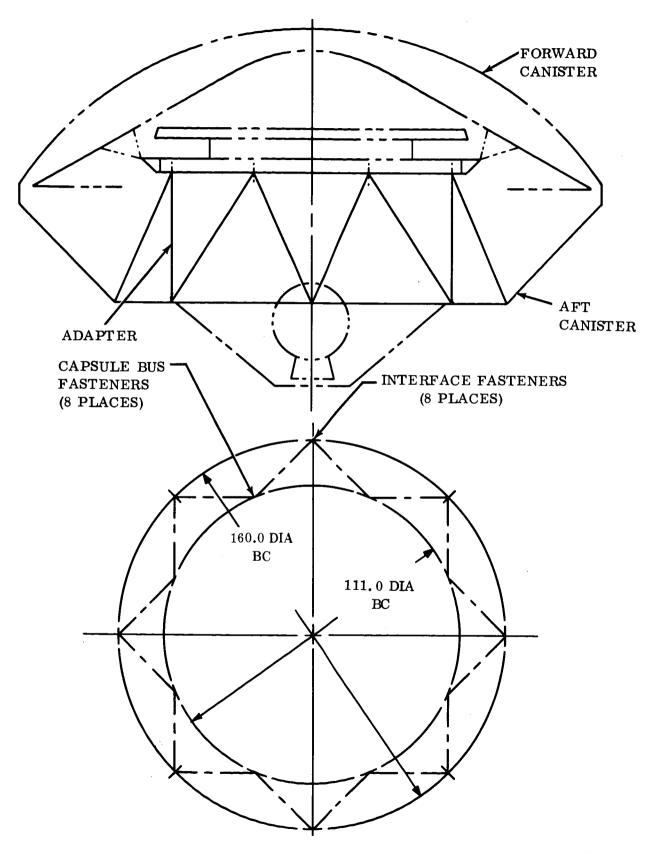
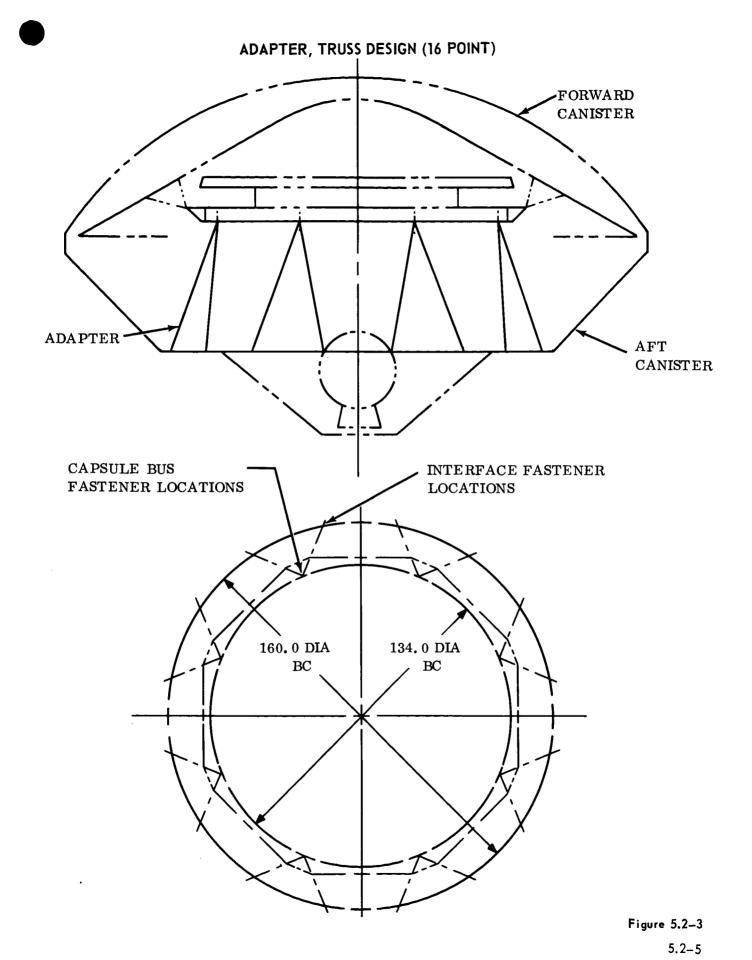


Figure 5.2-2

5.2-4



REPORT F694 • VOLUME II • PART B • 31 AUGUST 1967

ADAPTER, CONICAL PANEL DESIGN

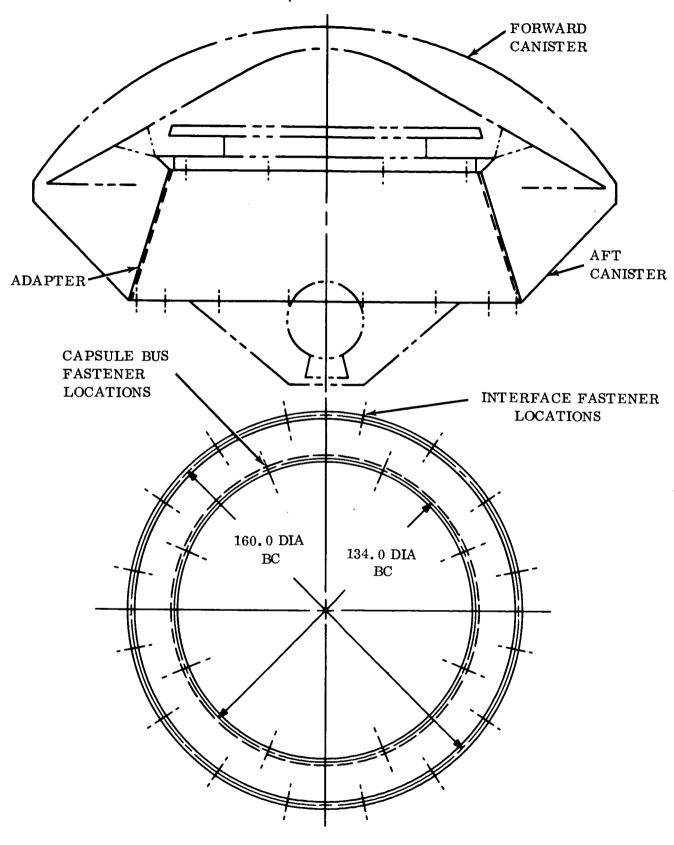


Figure 5.2-4

TRUSS COLUMN SIZE AND MATERIAL

Material	Tube Diameter (in.)	Wall Thickness (in.)
Aluminum Alloy	2.50	0.049
Titanium	2.00	0.063
Fiberglass	3.00	0.070

Figure 5.2-5

COMPARATIVE WEIGHT (LB/FT²) FOR CONICAL ADAPTERS

Construction	Al. Alloy		Mg.	Be.	Phenolic	S. Steel	Ti.
	2024	7075	Hk31A	V5804	Glass	15-7	6AL-4V
Honeycomb	0.700	0 .720	0.630	0.315	0.750	0.740	1.48
Waffle	0.422	0.422	0.349	0.142	0 .534	0.706	0.552
Ring-Stiffened	0.457	0.457	0.354	0.192	0.493	0.898	0.632
Axial Corr.	0.756	0.756	0.521	0.441	0 .600	1.100	0.729
Monocoque	1.09	1.09	0.853	0.424	1.20	2.03	1.48
Min. Gauges	0.010	0.010	0.010	0.010	0.010	0.005	0.008

Figure 5.2-6

WEIGHT COMPARISON OF STUDY DESIGNS

CONFIGURATION	WEIGHT ((b)
Truss Type (8-16)	35.0
Waffle	72.5
Ring-Stiffened	78.5
Honeycomb	120.0
Axial Corrugations	130.0
Monocoque	188.0

Figure 5.2-7

Configuration Approach	Structural Arrangement	Type of Construction	Type of Material
Integral	Angular ring + thermally - insulated stand- off joints + separation ring.	Semi-monocoque	Aluminum Alloy 2024
Separate	a) 8 attachment point truss to canister.b) 16 attachment point truss to canister.	Tubular Members	a) Aluminum6061-T6b) Titaniumc) Phenolicfiberglass
Separate	Conical panel	 a) Honeycomb b) Monocoque c) Ring stiffened d) Axial corrugation e) Waffle 	 a) Aluminum - 2024 b) Aluminum - 7075 c) Beryllium d) Magnesium e) Titanium f) Stainless stell g) Phenolic fiberglass

Preferred Configuration

Separate	Truss; 8	16 tubular	Aluminum	
	attachments		Alloy - 6061-T6	
	on canister.			

5.2.3.1 Separate vs Integral Adapter - Inasmuch as a selection between integral and separate adapters significantly influences the selection of canister approach, the two evaluations were made concurrently. The canister evaluation was described previously in detail in Part B, Section 5.1. For the sake of completeness in describing the adapter preferred approach selection procedure, those considerations which affected the adapter design are repeated herein. The evaluation which resulted in the selection of the separate adapter as the preferred configurational approach showed that both the integral and the two types of separate adapters were feasible and were close in their functional efficiency. The decision reached was based on the following considerations:

Separate Adapter (truss or conical panel):

- o Lower weight than integral approach (about 50 lbs. lower for more favorable separate adapter confingrations).
- o Minimized thermal path between Capsule Bus and Flight Spacecraft.
- o Superior capability to fulfill the requirements concerning capsule/ canister assembly techniques and guidance platform alignment.

Integral Adapter:

- o Superior clearance between the canister and the Aeroshell.
- o Caused canister pressure loads to be carried into the Aeroshell.
- 5.2.3.2 Truss vs Conical Panel Separate Adapter With the separate adapter selected as the superior configuration, the adapter evaluation next considered various truss and conical panel types of separate adapters. From the weight summary presented in Figure 5.2-7, the truss is significantly superior to any of the panel construction. In addition, it is better suited to attachment at concentrated points on the lander and spacecraft; it permits circulation of decontamination and heating gases; and it is more flexible to design changes. The truss type will readily accept the installation of an RTG on a growth version lander since it does not significantly impede thermal radiation.

Aluminum was selected as the material for the truss adapter because it is thermally compatible with the Capsule Bus and the canister, and can be readily fabricated.

5.2.4 Preferred Approach - The configuration selected consists of a truss-type separate adapter composed of 2.50 inch diameter aluminum alloy tubes and weighs 37.6 lb. The 16 tubes which make up the truss form a zig-zag pattern, as shown Figure 5.2-8, between the eight attachment points on the Capsule Lander and the eight attachment points on the aft canister. The adapter geometry was changed from the study design because of changes in the canister envelope. It was possible to reduce the truss 11 inches with a corresponding weight reduction. At each intersection, the 0.049 inch wall thickness tubes are welded to and joined by fittings which also function as the interface attachments. The adapter-tocanister end fittings used a fixed-plate nut which allows attachment of the adapter first to the Capsule Bus and then installation of the Capsule/Adapter Assembly within the canister aft section. The bolts for attaching the adapter to the canister are then installed from outside the canister with sealing washers to complete the installation. By means of jig drilling of the interface fitting after fabrication, the adapter will be made an interchangeable unit. In the same manner, the adapter will be machined at its interface points to maintain a close alignment between the Capsule Bus and Spacecraft. Thermal isolation between the capsule/ adapter/canister interfaces is not required since all three systems are in a nearly isothermal environment within the insulation blanket surrounding the canister. addition to providing the shortest and stiffest load path between the Capsule Bus and the Spacecraft, the truss-type adapter's widely spaced tubes should

PREFERRED ADAPTER CONFIGURATION (TRUSS-TYPE, SEPARATE)

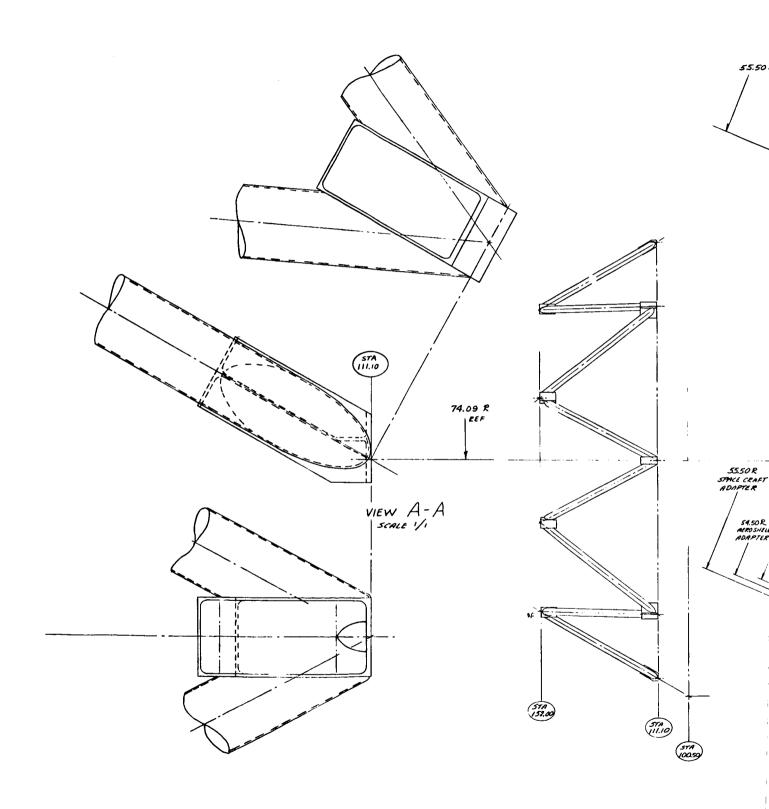
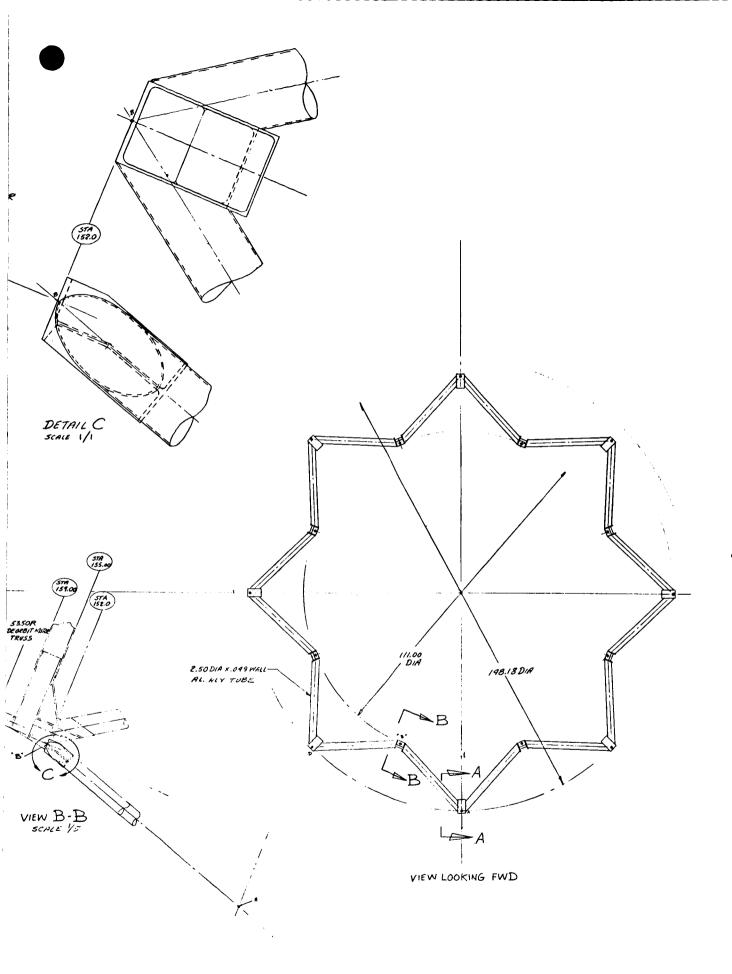


Figure 5.2-8 5.2-10-1

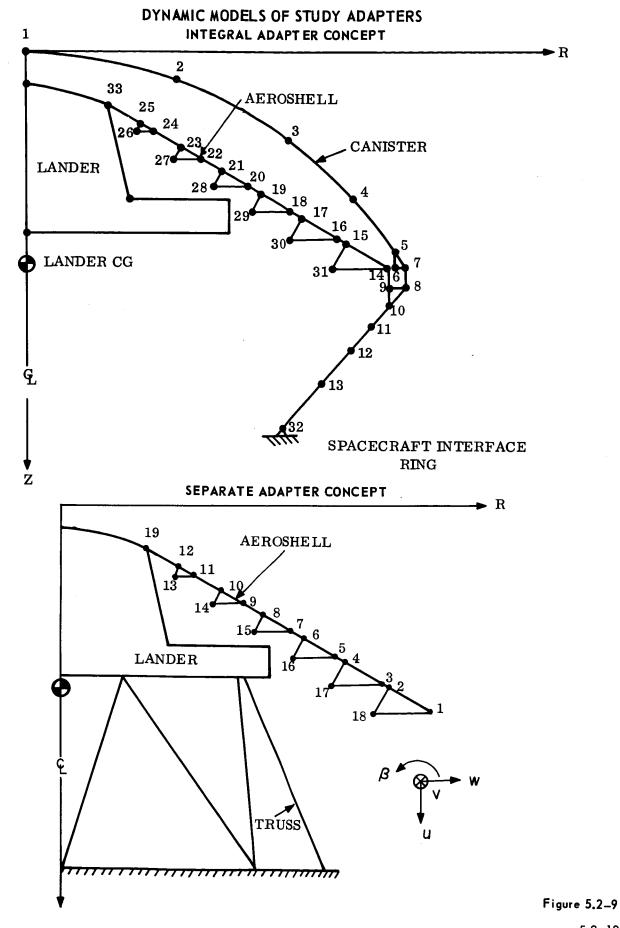


provide a minimum of obstruction to the circulation of the heated gases during the sterilization cycle. The use of eight attachments to the canister rather than a larger number reduces the number of support struts and fittings which result in a lower weight for the large, lightly-loaded structure.

The governing criterion for the design of the adapter is structural stiffness rather than strength margins and a natural frequency of 40 cps longitudinally was selected as the minimum design criterion. Because the loading is compressive and localized, skin and ring structures were considered inefficient for this application, and thus, the selection of a tubular-truss arrangement. Aluminum (6061-T6) was selected as the material for the sixteen tubes, because of its favorable fabrication techniques and thermal compatibility with adjoining structure.

5.2.5 Structural Analysis of Preferred Truss Adapter - The analysis presented here considers the preferred configuration specifically. The inertial loads of powered flight are introduced into the adapter at 8 locations and are carried by the truss members as column loads to 8 attachment points at the canister/adapter interface. Column loads were determined by use of a pin-ended truss computer program based on displacement compatibility at the end joints. External inertia loads are applied at the c.g. of the Capsule Bus and individual member loads and displacements are determined. Using maximum ultimate load factors. the critical column load computed is 3880 pounds. Using a column fixity factor of 1.3 (slightly better than pinned) the allowable column load computed is 9070 pounds. The computation shows that sufficient structural strength is available and that stiffness requirements will govern design detailing. 5.2.6 Adapter Dynamic Analysis - The dynamic characteristics of adapter designs both integral with and independent of the canister were investigated prior to the selection of a preferred design (Section 5.2.4). The dynamic models of each configuration are given in Figure 5.2-9. Analysis of the preferred truss design indicates fundamental frequencies of 43 cps axially and 15 cps laterally. The model shapes corresponding to the axial and lateral frequencies of the truss performed design (Figure 5.2-8) are given in Figures 5.2-10 and 5.2-11.

Evaluation of the dynamic response of the structures is preliminary since the total Space Vehicle elastic characteristics are not sufficiently defined at this date to permit a more comprehensive dynamic analysis. The adapter is the principal spring in the capsule lateral mode and a truss design can be easily made as stiff as is required to be compatible with the mechanical impedance



5.2-12

MODE SHAPE FOR FIRST AXIAL MODE

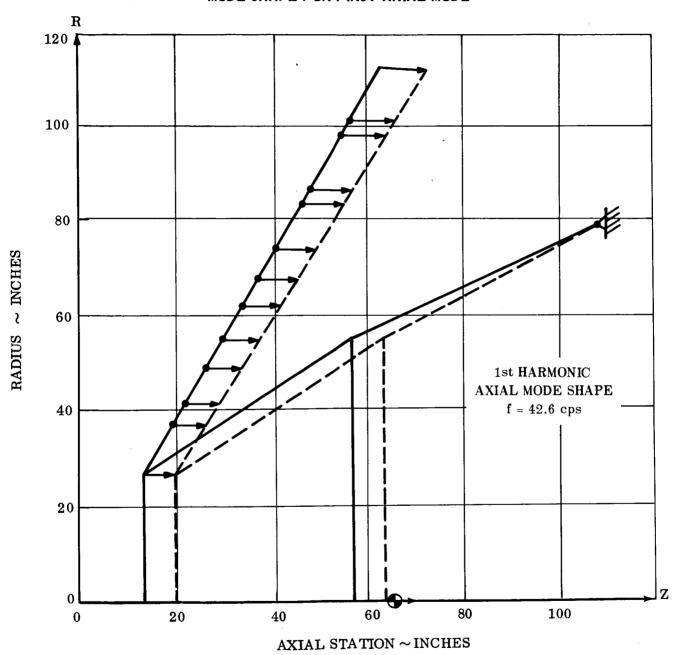
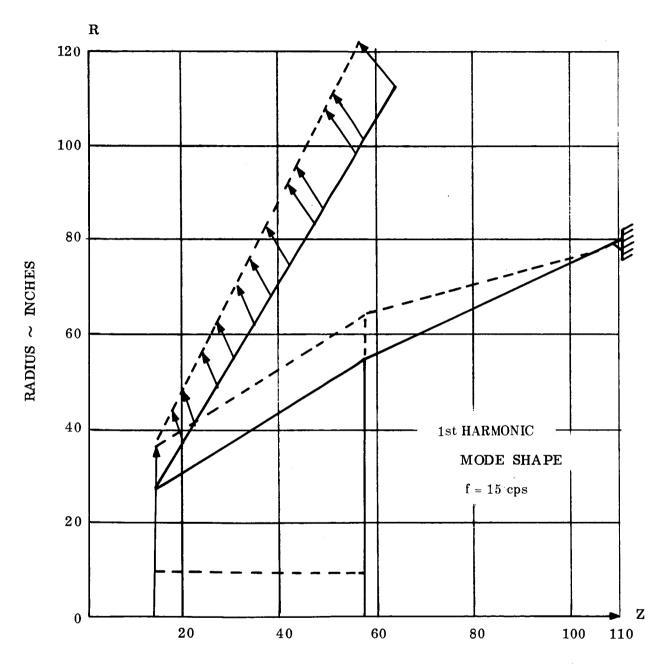


Figure 5.2-10

MODE SHAPE FOR FIRST LATERAL MODE

LANDER/TRUSS ADAPTER



AXIAL STATION ~ INCHES

Figure 5.2-11

of the VOYAGER systems and the dynamic environment.

5.2.7 <u>Capsule Separation</u> - The function of the Capsule Bus separation device is to separate the Capsule Bus from the Flight Spacecraft at a relative velocity of 1.25 ft/sec. The required separation velocity, as stated in Section 2.3.2.5, is 1.0 ft/sec or more. A value of 1.25 ft/sec was selected to minimize the time to separate the Capsule Bus from the spacecraft by a distance of 300m. (See Reference 5.2-1). The canister is estimated to separate at a rate of 4 to 6 ft/sec. Therefore, the design goal of at least a 1.4 V_{CB} requirement is met.

To physically separate the Capsule Bus, two alternate methods were considered:

- a. Utilize the aft-firing 22-1b engines both pitch and yaw of the RCS.
- b. Add the extra fuel, tankage and sequencing to accomplish the separation.
- c. Use eight compression springs one at each Capsule Bus/adapter attach point. The force to be released when explosive bolts were fired, springs to be retained on the adapter.

Selection criteria and evaluation comments are given in Figure 5.2-12. With no significant difference in any factor except weight, weight is the selection factor. On this basis use on the Reaction Control System is the preferred method of separating the Capsule Bus/Spacecraft.

CAPSULE BUS SEPARATION TECHNIQUE EVALUATION

	METRYS ICCTION COLFORD BILL	LISE COMPRESSION SPRINGS
SELECTION CRITERIA	USE REACTION CONTROL SISTEM	
1. Probability of Mission Success		
a) Reliability	No significant change in reliability. Adds one sequence step.	Very reliabile, passive mechanism
	One millisecond earlier operation.	
b) Effect on Flight Spacecraft	Exhaust plumes impinge on inside of aft canister. Spacecraft disturbance is small owing to uniformity of pattern and large inertia.	Force on Spacecraft equal to applied force, symmetrical except for variation in springs
2. System Performance		
a) Tip-off	Tip-off problem if a thruster fails or is outside limits.	Tip-off problem if some explosive bolts fire late.
b) Weight - 1973 - 1979	2.0 lbs (Added fuel and 2.4 lbs tankage)	12 lbs 12 lbs
3. Development Risk	No Additional risk	No risk
4. Versatility — (Increased velocity or weight)	More fuel required (available without change to the RCS)	Heavier springs and larger installa- tion areas required.
5. Cost	No increase.	No increase.

Figure 5.2-12

REFERENCES

5.2-1 - SEO 03BB002-2A21, "1973 VOYAGER Capsule Systems Constraints and Requirements Document", Revision 2, Jet Propulsion Laboratory, 12 June 1967.

5.3 AEROSHELL - The Aeroshell is a high drag decelerator that protects the VOYAGER payload during ballistic entry into the Martian atmosphere. It is a 120-degree blunted cone with a nose radius of 4.75 feet and a base diameter of 19 feet. The design entry corridor is defined at 800,000 feet by a range in velocities from 13,000 to 15,000 ft/sec, and a span in entry angles from vacuum graze to -20 degrees (Figure A2.1-3). The maximum loads (free stream dynamic pressure of 201 psf) occur for an entry at a velocity of 15,000 ft/sec and a flight path angle of -20 degrees into the VM-8 atmosphere. The maximum total heat (stagnation point total heat of 1192 BTU/ft²) occurs for entry at the graze boundary with a velocity of 15,000 ft/sec into the VM-3 atmosphere. We have conservatively designed for an oscillating entry with a maximum angle of attack of 20 degrees at peak dynamic pressure.

A summary of the studies leading to the preferred structural concept for the conical portion of the Aeroshell is given in Sections 5.3.1.1 through 5.3.1.3. Forty structural configurations were considered. Screening of these forty led to three promising candidates which were studied in greater depth. They were the beryllium sandwich with an aluminum core, magnesium ring-stiffened monocoque, and titanium semi-monocoque with aluminum rings. The lightest configuration is the beryllium sandwich; however, it was not selected because of the cost and difficulty in fabricating and inspecting such a large sandwich structure. The magnesium ring-stiffened monocoque is an attractive concept; but it is eliminated because of the numerous rings and the susceptibility of magnesium to corrosion. Our preferred concept, analyzed in Section 5.3.1.4, is the titanium semi-monocoque. This structure consists of a single-faced, longitudinally corrugated titanium shell with internal aluminum rings. We have high confidence in this concept because of successful flight experience with similar spacecraft structure.

A summary of the thermodynamic and materials studies and tests leading to the preferred entry heat protection concept for the entire Aeroshell is presented in Section 5.3.2. For the relatively mild entry heating environment, presented in Section 5.3.2.2, various approaches were considered for the thermal protection of the conical portion of the Aeroshell. Feasible approaches, Section 5.3.2.3, include heat sinks, radiative structures, high density charring ablators, low temperature sublimers, low density ceramics and low density charring ablators. The class of low density charring ablators was chosen for further investigation based on considerations of thermal efficiency, ease of fabrication, cost, development risk, and experience gained from past flight programs. Within this class of

materials, thirteen specific formulations were considered, including supported and unsupported silicone elastomerics, syntactically filled and/or chemically foamed, and two natural materials. For evaluation of the candidate materials, various test programs were conducted to determine the thermal, mechanical, physical and electrical properties, the fabrication aspects, and adhesive bond characteristics, and are reported in Section 5.3.2.4.

Thirteen candidate materials were evaluated (Section 5.3.2.5), using the VOYAGER selection criteria for weighing all relevant factors, incorporating the combined experience of both General Electric and McDonnell. As a result, the GE ESM 1004X, a fiber reinforced silicone elastomer, soft bonded to the structure with RTV-560 was selected as the preferred material. MDC S-20T, a silicone elastomer chemically foamed in a continuous phenolic honeycomb that is prebonded to the structure with HT-424, was selected as the "backup" concept. The required ablative heat shield thickness was computed using arc test data to calibrate the analytical model (Section 5.3.2.6).

Two unique design requirements were satisfied in our selection of the preferred heat shield and structural concept of the nose cap (spherical portion of the Aeroshell (1) it will not outgas during entry to interfere with ESP atmospheric sampling and TV viewing experiments, and (2) it is RF transparent to permit radar altimeter operation. For heat protection, we use a passive insulation comprised of aluminosilicate fibers and an inorganic binder (hardened Fiberfrax). The backup structure for the heat shield is a phenolic impregnated fiberglass sandwich with a honeycomb core.

5.3.1 <u>Structure</u> - A titanium, single-face longitudinally corrugated shell with internal aluminum rings is preferred for the conical portion of the 19-foot diameter VOYAGER Aeroshell (See Figure 5.3-1). Titanium alloy, 6Al-4V, 0.008 inch thick, is used for both the flat sheet and the corrugated sheet of the shell structure; aluminum alloy, 7178-T6, is used for the ring caps and webs.

Due to its large size, light weight, and high-angle conical shape, stability for collapsing pressure is an area of major concern in the Aeroshell design. The preferred configuration was designed without the need for a skin hoop load path. The corrugations function as longitudinal beams supported on an elastic foundation composed of discrete springs (rings). Each corrugation, plus its effective skin, acts as an individual structural beam because the 0.008 in. thick skin neither possesses sufficient stiffness to provide a continuous elastic foundation to support compressive stresses in the hoop direction, nor is it required. Loads normal to the shell surface are, therefore, beamed longitudinally to the rings on these individual beams. The rings provide stability for collapsing pressure and redistribute the lateral loads from unsymmetrical pressure into the overall shell. This design simplifies the strength and stability analyses and satisfies the requirement for a design as simple as practicable, as stated in Reference 5.3-1. Analyses of the preferred conical structure are given in Section 5.3.1.4 to verify analytically its structural integrity.

We expect deflections normal to the moldline in the external skin between corrugations when the structure is loaded. These deflections have been computed and their effect considered in the selection of the ablator. We performed a load test on a representative panel to confirm our conclusion that the preferred ablator would conform to the deflections without detrimental effect on the ablator or on the bondline.

Structural loads and temperatures used in the design of the Aeroshell are presented in Section 5.3.1.1.

Forty structural configurations were screened and the results presented in Section 5.3.1.2. Factors considered in this screening process were materials, fabricability, weight, cost, design complexity, development requirements, modification flexibility, and environmental compatibility. As a result of the screening, three structural configurations were selected for further evaluation and the results presented in Section 5.3.1.3. Analyses which support this evaluation and the basis for selecting the preferred conical structural configuration are also given in Section 5.3.1.3.

PREFERRED STRUCTURAL CONCEPT (19-FT AEROSHELL)

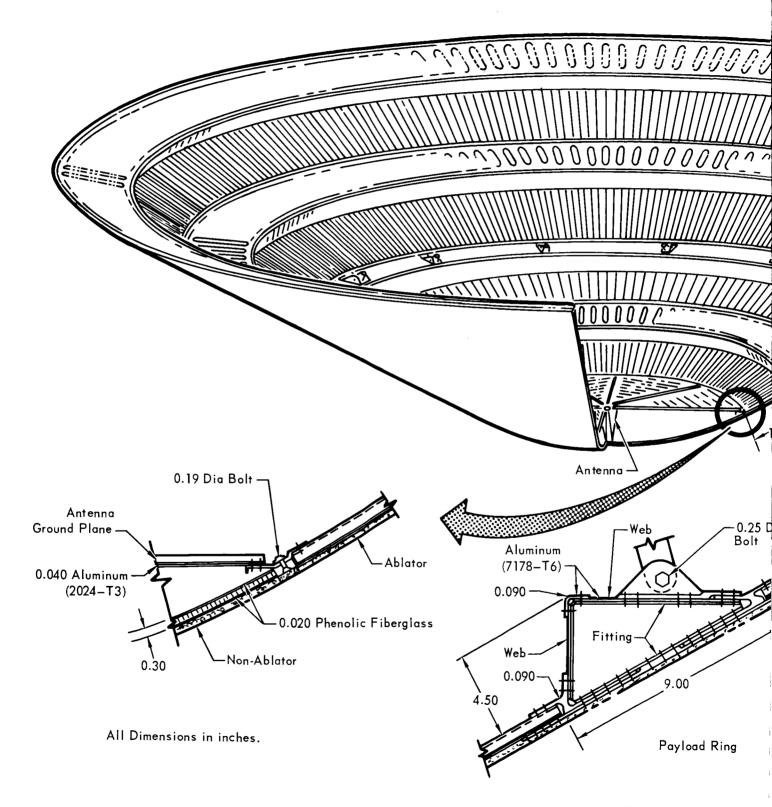
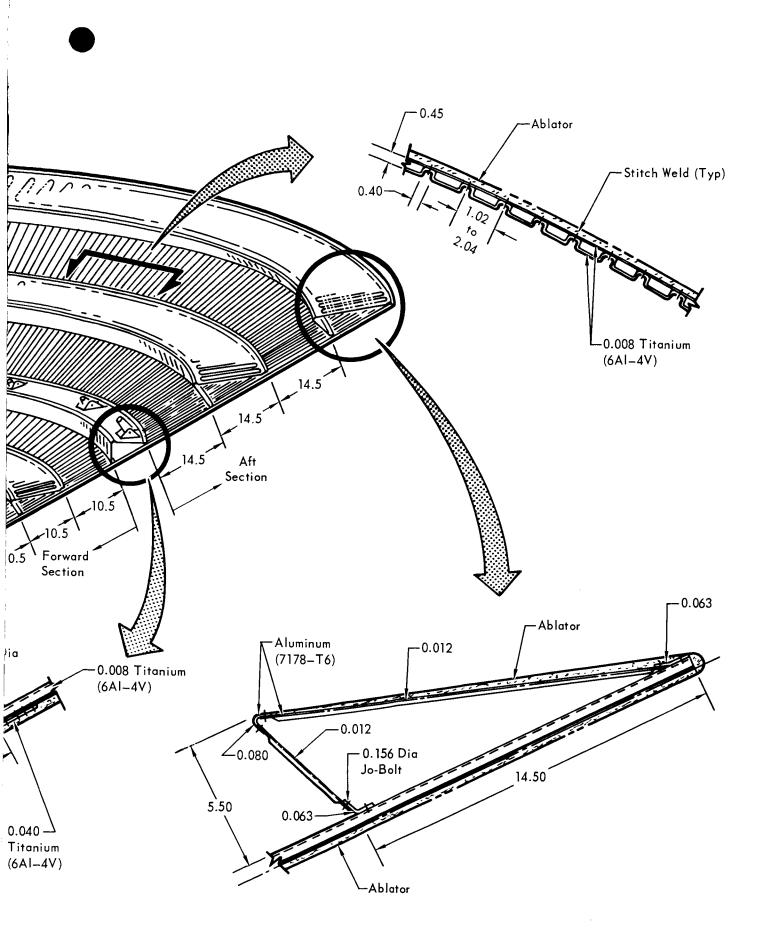


Figure 5.3-1

5.3-4 -1

REPORT F694 • VOLUME II • PART B • 31 AUGUST 1967



The spherical segment nose cap structure is a honeycomb sandwich with phenolic fiberglass skins and core. Its overall thickness is 0.30 in. with a face skin thickness of 0.020 in. The external pressure causes biaxial compression stresses in the face skins because of the spherical nose cap shape and isotropic design. The longitudinal component of the external pressure is introduced into the conical portion of the Aeroshell at the cone-sphere tangency ring. The basis for selecting this nose cap design and the analytical verification of its strength are given in Section 5.3.1.5.

- 5.3.1.1 Structural Loads and Temperatures Mars entry is the structurally significant mission phase. Investigation of loading conditions for other mission phases showed that most are non-critical inertia conditions for which the load factors are presented in Figure A 2.3.2-1. The basis for the structural loads and the methods of combining load and temperature are given in the Structural Design Criteria, Section A 2.3. The factor of safety (ratio of ultimate to limit load) is 1.25. No yielding is allowed at limit load and no failure at ultimate load. The data necessary to combine loads and temperatures are presented in the form of bondline temperatures and dynamic pressure time histories. The Aeroshell pressure distribution for the 120-degree ($R_{\rm N}/R_{\rm B}=0.5$) cone is also presented. A table of conditions is included for use with the load and pressure distributions to define discrete load levels. All load factors are based on an entry weight of 3650 pounds. The assumptions used in the internal loads and structural analyses are:
 - a. Applied external pressures on the shell are reacted by a rigid ring at the cone-sphere tangency.
 - b. Inertia loads from the shell structure are neglected (weightless shell).
 - c. No increase in the quasi-static load due to dynamic response because the rigid body aerodynamic oscillations are less than 3 cps and the lowest structural frequency, the shuttlecock mode, is about 22 cps.
 - d. Local panel design based on static considerations only, because the ablator characteristics eliminate significant panel dynamic response resulting from fluctuating pressures during entry.
- 5.3.1.1.1 <u>Load Conditions</u> The critical conditions of Figure 5.3-2 are based on design trajectories of the entry corridor for both the VM-8 and VM-3 model atmospheres. Trajectories in these atmospheres produce the maximum airload and total heating trajectories, respectively. A ballistic coefficient of 0.3 was used to determine the maximum dynamic pressure.

SUMMARY OF LOAD CONDITIONS ENTRY PHASE

	ENTR	Υ		MA	XIMUM DYNAMIC PR			
ATMOSPHERIC MODEL	٧ _e **	γ _e **	XAM	ALTITUDE	VELOCITY @ PMAX	* ^{η} A	$^{\star\eta}{}_{N}$	α
	10 ³ fps	deg	psf	10 ³ ft	10 ³ fps	EARTH g	EARTH g	deg
VM-8	15.0	-20.	201.	60.	9.40	-19.4 -21.5	2.2 0	20 0
	15.0	-14.1	69.	77.	9.40	-1.6 -4.4	.76 0	20 0
	13.0	-10.9	44.5	804	8.10	-3.3 -8.8	.49 0	20 0
VM-3	15.0	-20.	79.	155.	9.40	-7.6 -8.4	.87 0	20 0
	15.0	-14.1	38.5	185.	9.40	-3.7 -4.1	.41 0	20 0
	13.0	-10.9	25.	187.	7.75	-2.4 -2.7	.28 0	20 0

Ballistic Coefficient, m/C_DA = .3
*Limit Load Factors at Capsule c.g.
Entry Altitude = 800,000 ft.
VM-8 ~ Maximum Airload Atmosphere
VM-3 ~ Maximum Total Heating Atmosphere
**Design Trajectory Entry Conditions

5.3.1.1.2 Pressure Distribution - Pressure coefficient (local pressure divided by free stream dynamic pressure, $\Delta P/q$) distributions for the Aeroshell are presented in Figure 5.3-3 for an angle of attack of zero and 20 degrees. The design angle of attack of 20 degrees accounts for any single malfunction, off-nominal inertia and aerodynamic characteristics, winds and gusts, and is used with the design trajectories which define the entry corridor. These pressure distributions were generated by assuming a modified Newtonian flow for the 120-degree, $R_N/R_B=0.5$ (radius of nose divided by radius of base), Aeroshell. The circumferential pressure distribution on the conical section of the Aeroshell is defined by: $\Delta P/q=1.24-.509~{\rm Sin}~\theta-.0268~{\rm Cos}~2~\theta.$

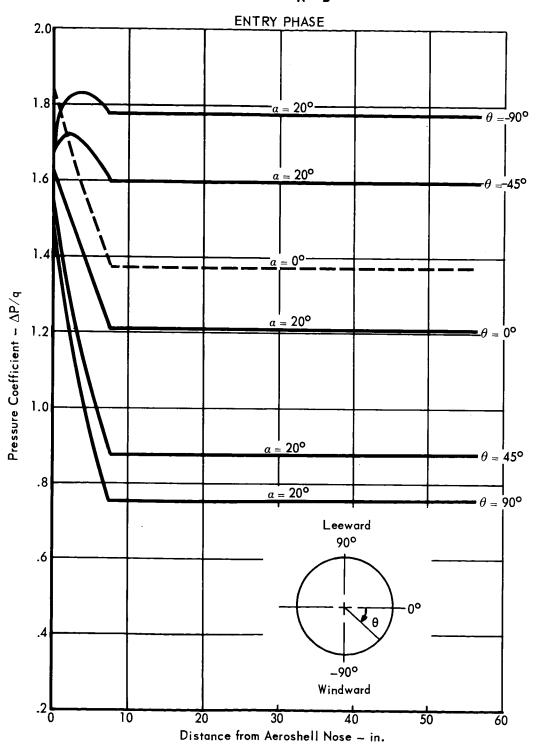
5.3.1.1.3 <u>Load-Temperature Relationship</u> - A comparison between the maximum loading condition and the maximum heating condition is shown in Figure 5.3-4. The ultimate design pressures for the maximum loading conditions are shown at the bottom of this figure.

The bondline temperature versus entry time is presented in Figure 5.3-5 for the maximum load and maximum heating trajectories. The temperature for different ablator weights is also shown for the maximum heating trajectory. The dynamic pressure is presented in Figure 5.3-6 for the same trajectories for which bondline temperatures were presented. These data permit the determination of load and temperature combinations for any specific entry time.

Investigation of combined loading and heating conditions revealed that the structure, for all the configurations considered, is critical for the maximum loading condition. A comparison of the maximum loading and maximum heating conditions with the strength of three structural configurations is shown in Figure 5.3-7. The trajectories for the two conditions are plotted in terms of ultimate pressure on the windward surface versus bondline temperature. It clearly indicates the maximum loading condition is the most critical. The structural temperature rise due to aerodynamic heating is insignificant for the maximum loading condition because the steep entry angle results in a small total heat input to the Aeroshell. However, the steep entry angle results in the highest aerodynamic loads.

AEROSHELL PRESSURE COEFFICIENT DISTRIBUTIONS HALF CONE ANGLE = 60°

DIA. = 19 ft. $(R_N/R_B = .5)$



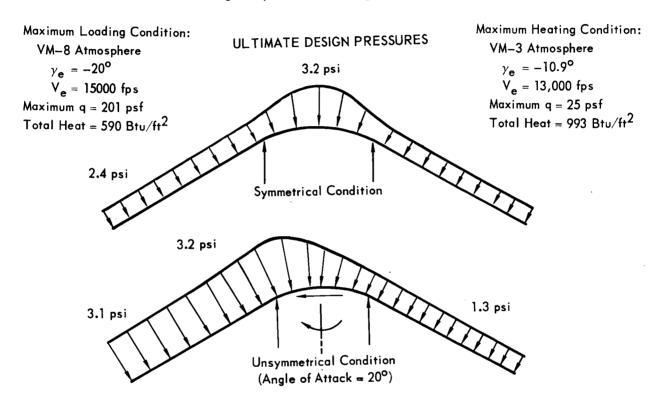
Note: Aeroshell Station 0.0 = Capsule Station 206

Figure 5.3-3

5.3-8

AEROSHELL PRESSURES

Flight Capsule Launch Weight = 5000 lb.



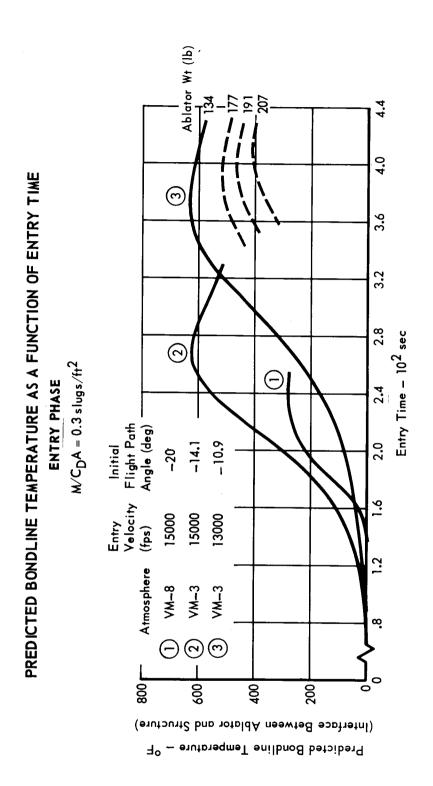
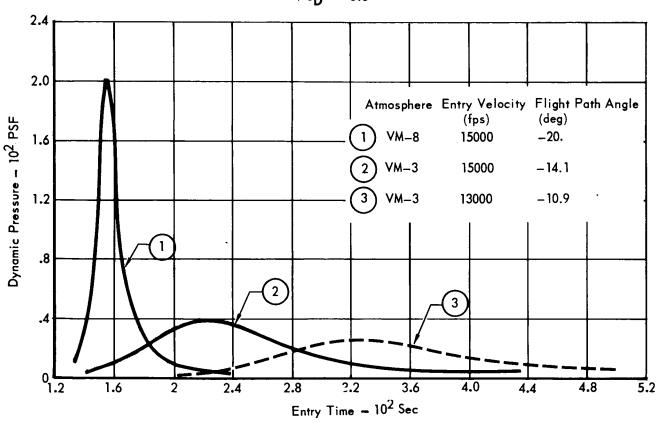


Figure 5.3-5

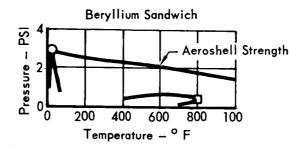
DYNAMIC PRESSURE AS A FUNCTION OF ENTRY TIME ENTRY PHASE

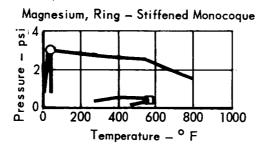


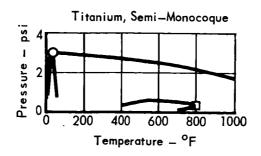


COMPARISON OF MAXIMUM LOADING AND HEATING CONDITIONS WITH AEROSHELL STRENGTH

- O Ultimate Load, Predicted Temperature (Maximum Loading Condition)
- ☐ Limit Load, Design Temperature (Maximum Heating Condition)







5.3.1.2 <u>Screening of Conical Structural Configurations</u> - This section describes the study leading to the three most promising configurations for the Aeroshell structure from forty configurations originally considered. In Section 5.3.1.3, these three configurations are evaluated in greater detail to select our preferred concept.

The spherical nose cap of the Aeroshell, is RF transparent for the radar altimeter antenna. Because this characteristic is not necessarily a requirement of the conical section, and because it is desirable to make the nose cap removable for access, only the conical section of the Aeroshell is evaluated here.

The Aeroshell geometry, used in this study, is shown in Figure 5.3-8.

5.3.1.2.1 <u>Design Approaches and Significant Characteristics</u> - The design configurations selected for evaluation were grouped into the four structural concepts shown in Figure 5.3-9. These concepts are representative of shell structures adaptable to an external pressure loading. All of the materials considered are not adaptable to all of the configurations. This is because the materials are not available in the form inherent to the design or are not compatible with certain fabrication techniques typical of the construction.

It is assumed that the payload (Capsule Lander) is supported by a ring on the Aeroshell at the cone-sphere tangency. This ring also provides for nose cap attachment and since the ring is typical for all configurations it is not included in the evaluation. All concepts require a ring at the base (large end) of the Aeroshell for stability and intermediate rings are included in those designs where required to optimize the structure.

5.3.1.2.2 <u>Material Candidates</u> - The materials selected for consideration include those commonly used for aerospace vehicle structures in addition to some newer developed materials. It was realized that some would be dropped from consideration early in the evaluation; however, one purpose of this study is to record the materials considered and the reasons why they were not considered further. In general, the evaluation is directed toward the comparison of basic materials. If the various alloys or forms of the materials exhibit appreciable differences for the particular characteristic being discussed, this fact is pointed out. The basic materials considered are:

- a. Aluminum
- b. Beryllium
- c. Boron filament

AEROSHELL GEOMETRY

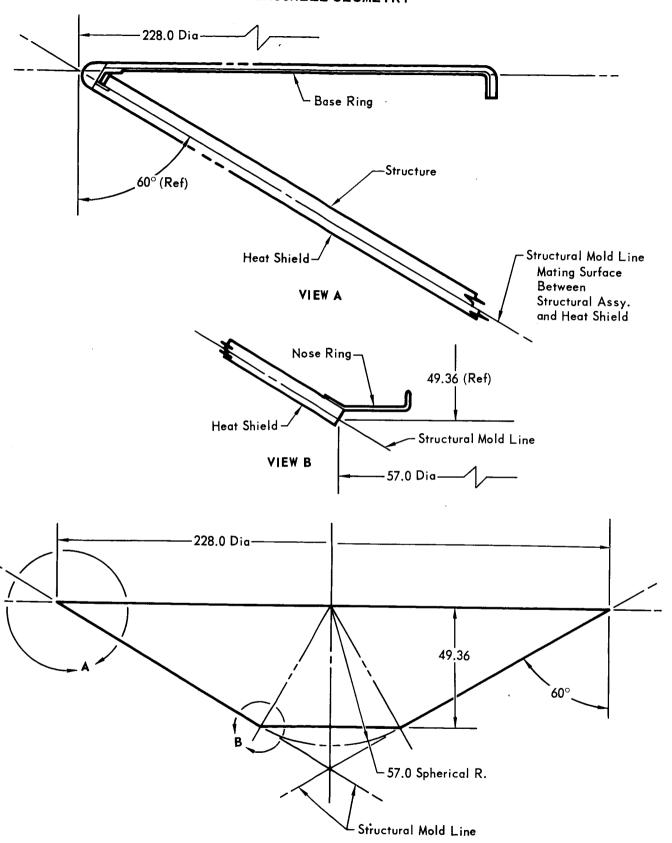
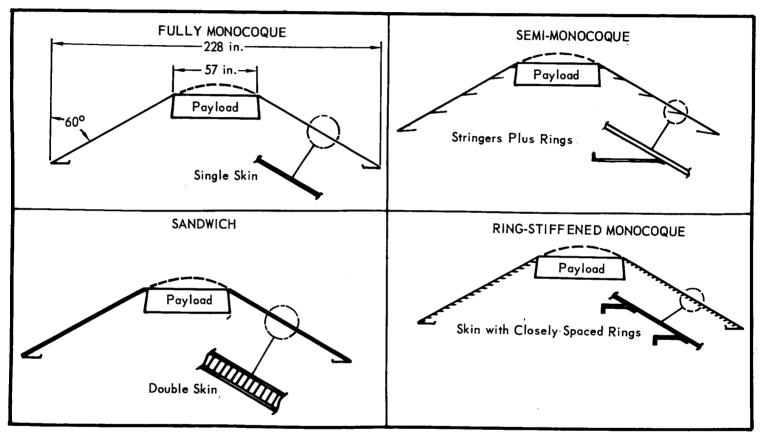


Figure 5.3-8

STRUCTURAL CONCEPTS



- d. Fiberglass
- e. Magnesium
- f. Titanium

The bondline temperature is limited to a maximum design limit of 800°F by the adhesive used to bond the heat shield to the structure. As the advantages of refractory metals (columbium, molybdenum, and tantalum) lie in their high temperature capability and because of their greater density and resulting higher weight, these materials were not considered competitive for a structure employing an ablative heat shield.

The properties of a material which contribute to its structural efficiency are density, temperature limit, minimum usable thickness, and mechanical properties. Figure 5.3-10 presents these properties for the candidate materials. Two factors are reflected in establishing the minimum practical gages - (1) resistance to handling damage and (2) availability. No accepted standard for determining resistance to handling damage exists outside of actual shop experience. The minimums shown have been established after discussion with metal fabricators, metallurgists, and manufacturing personnel. Availability is not as restrictive in establishing minimum values because available stock thicknesses can be chemically machined to thinner gages if handling limits permit. Technical difficulties in welding thin gages establish the minimum thicknesses for resistance welding aluminum and magnesium.

Figure 5.3-11 presents the available minimum thicknesses with corresponding sheet sizes. Included are typical costs for the stock material. The prices will vary depending on amount of material ordered, tolerances, and alloy. This information indicates the present pricing situation and is usable for establishing relative rather than actual cost factors.

The Aeroshell will be exposed to a variety of environments. Compatibility of the materials with the expected environments is important in selecting the preferred material. Figure 5.3-12 grades these compatibilities.

Fabrication complexity is usually reflected in the cost factor - the greater number of fabrication operations required for a material, the higher the cost. If joining methods are limited, increase in weight could result from extra material being required at the joints and from added mechanical fasteners. Figure 5.3-13 is a list of the characteristics which contribute to the complexity of the fabrication cycle for the candidate materials.

CANDIDATE MATERIAL PROPERTIES

		MINIMUM GAGES	10	H	DESIGN		PROPERTIES	ES
MATERIAL	STRUCTURE (1)	SANDWICH FACE SHEET	RESISTANCE WELDING	$(LB/IN.^3)$	TEMPERATURE LIMIT (°F)	F _{tu} (KSI)	F _{ty} (KSI)	$F_{tu}(KSI) = F_{ty}(KSI) = E(106 PSI)$
Aluminum (7178—T6)	.012	010.	.025	101	200	85	75	j.01
Beryllium (Cross-Rolled)	020	010.	Not Recommended	990'	008	70	20	42.0
Boron Composite (Aluminum Matrix)	(2)	(2)	(2)	001.	200			24.0
Fiberglass (Phenolic)	0:00	.020	Not Applicable	590.	625	31(3)		3.0(3)
Magnesium (HM21A-T81)	910.	Not Recommended	.025	.064	095	33	22	6.4
Titanium (6A1-4V)	800°	500°	800°	191.	008	139	131	16.0

(1) Structures utilizing mechanical fasteners or bonding other than sandwich.

⁽²⁾ Determined by matrix material.

⁽³⁾ Based on Laminated Construction

MATERIAL AVAILABILITY AND COST

Aluminum (7178-T6)

.010016	36 × 120	(\$2.67/ІЬ)
.016020	48 × 144	•
.020025	54 × 144	
.025036	60 × 144	

Beryllium (Cross Rolled)

.020 .015019	40 × 60 5 × 12	(\$615.00/Ib)
(Ingot Sheet)		
.001010	2 × 4 - 4 × 8	
.010 - 125	1 = 8 12 = 24	

Boron Filament (in development)

(\$300.00/lb)
(2 year projection)

Fiberglass (Phenolic)

\$2.00/lb)

38, 44, 50, 60 and 72 widths \times lengths to 499 yds.

Magnesium (HM21A-T81)

$$.016 \times 36 \times 144$$
 (\$9.28/lb) $.016 \times 48 \times 84$

Titanium 6AI-4V)

$$.012 \times 20 \times 84$$
 (\$70.00/1b) $.016 \times 48 \times 84$

NOTE: All dimensions in inches except as noted.

MATERIAL COMPATIBILITY

CONDITION	ALUMINUM	BERYLLIUM	FIBERGLASS	MAGNESIUM	TITANIUM
Atmosphere (Earth)	Good	Fair	Good	Poor	Excellent
Heat Sterilization	N/E	N/E	N/E	N/E	N/E
ETO Decontamination	N/E	N/D	N/E	Questionable	N/E
Space Vacuum	N/E	N/E	N/E	N/E	N/E
Space Radiation	N/E	N/E	N/E	N/E	N/E

Legend

N/E No Effect

N/D No Data Available

Figure 5.3-12

MATERIAL FABRICATION CHARACTERISTICS

OPERATION	ALUMINUM (7178–T6)	BERYLLIUM (CROSS-ROLLED)	MAGNESIUM (HM21A-T81)	TITANIUM (6Al-4V)
Machine Mill	Excellent	Poor	Excellent	Good
Chemical Mill	Yes	Yes	Yes	Yes
R.T. Forming	3t (0 Cond.)	No	No	6t
E.T. Forming	Not required	5t	6t	2t
Post Form. H.T.	Yes (Age to Cond T6)	No	No	Yes
Resistance Weld	Fair (Above t = .025)	No	Good (Above t = .025)	(Stress Relief) Good
Fusion Weld	Poor	No	Good	Good
Post Weld H.T.	No	No	No	Yes (Stress Relief)

Note:

Bend radius in terms of material thickness, t

R.T. indicates "room temperature"

E.T. indicates "elevated temperature"

H.T. Indicates "Heat Treat"

- 5.3.1.2.3 <u>Candidate Structural Configurations</u> Figure 5.3-14 presents the configurations selected for consideration. All configurations provide the surface required for installation of the heat shield. Evaluation comments are also given and include:
 - a. Design Complexity and Familiarity
 - b. Joining Characteristics
 - c. Inspectability
 - d. Accessibility
 - e. Volume Efficiency
 - f. Tooling Complexity
 - g. Development Requirements
 - h. Modification Sensitivity
- 5.3.1.2.4 Structural Weight Comparison The competing configurations were analyzed using the loads presented in Section 5.3.1.1. The weights are based on the structural analysis and state-of-the-art construction methods. The configurations selected are not the only ones possible, but are considered the most logical In addition to the structural weight, a weight for the heat shield is included, as this varied with each material used. The weight summary for all of the configurations is presented in Figure 5.3-15. The configurations utilizing intermediate rings, except the single-faced longitudinal stringers, were designed using the typical ring configuration shown in Figure 5.3-16. Note that the outboard ring cap is mounted on the inboard surface of the shell structure. For the single-faced longitudinal stringer configurations, it was found that a lighter weight shell structure would result if the number of stringers between rings were optimized for each section. The ring configuration for this approach is shown in Figure 5.3-17. In this case, the ring cap is outboard of the skin and stringers. The effects of this difference will be discussed later. The weights, shown in Figure 5.3-15, are based on rings made of magnesium. Figure 5.3-18 presents a summary of typical ring weights for other candidate materials.
- 5.3.1.2.5 <u>Configuration Evaluation</u> The extreme weight difference between the fully monocoque and the other structural concepts shown in Figure 5.3-15 led to deleting this concept from further consideration. From each of the three remaining concepts (sandwich, ring-stiffened monocoque, and semi-monocoque), we selected for further study the configuration that is the lightest weight, consistent with good producibility.

STRUCTURAL CONFIGURATIONS

COI	NFIGURATION	COMMENTS	
MONOCOQUE		o Familiar simple design. o Simple joints but may be heavy due to thickness involved — adaptable to all joining techniques. o Easily inspectable. o Excellent access for modifications. o Best volume efficiency. o Simple tooling requirements. o Minimum development requirements. o Poor equipment support capability. o Good opening and cut-out capability but require heavy edging members . o Easy to increase load-carrying capability.	SINGLE-FACED LONGITUDINAL STRINGERS WITH RINGS
HONEYCOMB SANDWICH	<u> </u>	o Familiar design of average complexity. o Panel sizes limited by facility capability — joints are typically heavy. o Extremely difficult to inspect — extensive quality control required during fabrication. o Poor accessibility for modification. o Good volume efficiency. o Complex tooling and facility requirements. o Minimum development requirements. o Poor equipment support and cut-out capability — provisions are heavy. o Difficult to change load-carrying capability.	WAFFLE CONSTRUCTION
DOUBLE-FACED TRUSS (CIRCUMFERENTIAL)	>>>>>	o Unfamiliar and complex design. o Limited to bonding, brazing, or blind fasteners for attaching skins. o Extremely difficult to inspect. o Poor accessibility for modification. o Good volume efficiency. o Extensive development of fabrication and testing techniques required. o Extensive and complicated tooling required. o Poor equipment support and cut-out capability. o Difficult to change load-carrying capability.	RING-STIFFENED MONOCOQUE
DOUBLE-FACED TRUSS (LONGITUDINAL WITH RINGS)		o Unfamiliar design of average complexity. o Limited to bonding, brazing, and blind fasteners for attaching skins — panel and circumferential joints extremely complicated. o Extremely difficult to inspect. o Poor accessibility for modification. o Rings reduce volume efficiency. o Considerable development of fabrication and testing techniques required. o Extensive tooling required. o Basic structure adaptable to equipment support and cut-outs with nominal modification. o Nominal capability for accepting load-carrying modification.	DOUBLE-FACED STRINGERS (SEPARATE) WITH RINGS
DOUBLE-FACED CORRUGATIONS (CIRCUMFERENTIAL)		o Complex design o Closure skin attachment limited to bonding, brazing or blind fasteners — panel joints complicated. o Difficult to inspect. o Poor accessibility for modification. o Good volume efficiency. o Extensive and complicated tooling required. o Some development of fabrication techniques required. o Poor equipment support and cut-out capability. o Difficult to change load-carrying capability.	DOUBLE-FACED STRINGERS (INTEGRATED) WITH RINGS
DOUBLE-FACED CORRUGATIONS (LONGITUDINAL WITH RINGS)		o Familiar design of average complexity. o Closure skin attachment limited to bonding, brazing, or blind fasteners. o Difficult to inspect. o Poor accessibility for modification. o Rings reduce volume efficiency. o Nominal tooling and testing development. o Nominal tooling requirements. o Basic structure adaptable to equipment support and cut-outs with nominal modifications. o Nominal capability for accepting load-carrying modifications.	SINGLE-FACED LONGITUDINAL CORRUGATIONS WITH RINGS

Figure 5.3-14

5.3-22 -(

CONFIGURATION	COMMENTS
	o Simple and familiar design. o Adaptable to all methods of joining. o Easy to inspect — some inspection complication for hat section stringers without lightening holes. o Zee stringer configuration easily accessible — hat stringer configuration nominally accessible for modification. o Rings reduce volume efficiency — usable volume available between stringers. o Tooling complexity introduced by ML ring. o Greater than nominal tooling development required for ML ring. o Basic structure adaptable to equipment support and cut-outs with least modifications. o Difficult to change load-carrying capability.
	o Simple and familiar design. o Adaptable to all joining methods. o Easy to inspect. o Excellent access for modification. o High volume efficiency. o Tooling complicated by machining or attaching skin to grid. o Development of machining or attaching skin to grid required. o Poor equipment support capability. o Nominal cut-out capability. o Difficult to change load-carrying capability.
	o Familiar design. o Minimum skin joints but numerous ring joints — adaptable to all. joining techniques. o Easy to inspect o Excellent access for modification. o Numerous rings reduce volume efficiency — considered worse than other ring concepts due to close ring spacing. o Extensive tooling required as each ring is different. o Extensive tooling and testing development. o Basic structure questionable for adapting to equipment mounting and cut-outs. o Nominally adaptable to change load-carrying capability.
	o Familiar design of average complexity. o Closure skin attachment limited to bonding, brazing, or blind fasteners. o Difficult to inspect. o Poor accessibility for modification o Rings reduce volume efficiency. o Nominal tooling and testing development. o Nominal tooling requirements. o Basic structure adaptable to equipment support and cut-outs with nominal modification. o Nominal capability for accepting load-carrying modification.
	o Familiar design of average complexity. o Closure skin attachment limited to bonding, brazing, or blind fasteners. o Difficult to inspect. o Poor accessibility for modification. o Rings reduce volume efficiency. o Above nominal tooling required. o Development of machining or attaching integral skin required. o Basic structure adaptable to equipment support and cut-outs with nominal modification. o Nominal capability for accepting load-carrying modification.
	o Simple and familiar design. o Adaptable to all methods of joining. o Easy to inspect — some complication if corrugations do not have lightening holes o Relatively accessible for modifications. o Rings reduce volume efficiency. o Nominal tooling requirements. o Nominal tooling and testing developments. o Basic structure adaptable to equipment support and cut-outs with nominal modification. o Nominal capability for accepting load-carrying modifications.

WEIGHT COMPARISON OF CANDIDATE AEROSHELL STRUCTURAL CONFIGURATIONS

STRUCTURAL	CONFIGURATION			·	WEIGHTS		
CONCEPT	CONFIGURATION	MATERIAL	SHELL-LBS.	RINGS-LBS.	ABLATOR-LBS.	TOTAL UNIT - LB FT2	COMMENTS
Fully Monocoque		Aluminum Beryllium Boron-Aluminum	1498.3 557.1	20.7 17.0	207.2 133.6	5.63 2.30	Fully Monocoque Construction is uncompetitive weight wise, not recommended for further consideration.
	Monocoque	Composite Fiberglass Magnesium	1038.6 1691.9 1136.7	20.7 25.0 21.0	207.2 177.1 190.8	4.12 6.17 4.39	
Sandwich		Titanium	1999.5	20.6	133.6	7.01)
Sanawich	Honeycomb Sandwich	Aluminum Beryllium Fiberglass Magnesium	177.5 123.6 236.7 168.7	20.7 17.0 25.0 21.0	207.2 133.6 177.1 190.8	1.32 .90 1.43 1.24	Beryllium Sandwich is recommended for further evaluation. This configuration is the lightest of all those considered. Although Beryllium fabrication is difficult the single curvature, bonded sandwich construction is simple and straight forward.
}		Titanium	178.0	20.6	133.6	1.08	1
	Double-Faced Truss (Circumferential)	Titanium	303.3	20.6	133.6	1.49	
	Double-Faced Truss	Titanium	232.3	111.8	133.6	1.56	
	(Longitudinal) Double-Faced	Beryllium Titanium	198.8 306.9	17.0 20.6	133.6 133.6	1.14 1.51	
-	Corrugations (Circumferential)						
	Double-Faced Corrugations (Longitudinal)	Beryllium Titanium	199.8 197.2	111.8	133.6 133.6	1.45 1.44	
	Double-Faced Stringer (Separate)	Aluminum Beryllium Magnesium Titanium	145.3 168.3 137.8 179.8	111.8 111.8 111.8 111.8	207.2 133.6 190.8 133.6	1.52 1.35 1.44 1.39	
	Double-Faced Stringer (Integral)	Aluminum Magnesium Titanium	201.3 156.0 250.9	111.8 111.8 111.8	207.2 190.8 133.6	1.70 1.50 1.62	
Semi- Monocoque	Single-Faced Longitudinal Corrugations	Aluminum Magnesium Titanium	114.5 116.7 137.5	111.8 111.8 111.8	207.2 190.8 133.6	1.41 1.37 1.25	Of the Semi-Monocoque concepts studied, Titanium is the most efficient. Of the titanium configurations, the single-faced longitudinal corrugation design is recommended for further evaluation. The weight advantage shown for the single-faced longitudinal stringer designs is not as great as indicated when certain non-optimum factors are considered,
	Single-Faced Longitudinal Z Stringers	Aluminum Magnesium Titanium	106.4 95.5 134.7	111.8 111.8 111.8	207.2 190.8 133.6	1.39 1.30 1.24	 e.g., additional fasteners and corrosion protection. In addition, the single-faced longitudinal corrugation design is a less complicated configuration with which McDannell has considerable experience (i.e. Mercury adapter and Air Force Gemini adapter).
	Single-Faced Longitudinal Hat Stringers	Aluminum Magnesium Titanium	95.6 87.0 122.5	111.8 111.8 111.8	207.2 190.8 133.6	1.35 1.27 1.20	
	Waffle Construction	Aluminum Magnesium Titanium	319.2 308.2 412.1	20.7 21.0 20.6	207.2 190.8 133.6	1.78 1.69 1.85	
Ring Stiffened Monocoqu e	7	Aluminum Beryllium Magnesium Titanium	176.8 87.5 141.4 227.7	72.0 61.0 84.0 76.6	207.2 133.6 190.8 133.6	1.49 .92 1.36 1.43	Of the ring stiffened monacoque concepts analyzed, the configuration using Beryllium is the most efficient. However, Beryllium sheet metal fabrication is extremely complex and has had limited application. Therefore, the magnesium structure is selected over the Beryllium for further evaluation.
	Ring Stiffened Monocoque						

Selected For Further Evaluation

Figure 5.3-15

TYPICAL RING CONFIGURATION

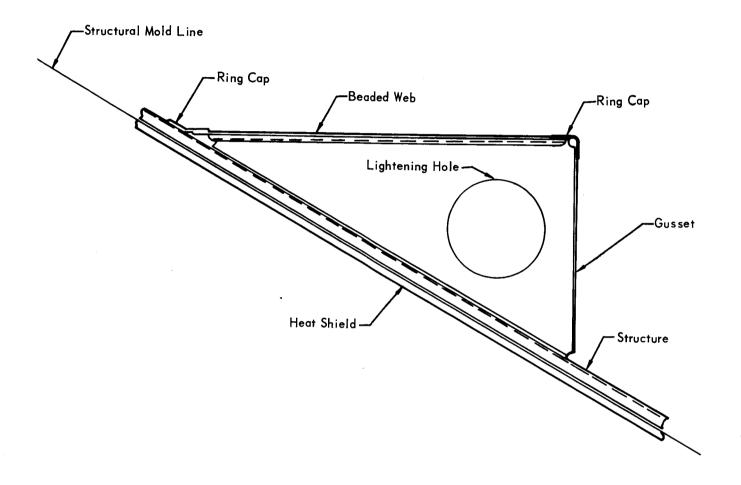


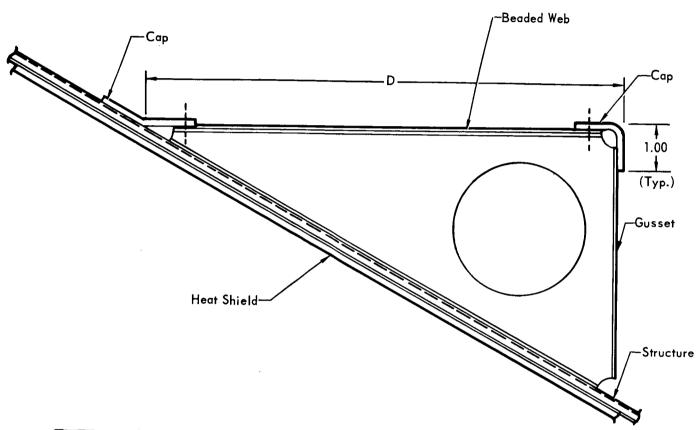
Figure 5.3-16

Figure 5.3-17

5.3-25

TYPICAL KING WEIGHT SUMMARY

Ring No. 4



MATERIAL	CAP THICKNESS	RING DEPTH(D)	WEB THICKNESS	GUSSET THICKNESS	GUSSET SPACING	RING WT.(LBS.)
Aluminum	.065	10.28	.010	.010	19.6	15.9
Beryllium	.050	5.95	.010	.010	34.4	7.5
Magnesium	.097	10.45	.016	.016	19.4	15.6
Titanium	.045	9.75	.010	.010	20.1	19.6

(All dimensions in inches)

Figure 5.3-18

Configurations selected for further study are:

- a. Beryllium sandwich with aluminum honeycomb core
- b. Magnesium ring-stiffened monocoque
- c. Titanium semi-monocoque (single-faced longitudinal corrugations with aluminum rings)

The selected configurations are highlighted in Figure 5.3-15. The reasons for selecting them are discussed below.

<u>Sandwich</u> - Figure 5.3-15 illustrates that, in general, structures made of beryllium offer an appreciable weight advantage. However, a review of the other characteristics and qualities offset this advantage. These are:

- a. Limited experience as a structural material
- b. Complicated fabrication requirements
- c. Questionable environmental compatibility
- d. Limited joining capability
- e. High material and fabrication costs

The honeycomb sandwich is not affected by these factors as much as the other beryllium configurations, e.g., single curvature, bonded construction.

Once the closure skin is installed on the sandwich configurations, there is no reliable non-destructive way to inspect the structure. This limitation compromises the structural confidence in sandwich construction and favors single face designs. Although this would seem to eliminate the sandwich structures from further consideration, the outstanding structural efficiency of beryllium prompted us to include it for further evaluation.

<u>Ring-Stiffened Monocoque</u> - Of the ring-stiffened monocoque concepts, the configuration using beryllium is the most efficient. However, beryllium sheet metal fabrication is extremely complex and has had limited application. Therefore, the more conventional magnesium structure was selected over beryllium for further evaluation.

<u>Semi-Monocoque</u> - Of the semi-monocoque concepts studied, the waffle construction was eliminated because of weight with no particular design or fabrication advantage.

For the sheet-stringer designs, resistance welding the stringers or corrugations to the skin is the preferred method of attachment to minimize weight and cost. The minimum practical thickness for resistance welding aluminum or magnesium is 0.025 inch. Since 0.012 and 0.016 inch thick material is the required

structural thickness for aluminum and magnesium, respectively, weld lands would be required, adding to the weight shown. Fabrication complexity would also be increased since additional operations are required to reduce the material thickness between the weld lands to the optimum structural thickness. An alternate solution is to rivet, rather than weld, using an aluminum or magnesium structure of the optimum thickness. This results in added complexity because the numerous rivet heads would interfere with heat shield installation. In addition, the weights in Figure 5.3-15 do not include an allowance for corrosion protection required for the aluminum and magnesium configurations. No similar problems exist for titanium (i.e. thin gage titanium is readily resistance welded and no corrosion protection is required), therefore, it is preferred.

Of the titanium sheet-stringer designs, the weight advantage shown for the single-faced longitudinal stringer configurations is not as great as indicated when certain non-optimum factors are considered. As can be seen from Figure 5.3-17, additional mechanical fasteners are required at each ring joint. The mold line gaps resulting at each end of the outboard flange of the ring cap will require a filler to provide a smooth mounting surface for the heat shield. The faying surfaces between the outboard ring cap and the shell is twice that of the other ring concept, requiring double the amount of dissimilar metal corrosion protection (tape between the titanium stringers and magnesium ring caps). Finally, the complexities in design, fabrication and development are sufficient to eliminate the single-faced longitudinal stringer configuration in favor of the less complicated single-faced longitudinal corrugation configuration. The latter is, therefore, selected for further evaluation.

Rings - The ring weights, shown in Figure 5.3-18, indicate beryllium to be the most efficient metal. However, the disadvantages of using beryllium, stated earlier, eliminate this material from further consideration. The slight weight advantage shown for magnesium does not offset the cost and fabrication advantages of aluminum. For this reason, aluminum is selected as the preferred ring material.

- 5.3.1.3 <u>Final Configuration Selection</u> Three configurations were selected in Section 5.3.1.2 for evaluation in greater detail. The final evaluation and selection is made in Section 5.3.1.3.5. The structural analyses which follow are a part of this evaluation. The configurations are:
 - o Beryllium face sheets with aluminum core from the sandwich concept.
 - o Magnesium from the ring-stiffened monocoque concept.
- o Titanium single-faced corrugation from the semi-monocoque concept. With all requirements satisfied in the structural design of spacecraft, general instability is usually not the critical mode of failure. However, the VOYAGER Aeroshell is unique. Due to its large size, light weight, and high-angle conical shape, general stability is an area of major concern. Because of this uniqueness, major attention was given to shell instability and aft ring instability. The methods used to predict both of these modes of failure are presented in Section 5.3.1.3.1. The detailed analyses of the three candidate configurations follows. Methods of analysis unique to each configuration are discussed when they are used. 5.3.1.3.1 General Methods of Analysis Shells subjected to external collapsing pressures may fail by general, panel or local instability. The local instability modes occur in many forms, such as face sheet wrinkling, core shear crimping, intracell buckling, and local buckling of ring or skin elements.

This section deals with shell instability and aft ring instability. For the sandwich and ring-stiffened monocoque configurations, general and panel instability are reduced to shell instability by the absence of major rings between the forward and aft rings. These rings establish shell boundary conditions. The forward ring provides a rigid, simple support boundary condition. The aft ring provides a flexible boundary condition. Therefore, by properly matching aft ring and shell stiffnesses, a combined shell and aft ring instability mode of failure is critical and is hereafter referred to as a shell instability mode of failure.

We have selected an "equivalent cylinder" approach to check for shell instability. A discontinuity analysis is performed to obtain the aft ring radial compression loads, and the ring is checked for instability using these loads. In practice, this is an iterative process because of the mutual dependence of the ring stability on the shell stiffness and shell stability on ring stiffness.

Equivalent Cylinder Approach to Shell Stability - A method of analysis similar to that recommended by Weingarten and Seide (Reference 5.3-2) is used to insure shell stability for a uniform external pressure. The method is to convert

the conical shell to an equivalent cylinder, assuming inextensible rings, and to apply cylinder theory to predict the buckling strength. The equivalent cylinder, shown on the right side of Figure 5:3-19, is one which has a length (L) equal to the meridional length of the cone and a radius (R) equal to the average normal radius of the cone. The radius of the equivalent cylinder is,

$$R = \frac{r_1 + r_2}{2 \cos \alpha} \tag{1}$$

where

 r_1 = radius at small end of cone.

 r_2 = raduis at large end of cone.

 α = half cone angle.

Since this method was developed for inextensible rings, extensible rings leads to unconservative results because the radial displacement of the extensible aft ring increases the hoop load in the shell. Ring extensibility is accounted for by using an effectively longer cone; one which has the same radial displacements as the actual cone in the area of maximum hoop load. A schematic diagram of the effectively longer cone is shown on the left side of Figure 5.3-19. The equivalent cylinder is larger and has a radius (R') equal to the average normal radius of the effectively longer cone and a length (L') equal to the meridional length of the effectively longer cone. In the following analyses, R' is interchangeable with R and L' is interchangeable with L depending on whether aft ring extensibility is being considered or not.

The theoretical buckling strength of the equivalent cylinder under lateral pressure is predicted by an expression developed by Batdorf (Reference 5.3-3) for simply supported isotropic cylinders.

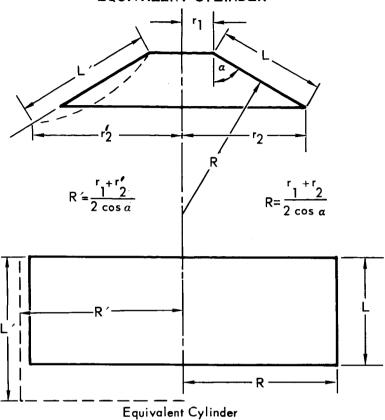
$$P_{\rm cr} = \frac{C_{\rm p} \pi^2 D}{RL^2} \tag{2}$$

where

 P_{cr} = critical buckling pressure, psi

C_p = buckling coefficient for isotropic cylinder subjected to lateral
 pressure

METHOD FOR DETERMINING AN EQUIVALENT CYLINDER



$$C_{p} = \begin{cases} \left[\frac{1 + \left(\frac{nL}{\pi R}\right)^{2}}{\left(\frac{nL}{\pi R}\right)^{2}} + \frac{12 z^{2}}{\pi^{4} \left(\frac{nL}{\pi R}\right)^{2}} \right] \end{cases}$$
(3)

D = flexural rigidity of shell, $1b-in^2$

L = length of equivalent cylinder, in.

R = radius of equivalent cylinder, in.

n = number of circumferential waves

Z = curvature parameter

$$Z = \frac{L^2}{Rt} \sqrt{1 - v^2}$$
 (4)

t = thickness of the isotropic shell

ν = Poisson's ratio

For a given shell configuration, the number of circumferential waves, n, is varied until a minimum value of the buckling coefficient, C_p , is obtained.

Batdorf has also developed a similar buckling coefficient expression for simply supported isotropic cylinders subjected to hydrostatic pressure:

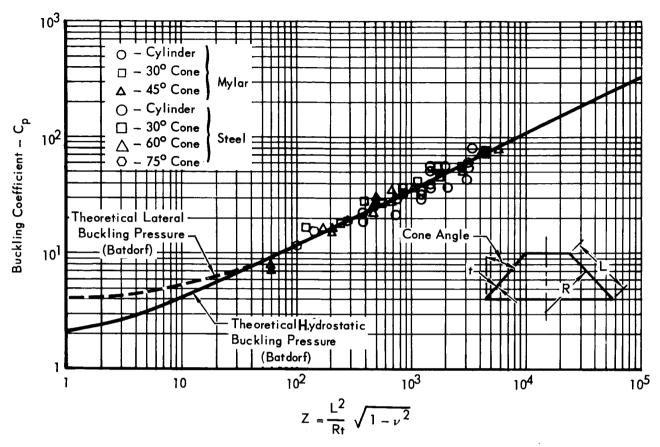
$$C_{p} = \left\{ \frac{\left[1 + \left(\frac{nL}{\pi R} \right)^{2} \right]^{2}}{\frac{1}{2} + \left(\frac{nL}{\pi R} \right)^{2}} + \frac{12 z^{2}}{\pi^{4} \left[1 + \left(\frac{nL}{\pi R} \right)^{2} \right] \left[\frac{1}{2} + \left(\frac{nL}{\pi R} \right)^{2} \right]} \right\}$$
(5)

Symbol definitions are the same as before. This buckling coefficient is used in Equation (2) to obtain the critical buckling pressure for hydrostatically loaded cylinders.

The experimental data of Reference 5.3-2 for cones are plotted on Figure 5.3-20. Batdorf's theoretical predictions for both lateral and hydrostatic loading is also shown. Agreement is excellent.

For the ring-stiffened monocoque concept, we have assumed the equivalent cylinder approach is also applicable. The theoretical buckling strength of the equivalent cylinder is predicted by an equation developed for simply supported ring-stiffened cylinders subjected to lateral pressure (Reference 5.3-4). This

COMPARISON OF THEORETICAL BUCKLING SOLUTION WITH TESTS OF MYLAR AND STEEL CYLINDERS AND CONES



equation, when divided by R/\bar{t} , yields the critical pressure:

$$P_{cr} = \frac{5.51 \, \gamma^{1/2} \, E^{\left(\rho/t\right) \, 3/2}}{\left(\overline{t}/t\right)^{1/4} \, \left(R/t\right)^{3/2} \, \left(L/R\right) \, \left(R/\overline{t}\right)}$$
(6)

where

P = critical buckling pressure, psi

γ = correlation factor to account for difference between theory and experiment (0.9 for ring-stiffened monocoque, Reference 5.3-4)

E = modulus of elasticity of shell, psi

ρ = radius of gyration of shell in the circumferential direction, in.

t = thickness of face sheet, in.

t = effective thickness of stiffened cylinder in the circumferential direction, in.

R = radius of equivalent cylinder, in.

L = length of equivalent cylinder, in.

Since the external pressures are reacted at the small end of the shell, meridional tension loads in the shell result. These tension loads increase the shell stability. Therefore, the use of the method outlined here is conservative for both the isotropic cone and the ring-stiffened monocoque cone.

In conclusion, the critical buckling pressure for a laterally loaded isotropic cone is found by:

- a Converting the cone to an equivalent cylinder.
- o Obtaining the buckling coefficient from Equation (3) or from Figure 5.3-20
- o Substituting the buckling coefficient and other parameters into Equation (2).

The critical buckling pressure for a laterally loaded, ring-stiffened monocoque cone is found by:

- o Converting the cone to an equivalent cylinder
- o Substituting parameters into Equation (6).

Aft Ring Stability in High-Angle Cones - Unsymmetrical pressures occurring during the maximum loading condition result in unsymmetrical radial loads applied to the rings. For ring stability analysis, we have assumed that the maximum unsymmetrical load applied to the ring is uniform around the circumference.

The rings are restrained at the moldline by the shell; therefore, the ring displacements are normal to the shell. For rings installed in cones, this results

in a ring buckled mode which is partly out-of-plane. An analysis by Cheney (Reference 5.3-5) is used to predict the buckling strength for rings restrained to displace normal to the shell surface. This expression for the lowest buckling mode (n=2) and neglecting torsional, in-plane, and tangential restraint by the shell is:

$$P_{cr} = \frac{9}{r^{3}(4 \sec^{2} \alpha - 1)} \left[EIy + \frac{EI_{x}tan^{2} \alpha \left(JG + \frac{4E\Gamma}{r^{2}} \right)}{\left(JG + \frac{4E\Gamma}{r^{2}} \right) + \frac{EIx}{4}} \right]$$
(7)

where:

p_{cr} = critical radial load, 1b/in

r = radius, in.

 α = half cone angle, degrees

EIy = in-plane flexural rigidity, $1b-in^2$

 $EI_{\mathbf{v}} = \text{out-of-plane flexural rigidity, } 1b-in^2$

 $JG = torsional rigidity, 1b-in^2$

 Γ = warping constant, in⁶

The warping constant, Γ , is defined by the expression:

$$\Gamma = \frac{1}{144} \sum (bt)^3 \tag{8}$$

where:

b = length of each ring element, in.

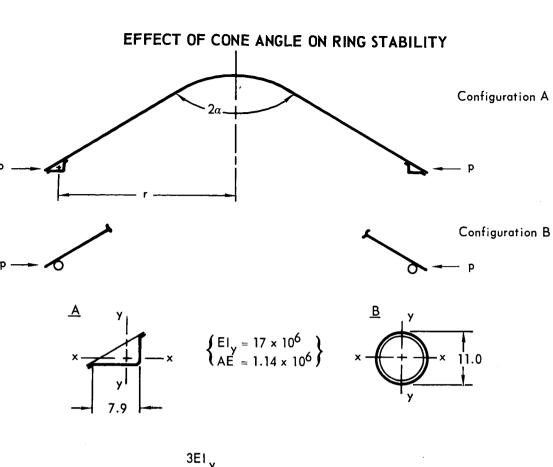
t = thickness of each ring element, in.

The effect of cone angle on ring stability for two examples is shown on Figure 5.3-21. Chencey's expression reduces to the classical in-plane buckling equation when $\alpha = 0$:

$$p_{cr} = \frac{3EI_y}{r^3}$$

The general buckling equation for rings possessing no out-of-plane flexural rigidity and no torsional rigidity reduces to the following expression when the half-cone angle is 60 degrees, as shown at point (a) on the figure:

$$p_{cr} = \frac{.6EI_{y}}{r^{3}}$$
 (9)



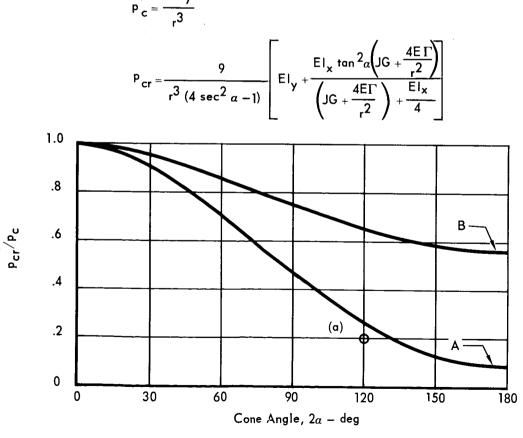


Figure 5.3-21 5.3-36

Very recent tests indicate that this is a conservative method of analysis. See Summary of Tests in Section 5.3.1.3.4 for a description of the tests.

5.3.1.3.2 <u>Beryllium Sandwich</u> - Of the sandwich concepts, Figure 5.3-9, the configuration with beryllium face sheets was found to be the lightest. The sandwich consists of face sheets of 0.010 in. thick, cross-rolled beryllium sheet and the core consists of 0.66 in. thick aluminum honeycomb, weighing 2 lb/ft³ and having 3/16 in. cells. The magnesium base ring is 7.9 inches deep.

The properties of beryllium cross-rolled sheet are:

o Ultimate tensile strength = $70,000 \text{ lb/in}^2$

o Yield tensile strength = $50,000 \text{ lb/in}^2$

o Modulus of elasticity = $42,000,000 \text{ lb/in}^2$

o Poisson's ratio (v) = 0.04

The properties of magnesium alloy, HM21A-T81, are:

o Ultimate tensile strength = $33,000 \text{ lb/in}^2$

o Yield tensile strength = $25,000 \text{ lb/in}^2$

o Yield compressive strength = $22,000 \text{ lb/in}^2$

o Modulus of elasticity = $6,400,000 \text{ lb/in}^2$

o Poisson's ratio (v) = 0.33

Analyses presented in this section are divided into internal loads, shell stability, local stability, shell strength, aft ring stability and dynamic analysis. The loads used in these analyses are defined in Section 5.3.1.1

Internal Loads - Internal loads for this configuration were obtained using the SABOR III program (Ref. 5.3-6). This program is a linear elastic analysis of thin (homogeneous) shells of revolution under ayammetric or axisymmetric loading by the matrix displacement method. The beryllium sandwich is idealized as an equivalent homogeneous shell having the same flexural rigidity, EI, and extensible rigidity, AE. For the sandwich:

$$EI = \frac{E_f t_f h^2}{2(1 - v^2)}$$

and

$$AE = \frac{2E_f t_f}{(1 - v^2)}$$

where:

 $E_f = modulus of elasticity of face sheet, <math>lb/in^2$

 t_f = thickness of face sheet, in.

h = distance between face sheet centroids, in.

ν = Poisson's ratio

For the equivalent homogeneous shell,

$$EI = \frac{E_e t_e^3}{12(1-v^2)}$$

and

$$AE = \frac{E_e t_e}{(1-v^2)}$$

where

 E_{ρ} = effective modulus of elasticity of equivalent shell, $1b/in^2$

t = effective thickness of equivalent homogeneous shell, in.

Equating rigidity and solving for t_e and E_e , the following equivalent homogeneous shell properties are obtained:

$$t_e = \sqrt{3} h$$

$$E_e = \frac{2 E_f t_f}{\sqrt{3} h}$$

For the beryllium sandwich,

$$h = .67 in.$$

$$E_f = 42.0 \times 10^6 \text{ lb/in.}^2$$

$$t_f = .010 in.$$

Therefore.

$$t_e = \sqrt{3}$$
 (.67) = 1.16 in.

and

$$E_e = \frac{2 (42.0 \times 10^6 \times 0.010)}{\sqrt{3} \times .67} = 7.25 \times 10^5 \text{ lb/in}^2$$

These effective properties were used in the program and internal meridional and circumferential shears, bending moments, and axial loads were determined throughout the shell. Internal loads for the windward and leeward sides of the Aeroshell are shown in Figure 5.3-22. Transverse shear, circumferential moment, and hoop load for a typical shell element located at the point of maximum hoop load is shown in Figure 5.3-23.

<u>Shell Stability</u> - For this analysis, we conservatively assumed that the pressure on the windward side acts around the entire shell. The steps for assuring stability were discussed in Section 5.3.1.3.1. They are:

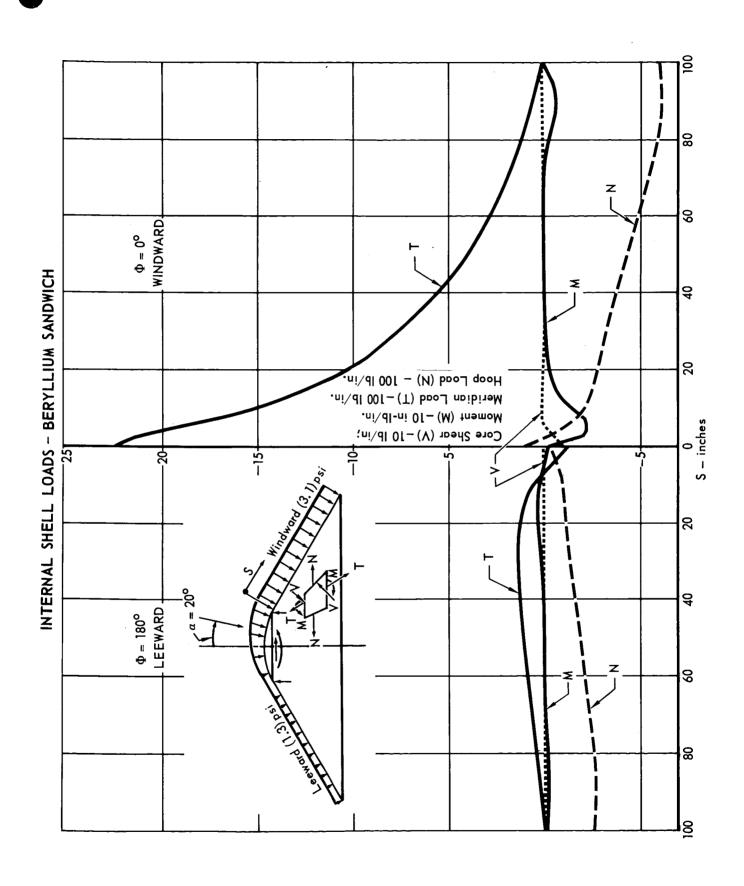


Figure 5.3-22 5.3-39

TYPICAL CIRCUMFERENTIAL SHELL LOADS BERYLLIUM SANDWICH

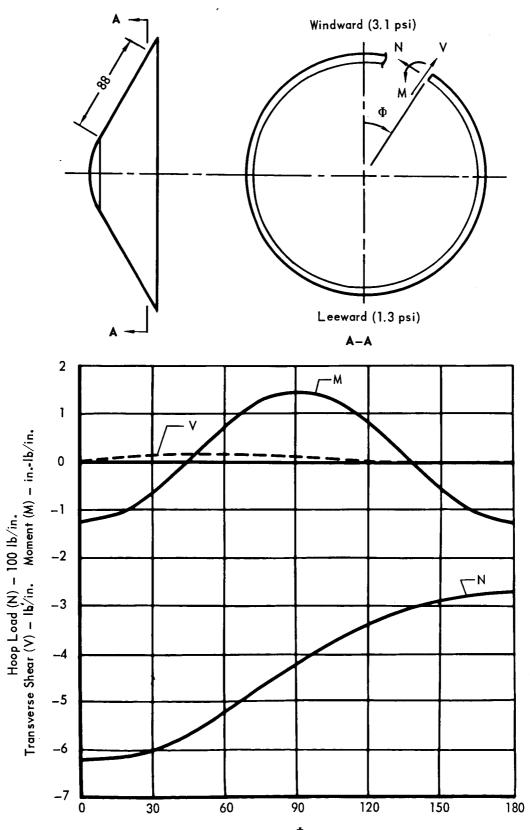


Figure 5.3-23

5.3-40

- (1) Determine the radial displacements of the shell considering an extensible aft ring.
- (2) Determine an effectively longer cone which has the same displacements at the point of maximum hoop load and at the aft ring as the actual cone.

 The effectively longer cone has an inextensible aft ring.
- (3) Determine the equivalent cylinder by procedure previously discussed, equation (1) of Section 5.3.1.3.1.
- (4) Find the critical buckling pressure, equation (2) of Section 5.3.1.3.1.

The radial displacements of the beryllium sandwich shell are shown on Figure 5.3-24. Also shown on this figure is the effectively longer cone with an inextensible aft ring. The effectively longer cone has the same radial displacements as the actual cone at the point of maximum hoop load and at the aft ring. The figure shows the following dimensions for the effectively longer cone:

$$r_1 = 28.5 in.$$

$$r_2' = 147.5 in.$$

$$L' = 138 in.$$

$$\alpha = 60 \text{ deg.}$$

By equation (1) of Section 5.3.1.3.1, the radius of the equivalent cylinder is:

$$R' = \frac{r_1 + r_2'}{2 \cos \alpha} = \frac{28.5 + 147.5}{2 \cos 60^{\circ}} = 176 \text{ in.}$$

The equivalent homogeneous shell properties, given before, are:

$$t_e = 1.16 in$$

$$E_e = 7.25 \times 10^5 \text{ lb/in}^2$$

$$v = 0.04$$

and the flexural rigidity, D, is:

$$D = \frac{E_{e}t_{e}^{3}}{12[1-v^{2}]} = \frac{(7.25 \times 10^{5})(1.16)^{3}}{12[1-(.04)^{2}]} = 9.43 \times 10^{4} \text{ lb-in.}^{2}$$

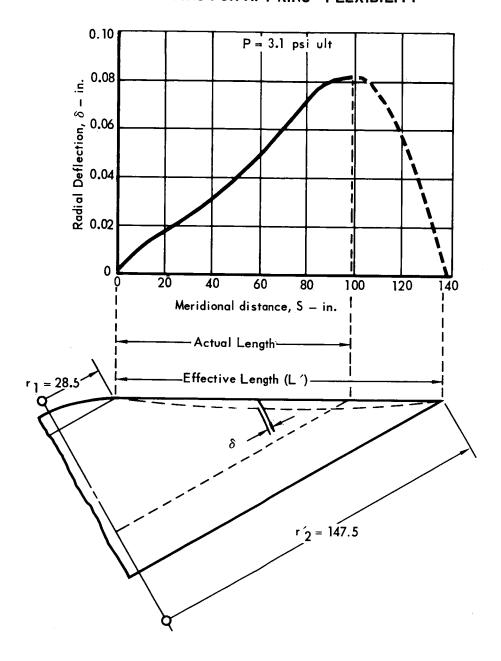
Using equation (4) of Section 5.3.1.3.1, the curvature parameter, Z is:

$$Z = \frac{L'^2}{R't_0} \qquad \sqrt{1 - v^2} = \frac{(138)^2}{(176)(1.16)} \sqrt{1 - (.04)^2} = 93.5$$

From Figure 5.3-20, the buckling coefficient (C_p) for lateral pressure is:

$$C_p = 11.5$$

EQUIVALENT CYLINDER FOR BERYLLIUM SANDWICH, ACCOUNTING FOR AFT RING FLEXIBILITY



The critical buckling pressure, P_{cr} , using equation (2) Section 5.3.1.3.1, is,

$$P_{cr} = \frac{C p^{\pi^2} D}{R'L^2} = \frac{(11.5) \pi^2 (9.43 \times 10^4)}{(176)' (138)^2} = 3.18 psi$$

The maximum pressure, P, on the windward side of the shell (Figure 5.3-4) is 3.10 psi ultimate; therefore, the shell is stable.

Local Stability - The beryllium sandwich structure is subject to three local instability modes of failure. They are: (1) intracell buckling, (2) face sheet wrinkling, and (3) core shear crimping. In general, intracell buckling is critical with thin face sheets and large core cell sizes, face sheet wrinkling is critical for light density cores, and shear crimping with thin sandwiches and thin face sheets. Each failure mode involves the core, to some extent. We have used a 2.0 lb/ft³ aluminum core having a 3/16 (0.188) in. cell size.

The analysis for local instability is based on two simplifying assumptions: (1) meridional tension loads and their stablizing effects are neglected, and (2) shear loads in the face sheets are neglected because they are small in the region of maximum hoop load where this analysis is applicable.

The results of analyses for local instability are presented in Figure 5.3-25. The equations shown are from the references indicated, modified to include the plasticity reduction factor, η . Values for η are found in Reference 5.3-7.

From Figure 5.3-22, the maximum hoop load, N, is 630 lb/in. Therefore, the maximum hoop stress is:

$$\sigma = \frac{N}{2t_f} = \frac{630}{(2)(.010)} = 31,500 \text{ psi (ultimate)}$$

It is shown that the critical stresses for the local instability failure modes exceed the actual stress by a comfortable margin.

Shell Strength - The beryllium face sheets are designed to withstand the biaxial state of stress existing throughout the shell. The stresses in the face sheet must not exceed the material yield strength under limit loads or the material ultimate strength under ultimate loads. For beryllium, the stresses occurring at limit load are critical because the yield strength is 71 percent of the ultimate strength while limit load is 80 percent of the ultimate load. To include interaction of the meridional and hoop stresses, we have computed an effective stress (σ_e) using von Mises yield criteria, (Reference 5.3-9).

LOCAL SANDWICH STABILITY

BERYLLIUM FACE SHEETS, 0.010 IN. ALUMINUM CORE, 2.0 lb/ft³

FAILURE MODE	METHOD OF ANALYSIS	CRITICAL STRESS, $\sigma_{ m cr}$	
Intracell Buckling	$\frac{\sigma_{cr}}{\eta} = 0.764 \text{E}_f \left(\frac{\uparrow_f}{\text{S}}\right)^{3/2}$ Ref: 5.3-4	63000 psi	
Sheet Wrinkling	$\frac{\sigma_{\rm cr}}{\eta} = 0.79 (E_{\rm f} E_{\rm c} G_{\rm c})^{1/3}$ Ref: 5.3–4	57000 ps i	
Shear Crimping	$\frac{\sigma_{cr}}{\eta} = \frac{G_c}{2t_f} (h_c + 2t_f)$ Ref: 5.3-8	65000 psi	

Nomenclature: Ef = Modulus of elasticity of face sheet, 42×10^6 psi

 E_c = Modulus of elasticity of core (parallel to cell axis), 24,000 psi

 G_c = Shear modulus of core, 9000 psi

 t_f = Face sheet thickness, 0.010 in.

h_c = Core thickness, 0.66 in.

 $\eta = Plasticity reduction factor$

S = Core cell size, 0.187 in.

The effective stress at limit load must not exceed the yield strength (F $_{ty}$) of the face sheet material. The equation for σ_e , the effective stress, is:

$$\sigma_e = \sqrt{\sigma_h^2 + \sigma_m^2 - \sigma_h^2 \sigma_m + 3\tau^2}$$

where:

Oh = Limit hoop stress in face sheets, psi

 $\sigma_{\rm m}$ = Limit meridional stress in face sheets, psi

7 = Limit shear stress in face sheets, psi

The meridional and hoop stresses are maximum on the windward side of the shell where the shear stresses are low. The effective stress for this location is shown in Figure 5.3-26. A discontinuity in the curve occurs because the thickness of both face sheets is increased from 0.010 in. at a meridional distance of 20 in. from the small end of the shell to 0.020 in. at the small end of the shell.

Aft Ring Stability - The aft ring must possess sufficient flexural and extensible stiffness to enable the shell to carry the prescribed pressure efficiently. A discontinuity analysis was performed, considering ring and shell flexibilities, to determine the interrelationship between ring flexural rigidity, ring extensional rigidity, and shell flexibility. The results are presented on Figure 5.3-27. It was found that both ring flexural rigidity and ring extensional rigidity influence stability. The curve labeled "balanced design" on the bottom of the figure represents the boundary between the ring instability mode of failure and the shell instability mode of failure. We have designed the ring for the beryllium sandwich so that it falls at point (a). This represents a design that is equally critical in stability of the sandwich and stability of the ring. Figure 5.3-27 was greatly simplified by neglecting out-of-plane rigidity and torsional rigidity of the ring, therefore, slightly more ring stability can be expected when these two additional items are considered.

A discontinuity analysis at the shell-ring intersection indicated that the ring will be required to sustain the in-plane loads shown on Figure 5.3-28. The ring we have used has the following properties:

 EI_y = in-plane flexural rigidity, 17 x 10^6 1b-in²

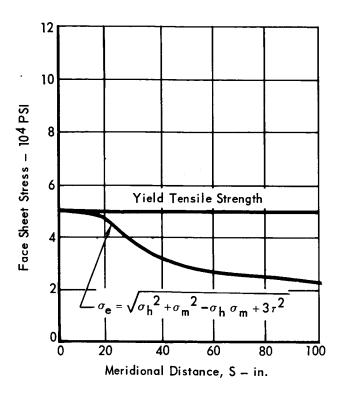
 EI_x = out-of-plane flexural rigidity, 2.3 x 10^6 $1b-in^2$

JG = torsional rigidity, $2.5 \times 10^6 \text{ lb-in}^2$

Er = warping rigidity, 735 lb-in^4

r = radius to ring centroid, 109 in

VON MISES YIELD CRITERIA FOR BIAXIAL STRESSES Beryllium Sandwich



AFT RING FLEXURAL AND EXTENSIONAL RIGIDITY REQUIREMENTS **FOR** SHELL STABILITY

BERYLLIUM SANDWICH

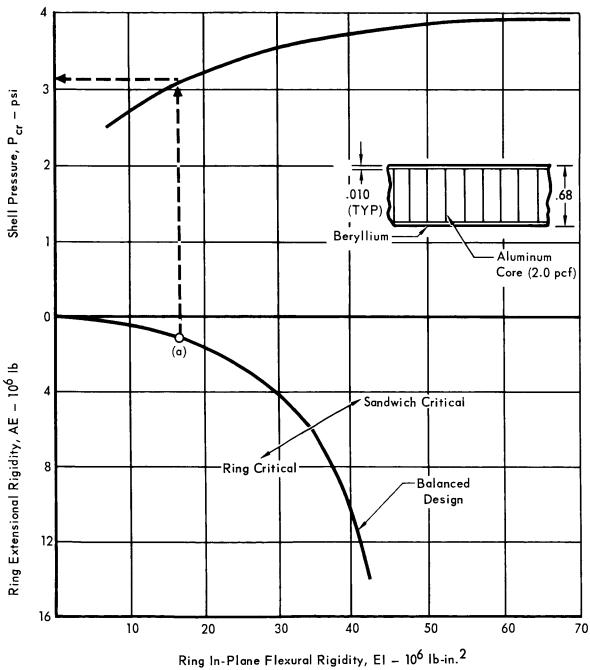


Figure 5.3-27

AFT RING LOADS - BERYLLIUM SANDWICH

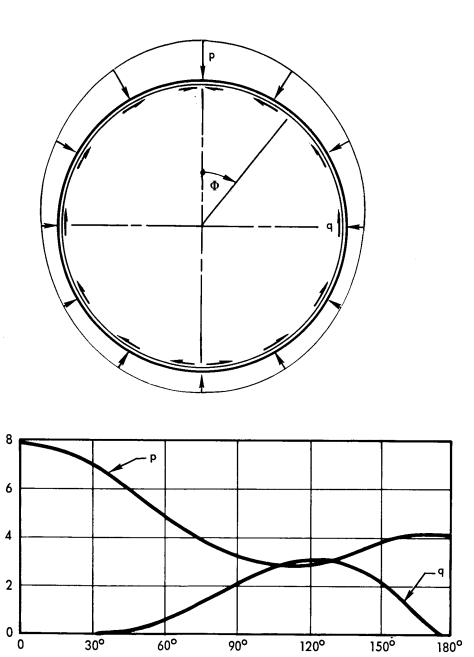


Figure 5.3-28

Φ

Shear, q — Ib/in. Radial Load, p — Ib/in The ring buckling strength, when installed on a 60 degree half-angle cone ($\alpha = 60^{\circ}$), equation (7), Section 5.3.1.3.1.

$$p_{cr} = \frac{9}{r^{3} (4 \sec^{2} \alpha - 1)} \left[EI_{y} + \frac{EI_{x} \tan^{2} \alpha \left(JG + \frac{4E\Gamma}{r^{2}} \right)}{\left(JG + \frac{4E\Gamma}{r^{2}} \right) + \frac{EI_{x}}{4}} \right]$$

$$p_{cr} = \frac{9}{(109)^{3} (4 \sec^{2} 60^{\circ} - 1)} \left[17.0 \times 10^{6} + \frac{(2.3 \times 10^{6})(\tan^{2} 60^{\circ})(2.5 \times 10^{6} + \frac{4 \times 735}{(109)^{2}})}{(2.5 \times 10^{6} + \frac{4 \times 735}{(109)^{2}}) + \frac{2.3 \times 10^{6}}{4}} \right]$$

$$p_{cr} = 10.8 \text{ lb/in}$$

As shown, in Figure 5.3-28, the maximum radial load (p_r) is,

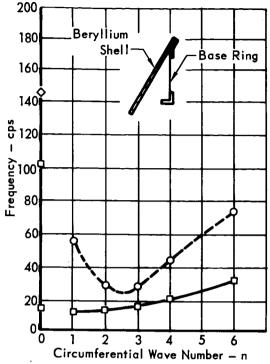
$$p_r = 8.0 \text{ lb/in.}$$

Dynamic Analysis - Frequencies and mode shapes have been calculated for two configurations of the beryllium sandwich Aeroshell. The first configuration is with the base ring unrestrained, and the second is with the base ring restrained. In both configurations, the Aeroshell was fixed at the small end. To determine the overall system lowest frequency, six harmonics (number of circumferential waves in mode shape) were considered. This was accomplished with the aid of the Sabor III Program. Essentially, the Sabor Program develops a system stiffness matrix and a consistent mass matrix for each harmonic for any arbitrary shell of revolution by the finite element approach. With these two matrixes the system natural frequencies and mode shapes can be determined for each harmonic.

Figure 5.3-29 shows the lowest frequencies of each harmonic analyzed for the two configurations. The results of this study served to identify the harmonic having the lowest system frequency for the given structure. The lowest frequencies are in the unrestrained ring configuration, and Figure 5.3-29 shows that the motion is predominantly ring motion. If the base ring is restrained, the ring frequencies are much higher than the lowest frequency and the predominant motion is shell motion. For the two configurations analyzed, the beryllium sandwich shell with the base ring restrained is much more desirable. Although, by restraining

MODE SHAPES AND FREQUENCIES

BASE RING UNRESTRAINED



- O Predominantly Shell MotionD Predominantly Ring Motion

Mass Loading Effect of Ablator is Included in Analysis. Aeroshell
Meridian

Mode Shape
Normalized
to Maximum
Deflection

M = 1 N = 3

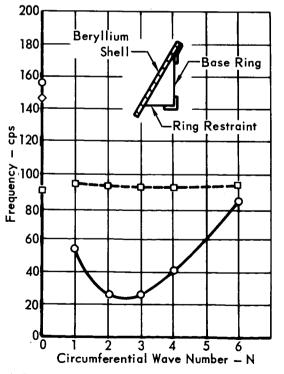
Radius

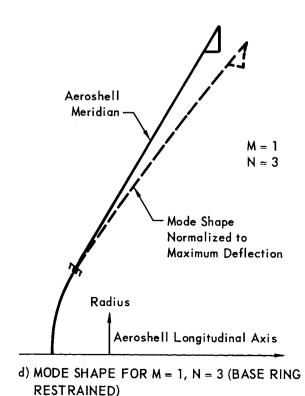
Aeroshe II Longitudinal Axis

b) MODE SHAPE FOR M = 1, N = 3 (BASE RING UNRESTRAINED)

a) FREQUENCY vs CIRCUMFERENTIAL WAVE NUMBER

BASE RING RESTRAINED





c) FREQUENCY vs CIRCUMFERENTIAL WAVE NUMBER

Figure 5.3-29

5.3 - 50

the ring, the shell frequencies are not increased appreciably, the problem of dynamic ring instability is avoided.

5.3.1.3.3 <u>Magnesium Ring-Stiffened Monocoque</u> - Of the ring-stiffened monocoque concepts, Figure 5.3-9, the configuration using beryllium for both the rings and skin is the lightest. However, fabrication of this beryllium concept is difficult and is not considered to be consistent with the structural objectives of this program. Therefore, the next lightest configuration using HM21A-T81 magnesium for both the rings and skin is selected for this study.

The magnesium, ring-stiffened monocoque configuration consists of a single magnesium skin, 0.050 in. thick, stabilized by rings. The rings are channel sections 1.20 inches deep with a thickness of 0.020 inch. Thirty-four rings, spaced from 3.3 inches at the small end to 2.3 at the large end, are used. A magnesium ring, 9.0 inches deep, is used at the base of the shell.

The properties of magnesium alloy, HM21A-T81, are:

Ultimate tensile strength = $33,000 \text{ lb/in}^2$

Yield tensile strength = $25,000 \text{ lb/in}^2$

Yield compressive strength = $22,000 \text{ lb/in}^2$

Modulus of elasticity = $6,400,000 \text{ lb/in}^2$

Poisson's ratio (ν) = 0.33

Analyses presented in this section are divided into internal loads, shell stability, local stability, shell strength and dynamic analysis. An aft ring stability analysis is not shown because it is very similar to the analysis of the aft ring for the beryllium sandwich. The loads used in these analyses are defined in Section 5.3.1.1.

Internal Loads - The SABOR III Program was used to obtain internal loads in the skin of this configuration. The influence of rings was included by combining the ring in-plane, out-of-plane, and torsional stiffnesses with the skin stiffness at the ring-skin nodal circles. Knowing the ring stiffnesses and the displacements at the ring-skin intersection, determined by the SABOR program, it is possible to compute the external and internal ring loads.

Internal meridional and circumferential shears, bending moments, and axial loads in the skin, resulting from the unsymmetrical pressure distribution (Figure 5.3-4), were determined throughout the shell. Internal skin loads for the windward and leeward sides of the Aeroshell are shown in Figure 5.3-30. Transverse shear, circumferential moment, and hoop load for a typical ring located at the point of maximum hoop load are shown in Figure 5.3-31.

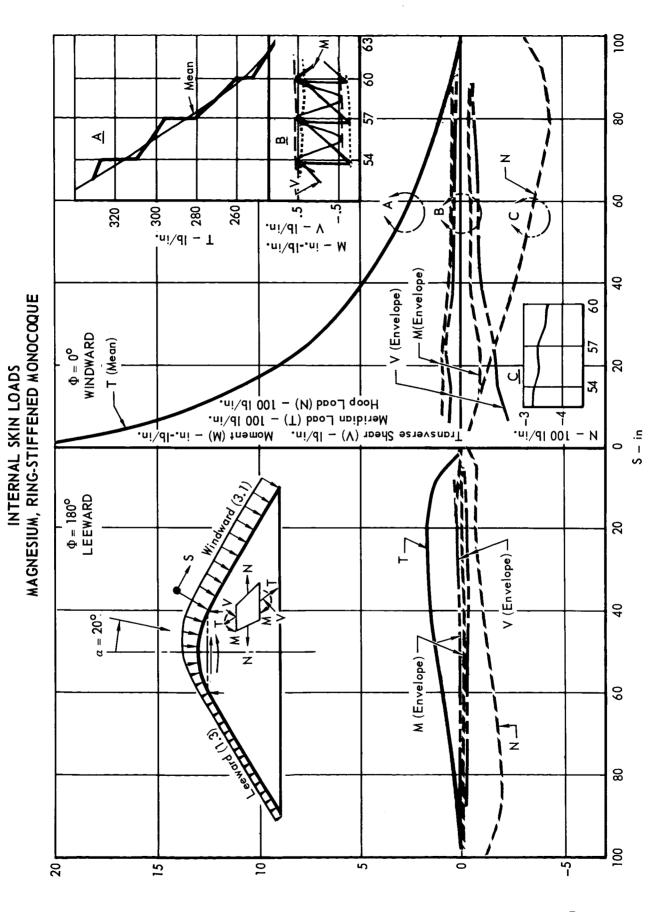
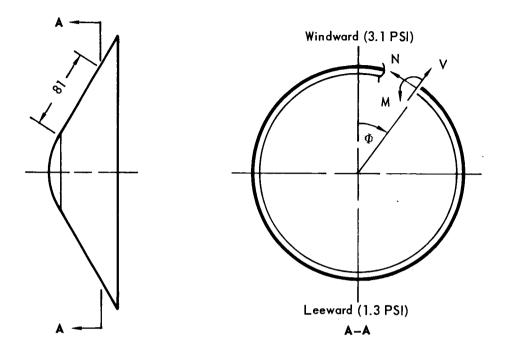


Figure 5.3-30

5.3-52

INTERNAL RING LOADS MAGNESIUM, RING-STIFFENED MONOCOQUE



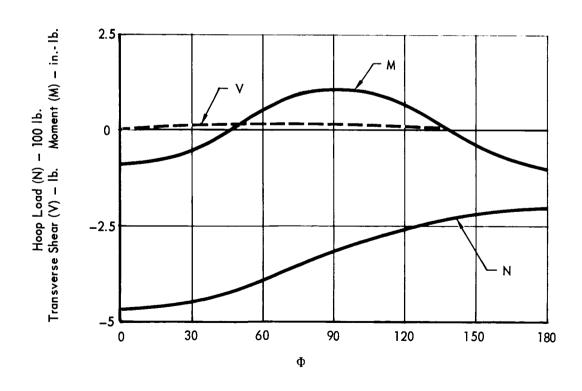


Figure 5.3-31

<u>Shell Stability</u> - For this analysis, we conservatively assume that the pressure on the windward side acts around the entire shell. Steps for assuring stability were discussed in Section 5.3.1.3.1. These are:

- (1) Determine the radial displacements of the shell considering an extensible aft ring.
- (2) Determine an effectively longer cone which has the same displacements at the point of maximum hoop load and at the aft ring as the actual cone. The effectively longer cone has an inextensible aft ring.
- (3) Determine the equivalent cylinder by the procedure previously discussed, equation (1), Section 5.3.1.3.1.
- (4) Find the critical buckling pressure, equation (6), Section 5.3.1.3.1.

Considering the radial displacements of the magnesium ring-stiffened monocoque configuration, the dimensions of the effectively longer cone were determined by a procedure similar to that given for the beryllium sandwich. The dimensions of the effectively longer cone are:

$$r_1 = 28.5 in.$$

$$r_2^1 = 117.5$$
 in.

$$L' = 103 in.$$

$$\alpha = 60 \text{ deg.}$$

By equation (1), Section 5.3.1.3.1, the radius of the equivalent cylinder is:

$$R' = \frac{r_1 + r_2'}{2 \cos \alpha} = \frac{28.5 + 117.5}{2 \cos 60^{\circ}} = 146 \text{ in.}$$

The shell properties, defined after equation (6), Section 5.3.1.3.1, are:

$$E = 6.4 \times 10^6 \text{ psi}$$

$$\rho$$
 = .42 in.

$$t = 0.050 in.$$

$$\bar{t} = 0.066 \text{ in.}$$

The correlation factor, γ , is 0.90, Reference 5.3-4.

Using equation (6), the critical buckling pressure, P_{cr} , is:

$$P_{cr} = \frac{5.51 \text{ y}^{1/2} \text{ E} \left(^{\rho}/_{t}\right)^{3/2}}{\left(\overline{t}/_{t}\right)^{1/4} \left(\frac{R}{_{t}}\right)^{3/2} \left(\frac{L}{_{R}}\right)\left(\frac{R}{_{T}}\right)}$$

$$P_{cr} = \frac{5.51(.90)^{1/2}(6.4\times10^6)(.42/.050)^{3/2}}{(.066/.050)^{1/4}(146/.050)^{3/2}(103/146)(146/.066)}$$

Pcr = 3.10 psi

The maximum pressure (P) on the windward side of the shell (Figure 5.3-4) is 3.10 psi ultimate; therefore, the shell is stable.

Local Stability - For this structural configuration, it is important that local buckling of the skin and rings does not precede shell instability. This analysis for local instability is based on two simplifying assumptions: (1) meridional tension loads and their stabilizing effects are neglected, and (2) shear loads in the skin are neglected because they are small in the region of maximum hoop load where this analysis is applicable.

After investigating several approaches for determining the local buckling strength, it was decided that the work of Becker (Reference 5.3-10) is most applicable. The equation used to predict local buckling strength, f_{cr} , is:

$$f_{cr} = \frac{K_s \pi^2 E}{12(1-v^2)} \left(\frac{t_s}{b_s}\right)^2$$

where:

 K_S = buckling coefficient

E = modulus of elasticity, psi

 t_S = thickness of skin, in.

 $b_s = ring spacing, in.$

v = Poisson's ratio, .33

The buckling coefficient, K_s , was obtained from Reference 5.3-10 (Figure 14) by treating the skin as a flat plate in compression stiffened by zee section stiffeners. For this configuration $b_w/b_s = 0.43$, $b_f/b_w = 0.39$, and $t_w/t_s = 0.40$ resulting in $K_s = 3.7$.

Summarizing the mechanical and geometrical properties of the shell:

 $E = 6.4 \times 10^6 \text{ lb/in.}^2$

 $t_s = 0.050 in.$

 $b_{S} = 2.50 in.$

Substitution into the previous equation results in a critical buckling stress of 8700 psi. From Figure 5.3-30, the maximum hoop load (N) in the skin is 420 lb/in and the maximum stress in the skin is:

$$f = \frac{N}{t} = \frac{430}{0.050} = 8600 \text{ psi}$$

Therefore, the shell has sufficient strength for local stability. The actual hoop stresses over the length of the shell and the allowable hoop stresses, computed with this method, are shown on Figure 5.3-32.

Shell Strength - The magnesium skin is designed to withstand the biaxial state of stress existing throughout the shell. The stresses in the face sheet must not exceed the material yield strength under limit load or the material ultimate strength under ultimate load. For HM21A-T81 magnesium, the stresses occurring at limit load are critical because the yield strength is 75 percent of the ultimate strength while limit load is 80 percent of the ultimate load. To include interaction of the meridional and hoop stresses, we have computed an effective stress (σ_e) using von Mises yield criteria (Reference 5.3-9). The effective stress at limit load must not exceed the uniaxial yield strength (F_{ty}) of the skin material. The equation for the effective stress, σ_e , is:

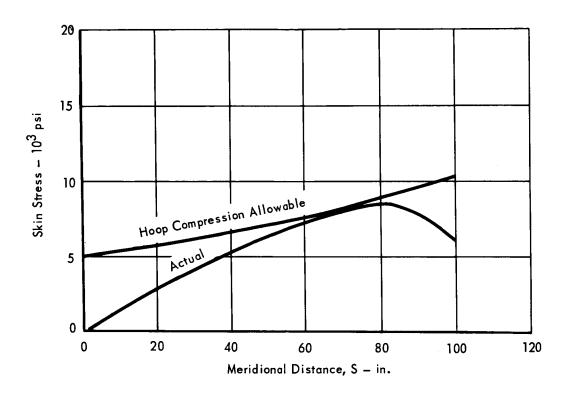
$$\sigma_{e} = \sqrt{\sigma_{h}^{2} + \sigma_{m}^{2} - \sigma_{h}\sigma_{m} + 3\tau^{2}}$$

where: σ_h = limit hoop stress in skin, $1b/in^2$ σ_m = limit meridional stress in skin, $1b/in^2$ τ = limit shear stress in skin, $1b/in^2$

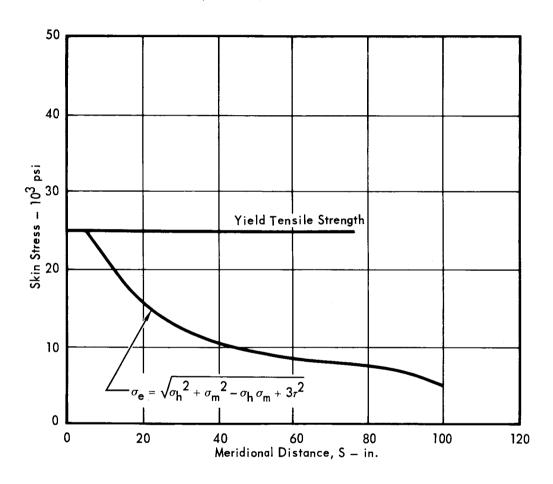
The meridional and hoop stresses are maximum on the windward side of the shell where the shear stresses are low. The effective stress for this location is shown in Figure 5.3-33. A discontinuity in the curve occurs because the skin thickness is increased from 0.050 in. at a meridional distance of 8.0 in. from the small end of the shell to 0.072 in. at the small end of the shell.

Dynamic Analysis - A vibration analysis was conducted and it indicates that the lowest frequency mode occurs at 23 cps in the second harmonic. The result of increasing the number of rings is to raise the frequency for the higher number harmonics. It was found that in the limit, the number of rings in the shell does not greatly influence the value of the minimum frequency. An explanation is that as the circumferential wave number increases, the rings bend into shorter wavelengths making the effective stiffness of the ring greater. This results in higher natural frequencies of the shell at the higher harmonics.

HOOP COMPRESSION STRESS Magnesium Ring-Stiffened Monocoque



VON MISES YIELD CRITERIA FOR BIAXIAL STRESSES MAGNESIUM, RING-STIFFENED MONOCOQUE



5.3.1.3.4 <u>Titanium</u>, <u>Semi-Monocoque</u> - Of the semi-monocoque concepts, Figure 5.3-9, the configuration using a titanium single-faced, longitudinally corrugated shell with internal aluminum rings was selected for this study. This selection is based on considerations of weight and complexities in design, fabrication and development.

The conical shell consists of two sheets of 0.008 inch thick titanium alloy, 6Al-4V. The outer skin is smooth and is stitch welded to a corrugated inner skin. The corrugations in the meridional direction are 0.53 inch high and the pitch varies from 1.05 inches at the small end of the shell to 2.10 inches at a meridional distance of 32.9 inches. At this location, the shell is spliced and the number of corrugations is doubled so that the pitch again varies from 1.05 inches to 2.10 inches at the base. This configuration is designed without the need for a hoop load path in the skin. Circumferential strength and stiffness is provided by seven internal rings. These rings are channel sections, stabilized by gussets, and vary in depth from 3.2 inches at the small end to 15.7 inches at the base. The properties of the titanium used in the shell are:

Ultimate tensile strength = $139,000 \text{ lb/in}^2$ Yield tensile strength = $131,000 \text{ lb/in}^2$ Yield compressive strength = $138,000 \text{ lb/in}^2$

Modulus of elasticity = $16,000,000 \text{ lb/in}^2$

Poisson's ratio (ν) = 0.32

The properties of aluminum used in the rings are:

Ultimate tensile strength = $85,000 \text{ lb/in}^2$ Yield tensile strength = $75,000 \text{ lb/in}^2$

Modulus of elasticity = $10,500,000 \text{ lb/in}^2$

Poisson's ratio (ν) = 0.33

Analyses presented in this section are divided into internal loads, shell strength, ring stability, dynamic analysis, and summary of tests. The loads used in these analyses are defined in Section 5.3.1.1.

Internal Loads - External pressures are carried to the internal rings by the corrugations and effective skin acting as beams. Internal loads in these meridional beams were obtained by considering the beams continuously supported at the rings. Shears, bending moments and axial loads for a meridional beam of unit width on the windward side are shown in Figure 5.3-34. Since all loads are reacted at the small end of the shell, meridional tension is developed throughout the shell.

MERIDIONAL LOADS (WINDWARD SIDE) TITANIUM, SEMI-MONOCOQUE

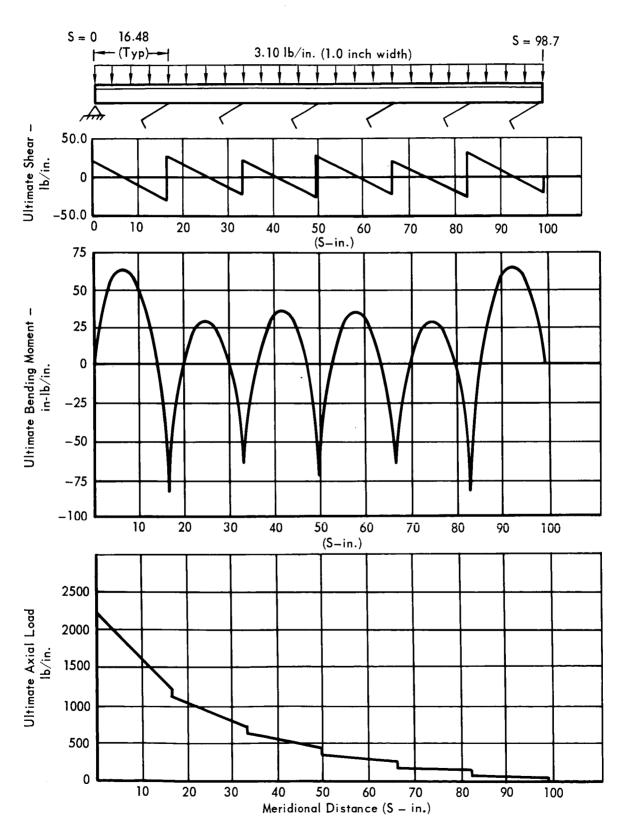


Figure 5.3-34

5.3-60

• 31 AUGUST 1967

REPORT F694 • VOLUME II • PART

The beam bending moments were not decreased to account for the effect of this meridional tension.

Pressures applied to the Aeroshell result in radial loads applied to the rings. The unsymmetrical components of these loads are balanced by shear forces. A balance is shown in Figure 5.3-35 for ring number four located a meridional distance of 49 inches from the cone-sphere tangency. These loads result in internal shear and bending moment and axial load in the ring. The internal shear and bending moment are small and previous studies have shown that for this radial load distribution, it is adequate to provide hoop strength to withstand the maximum radial load uniformly distributed around the circumference.

Shell Strength - The meridional distribution of stresses in the shell are shown in Figure 5.3-36 for the 3.10 psi ultimate pressure on the windward side. Part (a) of the figure shows the stress distribution in the meridional direction for the skin (outboard element) side of the corrugation. Between rings, the bending moment in the corrugation produces a compressive stress in the skin. Near the small end of the shell, the axial tension load is large enough to produce a tension stress throughout the section. Only near the base of the shell does the tension load become so small that the net stress in the skin is compression. Part (b) of the figure shows the stress distribution in the meridional direction for the inboard element of the corrugation. Over the rings, the bending moment in the corrugation produces a compressive stress in this element of the corrugation. Near the base of the shell, the axial load has reduced so that the net stress in the element is compression. Comparing the allowable and actual strength of the corrugations from Part (a) and Part (b) of Figure 5.3-36, it is seen that the critical location for compression is at the sixth ring. At this location, the stress is 16,800 psi and the allowable stress is 29,000 psi. The critical location for tension is at the small end of the cone where the stress is 96,000 psi and the ultimate allowable stress is 139,000 psi.

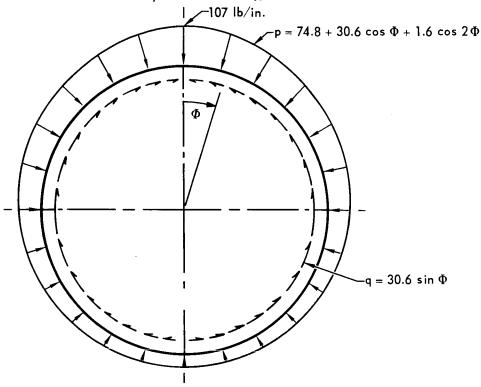
Since this configuration is designed without the need for a hoop load path in the shell, radial deflection under load induces stresses in the 0.008 inch thick external skin. It deflects inward between corrugations, as shown on Figure 5.3-37. Ignoring the effect of the ablator because of its low modulus of elasticity, the following expression was derived for finding the deflection of the skin relative to the corrugation:

$$a = 2.83 \sqrt{\frac{p\Delta_r}{\pi n}}$$

TYPICAL RING LOADS

(RING NO. 4)

TITANIUM, SEMI-MONOCOQUE



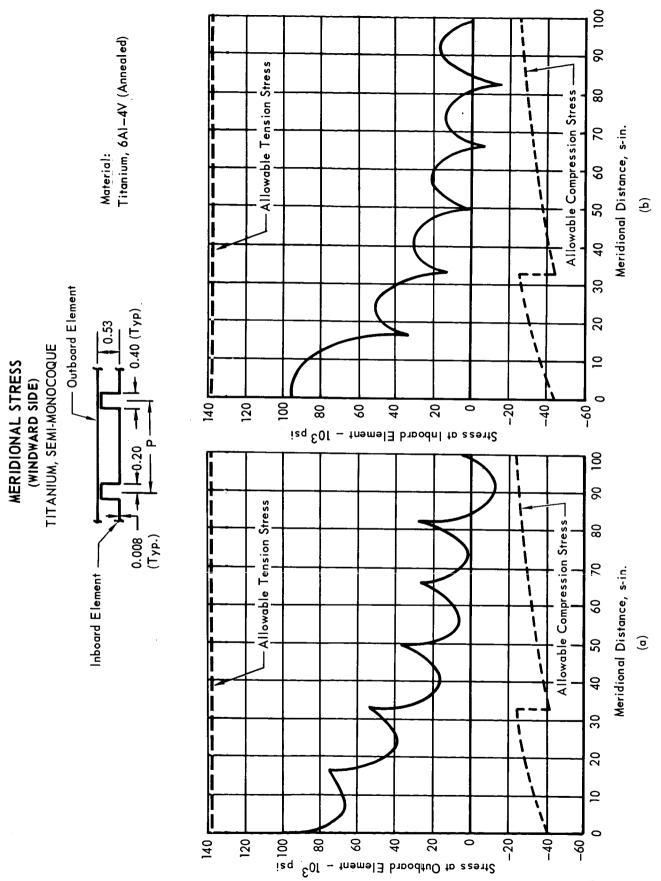
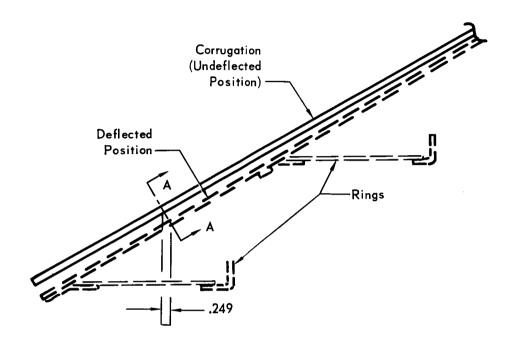


Figure 5.3-36 5.3-63

EXTERNAL SKIN DEFLECTIONS DUE TO LIMIT EXTERNAL PRESSURE

TITANIUM SEMI-MONOCOQUE



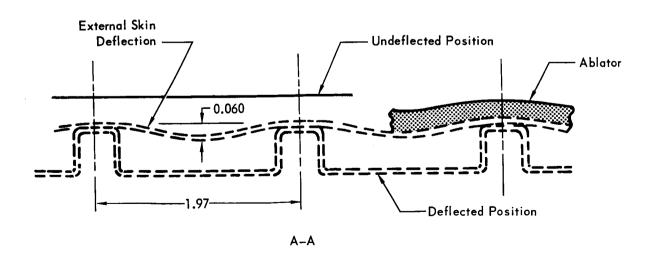


Figure 5.3-37

where: a = deflection amplitude, in.

p = corrugation pitch, in.

 Δ_r = radial deflection, in.

n = number of corrugations

The maximum radial deflection occurs in the shell between the sixth and seventh ring. There are 352 longitudinal corrugations in this area with a pitch of 1.97 inches. For the limit pressure of 2.48 psi on the windward side, the shell radial deflection is 0.249 inch due to ring flexibility and 0.020 inch due to bending of the corrugations between rings. Substituting in the previous expression:

$$a = 2.83 \sqrt{\frac{p\Delta_r}{\pi n}} = 2.83 \sqrt{\frac{1.97 \times .249}{\pi \times .352}}$$

a = 0.060 inch

The bending stress in the skin due to this deflection is 49,300 psi, well below the 131,000 psi yield strength of the material.

A test was conducted by loading a representative ablator-covered Aeroshell panel, to investigate the effect of this deflection. There was no detrimental effect on the shell structure, the ablator, or the ablator bond. The test results are discussed under the Summary of Tests that follows.

Ring Stability - The rings are analyzed using the method discussed in Section 5.3.1.3.1. For stability analysis, loads acting on the windward side are assumed to act uniformly around the circumference. The general stability equation reduces to the following form (Equation 9, Section 5.3.1.3.1) for rings having low out-of-plane rigidity and low torsional rigidity when installed on 60 degree half-angle conical shells:

$$p_{cr} = \frac{0.6 \text{ EI}}{r^3}$$

For ring number 4, shown on Figure 5.3-35

$$EI = 61.5 \times 10^6 \text{ lb-in}^2$$

$$r = 66.0 in$$

Therefore,

$$p_{cr} = \frac{0.6 \times 61.5 \times 10^6}{(66.0)^3} = 128.0 \text{ lb/in}$$

and,

$$p_{act} = 107.0 \text{ lb/in}$$

<u>Dynamic Analysis</u> - A modal vibration analysis was conducted considering the Aeroshell fixed at the cone-sphere tangency. Results indicate that the lowest frequency for this configuration is 22 cps, and is primarily a shell mode. The lowest pure torsion mode is approximately 70 cps. This configuration is similar to the other configurations analyzed except that greater frequencies are encountered in the higher number circumferential waves. This is due to the additional dynamic stiffness present in the higher harmonics.

<u>Summary of Tests</u> - The following structural tests, conducted to aid in the evaluation of the titanium, semi-monocoque configuration, are reported in this section:

- a. Acoustic tests of titanium panels
- b. Static test of titanium panel
- c. Ring stability tests
- d. Compatibility tests of titanium with Freon 12

Additional environmental tests of ablator covered titanium panels used in Tests (a) and (b) are discussed in Section 5.3.2. Testing procedures for all tests are discussed in Section VI B 1.1.

- a. Acoustic Tests of Titanium Panels Response to aerodynamic buffeting flow and susceptibility to panel flutter during Mars entry are dynamic phenomena considered in the evaluation of the structural configurations. The objective of this test was to investigate the effects of the ablator on the dynamic characteristics of the panels and, consequently, on the flutter susceptibility and buffet response. One titanium panel was provided for each of four different ablators. The ablators are fully described in Section 5.3.2. Each panel was tested before and after the ablator was applied to determine the vibration response to acoustic excitation. The results of the test indicate that:
 - (1) The panel is designed by static loads, only, because the ablator essentially eliminates the dynamic loads.
 - (2) There is no significant difference in the energy absorbing characteristics of the four different ablators.

Four panels, representing the titanium semi-monocoque configuration near the base of the Aeroshell, were fabricated. The panels were cylindrical segments, 34 inches long and 36 inches wide, with a radius of curvature of 72 inches. Titanium alloy 6A1-4V, 0.008 inch thick, was used for the

smooth outer sheet and the corrugated inner sheet. The corrugations were parallel to the longitudinal axis of the panel and had a pitch of 2.1 inches. Aluminum ring segments were attached to each end and to the middle of the panel.

These panels were tested at the acoustic response facility at General Electric, Philadelphia. Figure 5.3-38 shows the front and back sides of a panel as installed in the acoustic test facility. Microphones and accelerometers were used to measure the acoustic environment imposed on the panels and the panel vibration response, respectively. All data were recorded on magnetic tape for later data reduction and analysis.

Analysis of test data provided overall and octave band sound pressure levels for the acoustic data; overall root-mean-square acceleration and power spectral densities for the vibration response data; and the acceleration response to acoustic pressure transfer functions.

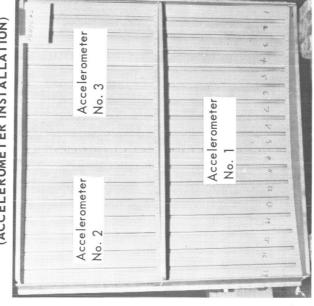
A comparison of the panel response to acoustic excitation is shown in Figure 5.3-39(a) for the panels with and without an ablator. The significantly large reduction (about 85%) in panel response shown is considerably greater than would be predicted by considering only the mass loading effect of the ablator (about 29%). The frequency distribution of the acceleration pressure transfer function for a typical panel with and without an ablator is shown in Figure 5.3-39(b). Examination of these two figures indicates that the ablator, in addition to mass loading the panel, provides additional complex stiffness resulting in a significant reduction of the vibratory response. No significant difference was noted in the energy absorbing characteristics of the four ablators tested.

The entry environment external to the Aeroshell is estimated to be 130 db. At this level of acoustic input, the panel response was very small. With this small response, the design dynamic load factor can be unity; hence, panel design can be based on static considerations. With a small dynamic response of the Aeroshell to the acoustic environment, the entry vibration environment of the Capsule Lander will be correspondingly small.

b. <u>Static Test of Titanium Panel</u> - The titanium semi-monocoque configuration is designed without the need for a hoop load path in the shell. All pressure loads are transferred by bending in the corrugations to the rings. When the shell is loaded, the skin between corrugations deflects



(ACCELEROMETER INSTALLATION) b) PANEL BACK SIDE



(MICROPHONE INSTALLATION)

c) ACOUSTIC TEST SETUP

MICROPHONE NO. 2

MICROPHONE NO. 1 (Internal)

MICROPHONE NO. 3

.36 in. 34 in.

Figure 5.3-38

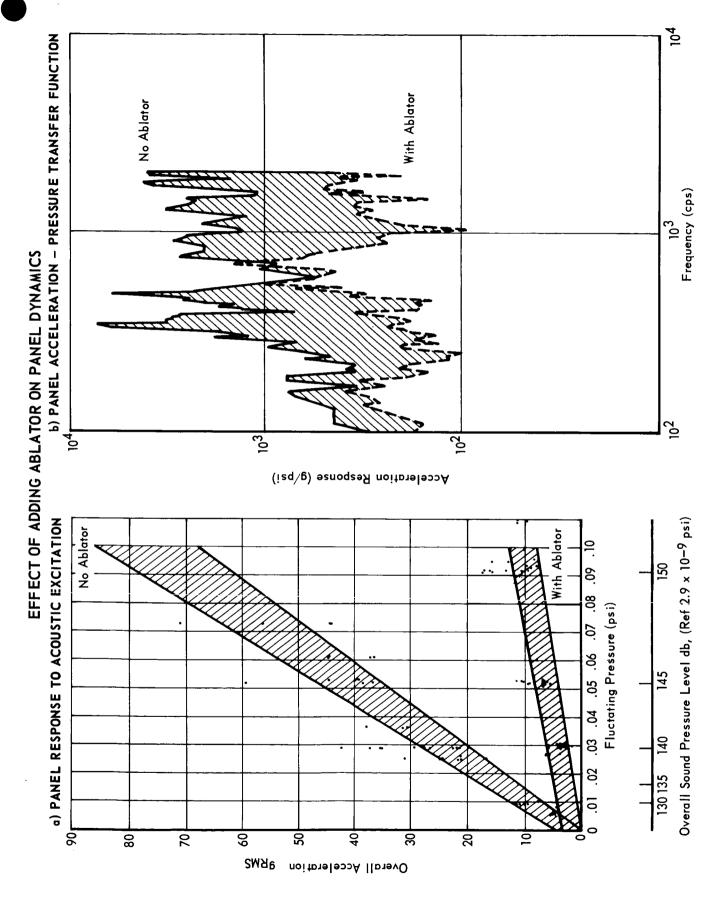


Figure 5.3-39 5.3-69

normal to the mold line as shown on Figure 5.3-37. The majority of this deflection is due to radial deflection of the rings with the balance due to bending of the corrugations between rings as discussed in the <u>Shell Strength</u> portion of this section.

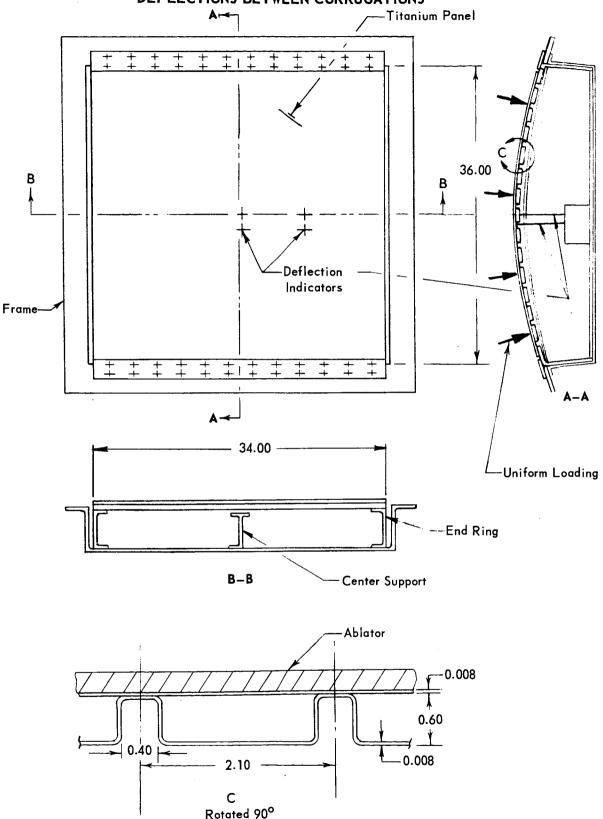
The objective of this test was to demonstrate that the skin deflections between corrugations had no detrimental effect on the ablator or on the ablator bondline. The maximum radial deflection occurs in the bay between the sixth ring and the aft ring of the Aeroshell; therefore, the test panel and fixture were designed to simulate deflections in this area. One of the panels described in the previous test "Acoustic Tests of Titanium Panels" was used. It was loaded to induce deflection between corrugations and no adverse effect was noted.

The ablator covered panel used in this test had been subjected to acoustic noise, decontamination, sterilization, cold soak, and hard vacuum exposure as reported in Section 5.3.2. The ablator was ESM1004AP, which is similar to the preferred ablator, ESM1004X; the primary difference is the density, 34.7 lbs/ft³ for ESM1004AP and 16.6 lb/ft³ for ESM1004X. The panel was modified by removing the center ring and building the panel into a rigid steel frame and test fixture as shown in Figure 5.3-40. The test fixture incorporated a support at the midspan which had a 0.25 inch space between it and the panel prior to applying the pressure. Load was applied by partially evacuating the air within the fixture.

When load was applied to the panel, the corrugations acted as beams between the end rings and deflected until they contacted the center support on the fixture. With the longitudinal sides of the panel restrained by the frame, the skin was forced to deflect between corrugations, thereby simulating the desired conditions. Deflection of the skin relative to the corrugations is expected to be 0.060 inch on the Aeroshell, at limit pressure, as shown on Figure 5.3-37. On this panel test the deflections between corrugations were not all uniform, some being more than 0.060 inch and some less, with the maximum being 0.090 inch.

Even though the panel experienced deflections higher than anticipated in the Aeroshell, the ablator followed the contour of the skin and corrugations and no detrimental effect on the ablator, the bondline, or the titanium corrugations was observed. The lighter density of the preferred ablator is not expected to change these results.

STATIC TEST OF TITANIUM PANEL TO DETERMINE THE EFFECT OF DEFLECTIONS BETWEEN CORRUGATIONS



All dimensions are in inches

Figure 5.3-40

c. Ring Stability Tests - A method of analysis for predicting the instability mode of failure for rings installed in high-angle cones was developed by Cheney in Reference 5.3-5. This method is based on the assumption that the ring is restrained to buckle normal to the shell mold line and is elastically supported by the shell. The objective of this test was to verify this method. Tests were conducted and the results are being evaluated.

Two rings of different configurations, 76 inches in diameter, were tested to failure. The rings were assembled into the test fixture shown in Figure 5.3-41. Meridional strips, representing the shell, were used for the following reasons:

- 1. They simulate the meridional beams in the titanium semi-monocoque shell structure.
- 2. They minimize tangential support to the ring by being free to rotate laterally about the single-point support at the fixture end.
- 3. They allow positive determination of the load in the ring because they provide no hoop strength and have a simple support at the fixture end.

An evenly distributed pressure was applied by partially evacuating the air within the test fixture. Additional discussion of the test procedure is given in Section VI B 1.1.

The two ring configurations are shown in Figure 5.3-41. Configuration (A) was a channel section ring with little torsional and out-of-plane rigidity. Lateral stability of the inboard cap was provided by local clips spaced at 6-inch intervals. Configuration (B) was a triangular-shaped torque box ring with significant torsional and out-of-plane rigidity. A comparison of the results from these two tests will show the effect of torsional and out-of-plane rigidity on the ring buckling strength. The rings were loaded to failure; ring configuration (A) failed at 5.6 psi and configuration (B) at 8.1 psi. Photographs of the test specimen before the test and the ring failures after the test are shown in Figure 5.3-42.

In the development of the general ring buckling equation, Cheney assumed that the ring is rigidly supported in the direction of the shell meridian and has elastic support from the shell in the radial and tangential ring directions and in rotation. The elastic supports are represented by a set of springs as shown in Figure 5.3-43; $k_{_{\rm X}}$ is the radial support, $k_{_{\rm Z}}$ is the tangential support, and $k_{_{\rm R}}$ is the rotational support.

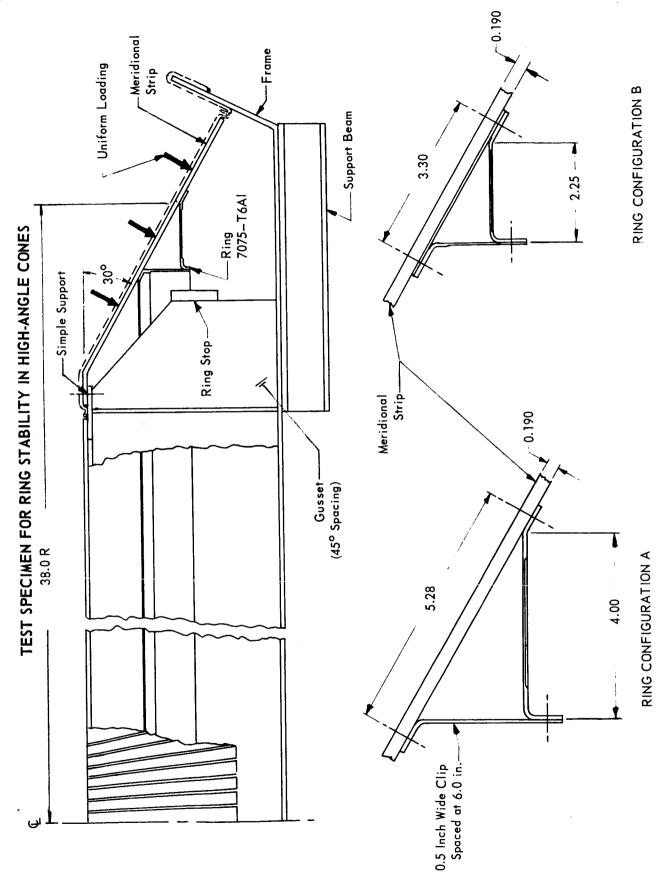
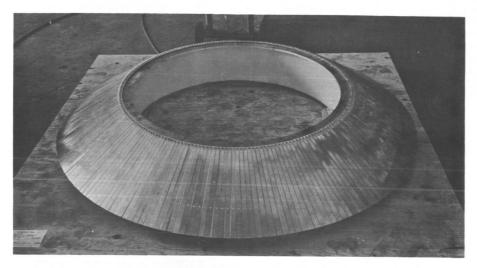
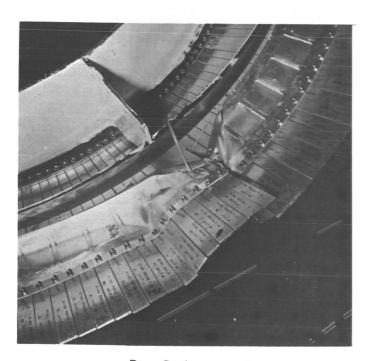


Figure 5.3-41 5.3-73

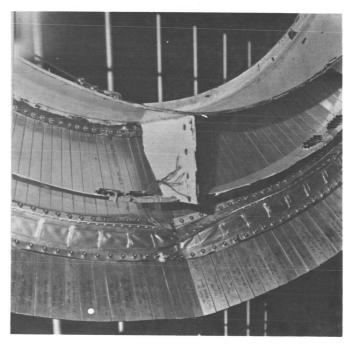
RESULTS OF TESTS FOR RING INSTABILITY IN HIGH-ANGLE CONES



Test Specimen Before Test

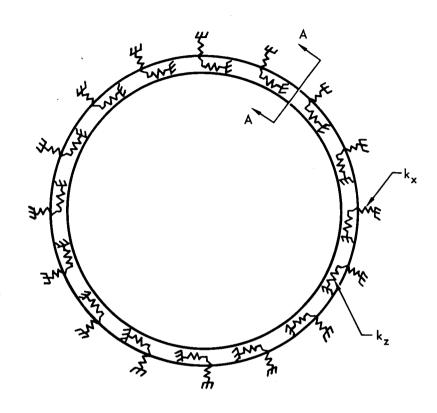


Ring Configuration A



Ring Configuration B

ELASTIC SUPPORT PROVIDED TO RINGS BY SHELL



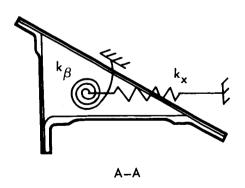


Figure 5.3-43

For our tests, these elastic supports are provided by the meridional strips. By including only the elastic tangential support in the general ring buckling expression, the pressure to cause failure of ring configuration (B) is 8.0 psi.

One significant conclusion is that the contribution to ring stability by the elastic supports is greater than expected for these tests.

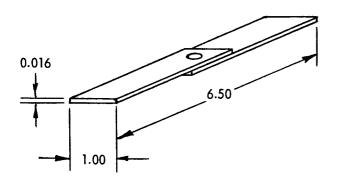
We have conservatively assumed in the <u>General Methods of Analysis</u> of Section 5.3.1.3.1 that the elastic supports provided by the Aeroshell have a negligible effect on ring stability. Upon completing the evaluation of test results and reevaluation of the Aeroshell, we can reduce the conservatism and more precisely define the ring instability mode of failure.

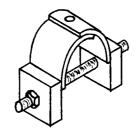
d. <u>Compatibility Tests of Titanium with Freon 12</u> - The possibility of the titanium alloy, 6A1-4V (selected for the structure of the Flight Capsule), being damaged as a result of general or galvanic corrosion is remote in view of its excellent corrosion resistance and noble position in the galvanic series. However, the possibility of damage through stress corrosion must be considered. To date, failure of titanium production hardware as a result of stress corrosion has been limited to tankage which failed during pressure testing, as reported in References 5.3-11, 5.3-12 and others.

Compounds containing chlorine have been known to cause stress corrosion failure of titanium under certain conditions, References 5.3-13, 5.3-14 and others. The Freon 12 component of the gas mixture, used for decontamination (Reference 5.3-15), contains chlorine. The purpose of this test is to investigate the effect of Freon 12 on resistance welded titanium.

The test flow for the 12 specimens used in this test is shown on Figure 5.3-44 (c). The spot welded specimens were fabricated from 6A1-4V. annealed titanium, Figure 5.3-44(a), and nine of them were loaded as shown in Figure 5.3-44(b). The remaining three specimens were tested to failure in lap shear. Three of the loaded specimens were kept at room ambient condition in air to serve as unexposed control specimens. Six of the loaded specimens were exposed to six cycles of 12% ethylene oxide (ETO) - 88% Freon 12 at 122°F, with an ethylene oxide concentration of 600 ± 50 mg/liter of atmosphere and a relative humidity of $50 \pm 5\%$. Each of the six cycles was of 30 hours duration (one hour heat up plus 28 hours stabilized exposure plus one hour cool down). Three of these specimens were exposed to one heat sterilization cycle following the decontamination cycles.

COMPATIBILITY TESTS OF TITANIUM WITH FREON 12





(a) SPOT WELDED SPECIMEN

(b) LOADED SPECIMEN

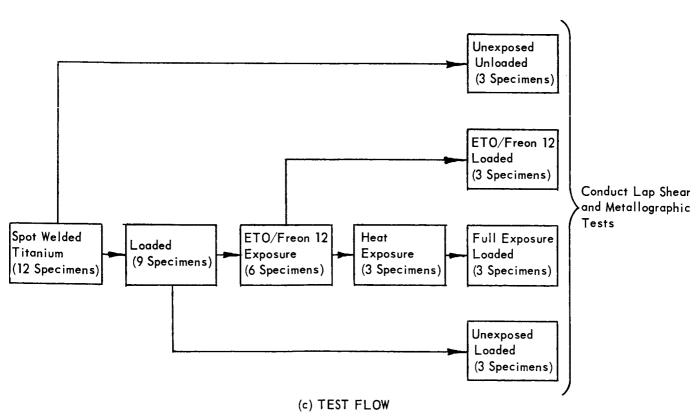


Figure 5.3-44

This consisted of a 92 hour exposure at 275°F in nitrogen. All specimens were tested to failure in lap shear, including the three unexposed control specimens. The specimens were also examined metallographically.

The results of the lap shear tests are as follows:

ULTIMATE LOAD IN POUNDS

Spec	imen Unexpose	d Unexposed	ETO/Freon 12	ETO/Freon 12
Test	(unloade	d) (loaded)	(loaded)	Plus one Heat Cycle (Loaded)
#1	738	651	642	714
#2	686	727	740	775
#3	723	732	711	683
AVERAGE	716	703	698	724

These results are within the expected scatter. No detrimental effects were evident from exposure to the test environment. The results of the above tests were corroborated by R. Corski of Dupont (Reference 5.3-16) who reported the results of a similar test where 6A1-4V titanium was prestressed to 125,000 psi and exposed to the specific Freon 12/ETO mixture for 168 hours without evidence of cracking.

5.3.1.3.5 <u>Conclusions</u> - The preceding analyses established the detail design and verified the weights of the three remaining configurations.

The final evaluation is presented in Figure 5.3-45. Each configuration was rated from one (1) to one hundred (100) for each parameter, the higher numbers reflecting the better conditions. Weighting factors, reflecting the relative value of each parameter to overall system optimization, were applied to the assessed numerical values. These parameters and their associated weighting factors are:

a.	Probability of mission success (confidence)	0.35
Ъ.	System performance (weight)	0.20
c.	Development risk	0.20
d.	Versatility	0.15
e.	Cost (fabrication)	0.10

The establishment of this numerical rating system is described in Section 1.0.

The numerical ratings of the individual parameters were added to obtain the total for each configuration, with 100 being a perfect score. The totals were compared to establish their relative position.

As a result of this evaluation, the titanium single-faced, longitudinal corrugations with aluminum rings is recommended as the preferred structural configuration for the conical section of the Aeroshell.

Structural confidence in the preferred configuration is high because we have considerable experience with this design. Complete material property data for design and analyses are available. Process specifications covering fabrication and quality control are established and in use. One similar application is the structure of the Mercury adapter. This is a single-faced, longitudinally corrugated conical shell of resistance welded titanium. The smooth and corrugated skins are 0.010 and 0.016 inches thick, respectively. Another, more recent, application is the Air Force Gemini adapter. This is also a single-faced, longitudinally corrugated conical shell of resistance welded titanium. Both the smooth and corrugated skins are 0.010 inch thick. The rings of these adapters are aluminum.

FINAL CONFIGURATION SELECTION

STRIICTIIRAI			SELECTION FACTOR		
CONFIGURATION	CONFIDENCE	WEIGHT	DEVELOPMENT	VERSATILITY	FABRICATION
Beryllium Honeycomb Sandwich (2 lb/cu ft aluminum core) TITITITITITITITITITITITITITITITITITITI	Extremely difficult to inspect. Low structural confidence.	0.90 lb per sq ft. Lightest of all configurations studied. 20.0	Considerable development required in joint design and processing.	Poor accessibility for modification. Good volume efficiency.	Added tools and complexity. Exactness of bond components difficult to control.
Titanium Single-Faced Longitudinal Corrugations with Aluminum Rings	Simple and familiar design easy to inspect. High confidence due to similar experience.	1.25 lb per sq ft 14.0	Extensive experience with similar structures. Some development required in assembling large structure.	Relatively accessible for modification. Rings reduce volume efficiency.	Standard fabricating procedures
Magne sium Ring Stiffened Monocoque	Unfamiliar complex design. Easy to inspect.	1.36 lb per sq ft plus addition of required corrosion protection.	Some development work required in forming magnesium rings and in assembling large structure.	Excellent access for modification. Lowest volume efficiency due to numerous rings.	Additional hot forming tools and assembly requirements.
V Preferred Design					

Figure 5.3-45

5.3.1.4 <u>Preferred Concept - Conical Structure</u> - A titanium single-faced, longitudinally corrugated shell with internal aluminum rings was selected as the preferred structural concept as a result of the analyses presented in Sections 5.3.1.2 and 5.3.1.3. Details of this concept are shown in Figure 5.3-1 and in Section A 3.2.1.3.

The conical portion of the Aeroshell consists of a forward and aft section, jointed at the payload ring approximately 21 inches from the cone-sphere tangency. Each section consists of a 0.008 inch thick titanium, 6Al-4V, smooth outer skin stitch welded to a 0.008 inch thick corrugated inner skin. The ablator is bonded to the smooth outer skin. In the forward section, the corrugation height is 0.45 inch and the pitch varies from 1.02 inches at the cone-sphere tangency point to 2.04 inches at the payload ring. In the aft section, the corrugation height is 0.45 inch, and the pitch varies from 1.17 inches at the payload ring to 2.04 inches at the base of the shell. This configuration is designed without the need for a hoop load path in the skin. Circumferential strength and stiffness is provided by the four internal rings and by the spherical segment nose cap structure which incorporates a ring at the cone-sphere tangency point. The four internal rings are triangular torque boxes comprised of three caps and two beaded webs with the shell providing the third web, as shown in Figure 5.3-1.

Aluminum bipod trusses attach to the Lander at eight points and to the Aeroshell at 16 equally spaced points at the payload ring. The meridional component of the bipod loads at the 16 attach points is distributed into the shell by a splice plate adjacent to the payload ring. The radial component is distributed into the shell by the payload ring.

5.3.1.4.1 <u>Structural Loads</u> - The preferred concept is designed for the external pressure and temperature as previously given in Section 5.3.1.1. Net shell loads are shown in Figure 5.3-46. The loads differ from those used for the trade study because the relieving effects of shell inertia are included and the payload is supported further aft, 21 inches from the cone-sphere tangency point. The discrete loads for any trajectory can be determined from the distribution, (see Figure 5.3-46) i.e., the loads for entry are computed by multiplying the distributions by the dynamic pressure of Figure 5.3-2. All other data, including the table of conditions and trajectories, which are presented in Section 5.3.1.1 are valid for the preferred concept.

CAPSULE BUS NET ULTIMATE BENDING MOMENT, SHEAR, & AXIAL LOAD PER UNIT DYNAMIC PRESSURE ENTRY PHASE PREFERRED CONCEPT

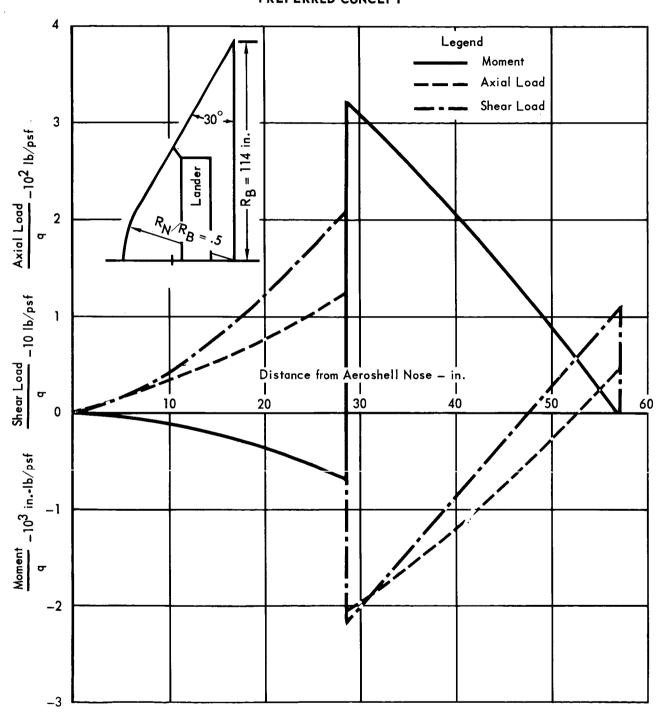


Figure 5.3-46

5.3.1.4.2 Structural Analyses - This section contains a summary of the detail structural analyses of the preferred concept. It is shown to demonstrate that our choice of materials and material gages is adequate for the expected environment. The materials used in the conical section are titanium, 6A1-4V, and aluminum, 7178-T6.

The mechanical properties of titanium alloy are:

139,000 lb/in² Ultimate tensile strength

Yield tensile strength = $131,000 \text{ lb/in}^2$

16,000,000 lb/in² Modulus of elasticity

Poisson's ratio (v) 0.32

The mechanical properties of aluminum alloy are:

 $85,000 \text{ lb/in}^2$ Ultimate tensile strength Yield tensile strength

= 75,000 lb/in² 10,500,000 lb/in² Modulus of elasticity

Poisson's ratio (v)

This section is divided into Internal Loads, Shell Strength, and Ring Stability.

Internal Loads - Exploded free bodies of the forward section, payload ring and aft section are shown in Figure 5.3-47. Loads applied to the bipods from the Lander were determined by assuming that the Lander and Aeroshell structures are rigid, i.e., plane sections remain plane. The forward section of the Aeroshell is subjected to meridional compressive loads and the aft section is subjected to meridonal tension loads.

To obtain the distribution of meridional shell loads at the payload ring, the two mold line ring caps and splice plate are treated as a beam on an elastic foundation, the foundation being provided by the corrugations. Hetenyi, Reference 5.3-17, gives the following expression for foundation reactions to a beam subjected to concentrated loads:

$$T = \frac{P\lambda}{2} e^{-\lambda x} (\cos \lambda x + \sin \lambda x)$$

where: T = foundation reaction (meridional shell load) lb/in

P = concentrated meridional load, 1b

 $\lambda = \sqrt[4]{\text{K/EI}}$, in⁻¹

 $K = foundation modulus, 1b/in^2$

I = moment of inertia of beam, in⁴

E = Young's Modulus, 1b/in²

x = distance from concentrated load, in

INTERNAL LOADS AT PAYLOAD RING PREFERRED AEROSHELL DESIGN

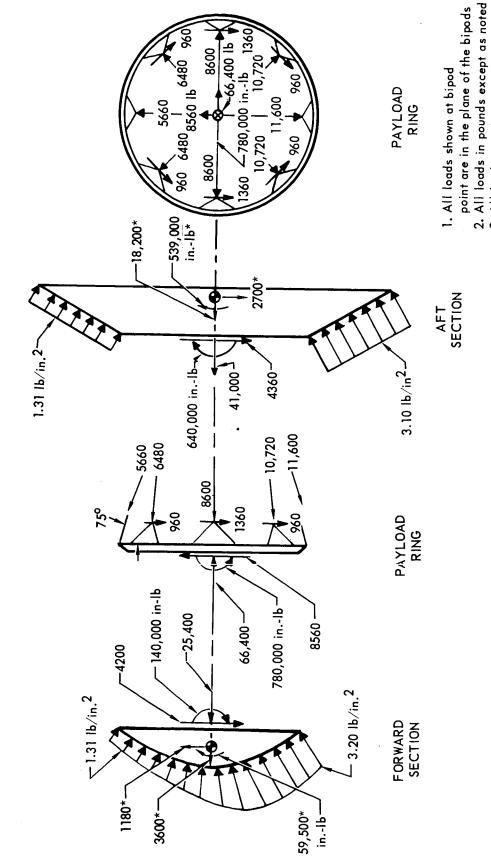


Figure 5.3-47 5.3-84

4. * - Shell Inertia Loads

3. All loads are ultimate

The meridional component of the concentrated bipod loads varies from 11,200 lb on the windward side to 5470 lb on the leeward side. A plot of meridional loads at the payload ring is shown as the solid lines on Figure 5.3-48. Also shown is the distribution if loads from the Lander were uniformly distributed instead of concentrated at the 16 points. This shows that the discrete loads from the bipods have only a minor effect on the internal meridional loads in the shell.

External pressures are carried to the internal rings by the corrugations and effective skin acting as beams. Internal loads in a meridional beam of unit width were obtained by considering the beam as being continuously supported at the rings. Shears, bending moments and axial loads for a meridional beam of unit width on the windward side are shown in Figure 5.3-49. The bending moments were not increased to account for the effect of meridional compression forward of the payload ring or decreased to account for the effect of meridional tension aft of the payload ring.

Four internal rings provide strength and stiffness to the shell in the circumferential direction. All rings have triangular cross sections.

A free body of the payload ring is shown in Figure 5.3-50. All loads in the plane of the ring are shown. They are the radial component of the bipod loads, the loads from external pressure which are carried to this ring by the corrugations, and the shear flow from the shell.

The loads on the remaining three rings are the in-plane components of the collapsing pressures. Figure 5.3-51 shows the unsymmetrical pressures and reacting shears applied to the aft ring. A free body of the ring cross section is also shown to illustrate how the external pressures, which are carried to the ring by the corrugations acting as beams, are redistributed within the ring.

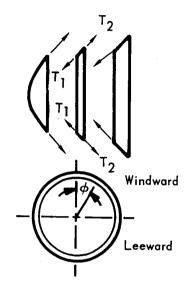
Shell Strength - The corrugations in the forward section of the Aeroshell are subjected to both normal and meridional compression loads. These compression loads magnify the bending moments shown in Figure 5.3-49. Each corrugation is treated as an individual beam column to account for this magnification. The following expression (Reference 5.3-18) is used to predict the maximum moment in a beam column, pinned at one end and restrained at the other.

$$M_{\text{max}} = \text{wlj} \left[\frac{\text{tan } U(\text{tan } U/2 - U/2)}{\text{tan } U - U} \right]$$

where: w = normal load, lb/in

1 = length of beam column, in

DISTRIBUTION OF SHELL LOADS AT PAYLOAD RING PREFERRED AEROSHELL DESIGN



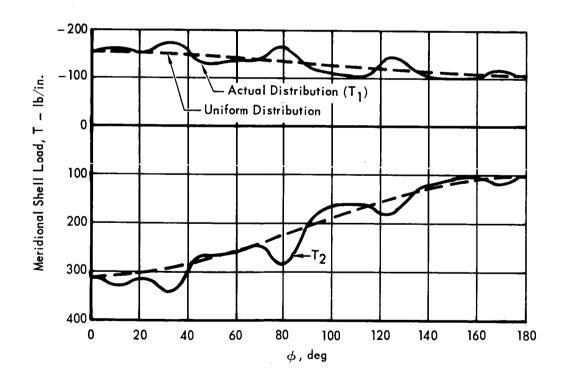


Figure 5.3-48

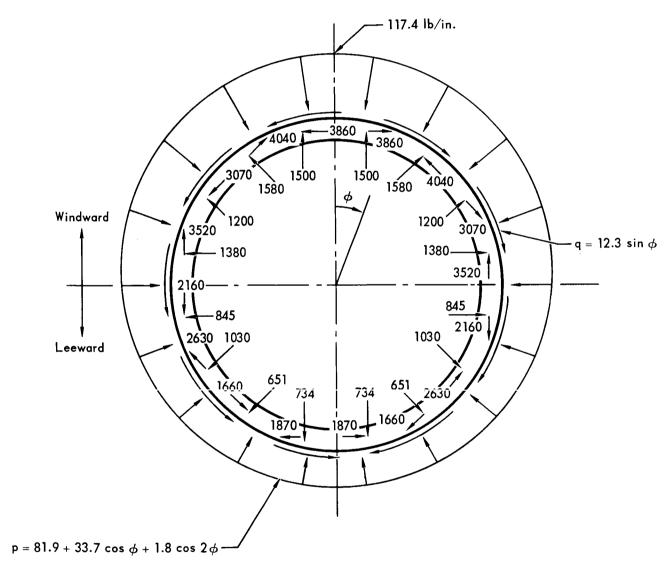
MERIDIONAL LOADS (WINDWARD SIDE) PREFERRED AEROSHELL DESIGN S = 0S = 98.7 3.10 lb/in. (1.0 inch width) Ultimate Bending Moment – in-lb/in. Ultimate Shear – lb/in. -25 (S ~ in.) (S - in.) Ultimate Axial Load — Ib/in. -100

Figure 5.3-49 5.3-87

Meridional Distance (S - in.)

-200

IN-PLANE FORCES ON THE PAYLOAD RING PREFERRED AEROSHELL DESIGN

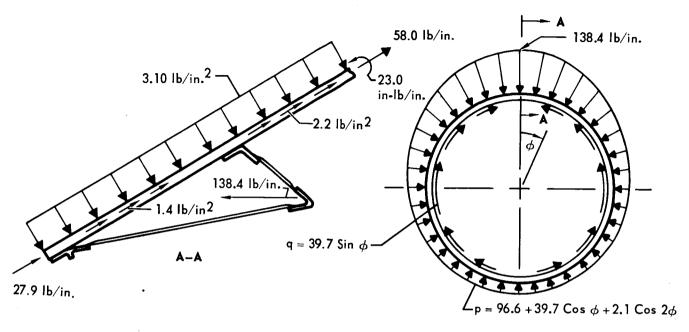


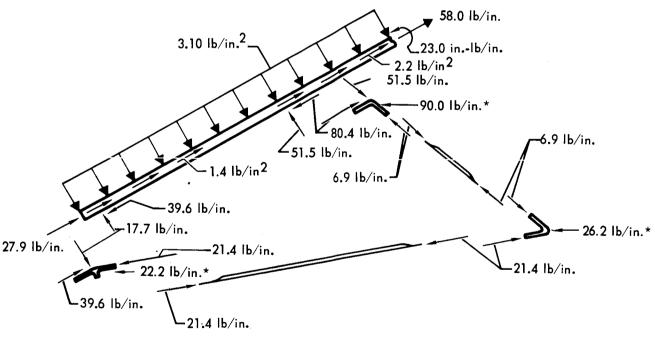
All loads in pounds except as noted

Figure 5.3-50

5.3 - 88

AFT RING LOADS PREFERRED AEROSHELL DESIGN





* Radial Component of Hoop Load in Caps

Figure 5.3-51

 $j = \sqrt{EI/P}$, in

E = Young's Modulus, 1b/in²

I = moment of inertia of beam, in 4

P = axial load, 1b

 $U = \frac{1}{i}$, in/in

The critical corrugation is in the first bay forward of the payload ring on the windward side and has the following loads and geometrical properties:

P = 160 lb/in (ultimate) Reference: Figure 5.3-49

 $w = 3.1 lb/in^2 (ultimate)$

 $E = 16 \times 10^6 \text{ lb/in}^2$

 $I = .00085 \text{ in}^4/\text{in}$

j = 9.20 in

U = 1.14 in/in (for 1 = 10.5 in, Figure 5.3-1)

Substitution into the previous equation gives a maximum moment of 45 in-lb/in occurring at the support provided by the first ring forward of the payload ring. This moment, producing compression in the inboard element, when combined with the axial load of 160 lb/in, results in a compressive stress in the corrugation of 29,000 psi. The allowable compression stress is 30,700 psi.

The meridional distribution of stresses in the shell are shown on Figure 5.3-52 for the 3.1 psi ultimate pressure occurring on the windward side. Magnification for beam column effects was included forward of the splice plate where the axial load is compressive and was not included aft of the splice plate where the axial load is tensile. Also shown on this figure are the allowable stresses. The allowable compression stress is limited by local buckling and the allowable tension stress by the ultimate strength of the material.

The preferred concept is designed without the need for a hoop load path in the shell. However, as a result of the shell radial deflection under load, stresses are induced in the 0.008-inch thick external skin when it deflects inward between corrugations, as shown on Figure 5.3-53. The deflection shown (0.064 in.) was determined by the method previously discussed in Section 5.3.1.3.4 for the titanium semi-monocoque configuration.

The bending stress in the skin due to this deflection is 52,500 psi, well below the 131,000 psi yield strength of the material.

MERIDIONAL STRESS (WINDWARD SIDE) PREFERRED AEROSHELL DESIGN

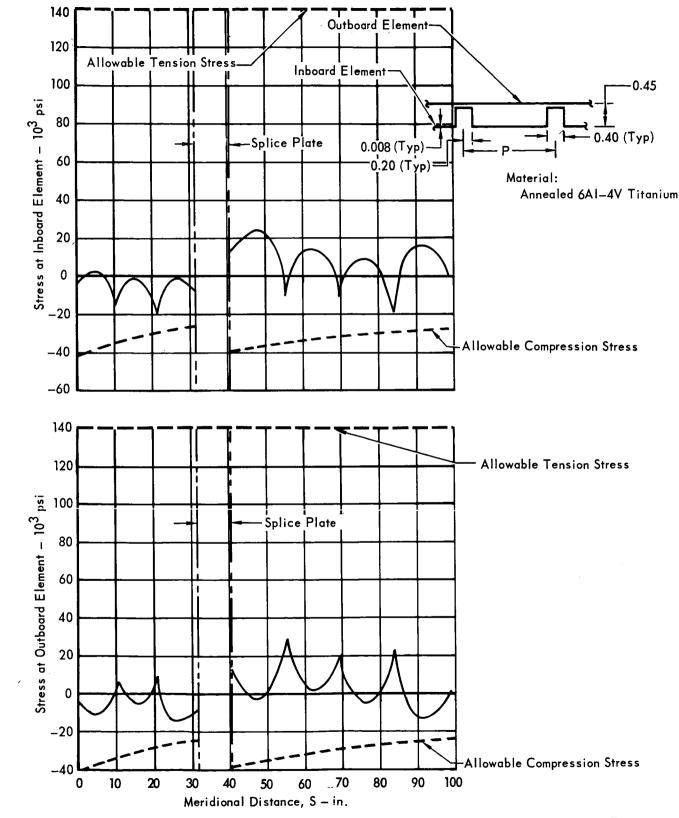
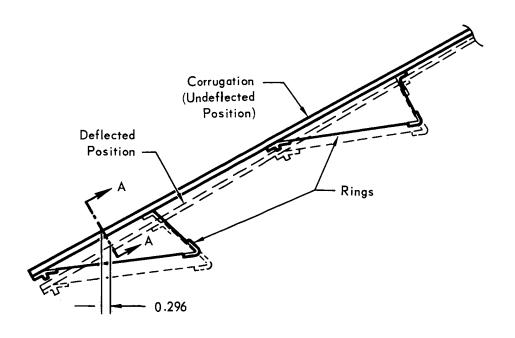


Figure 5.3-52

EXTERNAL SKIN DEFLECTIONS DUE TO LIMIT EXTERNAL PRESSURE PREFERRED AEROSHELL DESIGN



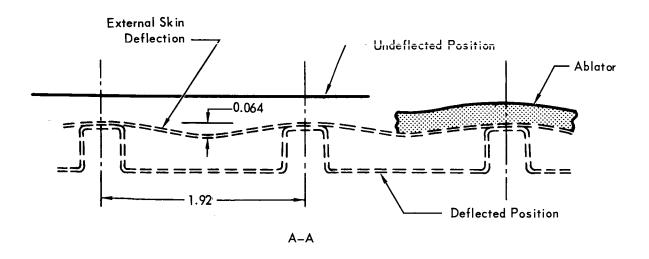


Figure 5.3-53

A test was conducted by loading a representative ablator covered Aeroshell panel, to investigate the effect of this deflection. There was no detrimental effect on the shell structure, the ablator, or the ablator bond. The test results are discussed in Section 5.3.1.3.4.

Ring Stability - Stability is insured by using the method presented in Section 5.3.1.3.1, General Methods of Analysis. For stability analysis, loads acting on the windward side are assumed to act uniformly around the circumference. The forward three rings are not critical for instability because of their inherent stiffness when designed for strength to carry hoop compression. The aft ring is critical for instability and has the following properties:

EI_x = 3.96 x
$$10^7$$
 $1b-in^2$
EI_y = 2.54 x 10^8 $1b-in^2$
JG = 1.65 x 10^6 $1b-in^2$
EΓ = 1.0 x 10^3 $1b-in^4$
α = 60 deg
r = 102.7 in

As given in Section 5.2.1.3.1, the stability equation for rings possessing in-plane, out-of-plane and torsional rigidity is: $p_{cr} = \frac{9}{r^3(4 sec^2 \alpha - 1)} \left[EI_y + \frac{EI_x \tan^2 \alpha (JG + 4 E\Gamma/r^2)}{(JG + 4 E\Gamma/r^2) + \frac{EI_x}{4}} \right]$

$$P_{cr} = \frac{9}{(102.7)^{3}[4(4)^{-1}]} \left[2.54 \times 10^{8} + \frac{3.96 \times 10^{7} (1.732)^{2} \left(1.65 \times 10^{6} + \frac{4 \times 1.0 \times 10^{3}}{(102.7)^{2}}\right) + \frac{3.96 \times 10^{7}}{\left(1.65 \times 10^{6} + \frac{4 \times 1.0 \times 10^{3}}{(102.7)^{2}}\right) + \frac{3.96 \times 10^{7}}{4}} \right]$$

$$P_{cr} = 150 \text{ lb/in}$$

 $P_{act} = 138.4 \text{ lb/in (Figure 5.3-51)}$

5.3.1.4.3 <u>Dynamic Analysis</u> - The vibration characteristics of the Aeroshell (i.e. vibration mode shapes and natural frequencies) are used in the analyses to determine the response of the Flight Capsule to launch and entry environments. Therefore, during Phase B, a major emphasis was placed on dynamic modeling and determination of the vibration characteristics of the Aeroshell. Preliminary estimates of the launch and entry environments indicate that the dynamic characteristics of the Aeroshell are satisfactory and no significant problems are anticipated in Aeroshell response or from coupling of these dynamic

characteristics with the Lander and Launch Vehicle.

A modal vibration analysis was conducted with two different sets of boundary conditions simulating the Aeroshell-Lander tie points. As a result of this study, it was found that the Aeroshell structural frequencies varied signficantly, depending upon location of the structural tie points between the Aeroshell and Lander.

The two sets of boundary conditions imposed on the structure were as follows:

(1) Aeroshell fixed at cone-sphere tangency point; (2) Aeroshell pinned at ring number two, the Lander tie point.

A number of harmonics (number of circumferential waves in mode shape) was considered to determine the overall system lowest frequencies. Figure 5.3-54(a) shows frequency versus number of waves in circumferential mode shape for the Aeroshell fixed at the cone-sphere tangency point. Figure 5.3-54(b) shows a typical mode shape for harmonic number 2.

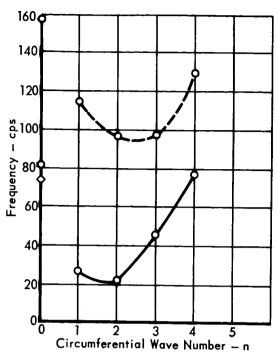
As one might expect, the frequencies are much higher for the Aeroshell-Lander tie at ring 2 than they are for the tie at the cone-sphere tangency of the Aeroshell. A preliminary analysis indicates that the lowest system frequency is 85 cps for the Aeroshell-Lander mated at ring 2.

The ring construction in the preferred concept is somewhat different from that in most shell structures. Because the rings are torque boxes, they are capable of resisting twisting loads, as well as bending and hoop loads. A set of normal modes has been calculated that defines the system's lowest frequencies and eigenvectors (mode shapes). This is not necessarily a set of classical shell modes. Therefore, in any analyses which consider the coupling of Aeroshell modes with other Flight Capsule systems, care must be exercised to assure that all boundary conditions and interface constraints are properly modeled.

5.3.1.5 <u>Preferred Concept - Nose Cap Structure</u> - The spherical nose cap of the Aeroshell is used as a radome for the radar altimeter antenna and, therefore, must be RF transparent. This necessitates the use of a non-metallic structure.

The preferred nose cap structure is a reinforced plastic sandwich consisting of heat resistant phenolic (HRP) honeycomb core and phenolic fiberglass face sheets. It is assembled with a modified epoxy film adhesive (HT-435). The nominal sandwich section has a core which is 0.26 inch thick and face sheets that are each 0.020 inch thick. It is designed to be laid up, cured, and bonded directly to the inside surface of the pre-fabricated heat shield, in one assembly operation. The nose cap geometry is shown in Section A.3.2.1.

RING-STIFFENED, LONGITUDINALLY CORRUGATED AEROSHELL NORMAL MODE SHAPES AND FREQUENCIES



Mass Loading Effect of Ablator is Included in Analysis

O - Predominantly Shell Motion

M is Longitudinal
Wave Number

 \diamondsuit — Predominantly Torsion Motion

a) FREQUENCY vs CIRCUMFERENTIAL WAVE NUMBER

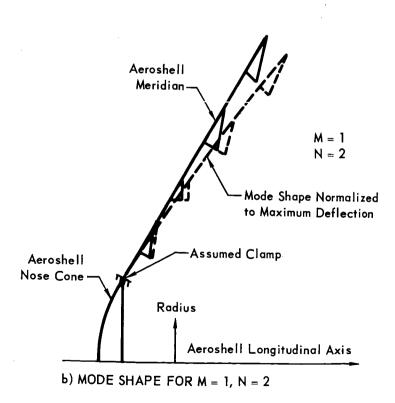


Figure 5.3-54

5.3.1.5.1 <u>Materials</u> - To minimize development time and cost, a major consideration was material and processing state-of-the-art. For the materials selected, most of the engineering properties for design and analyses and all processing procedures and techniques are currently available. Alternate materials are considered in Section 5.3.2; however, these alternate materials require more testing and evaluation, as they are not proven to the same degree as the selected materials.

The selected materials are:

MATERIAL COMPONENT

Phenolic-Fiberglass laminate Face Sheets

Phenolic-Fiberglass Core Material for Sandwich Structure

Honeycomb (2 1b/cu. ft. density)

HT-435 supported film adhesive - Adhesive for bonding the honeycomb

a modified epoxy core to the face sheets and for bonding the sandwich structure to

the heat shield

The mechanical properties of the phenolic-fiberglass laminate used in the face sheets are:

Compressive strength = $31,000 \text{ lb/in}^2$

Modulus of elasticity = $3,000,000 \text{ lb/in}^2$

Poisson's ratio (ν) = 0.125

5.3.1.5.2 <u>Structural Loads</u> - The loads for the nose cap are given in Section 5.3.1.1. The critical load condition is the maximum pressure at the stagnation point of 3.20 psi ultimate, as shown on Figure 5.3-4. At the time that this load occurs, there is no significant temperature rise in the structure due to aerodynamic heating.

5.3.1.5.3 Structural Configuration - Because of the nose cap's large radius of curvature, it was found to be instability critical. Due to its inherent flexural rigidity, a sandwich shell was found to be lighter than a monocoque shell for this application. The phenolic resin impregnated fiberglass cloth to be used in this configuration has sufficient mechanical properties at elevated temperatures (short times), a thermal expansion coefficient compatible with the heat shield material, and is economical to fabricate into the shape required. The layup of the phenolic fiberglass sandwich requires simple tooling with a minimum of development time. More data and experience with adhesive bonding, particularly for a bond line design temperature of 735°F, is available for the phenolic fiberglass sandwich, than for any of the alternate materials considered in Section 5.3.2.

Data available on the phenolic fiberglass material indicate no appreciable weight or strength loss under conditions of time, temperature and pressure similar to those expected for the mission of the VOYAGER Flight Capsule. Ethylene oxide, thermal sterilization and long term space environment compatibility tests are currently in progress on this material (see Section VI B 1.0).

McDonnell has extensive experience with the design, structural and thermal analysis, fabrication, and quality control of high strength, temperature resistant phenolic fiberglass structures. One similar application is the structure of the Gemini heat shield which is a double-faced honeycomb sandwich with the honeycomb and skins being phenolic fiberglass. Process specifications, covering fabrication and quality control, are established and are being used.

5.3.1.5.4 <u>Stability</u> - To check for instability, the classical buckling equation for homogeneous spherical shells, as given by Timoshenko (Reference 5.3-19), is used:

$$P_{cr} = \frac{2Et^2}{r^2 [3(1-v^2)]^{1/2}}$$

where: E = Young's Modulus, 1b/in²

t = shell thickness, in.

r = radius of curvature, in.

 ν = Poisson's ratio

For this analysis, the maximum pressure at the stagnation point was assumed to act uniformly over the nose cap. Experimental investigations have shown that buckling occurs at pressures much lower than predicted by theory. For spherical segment shells, the reduction in theoretical buckling pressure is a function of the geometrical parameter, λ :

$$\lambda = 2 [3(1-v^2)]^{1/4} (\frac{H}{t})^{1/2}$$

where: H = depth of spherical segment, in.

t = thickness of homogeneous shell, in.

ν = Poisson's ratio

The experimental results summarized by Homewood, Brine and Johnson (Reference 5.3-20) are shown in Figure 5.3-55. A conservative lower boundary of the test points has been used for design purposes.

GENERAL STABILITY OF SPHERICAL SEGMENT SHELLS

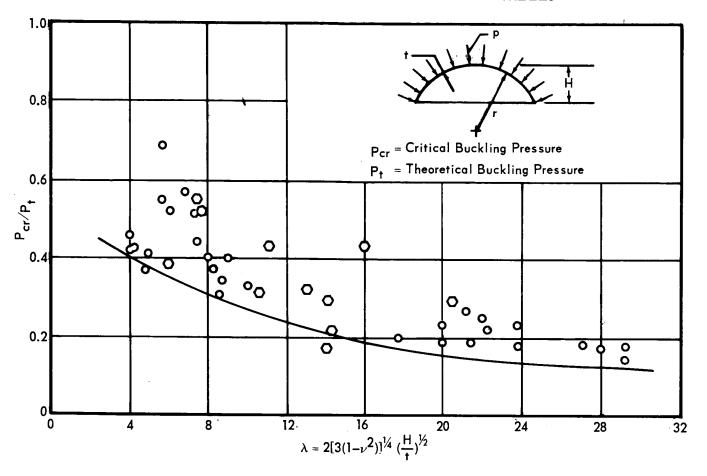


Figure 5.3-55

Sandwich shells are idealized as equivalent homogeneous shells as described in Section 5.3.1.3.2. The effective homogeneous shell thickness t_e , and effective modulus, E_e , are shown as follows:

$$t_e = \sqrt{3}$$
 h = $\sqrt{3}$ x.28 = .485 in.
 $E_e = \frac{2}{\sqrt{3}} \frac{E_f t_f}{h} = \frac{2x3.0x10^6x.020}{\sqrt{3}$ x.28 = 2.47 x 10⁵ lb/in.

For the selected design, the cap height is 7.6 inches which results in a geometric parameter, λ , of 10.1. From Figure 5.3-55,the ratio of actual buckling pressure to theoretical, $P_{\rm cr}/P_{\rm t}$, is 0.26.

Therefore:
$$P_{cr} = .26x \frac{2 \text{ Eete}^2}{r^2 [3(1-v^2)]^{1/2}} = .26x \frac{2x2.47x10^5 (.485)^2}{(57)^2 \{3[1-(.125)^2]\}^{1/2}} = 5.40$$

The maximum ultimate pressure at the stagnation point is 3.20 psi, therefore the nose cap is stable.

5.3.2 Heat Shield - The primary function of the VOYAGER Flight Capsule heat protection subsystem is to protect the Aeroshell structural SL and ESP from the aerodynamic heating encountered during entry into the Martian atmosphere. Studies were directed toward selection of a single heat shield material for the entire capsule. This approach resulted in the selection of a low density, charring ablator, the lightest concept offering the greatest flexibility in the range of possible environments and in future missions where subsystem growth is a consideration. However, evaluation of the ESP requirements showed a non-ablative nose cap is necessary. Therefore, the Aeroshell heat shield design consists of a non-ablative, hardened Fiberfrax, spherical nose cap, and a low density silicone elastromeric ablator (GE ESM 1004X) as the heat shield over the conical skirt of the Aeroshell structure. The Aeroshell base area is protected with a fiberglass cloth thermal curtain that covers the equipment and internal structure completing the thermal protection over the entire Capsule Bus. In this section, the thermal environments on the heat protection subsystems are analyzed, the various approaches and materials considered are presented, and the rationale for selection of the preferred design is developed. 5.3.2.1 Summary - The design of the heat protection system for VOYAGER Flight Capsule, compatible with the Aeroshell described in 5.3.1, is primarily based on the anticipated wide range of entry conditions; however, the design must consider all environmental conditions experienced prior to entry. These environments include ground handling; chemical decontaimination with ethylene oxide (ETO); dry heat sterilization; subsystem test and qualification; loads and vibrations during powered flight, and insertion into the interplanetary trajectory; cold soak and hard vacuum for 6 to 9 months during transit; loads and vibrations during midcourse maneuvers. insertion into the Mars orbit, and de-orbit periods; solar exposure during the descent period to provide temperature control; and exposure to the meteoroid environment during the descent phase (the Sterilization Canister shields the heat shield from this environment until just prior to de-orbit). These many environments have been described in Part A of this report. The entry heating environment is discussed in Section 5.3.2.2. This heating environment is quite mild when compared to Earth re-entry; peak convective heat fluxes for the selected configuration range from approximately 7 to 25 Btu/ft²-sec compared to 120 Btu/ft²-sec for Gemini and over 1000 Btu/ft²-sec for Apollo. However, the expected heating rate possesses substantial variations due to the wide range of possible entry conditions (entry path angles from vacuum graze to -20° down from the local horizon; entry velocities from 13,000 to 15,000 ft/sec) and the degree of atmospheric uncertainty (ten Martian

atmospheric models have been defined). In evaluating the heat protection subsystem, the entire entry environmental range was assessed and utilized in selecting the preferred approach, for selecting test criteria, in making final trade offs of candidate materials, and for sizing the selected system.

After evaluation of the entry environment, a trade-study was performed on various approaches to the heat protection system including heat sinks, radiative structures, high density charring ablators, low temperature sublimers, low density ceramics, and low density charring ablators. Based on the range of environmental considerations, thermal efficiency, subsystem flight experience, fabricability, cost, and development risk, the low density class of charring ablators was selected for the preferred approach on the conical portion of the Aeroshell. Within this class of materials, the formulations considered were; GE ESM 1004X, ESM 1030-1, ESM 1030-1(S), ESM 1030-2(S), MDC S-20T, N-603, the Apollo ablator, Microballoon Phenolic Nylon (MPN), Insulcork 2755, and balsawood. These permitted the trade study to consider supported and unsupported silicone elastromerics, syntatic and chemical foams, rigid formulations, natural materials, and rigid versus elastic bond systems.

To provide the basic data required to select the ablative heat protection, a materials program was initiated which contained literature surveys plus selected testing on the primary candidate materials. Thus, a common data base existed on each material prior to the evaluation process. This testing program considered thermal/mechanical/physical property measurements, material scale-up and fabrication, quality assurance, electrical characteristics, thermo-structural compatibility, and bond characteristics. The testing was complemented by past General Electric and McDonnell Douglas experience with systems containing materials similar to those under consideration.

The established VOYAGER selection criteria were used as a basis for weighing all relevent performance factors considered in the ablative material selection. Under each criteria, several factors were identified such that a full range of 63 variables were considered. Thus, in the final ablative material trade-offs, wherein 13 materials were evaluated, a total of 819 points of logic were considered to make the selection as comprehensive as possible.

GE ESM 1004X, a fiber reinforced silicone elastomer soft bonded with RTV-560 to the structure, was selected as the preferred concept. The MDC S-20T, a silicone elastomer chemically foamed in a continuous phenolic fiberglass honeycomb, prebonded to the structure with HT-424, was selected as the "back-up" concept. Although both of these ablators are silicone elastromerics and almost equivalent in thermal

performance, they are considerably different when one considers formulation, fabrication techniques, and bond process. Therefore, any development problems encountered with one approach are not likely to occur in both material systems. The selection of these two different types of heat shield fabrication and attachment methods guarantees having an efficient and reliable heat protection subsystem available on schedule. In addition, the studies showed that several other materials offer potential weight savings and excellent reliability with modest amounts of development.

A non-ablative heat shield and non-metallic support structure is utilized for the spherical nose cap region. The use of a different material was necessitated by the addition of two requirements imposed on the conical Aeroshell section:

(1) RF transparency of the composite shield-structure to the radar altimeter signal, and (2) essentially no outgassing products from the heat shield material, thus avoiding interference with the atmospheric sampling and TV viewing experiments. This latter requirement precluded the use of ablative materials for the nose cap heat shield. Window contamination from ablative product deposition was shown to occur in the Gemini flights, and also in the simulated entry heating plasma tests of the candidate ablative heat shield materials.

A study was initially undertaken to investigate the problems associated with conforming the ablative nose cap to the Entry Science Package requirements. To avoid contamination of the atmospheric composition, the probe sampler would have been extended beyond the boundary layer. To maintain a clear optical TV window, multiple layer windows would have been utilized and discarded at certain intervals during entry. Since this approach (1) required a more complicated design, (2) presented a potential danger to the heat shield from the rearward flow of window fragments, and (3) had a high probable risk of experiment failure (success of experiment measurements are of major importance on the 1973 mission), the ablative nose cap was discarded in favor of a non-ablative (passive) design.

The study of the passive heat protection approach for the nose cap included investigation of an aluminum phosphate — quartz fabric reinforced honeycomb sandwich used both as a thermal shield and support structure; a composite consisting of a dense alumina external skin with a low density alumina foam bonded to a fiber-glass laminated internal skin; and a low density, hardened Fiberfrax insulation system supported with a phenolic fiberglass honeycomb sandwich. In this manner both the integral heat shield/structure and supported heat shield approaches were considered for the nose cap region.

The nose cap heat shield assembly discussed herein includes the heat shield support structure, beryllium tip, antenna cavity foam and the TV camera window. The preferred nose cap heat shield material consists of a passive inorganic insulation processed from aluminosilicate fibers and an inorganic binder. This composite is adhesively bonded to a phenolic fiberglass honeycomb support structure. The hardened Fiberfrax insulation was selected as the preferred material on the basis of thermal structural performance (least heat shield weight), easier fabrication of the state-of-the-art materials, and greater versatility of tailoring the materials to meet specific requirements. Tests conducted in Phase B indicated that the preferred material can withstand the worst entry heat loads, has an easily predictable thermal response, is not affected by cold soak or vacuum, and has negligible outgassing and can be designed to satisfy the radar altimeter RF transmission requirements.

Immediately adjacent to the nose cap, a fused silica optical window is located to serve as a thermal cover for the TV camera. This window is fabricated from Corning 7940 fused silica, a material having the desired optical properties over the expected entry temperature range, and sufficient strength to accommodate the entry loads.

The large base area of the Aeroshell requires some protection during de-orbit rocket firing and entry to protect the structure and equipment from plume and wake heating, respectively. Thermal protection is provided with a fiberglass cloth attached over the inner Aeroshell surface and around the base of the Lander, and draped over the Lander. The curtain is sectioned to avoid interferring with Lander separation, and to permit removal of the Lander cover during parachute deployment.

- 5.3.2.2 <u>Design Environment and Constraints</u> The heat protection subsystem must be compatible with the VOYAGER Program and Mission requirements. In this section the ground, transit, and entry environments, the thermo-structural requirements, and nose cap constraints affecting the heat protection subsystem are described. The entry heating environment provides the major constraint on the heat shield design.
- 5.3.2.2.1 Ground Environment The VOYAGER heat shield must be compatible with those environments it will encounter after final fabrication and prior to flight. These include the normal environments (ground handling, system test, temperature, humidity, and fungus), and the bio-load reduction environments (dry heat sterilization and chemical decontamination). The normal environment levels summarize in Section A.2 are based on the recommended design level of severity for the uncontrolled OSE environments. Bio-load reduction environments are described in Section A.1.3.
- 5.3.2.2.2 <u>Transit Environment</u> The transit environment includes those conditions that the heat protection subsystem must be designed to withstand from lift-off through the beginning of entry into the Martian atmosphere (800,000 feet above the planet surface). These conditions include: ascent longitudinal and lateral loads, trajectory adjustment loads; space pressures, temperatures, radiation, and meteoroids, and de-orbit loads, temperatures, radiation, and meteoroids. These environments are defined in detail in Section A.2.2 and 2.3. Throughout transit the heat shield is protected from the meteoroid environment by the canister. (See Section 5.1) After separation, however, the shield is exposed during the entire de-orbit period. A preliminary estimate of the probability of no penetration, P(o), for the silicone elastomeric heat shield materials was based on a 325 ft surface area, a 6 hour de-orbit period, and the flux level for less than one Mars radius. This showed that for the short de-orbit period the probability of damage to the heat shield from meteoroids is quite small, 1-P(o)<10⁻⁸, but this potential damage must be re-evaluated prior to completion of a final design.
- 5.3.2.2.3 Entry Heating Environment During hypersonic flight in the Martian atmosphere the kinetic energy of the vehicle is dissipated by friction in heating the gas envelope surrounding the vehicle. Heat transfer analysis for Martian entry is complicated by the presence of gas compositions (mixtures of carbon dioxide, nitrogen, and argon) different than air, the media in which all past flight and the majority of ground test correlations have been accomplished. Therefore, the analytical techniques originally derived for Earth entry must be adjusted in

accordance with proper test data representative of the Martian atmosphere.

The low speed Martian entry velocities (13,000 to 15,000 ft/sec), coupled with shallow flight path angles (vacuum graze to -20°) and a low density atmosphere yield a relatively mild heating environment. However, because of the presence of CO_2 and N_2 , which leads to formation of the CN molecule, a substantial amount of non-equilibrium radiative heating may occur and must be added to the convective heating to define the total heating environment. Equilibrium radiation heating has been found to be negligible. In the ensuing paragraphs the analytical methods of predicting the convective and radiative heating for VOYAGER are described and applied to representative trajectories bounding the entry envelope and atmospheric models.

Atmospheric Models - Several authors have shown that the stagnation point heating rate and total heat for ballistic entry can be approximated by the following semi-emperical relationship:

$$\dot{q}_{\text{max}} = K \quad v_{\text{e}}^{3} \left(\frac{\beta \sin \gamma e}{H} \right)^{1/2}$$
and, $Q\sqrt{R} = K_{2} \quad v_{\text{e}}^{2} \left(\frac{\beta H}{\sin \gamma e} \right)^{1/2}$

where: \dot{q}_{max} = maximum heating rate

Q = total heat load

 V_{e} = entry velocity at 800,000 feet

 γ_e = entry path angle at 800,000 feet

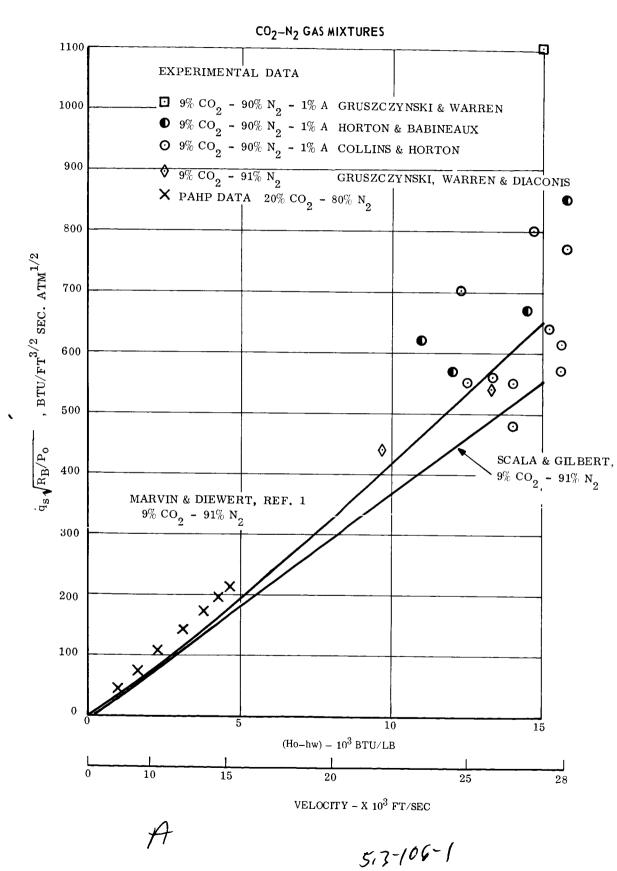
 β = ballistic parameter (M/C_DA)

H = scale height

 K_1 , K_2 = constants which differ in value for each gas composition

These equations show that the low scale height atmospheres (e.g. VM-8) will have the highest heating rates, whereas the high scale height atmospheres (e.g., VM-3) will present the largest total heat load and longest entry times. Comparisons of the constant K_1 were made for the various atmospheric compositions using as a reference the predictions of Marvin and Deiwert (Reference 5.3.2.21) for stagnation point heating as presented in Figures 5.3-56. It was found that the difference in the constant K_1 , for the VM-4 and VM-8 atmospheres (the lower values of scale height), is only 10% and that the predominant factor in ascertaining the most severe heating environments is the scale height. From these comparisons the VM-3 and VM-8 Martian atmospheres were determined to be the most severe entry environments for the heat shield design.

COMPARISON OF STAGNATION POINT HEAT TRANSFER THEORIES WITH EXPERIMENTAL DATA



REPORT F694 • VOLUME II • PART B • 31 AUGUST 1967

MCDONNELL ASTRONAUTICS

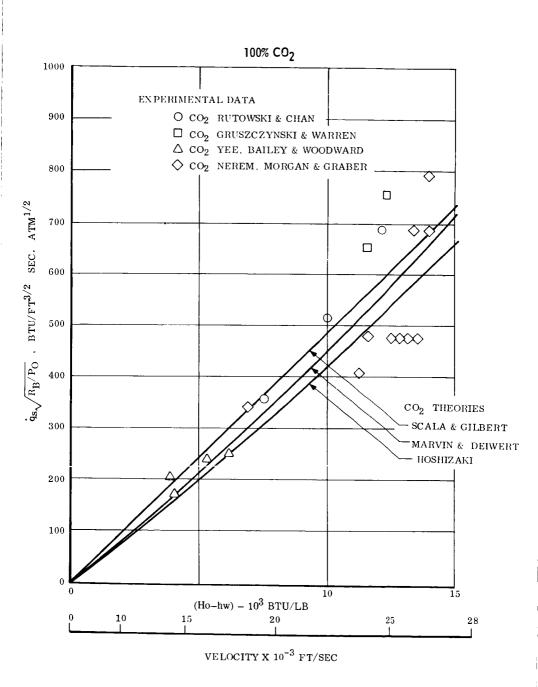
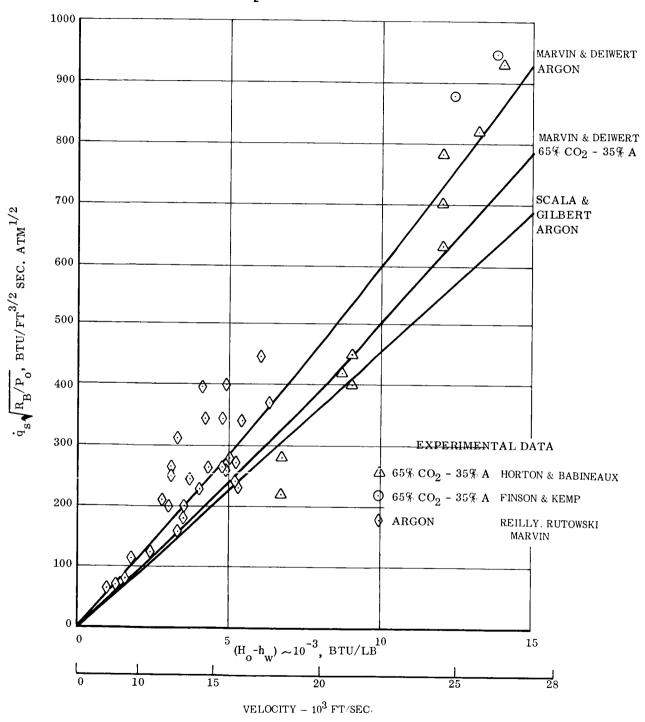


Figure 5.3-56

517-106-2





B

Entry Envelope - The Capsule Bus is designed to survive an orbital entry from any point in the entry angle and velocity envelope shown in Figure 5.3-57 for the spectrum of atmospheric models under consideration. Based on this envelope the heating environment was parametrically evaluated for the critical VM-8 and VM-3 atmospheric models, Figures 5.3-58, -59, and 60. The results identify the critical trajectories with respect to heating rate, total heat, and heating duration as follows:

Condition	Peak Heating Rate (24 BTU/ft ² -sec)	<pre>Highest Total Heat (1192 BTU/ft²)</pre>	Longest Heating Time (320 sec)
Velocity, Ve, ft/sec	15,000	15,000	13,000
Entry Angle, γe,	-20°	-14.1° (graze)	-10.9° (graze)
Atmosphere	VM-8	VM-3	VM-3

As shown in Figure 5.3-57, these three trajectories bound the entry envelope and were evaluated in detail. A nominal Capsule Bus ballistic parameter of 0.3 slugs/ft was assumed in the above trajectories, which is slightly higher than the 0.266 slugs/ft design value. Entry with the lower M/C_DA results in a 6% reduction in heating rate and total heat.

5.3.2.2.4 <u>Aerothemodynamic Entry Heating Definition</u> - The amount of heat protection material required to maintain the structure at an acceptable temperature level is directly influenced by the amount of convective and radiative heat transfer received by the vehicle during the Mars entry, the heating duration, and the thermal performance of the shield material exposed to the heating environment. The equilibrium aerodynamic convective heating to the capsule is calculated using the programs described in Figure 5.3-61. This figure summarizes the Planetary Aerodynamic Heating Program (PAHP), the Hot Gas Radiation Program (HGR), the Reaction Kinetics Ablation Program (REKAP), and the Ablation Boundary Layer Equilibrium Program (ABLE). The flow of these computer programs to yield the final heat shield requirements is shown in Figure 5.3-62. PAHP, HGR, and ABLE are environmental predictions and are discussed herein. REKAP is the ablation program for evaluating actual material response and is discussed in Section 5.3.2.6.

Special techniques have been developed for the prediction of the equilibrium convective heat transfer under the following conditions: non-continuous flow, base heating, angle of attack, and heating in the region of aft facing-steps and surface waviness. These special problems are discussed later in this section.

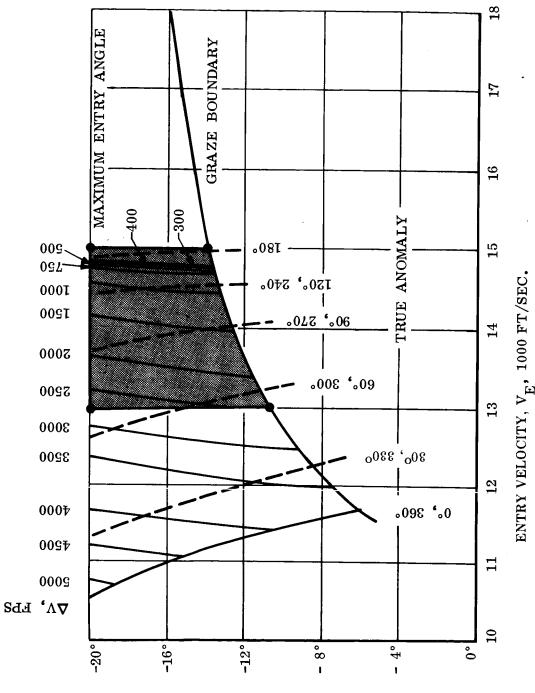
ENTRY CORRIDOR

4400-23,400 km RADIUS ORBIT

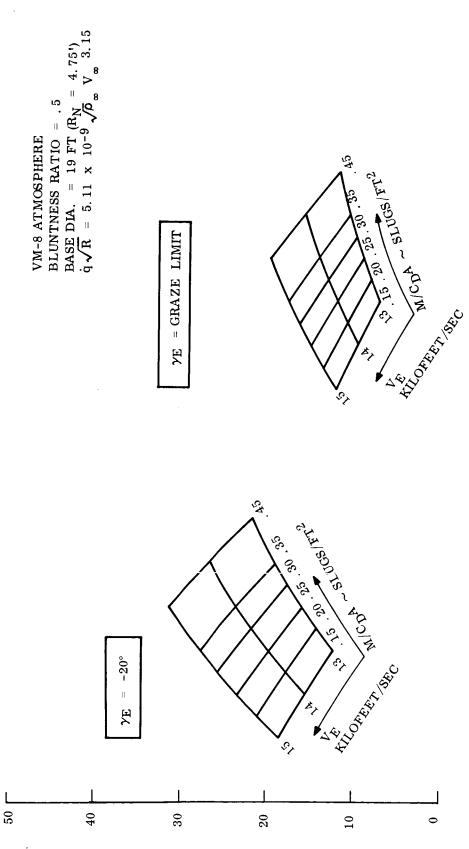
RETRO ANGLE = 0°

ENTRY HEIGHT = 800,000 FT.

• CRITICAL POINTS EVALUATED



ealex path angle, $y_{\rm E}$, degrees



STACNATION POINT HEAT TRANSFER RATE \sim BTU/FT²-SEC

Figure 5.3-58

Figure 5.3-59 5.3-110

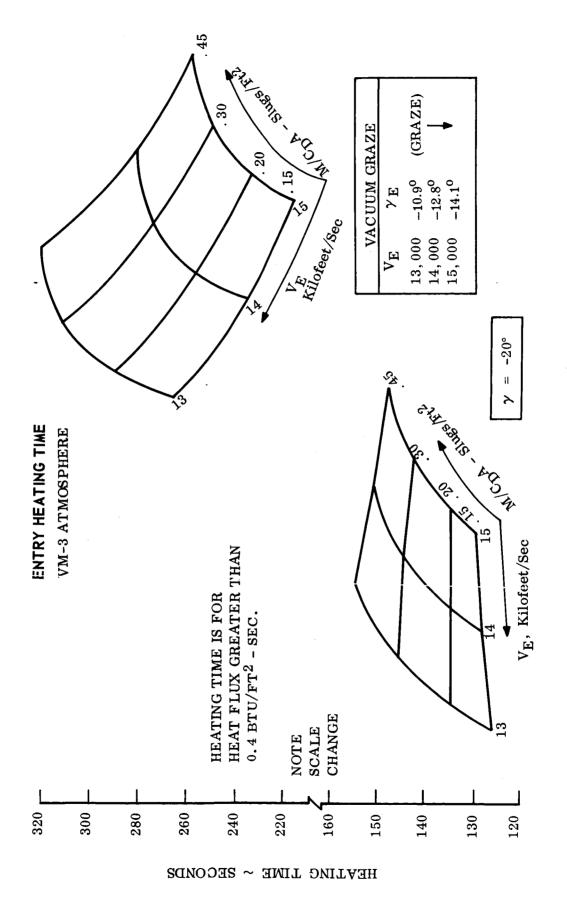


Figure 5.3-60

5.3-111

AEROTHERMODYNAMIC AND THERMAL PROTECTION SYSTEM CALCULATION PROCEDURE SUMMARY

AEROTHERMODYNAMIC BOUNDARY CONDITION Stagnation Point Convective Heat Transfer Local Laminar and Turbulent Heat Transfer Distribution Local Idow properties and boundary layer parameters required for boundary layer transition and mass transfer effects, ρ_e , μ_e , Γ_e , h_e , M_e , R_e , R_e , h (film coefficient) Planetary Aerodynamic Heating program includes provision for subsonic cooling/heating for low speed phase analysis Provision for calculation of above information at a maximum of 50 body locations. Other: For detailed design — Low density regimes defined by Knudsen number criteria—as applied to air atmosphere and earth entry Low density heat transfer in slips, transitional and merged flow included as correction to results calculated for continuum flow Aerodynamic heating in presence of non-equilibrium flow field are independently evaluated with edge of boundary layer flow conditions from flow field predictions. Free molecular heating estimated with $\alpha_T = 0.7$.
AERC AERC AERC AERC AERC AERC AERC AERC

Figure 5.3-61 5.3-112-/

from multiple flat based, recessed and domed a correlations of form.
$$\dot{\bf q}_{\rm L} := 0.0192~{\rm R}_{\rm e\triangle}^{...5} (\mu_{\rm e}/\triangle)\,(h_{\rm S}-h_{\rm W})$$

$$\dot{\mathbf{q}} = 0.014 \, \mathbf{R} \cdot \frac{75}{2} (\mu_{\mathbf{e}}/\triangle) (h_{\mathbf{s}} - h_{\mathbf{w}})$$

$$\dot{\mathbf{q}} = 0.014 \, R_{e\Delta}^{.75} (\mu_e/\triangle) (h_s - h_w)$$

$$\dot{\mathbf{q}}_{\mathbf{r}} = 0.014 \, \mathbf{R}_{\mathbf{e}\Delta}^{.75} (\mu_{\mathbf{e}}/\triangle) (h_{\mathbf{s}} - h_{\mathbf{w}})$$

$$\dot{\mathbf{q}}_{\mathbf{r}} = 0.014 \text{ Re}_{\triangle}^{.75} (\mu_{\mathbf{e}}/\triangle) (h_{\mathbf{s}} - h_{\mathbf{w}})$$

$$\dot{\mathbf{q}}_{\mathbf{r}} = 0.014 \, \mathbf{R}_{\mathbf{e} \triangle}^{-75} (\mu_{\mathbf{e}}/\triangle) (h_{\mathbf{s}} - h_{\mathbf{w}})$$

$$\dot{\mathbf{q}}_{\mathbf{r}} = 0.014 \, \mathrm{R_{e}}^{-.75} \left(\mu_{\mathbf{e}} / \triangle \right) \left(\mathbf{h_{s}} - \mathbf{h_{w}} \right)$$

$$r = 0.014 \text{ Re} \langle \mu_e / \triangle \rangle \langle n_s - n_w \rangle$$

where $R = \langle \alpha_s | A / \mu_s \rangle$

predictions made in 0.05 to 0.16, 0.66 to

3 microns spectrum. For FIRE flight-

extended to non-air gases.

Developed for NASA-Langley FIRE Flow

Field Contract (NAS1-3418) radiation

$$\dot{\mathbf{q}}_{\mathbf{r}} = 0.014 \, \mathbf{R}_{e}^{.75} (\mu_{\mathbf{e}}/\triangle) (\mathbf{h}_{\mathbf{s}} - \mathbf{h}_{\mathbf{w}})$$

$$\mathbf{q}_{\mathbf{r}} := 0.014 \, \mathrm{R_{e}}^{*,2} (\mu_{\mathbf{e}}/\Delta) (\mathsf{h_{s}} - \mathsf{h_{w}})$$
 where: $\mathrm{R_{e, }} = (\rho_{\mathbf{e}} \, \, \mathrm{u_{e}} \, \Delta/\mu_{\mathbf{e}})$

Radiation

Shock Layer Thermal and Spectral Shock 'ayer radiation Program (HGR) Shock Layer Thermal and Spectral Shock 'ayer radiation digital computer program Incident absorbed radiation
$$\dot{\mathbf{q}}_1 = \sum_{\boldsymbol{\phi}} \sum$$

compc site)

 $\frac{\partial}{\partial x} \left(k \frac{\partial T}{\partial x} \right) = \rho \epsilon \frac{\partial T}{\partial t} + H_{q_f} \left(\frac{\rho - \rho_c}{\rho_{f_p} - \rho_c} \right)^n 2 e^{-E/RT}$

Reaction Kinetics Ablation Program (REKAP)

5,3-112-

(1) Variable external boundary condition (
$$\dot{q}$$
 vs tin sink analysis)
(2) Option (1) plus decomposition in depth in acc gravometric analysis data converted to multiple Arrhenius relations
(3) Option (1) and or (2) with the transfer of radiation and emission including multiple reflecti

Option (1) and or (2) with the transfer of radiation in depth by absorption and emission including multiple reflections used for semitransparent materials. Boundary conditions: 40, 4RAD 4combustion

parent materials. Boundary conditions:
$$\dot{q}_0$$
, \dot{q}_R , $\sigma \in T_S^A$ Mass transfer effects defined as
$$\frac{\dot{q}}{\dot{q}_0} = \begin{bmatrix} 1 - .69 \left(\frac{m_{BL}}{m_{\theta}}\right)^{1/3} & \frac{1}{\rho_r} & \frac{1}{1/3} \\ \frac{\dot{q}}{\dot{q}_0} = \begin{bmatrix} e^{-.38} & \frac{C_P}{C_0 BL} & \phi_o & \frac{1}{\rho_r} & \frac{1}{1/3} \\ \frac{\dot{q}}{\dot{q}_0} = & \dot{m}_q & \begin{pmatrix} h_r - h_w \\ \dot{q}_c & \end{pmatrix}$$
 turbulent
$$\phi = \dot{m}_q & \begin{pmatrix} h_r - h_w \\ \dot{q}_c & \end{pmatrix}$$

laminar

ated with 17 component gas phase chemical model. The chemical reactions The surface recession and heat transfer with chemical reactions is evalu-

of extensive ground test data.

Ablation Boundary Layer Equilibrium Program (ABLE)

(mass and energy transfer) of Elastomeric at the surface of the material with each species in the boundary layer are determined as a function of temperature, pressure, and species concentration. Mass transfer effects may also be established from the correlation

The approach has been successfully applied

to the prediction of the surface response

materials in ground test facilities.

Surface Mass and Energy Transfer

AERO PRESSURE COEFFICIENTS ALLOWABIE STRUCTURE TEMPERATURE RECEIVED THERMAL RADIATION VEHICLE GEOMETRY BOUNDARY LAYER TRANSITION HOT GAS RADIATION PROGRAM (HGR) TRAJECTORY AERODYNAMIC HEATING (LAMINAR AND TURBULENT) FLOW CHART - DETERMINATION OF HEAT SHIELD REQUIREMENTS GAPS & STEPS HEATING LOW DENSITY EFFECTS ANGLE OF ATTACK BASE HEATING REACTION KINETICS ABLATION PROGRAM (REKAP) DYNAMIC HEATING PROGRAM (PAHP) PLANETARY AERO-HEAT SHIELD MATERIAL SURFACE THERMOCHEMICAL RESPONSE SURFACE HEAT TRANSFER ABLATING BOUNDARY LAYER SURFACE MASS LOSS EQUILIBRIUM PROGRAM (ABLE) PROPERTIES OF ATM THERMODYNAMIC DECOMPOSITION PARAMETERS THERMAL CONDUCTIVITIES MATERIAL PROPERTIES SPECIFIC HEATS DENSITIES Figure 5.3-62

REQUIREMENTS

SURFACE EMISSIVITY

5.3-113

Convective Heating Prediction - An investigation by Lew (Reference 5.3-22) determined that although the flow field was in a highly non-equilibrium state, the non-equilibrium convective heating rate was within 2% of the equilibrium value. Hence, for the purposes of this study it seems reasonable to employ the equilibrium convective heating rates as computed by the PAHP.

The procedure used for the calculation of the laminar convective heating distribution over a body is Lee's relationship (Reference 5.3-23) modified by Eckert's reference enthalpy techniques. For turbulent boundary layers, we used a relationship derived in (Reference 5.3-24), which satisfies both the momentum and integral energy equations and includes the effect of a finite pressure gradient. The above procedures for the calculation of the convective heat transfer in air have been verified by flight test data and by extensive hypersonic wind tunnel tests.

A study has been made to ascertain the accuracy of the existing stagnation point heat transfer theories when applied to planetary atmospheres. Figure 5.3-56 shows comparisons between experimental data reported in References 5.3-25 thru 34 and several existing theories. The method of computing the stagnation point heat transfer in the PAHP gives essentially the same result as the theory of Scala and Gilbert (Reference 5.3-35). The results shown in Figure 5.3-56 indicate that the PAHP gives good estimates of the convective heating in typical Martian atmospheres.

The thermodynamic properties of the VM-3 and VM-8 Mars atmospheric models used in the PAHP extend over the temperature range of 1000°R to 18,000°R. However, as has been shown experimentally in (Reference 5.3-36), the convective heat transfer results are only slightly different for the Mars atmosphere without argon than if air properties had been used.

A correlation to determine when boundary layer transition occurs was made based on extensive flight test data, and is shown in Figure 5.3-63. Also shown is the effect of mass injection rate on transition. Due to the low heating rates received by the VOYAGER Capsule, the ablation rates of the heat shield material are very small; thus, the low mass addition curve is used in determining the state of the boundary layer. Applying this transition criteria to the trajectories of interest indicated that, except for a short period of time in a steep VM-8 entry, the boundary layer flow will be laminar over the vehicle, Figure 5.3-64.

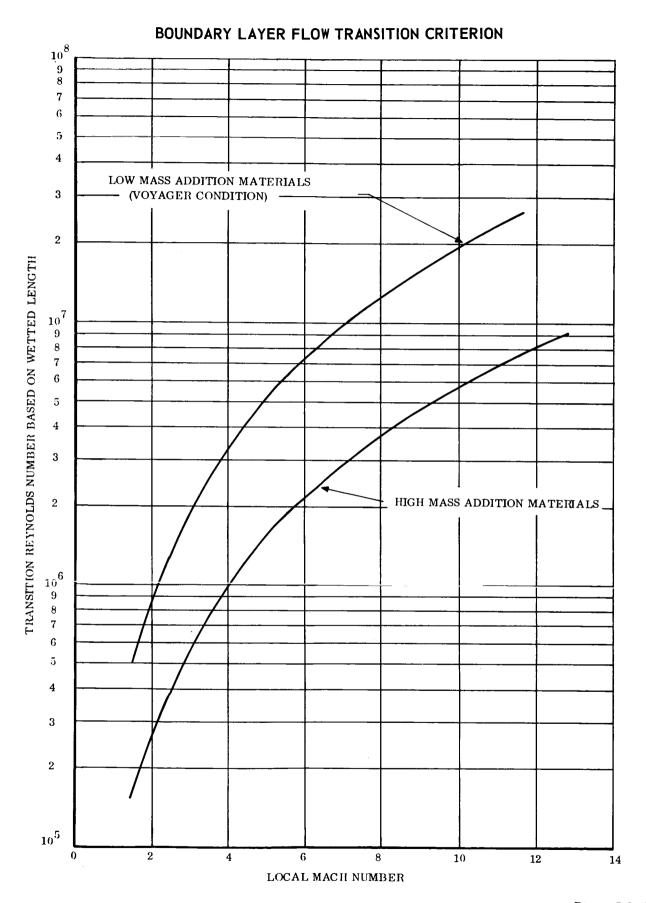


Figure 5.3-63 5.3-115

ENTRY REYNOLDS NUMBER HISTORY AT AFT END OF SKIRT

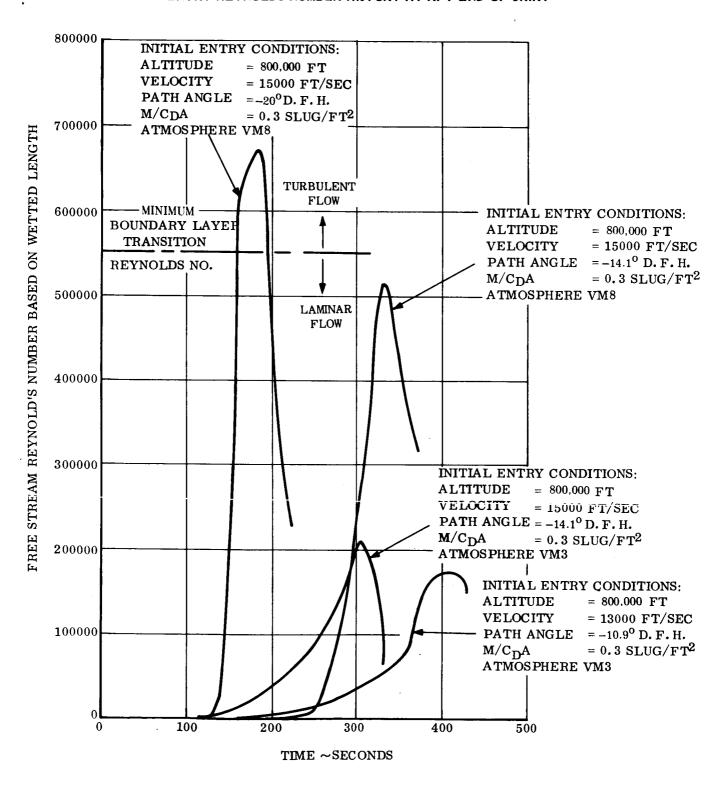


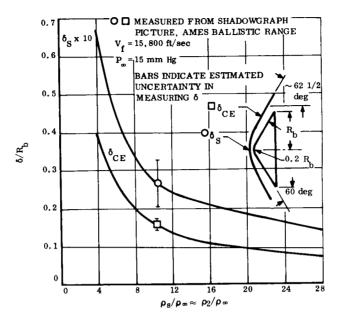
Figure 5.3-64

Hot Gas Radiative Heating Prediction - During planetary entry the hot gas cap surrounding the entry vehicle can emit an appreciable amount of radiation energy toward the vehicle surface. Determination of the magnitude of the radiative heating as seen by the vehicle surface must consider the following effects:

- o Equilibrium gas radiation
- o Non-equilibrium gas radiation
- o Boundary layer (ablation gas) effects and radiative coupling of flow field Equilibrium Radiation - The equilibrium radiation to the various points of the surface of the vehicle can be reasonably obtained with the use of 30% $^{
 m CO}_2$ -70% $\rm N_2$ (VM-3) radiation data of Reference 5.3-37. In these charts, self-absorption is taken into account. It assumes that the entire shock layer is at a uniform temperature equal to the stagnation value, which is obtained from the knowledge of the stagnation enthalpy and pressure along the trajectory. The shock stand off distance was obtained from the correlation presented in Reference 5.3.38 and shown in Figure 5.3-65. Results of these conservative calculations indicate that equilibrium radiation is negligible ($q_{r_e} = 10^{-1}$ Btu/ft²-sec) for the 30% CO₂ -70% N_2 atmosphere. Equilibrium radiation for the 100% CO_2 atmosphere (VM-8) is also relatively small. Although at a given density and velocity, the radiant intensity for 100% $\mathrm{CO_2}$ is less than for the 30% $\mathrm{CO_2}$ - 70% $\mathrm{N_2}$ atmospheres, the density at which the maximum heat flux occurs is greater. Consequently, a somewhat higher radiant heat flux results, (approximately 1 Btu/ft²-sec). This value, however, is small compared to the peak convective heat fluxes (24 Btu/ft 2 -sec) experienced in this atmosphere.

Non-Equilibrium Radiation - High non-equilibrium temperatures experienced by the gas as it passes through the hypersonic shock front cause a radiative heat flux in addition to the equilibrium value. Determination of the non-equilibrium portion of radiation has been made by use of the test data correlation presented in Reference 5.3.38 and shown in Figure 5.3-66. Utilizing this correlation, an analysis showed a significant increase in heating at the end of the skirt due to a relatively large shock stand off distance that accompanies this large vehicle. The uncertainty in predicting non-equilibrium radiation can be as large as a factor of 2 to 4. In the current study, we have used the conservative approach recommended in Reference 5.3.38 by using the prediction line which forms the upper bound of all available data and extrapoating down to the velocities of interest. This is an uncertainty in the environmental definitions, and, thus, has been identified as an

SHOCK STANDOFF DISTANCES USED FOR PRESENT CALCULATION



NON-EQUILIBRIUM HEAT TRANSFER RATE CORRELATION

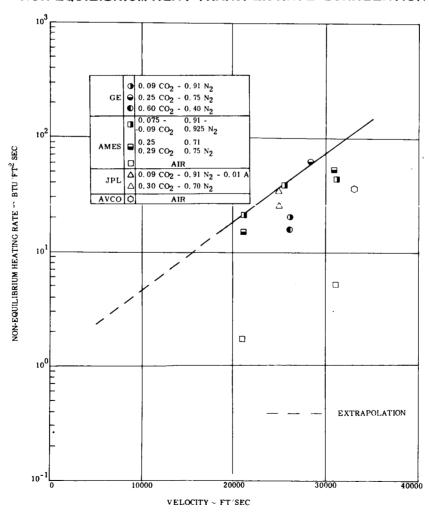


Figure 5.3-65 Figure 5.3-66

area to be fully investigated during subsequent phases of this program when final shield design thicknesses are required.

Boundary Layer Effect and Radiative Coupling of the Flow Field - Both the absorption effecs of the ablation gases and the radiation coupling effect have been neglected in this study. Since absorption reduces the net heat flux to the vehicle, neglecting it will yield a conservative analysis. When the radiation from the shock layer is relatively large in comparison to the energy influx to the shock layer, there occurs a reduction in shock layer temperature, hence, reduction in radiation level. Since the radiation heating level for Martian entry is small to begin with, a negligible reduction from the adiabatic level occurs. Therefore, this small effect is neglected in this analysis. As in the case of the absorption effect, the result is a conservative one.

Entry Heating Environment - Using techniques previously described, the aero dynamic heat flux histories have been computed for zero angle of attack, cold wall conditions, and no mass addition to the boundary layer. The calculations were made for the critical conditions previously defined by the atmosphere models and entry corridor. The hypersonic pressure distribution employed was obtained from modified Newtonian theory. Figure 5.3-67 gives the peak heating rate and the maximum total heat flux to the vehicle for the VM-3 and VM-8 atmospheres, and Figure 5.3-68 compares the convective and radiative heating for the two graze entry conditions into the VM-3 atmosphere. The peak convective stagnation point heat flux of 24 Btu/ft 2 -sec occurs for an entry into the VM-8 atmosphere at an entry velocity of 15,000 ft/sec on an initial entry path angle of -20°. The maximum convective heat input to the shield occurs for an entry into the VM-3 atmosphere at 15,000 ft/sec and a path angle of -14.1°, which yields a total heat load of 1192 Btu/ft². However, Figure 5.3-69 shows that the total convective heat pulse generated by an entry into the VM-3 atmosphere at 13,000 ft/sec and a path angle of -10.9°, yields a slightly higher backface temperatures than the fast entry case into the VM-3 atmosphere, although the total heat pulse is only 993 Btu/ft2. This is because the lower velocity trajectory for the shallower entry results in a longer flight time and, hence, slightly higher backface temperatures due to the longer "soaking" period.

The maximum local aerodynamic shear stress value of 0.4 lb/ft^2 , as predicted by the Reynolds analogy method, occurs for the fast, steep entry into the VM-8 atmosphere. Typical shear stress histories are presented in Figure 5.3-70 for entry into both heat shield design atmospheres (VM-3, and VM-8).

SUMMARY OF STAGNATION POINT AERODYNAMIC AND RADIATIVE HEATING

Mars Atmos- pheric Model	Entry Velocity, V _e FPS	Entry Path Angle, Y e deg	Convective Stagnation Point Heating		Non-Equilibrium Stagnation Point Radiation	
			Maximum Rate Btu/ft ² -sec	Total Heat Btu/ft ²	Maximum Rate Btu/ft ² -sec	Total Heat Btu/ft ²
VM-3	13,000	-10.9	6.4	993	3.4	304
VM-3	15,000	-14.1	11.0	1192	7.1	532
VM-3	15,000	-15	12.3	1084		
VM-3	13,000	-20	10.8	640		
VM-3	15,000	-20	15.7	. 870		
VM-8	15,000	-14.1	15.4	914		
VM-8	15,000	-20	24	590		

HEAT FLUX HISTORIES

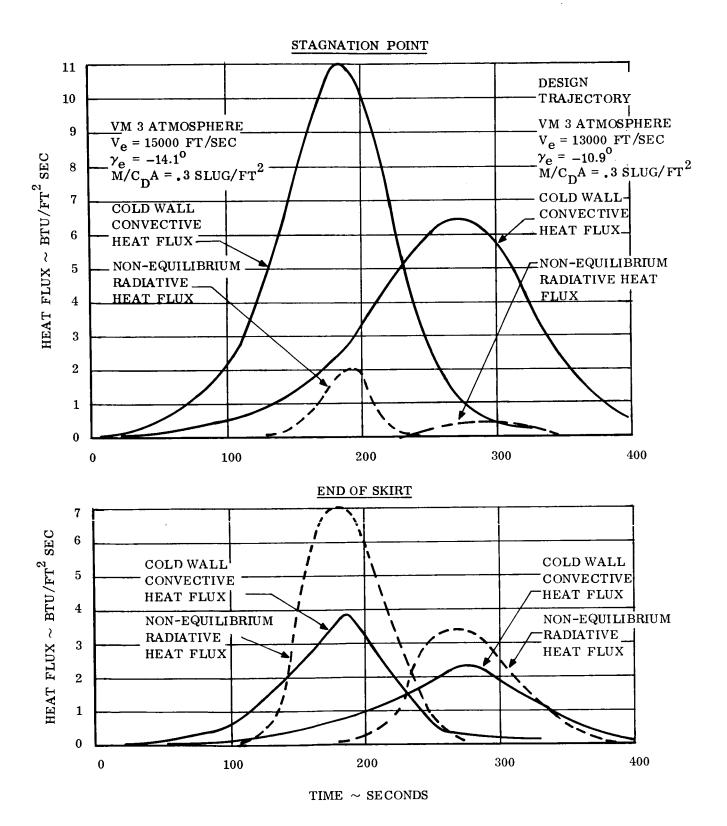


Figure 5.3-68 5.3-121

BACKFACE TEMPERATURE HISTORIES

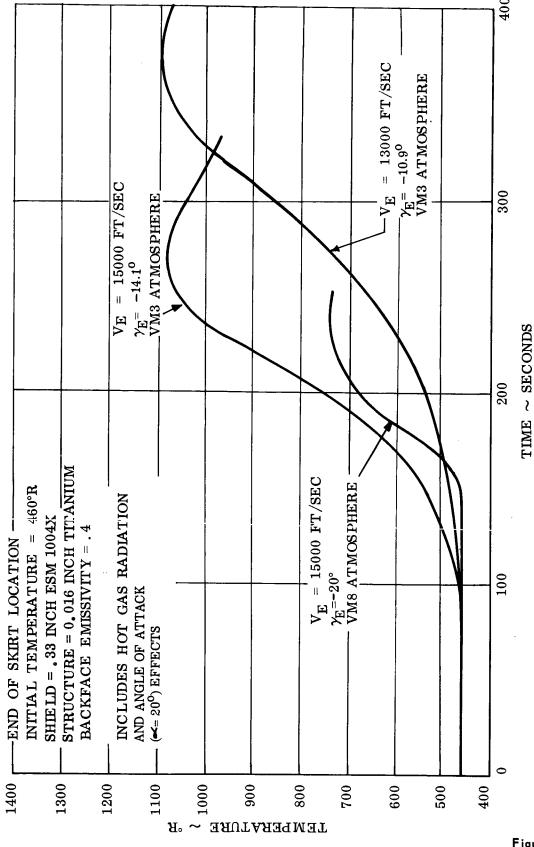


Figure 5.3-69

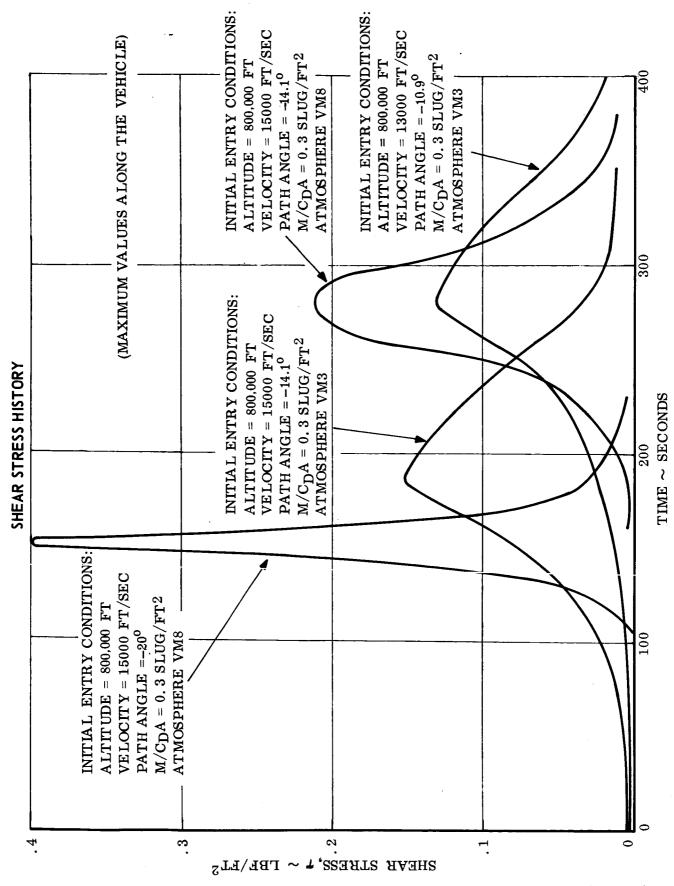


Figure 5.3-70 5.3-123

5.3.2.2.5 Special Problems - Special techniques have been derived for the prediction of heat transfer in a number of problem areas. These are based on empirical data which have been correlated in terms of local boundary layer flow parameters, that can be determined for the specific vehicle geometry, and flight conditions.

Heating in the Region of Aft Facing Steps - As a result of techniques used in the manufacture and assembly of the vehicle, surface irregularities will exist. The effect of a 0.1 inch rearward facing step on the convective heat transfer has been analyzed and, hence, on the overall heat shield weight. It was found that on the spherical nose cap region, no increase in the convective heat transfer occurs due to the low Reynolds numbers in that region. However, results were obtained at selected cone skirt stations and Figure 5.3-71 show the increase in the convective heating due to 0.1 inch aft facing steps for several entry conditions. In order to determine which case controls the design of the heat shield with steps, the Reaction Kinetics Ablation Program (REKAP) was used for each of the 3 cases presented as likely critical design cases. Body location 42.8" was evaluated on REKAP for the 15,000 ft/sec, -20° path angle case and was found to have a less severe thermal response of the shield-structure bond layer than the design case because of the shorter heating time. It appears that the low velocity graze entry is still the critical design case and since steps only marginally increase the heat pulse on the skirt of the vehicle for this trajectory, the heat shield penalty is small.

Angle of Attack Effects – Since the entry phase has a maximum angle of attack tolerance of \pm 20°, a technique was developed to determine the convective heat transfer to the vehicle under these conditions. Results have been obtained for a maximum angle of attack of 20° without roll, which is the most severe condition for any one spot on the shield. The method used to obtain the heat transfer to the vehicle at angle of attack is that presented in Reference 5.3–39, in conjunction with the appropriate pressure distribution for the configuration. This technique was applied to a high heating rate trajectory case into the VM-3 atmosphere (V_E = 15,000 ft/sec and γ_e = -20°), to illustrate the increase in peak convective heating distribution due to an angle of attack of 20°. The result of this investigation is presented in Figure 5.3-72 and is for a flight time of 120 seconds after entry at the referenced altitude, when the local heat transfer is a maximum.

EFFECT OF AFT FACING STEPS ON CONVECTIVE HEAT FLUX

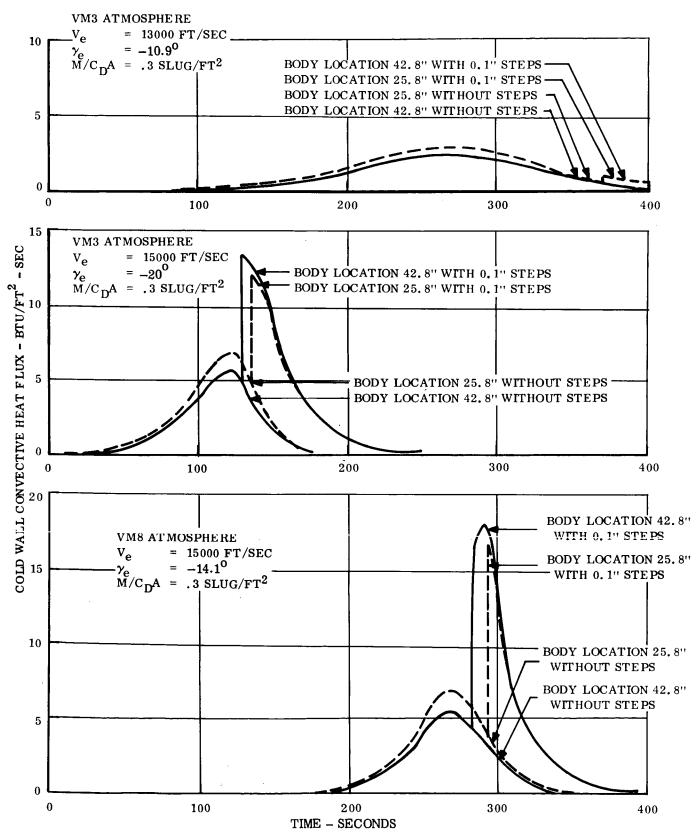


Figure 5.3-71 5.3-125

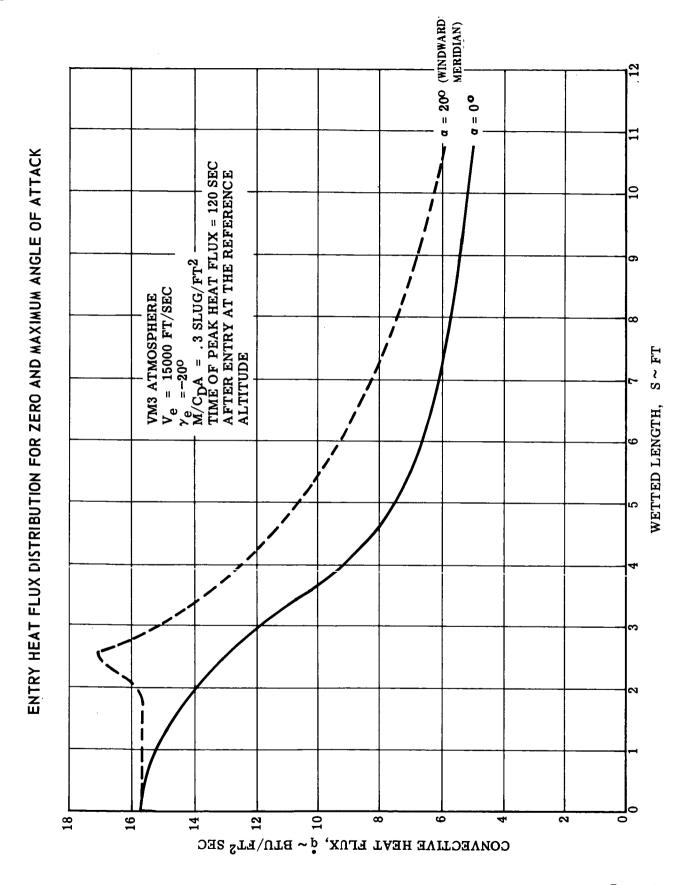


Figure 5.3-72 5.3-126

Low Density Effects - The aerodynamic convective heating in the low density region where continuous flow theory begins to deviate has been analyzed using the method of Cheng (Reference 5.3-40). The results show that for the peak heating trajectories the increase in heating rate predicted by non-continuous flow theory is only 5% above the value calculated by the standard boundary layer analysis. Therefore, this effect has been neglected in determining the environment for the design shield analysis.

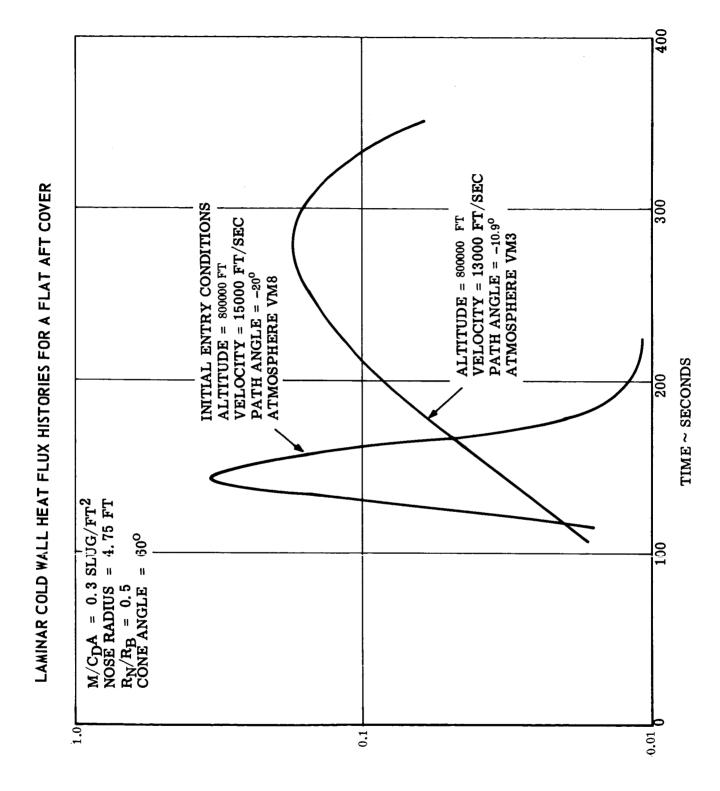
Base Heating - Heating to an assumed flat aftercover was estimated using the Planetary Aerodynamic Heating Program for the two trajectories selected to give the most severe environment. The separated flow convective heat transfer rates are evaluated with the expressions summarized in Figure 5.3-61 which have been previously verified by the MK 2 flight test data. Cold wall convective heat flux histories are presented in Figure 5.3-73. The heating rates were evaluated at the center of the flat aftercover because experience with smaller blunt sphere cone vehicles has indicated this area to have the most severe heat fluxes during detached flow heating at small angles of attack. The trajectories evaluated were a high velocity steep trajectory in the VM-8 atmosphere, which is expected to provide the most severe local heat transfer, and a low velocity shallow trajectory in the VM-3 atmosphere which gives the largest total heat load. Results show a peak cold wall heat flux of 0.35 Btu/ft²sec. The total cold wall heating for the VM-3 case is 27.6 Btu/ft².

Surface Waviness - Because of the lightweight structure of the VOYAGER Capsule, there is an inherent surface waviness due to fabrication techniques. For the fast steep entry into the VM-8 atmosphere, which provides the peak heat fluxes and loads, the results obtained using the technique described in Reference 5.3-41 show that the increase due to the surface waves is less than 1%. This effect was also neglected in the subsequent shield design analysis.

5.3.2.2.6 <u>Thermostructural Criteria</u> - The conical Aeroshell structure utilized in the ablative heat shield evaluation is fabricated from .008 in. titanium (6 Al-4V) sheet stock reinforced by longitudinal corrugations. The nose cap structure is a phenolic fiberglass honeycomb sandwich. This structure is fully described in Section A 3.2.1.3.

The structural temperature limits are:

	Design <u>Maximum</u>	Predicted <u>Maximum</u>
Phenolic fiberglass	735°F	640°F
Titanium	800°F	640°F



COPD WALL CONVECTIVE HEAT FLUX $\sim \text{BTU}/\text{FT}^2$ SEC

Figure 5.3-73 5.3-128 The heat shield thickness will be sized based on 640°F. The temperature difference between the design and maximum temperatures is the thermal design margin. The bond systems will be compatible with the 800°F maximum temperature.

5.3.2.2.7 ESP Constraints on Nose Cap - In addition to the ground, transit and entry environmental requirements used to select and size the ablative heat shield for the conical section, two additional requirements are imposed on the nose cap assembly which necessitated a change in the thermal protection and structural approach. These are RF transparency for the radar altimeter, and essentially no outgassing or particle emission from the nose cap material in order to prevent interference with ESP atmospheric sampling and TV viewing experiments.

RF Transmission Requirements - The nose cap heat shield material and its substructure must be RF transparent. Located immediately behind the nose cap is the primary antenna for the radar altimeter. For satisfactory operation of the radar system, the one-way transmission loss of the nose cap assembly must be less than 1.5 dB at the L-Band frequency. The nose cap must meet this requirement during the radar operation period, from 800,000 feet down to Aeroshell separation, which includes the entire entry heating period.

Atmospheric Composition Measurements - An accurate composition measurement of the Martian atmosphere will be significantly more difficult to obtain if heat shield reaction products are allowed to mix with the atmosphere samples to be measured. The gas composition inlet is at the apex of the nose cap, but since a $\pm 20^{\circ}$ angle of attack is possible, products from a larger nose cap area must be considered. If an ablative nose cap is utilized, ablation products such as silicon, aluminum, iron, hydrogen, carbon and their oxides, plus low molecular weight hydrocarbons such as methane and ethane may contaminate or mask the atmospheric composition measurement. In addition, either condensation of ablative char products or heat shield erosion particles present a strong possibility for clogging the mass spectrometer inlet system. For these reasons, a restriction of no outgassing is imposed on the nose cap heat shield material.

Television Viewing - Television imaging is directed at providing information on landing site location and detailed surface characteristics. Success in accomplishing these objectives depends upon good imagery at altitudes below 200,000 feet, i.e., during and after the peak heating period.

Thermal environmental conditions during these periods can strongly influence optical performance and in some cases can destroy viewing. Flow field emission, and absorbion of coatings on the optical window are the main contributors to these

difficulties. Their effects are summarized in the following table:

Environmental Phenomena	Cause	Effect on Television Viewing
Self-luminous flow field	Gas emission and burning ablation products	A veiling glare which reduces contrast and limits the visibility of dim objects
Light scattering	Deposition of ablative products on the viewing window	Increased background luminance giving the appearance of look-ing toward the sun through a dirty window
Light absorption	Heavy coating of the window of fine ablative products	Reduction in amount of energy available for image formation leading either to a loss of quality or a complete loss of recording capability
Optical wavefront degradation	Destruction of the smooth window surface by abrasion from ablative products	Break up of the ordering in the light bundle creating the effect of observing through a "ground glass"

As the table indicates, ablative products are the most troublesome and should be avoided if at all possible. They have the potential to eliminate useful imaging from the time it is most important down to the point of Aeroshell separation when the CBS has slowed and the contaminated window is removed.

Window contamination was noticed on the Gemini flights and was attributed to ablation product outgassing from silicone type materials that were heated during launch. The same window "dirtying" problem was experienced with all the candidate ablative heat shield materials in the screening tests conducted in the McDonnell plasma facility. In these tests, a glass window was flush mounted downstream from the ablative specimen, in order to simulate the entry flight condition in the Aeroshell.

Mars surface imaging is a prime experiment for the 1973 VOYAGER mission. To ensure good optical performance it is essential to provide a nose cap design free of serious outgassing and particle emittance. Hence, a non-ablative heat shield material approach was required for the nose cap portion of the entry heat protection subsystem.

5.3.2.3 <u>Selected Thermal Protection Approach</u> - The initial step in the heat shield material selection process is to choose the type of heat protection system offering the greatest potential of meeting the requirements imposed by the VOYAGER mission.
5.3.2.3.1 <u>Candidate Heat Protection Systems</u> - The thermal approaches investigated include metallic radiative (both hot and cold structure), heat sink, insulating non-ablators, high density charring ablators, low temperature sublimers, and low density charring ablators. An assessment has been made for each of these approaches in order to select one which will give the lightest system weight with the greatest degree of flexibility to meet the wide range of anticipated entry conditions. In addition, the flexibility of any approach to accept an off-nominal entry and its interaction with other Capsule subsystems was also considered in this selection.

Figure 5.3-74 and -75 summarize the various approaches relative to weight, sterilization and decontamination susceptability, low temperature and hard vacuum effects, RF transparency, fabrication, handling, cost, and flight experience. A review of this comparison shows the low density charring ablators offer the lightest weight approach with a minimum number of problems expected in their life cycle preceding entry. For specialized applications within the vehicle, such as providing a non-ablative material in the vicinity of TV windows and atmospheric sampling ports, the low density ceramics offer the best approach.

5.3.2.3.2 <u>Preferred Approach</u> - Based on all of the foregone considerations, the low density charring ablator on the conical Aeroshell, with a non-ablating ceramic nose cap, and a fiberglass thermal curtain over the Aeroshell base area, is the preferred VOYAGER Capsule Bus heat protection subsystem for the following reasons:

- a. Minimum subsystem weight
- b. Maximum flexibility and versatility to accommodate off-design conditions, including system growth considerations
- c. Fewer anticipated fabrication and development problems than with the other approaches
- d. Sensitivity to the sterilization/decontamination and low temperature/hard vacuum environments does not exist or can be circumvented by proper material formulation.
- e. Proven and reliable subsystem based on past flight experience.

Within the general category of ceramics and charring ablators, there are a large number of formulations ranging from very low (\sim 5 lb/ft³) to high (\sim 165 lb/ft³) densities. To help narrow this band, the impact of the relative mild Martian

UNIT WEIGHT COMPARISON OF SHIELD - STRUCTURAL CONCEPTS

UNIT WEIGHT BASELINE DESIGN UNIT WEIGHT	1.0	1.09	1.33	1.76	2.0	2.0
CRITICAL HEATING TRAJECTORY	$VM-3$ $V_{ m E}=15,000~{ m FPS}$	$\gamma_{\rm E} = -14.1^{\rm o}$	VM-8 V = 15,000 FPS	$\gamma_{\mathbf{E}} = -20^{\circ}$	VM-3 V = 15,000 FPS	Έ = 14.1°
CRITICAL LOADING TRAJECTORY	$V_{E} = 15,000 \text{ FPS}$ $\gamma_{E} = -20^{\circ}$					
	ABLATOR BERYLLIUM TMAX = 1250°F TMAX = 1250°F TTATE THE THE THE THE THE THE THE THE THE T					ABLATOR ALLOS THAX = CHO'S
CONCEPT	LOW DENSITY ABLATOR	HEAT SINK	RADIATIVE (HOT STRUCTURE)	RADIATIVE (COLD STRUCTURE)	LOW TEMPERATURE SUBLIMER	HIGH DENSITY CHARRING ABLATOR

Figure 5.3-74

5.3-132

CANDIDATE HEAT PROTECTION SYSTEMS

Figure 5.3-75

entry environment on the material performance was investigated. Within the design environment, the materials essentially respond as high temperature insulators. It can be shown by simple transformation of the transient conduction equation that for an equal unit weight of shield material, the parameter $k\rho/C\rho$ governs the in-depth temperature response. Although specific heat (Cp) is relatively insensitive to variation in density (ρ), the thermal conductivity (k) is, at moderate densities, proportional to density. Thus, decreasing the material's density, to the limit where mechanical properties become the controlling parameter, provides the most efficient heat shield material. Therefore, our efforts have been directed toward investigating low density ceramics (20 1b/ft³ range), and developing lower density charring ablators. In this latter respect, a 30% density reduction was achieved from the materials available at the start of this program, and a 50% reduction was found to be feasible.

- 5.3.2.3.3 <u>Description of Representative Low Density Ablators</u> Materials representing the low density ablators considered in this study include GE ESM 1030-1, ESM 1030-1B, ESM 1004X, ESM 1004XW, ESM 1030-1(S), ESM 1004X(S), ESM 1030-2(S), MDC S-20T, N-603, Apollo ablative material (5026-39HCG), microballoon phenolic nylon (MPN), Insulcork 2755, and balsawood. A description of each of these is summarized in Figure 5.3-76. Representative properties of each material are given in Section 5.3.2.4. Of the 13 candidate materials, the first 9 are silicone elastomeric composits, and represent low density versions of ablators used on previous spacecraft applications. While some of these low density materials are not totally developed for large scale fabrication, they represent logical extensions of past experience.
- 5.3.2.3.4 <u>Description of Candidate Nose Cap Materials</u> A material survey was undertaken to select the most suitable heat shield material and support structure that is transparent to RF signal, is non-outgassing during heating, and is also compatible with the ground, transit and entry environments. Our studies showed the inorganic ceramic materials to be most suitable in meeting all of the above requirements. To aid in the selection process, a request for information was sent to experienced ceramic fabricators. Brunswick and Whittaker Corporations responded, and their designs were included in the trade-off studies.

The basic nose cap materials and designs investigated in depth were:

a. An aluminum phosphate-quartz fiber reinforced honeycomb sandwich used both as a thermal shield and support structure (Brunswick).

CANDIDATE ABLATIVE HEAT SHIELD MATERIALS

MATERIAL	RESIN	FILLER	REINFORCEMENT	TYPE OF FOAM	DENSITY LB. FT3	CURE	BOND	COMMENTS
ESM 1030-1	EPOXY-SILICONE	NONE	INORGANIC FIBERS	CHEMICAL	18-19	ROOM TEMP; 3000F	RTV 560 ROOM TEMP. CURE	FREE FOAMED AT ROOM TEMP., SLIT TO THICKNESS, FLEXIBLE
ESM 1030-1 B	EPOXY-SILICONE	NONE	INORGANIC FIBERS	CHEMICAL	14-16	ROOM TEMP.; 3000F. 6000F	RTV 560 ROOM TEMP. CURE	FREE FOAMED AT ROOM TEMP., SLIT TO THICKNESS, FLEXIBLE
ESM 1004 X	METHYL-PHENYL IRON OXIDE SILICONE	IRON OXIDE	INORGANIC FIBERS	CHEMICAL	14-16	ROOM TEMP., 3000F	RTV 560 ROOM TEMP. CURE	FREE FOAMED AT ROOM TEMP., SLIT TO THICKNESS. FLEXIBLE
ESM 1004 XW	METHYL-PHENYL CALCIUM SILICONE CARBONA	CALCIUM CARBONATE	INORGANIC FIBERS	CHEMICAL	14-16	R00M TEMP., 3000F	RTV 560 ROOM TEMP. CURE	FREE FOAMED AT ROOM TEMP., SLIT TO THICKNESS, FLEXIBLE
ESM 1030-1 (S)	EPOXY-SILICONE	NONE	INORGANIC FIBERS AND SPLIT PHENOLIC GLASS HONEYCOMB	CHEMICAL	18–19	ROOM TEMP., 3000F	RTV 560 ROOM TEMP. CURE	FREE FOAMED AT ROOM TEMP SLIT TO THICKNESS. FLEXIBLE
ESM 1004 X (S)	METHYL-PHENYL SILICONE	IRON OXIDE	INORGANIC FIBERS AND SPLIT PHENOLIC GLASS HONEYCOMB	CHEMICAL	14-16	ROOM TEMP., 3000F	RTV 560 ROOM TEMP. CURE	FREE FOAMED AT ROOM TEMP SLIT TO THICKNESS. FLEXIBLE
ESM 1030-2 (S)	EPOXY-SILICONE	NONE	INORGANIC FIBERS AND SOLID PHENOLIC GLASS HONEYCOMB	CHEMICAL	16–18	ROOM TEMP., 3000F	RTV 560 ROOM TEMP. CURE	FREE FOAMED AT ROOM TEMP., SLIT TO THICKNESS, SOMEWHAT FLEXIBLE
MDC S-20 T	METHYL-PHENYL SILICONE	SILICA ECCOSPHERES CARBON	CONTINUOUS PHENOLIC GLASS HONEYCOMB	CHEMICAL & SYNTACTIC	18-21	ROOM TEMP., 3000F	HT 424 3250 F CURE	H 'C PRE-BONDED TO STRUCTURE. MATERIAL. TROWELLED IN AND FREE FOAMED AT ROOM TEMP. EXCESS TRIMMED OFF TO H. C THICKNESS
N-603	METHYL-PHENYL SILICONE	PHENOLIC MICRO BALLOONS. SILICA ECCOSPHEIYES	SPLIT PHENOLIC GLASS HONEYCOMB	SYNTACTIC	32-36	ROOM TEMP., 3000F	RTV 560 ROOM TEMP. CURE	TRIMMED TO THICKNESS. NOT FLEXIBLE
APOLLO HEAT SHIELD MATERIAL	EPOXY	PHENOLIC MICRO BALLOONS	SOLID PHENOLIC GLASS HONEYCOMB	SYNTACTIC	32-36	2500 F	HT424 TYPE 3250 F CURE	H C HARD BONDED TO STRUCTURE. MATERIAL TROWELLED IN AND CURED IN PLACE. RIGID
NPN	PHENOLIC	PHENOLIC MICRO BALLOONS. GROUND NYLON	NONE	SYNTACTIC	34-38	250° F	HT 424 TYPE 3250 F CURE	MADE IN SMALL PIECES IN MATCHED METAL MOLDS, RIGID
INSULCORK 2755	PHENOLIC (BINDER)	GROUND CORK	NONE		28–32	1 (HT 424 TYPE 3250 F CURE	APPLIED AS SHEETS. FLEXIBLE
BALSA WOOD	CELLULOSE	-	NONE	1	6-16		HT 424 TYPE 3250 F CURE	MACHINED TO FIT. RIGID

Figure 5.3-76 5.3-135

- b. A composite consisting of a dense alumina external skin with a low density alumina foam-bonded to a fiberglass laminated internal skin (Whittaker).
- c. A low density, hardened Fiberfrax insulation system supported with a phenolic-fiberglass honeycomb sandwich.

These candidate materials all have the required high temperature stability, and the necessary electrical/mechanical properties.

5.3.2.4 Properties of Candidate Ablative Materials — The heat shield materials study was directed toward assembling data from the literature and obtaining minimal but necessary test data on the major candidate materials to form a common data base. These data were used in calibration of the analytical techniques employed in material performance trade-offs, and in making relative assessment of the various materials. The primary function of the heat shield is to protect the Capsule from the entry heating pulse, thus making thermal performance a major material consideration. However the testing also provided information on other trade-off factors such as fabricability, mechanical integrity, quality assurance, etc. Assessment of these other factors is mandatory to the selection of the optimum heat protection subsystem.

During the test program the following material properties were measured for the candidate materials; thermal conductivity, specific heat, dynamic enthalpy, weight loss by thermogravimetric analyses, weight loss in vacuum, tensile stress-strain properties, thermal expansion, and relative bondability. Arc tests were conducted at both, the MDC and GE plasma facilities to investigate the over all material thermal performance and char integrity in a simulated entry heating environment. In addition, panels of ablator bonded to structure were cycled to low temperatures to evaluate low temperature mechanical integrity of the combination, and limited tests were performed to evaluate sensitivity to the decontamination (ETO)/ heat sterilization environments. In conjunction with other in-house activities, limited evaluation of the material's ability to support fungus growth was made. In the discussion of the decontamination-sterilization environmental effects it will be shown that the silicone elastomeric materials were not affected; therefore, the remainder of the testing was performed on samples that had not been pre-conditioned to the heat and ETO environment.

5.3.2.4.1 <u>Selection of Candidate Materials for Tests</u> - At the beginning of the testing program, there were several low density charring materials which prior independent analyses and experience of GE and McDonnell indicated were logical choices as the thermal protection system.

It has been reported by numerous workers in the ablation field that the low density elastomeric and plastic composites are very effective in the low to moderate heating rate regime (References 5.3-42, -43). In the mild environment, the insulation properties, conductivity and density, control the backface temperature rise, and thus, the heat shield weight requirements.

Low density ablators were selected for the Gemini and Apollo thermal protection systems (References 5.3-44, -45). For the lower Earth entry heat flux-shear conditions, which resemble the Martian heating conditions, the low density silicone ablators were preferred on the basis of weight, cost, and operational flexibility. (Reference 5.3-46)

A complete range of materials were evaluated including flexible silicone elastomers without honeycomb matrix (ESM 1030-1, ESM 1030-1B, ESM 1004X, ESM 1004XW); flexible silicone elastomers with split honeycomb matrix ESM 1030-1(S); ESM 1004X(S), flexible silicone elastomer in continuous pre-bonded honeycomb (S-20T); panel bonded elastomer in honeycomb ESM 1030-2(S); and a non-flexible elastomer in a split honeycomb matrix (N-603).

Although the materials selected for study are experimental, they are derivatives of existing systems which have been well characterized, have been subjected to extensive ground and flight tests, and have been produced for major space vehicle programs. The primary development effort has been in reducing the initial material density, thus increasing the material insulation properties. Therefore, though the materials themselves represent an extension of the current state-of-theart, the wide experience with this class of material minimizes the risk in their utilization.

For the past $5 \, 1/2$ years the Elastomeric Shield Materials (ESM) have been under development and in use by the General Electric Company, Re-Entry Systems Department. Initially, these materials were supported by continuous honeycomb and had a density of about 55 lb/ft³. During this development period ESM has been formulated with densities from 5 to 90 lb/ft3. In addition, strength and char retention capability improvements have substantially improved so that the continuous honeycomb initially required was replaced by split honeycomb and finally by fiber reinforcement alone. ESM has been fabricated by slitting sheets from loaves, by molding, and by a spray application. Various formulations of the material have been fully characterized and a complete set of specifications exist for them. These materials have been fabricated as prime entry heat protection, or have been used on local areas and flown on several different vehicles including MK 12, MBRV, Mark 3 flap, MA-8, AF Program 437AP, X-15, STV, and AF Program 241. Concurrently, with ESM development, activities have been underway to find the optimum bond system, means of its application and quality control; current ESM applications are via a soft RTV-560 bond first applied to the substrate and followed by the pieces of the ESM. Recent improvements in this area have shown that bonds as thin

as 3 to 5 mils are feasible, even though current practice calls for 10 mils.

In a like manner, McDonnell has extensive experience since 1960 with the silicone elastomers supported by continuous phenolic glass honeycomb pre-bonded to the structure with a rigid bond, HT-424. Large scale heat shields (up to 46 ft²) of this type have had extensive flight experience on the NASA-Gemini, Gemini-B, and ASSET programs. As a result, proven techniques have been developed for application of the honeycomb, quality control of the bond, filling the honeycomb cells, and quality of the final shield material. Low density silicone elastomeric ablators have been under development for the past 5 years and several formulations have been characterized and proposed for programs, including M-2, X-15 and HL-10. This experience provided the base for assessing the rigid bonded heat protection systems evaluated in this study.

5.3.2.4.2 Ground Environment Tests - One of the requirements of the system is compatability with both chemical decontamination and dry heat sterilization. Consequently, it was imperative that the capability of the various materials to withstand these unique environments without property deterioration be determined. The ability of the materials to support fungus growth was also evaluated. In this study phase, only preliminary data were obtained to note if there were any interactions with these ground environments. In the next phase, all design data will be generated on materials that have been previously exposed to the decontamination/sterilization cycles.

Decontamination and Sterilization - Tensile specimens were cut from GE ESM 1030-1, ESM 1004, N-602* Gemini Heat Shield Material, Insulcork 2755 and balsawood. Thickness and weight measurements were made on all, and tensile properties determined on one-third of the samples of each material. The remaining specimens were exposed to the ethylene oxide-freon 12 mixture at 50°C and 50% relative humidity for a total of 168 hours. Thickness and weight measurements were again made on all, and tensile properties on one-half of the specimens of each material. The remaining samples were exposed to 300°F for 72 hours, and the above measurements made on all specimens.

Only Insulcork 2755 and balsawood exhibited approximately a 5% increase in weight and a 10% increase in thickness after the decontamination exposure. The dimensional changes were retained after the dry heat exposure. These changes could indicate an irreversible reaction between the cellulose and the ethylene oxide.

^{*} Material for these samples was formulated with RTV 602 rather than with RTV 603.

The tensile properties of the silicone based heat shield materials were not appreciably affected by the decontamination-sterilization cycles. Insulcork 2755, however, exhibited a 15% loss in strength after the ethylene oxide exposure which was not recovered after the dry heat cycle as would be expected (Reference 5.3-47). The ethylene oxide exposure produced no effect on the elongation of Insulcork. However, after the dry heat exposure, there was a 60% decrease. The combination of environments lowered the tensile strength of the balsawood by approximately 50%. Fungus Tests - Fungus tests were conducted according to MIL Standard 810B (proposed). The samples were run in a Petrie dish. This is a more severe condition than the hanging method. Samples of ESM 1004, ESM 1030, N-602, Gemini heat shield material, and Insulcork were exposed. Only Insulcork supported fungus growth. 5.3.2.4.3 Mechanical/Physical Characteristics Tests - This group consisted of tensile, thermal expansion and bond shear tests. Tensile Properties - Tensile strength and elastic modulus (and/or stress-strain curve) are required for thermostructural analyses. These properties were measured at temperatures ranging between -220° and 300°F using a standard tensile test spec-

Strain values were estimated from test machine crosshead travel. Where possible, however, a strain gage extensometer was used for strain measurement on specimens at temperatures below their glass transition. Results of the tensile tests and densities are presented in Figure 5.3-77.

imen.

The unsupported materials exhibited essentially linear stress-strain behavior whereas the effect of the honeycomb in the supported materials results in generally non-linear stress-strain behavior above the glass transition temperature, and a high degree of anisotropy. Due to the non-linear stress-strain behavior of the supported materials, actual tensile strength is reported for both principal honeycomb directions at each test temperature.

Thermal Expansion Tests - Thermal expansion data, in addition to tensile properties, are required in thermostructural analyses for calculation of thermal stresses. The data were obtained on rectangular solid specimens (3/4 inch x 3/4 inch x 3.0 inches) using a quartz tube dilatometer. Results of all thermal expansion tests are shown in Figure 5.3-78. The unsupported materials exhibited continuous contraction upon cooling throughout the temperature range of the test (room temperature to -300°F). The two materials supported in solid honeycomb, S20-T and ESM 1030-2(S), revealed their highly anisotropic behavior. Both of these materials expanded perpendicular to the honeycomb ribbon when cooled from room temperature to -100°F;

TENSILE PROPERTIES OF CANDIDATE HEAT SHIELD MATERIALS

MTL	DENSITY (LBS/FT ³)	TEST TEMP. (°F)	TENSILE STRENGTH (PSI)	(1) ELONGATION (%)	ELASTIC MODULUS (PSI)
ESM 1030-1	18.5±0.5	300 75 -50 -100 -150	10.1 20.5 33.6 125 199	35 45 56 (2) (2)	20 45 60 (2) 22,300(3)
ESM 1004X	13.3±0.5	300 75 -50 -150 -220	7.2 9.4 12.6 37.4 223	17 22 22 41 (2)	43 43 58 95 22,500(3)
\$20-T	19.7±1.5	300 300 75 75 -150 -150 -200 -200	75.5* 22.5** 84.8* 19.2** 221(4) 51.1 237(4) 156		
ESM 1030-2	17.0±0.5	75 75	50.3* 10.6**		

NOTES:

- (1) Estimated from test machine crosshead travel
- (2) No reliable estimate below glass transition temperature
- (3) Modulus measured using strain gage extensometer
 - *Parallel to H/C Ribbon
 - **Perpendicular to H/C Ribbon
- (4) Based on initial delamination, ultimate loads were higher

NOTE: REPORTED VALUES AVERAGE OF THREE - FIVE TEST SPECIMENS

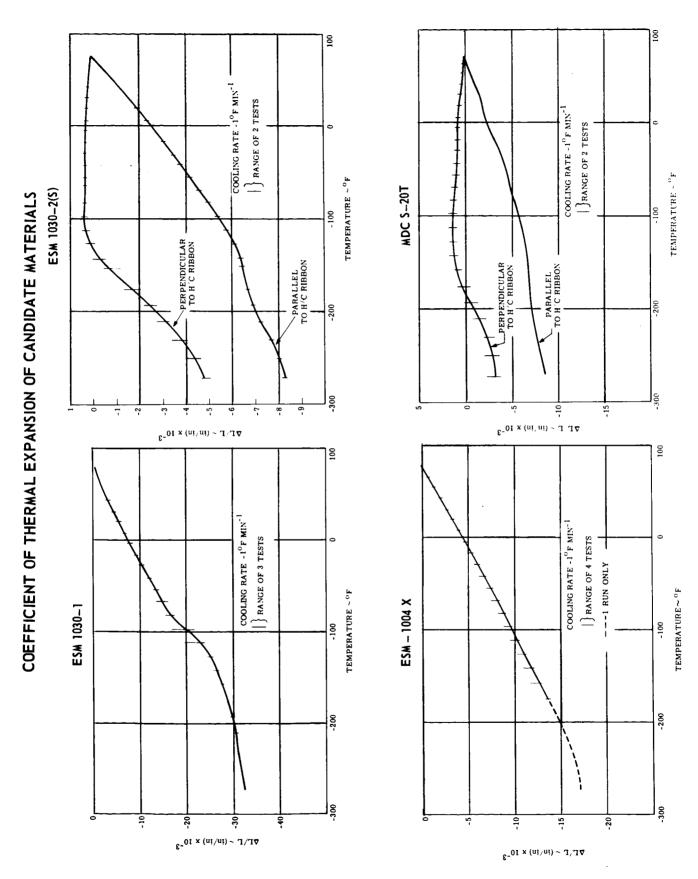


Figure 5.3-78 5.3-142

but contracted at further cooling to -300°F. These same materials, however, contracted continuously parallel to the honeycomb ribbon when cooled. This behavior is similar to that shown by unfilled phenolic glass honeycomb (Reference 5.3-48). Although a detailed mechanistic explanation of this behavior will not be attempted at this time, such behavior could be due to the extremely low elastic modulus of the ablative filler in both S20-T and ESM 1030-2(S) which does not completely inhibit the honeycomb contractions.

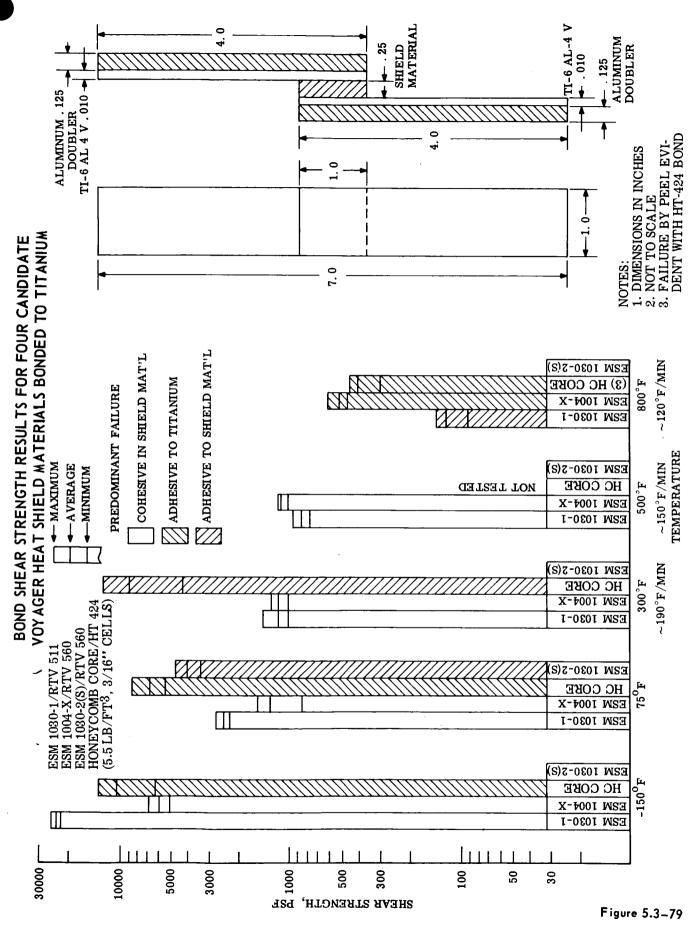
<u>Bondability Tests</u> - Shear tests were conducted to evaluate the relative ability of the candidate heat shield materials to bond to foil gage titanium and to develop preliminary shear strength data at several temperatures.

The single lap test specimen configuration was chosen for these measurements for ease of fabrication. Specimens were pin loaded in clevis grips in an Instron testing machine using spacer blocks to reduce bending to a minimum. Results of the bond shear tests, including average rates of temperature increase, are shown graphically in Figure 5.3-79. The data indicate that any of the shield material/bond systems tested have sufficient bond strength up to 800°F for the VOYAGER heat shield application where low shear loads are expected. Loading of the large 34" x 36" titanium panels to cause deflections was also performed. The test description, results, and conclusion are discussed in Section 5.3.1.

5.3.2.4.4 <u>Thermal Performance Tests</u> - This group of tests consisted of specific heat, dynamic enthalpy, thermal conductivity, thermo-gravimetric analysis, weight loss in vacuum, and arc plasma ablation tests.

<u>Specific Heat</u> - The specific heat data of ESM 1030-1, ESM 1004-X, and S20-T are given in Figure 5.3-80. The measurements were performed on the Perkin-Elmer Differential Scanning Calorimeter (DSC-1) to which an overall tolerance of ±5% is assigned for specific heats.

ESM 1030-1 offers the highest value followed by S-20T and ESM 1004X. Since the DSC instrument utilizes a sample size on the order of 1/8" diameter and about .030" thick with a mass of approximately 20 - 30 milligrams. A representative microscopic section of the S-20T honeycombed material could not be tested to determine the composite effective specific heat, therefore a value was computed. Figure 5.3-81 shows the individual and weighted average specific heat functions of S20-T. Dynamic Enthalpy - The concept of a dynamically measured enthalpy function is presented graphically in Figure 5.3-82. This quantity is also directly measured for virgin shield materials by differential scanning calorimetry (DSC). A sample of material is heated at a programmed rate (36 or 72°F/min. for these materials)



SPECIFIC HEAT OF ESM1030-1, ESM1004X, AND MDC S-20T

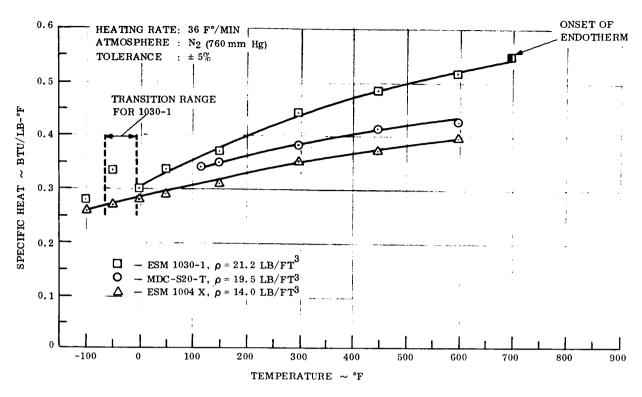


Figure 5.3-80

MDC S-20T: INDIVIDUAL COMPONENT AND COMPOSITE SPECIFIC HEAT

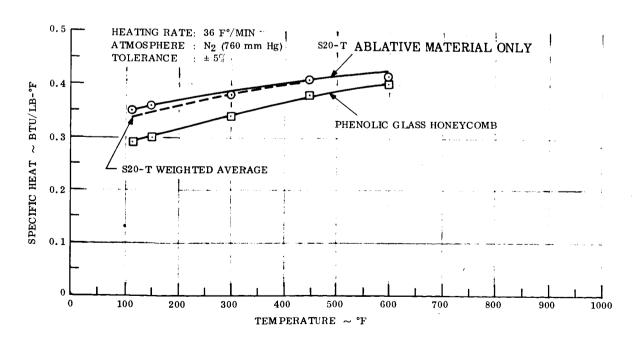
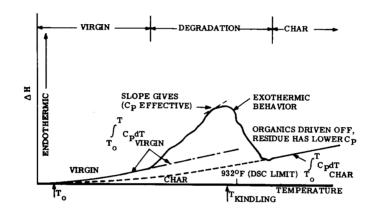
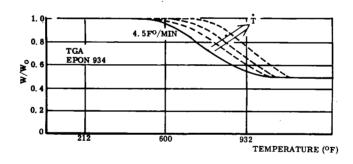


Figure 5.3-81 5.3-145

GENERALIZED DYNAMIC ENTHALPY BEHAVIOR





and the enthalpy (the heat energy required to raise its temperature) is continuously recorded as a function of temperature. A recently developed modification to the DSC technique is shown in Figure 5.3-83 where the parametric dependence of the dynamic enthalpy function of ESM 1030-1 is given as a function of gaseous environment and pressure.

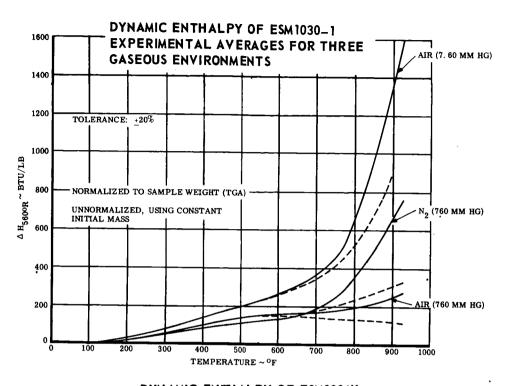
The results of dynamic enthalpy runs on ESM 1030-1 and 1004X in air and nitrogen at various pressures are presented in Figure 5.3-83. Note in the 1004X data, an exothermic reaction occurs at about 725°F. This has no great significance for the VOYAGER gaseous environment since $\rm CO_2$ and $\rm N_2$ are the expected atmospheres for Mars.

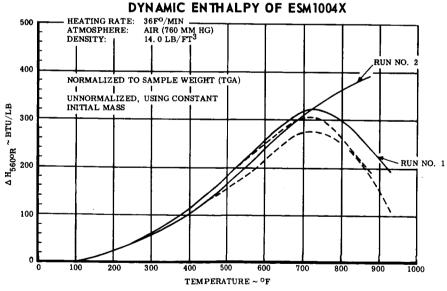
Thermal Conductivity - Thermal conductivity data for ESM 1030-1, ESM 1004X, and S20-T were obtained using a TC-1000 Thermal Conductivity Comparator and are presented in Figure 5.3-84. Measurements on ESM 1004X were made in triplicate in air and nitrogen environments at 1 atmosphere pressure. Nitrogen and air have practically identical thermal conductivities at these temperature levels. Two samples of ESM 1030-1 were measured in air at one atmosphere from -200°F to 450°F and in vacuum, 10^{-3} to 10^{-4} torr over a shorter range.

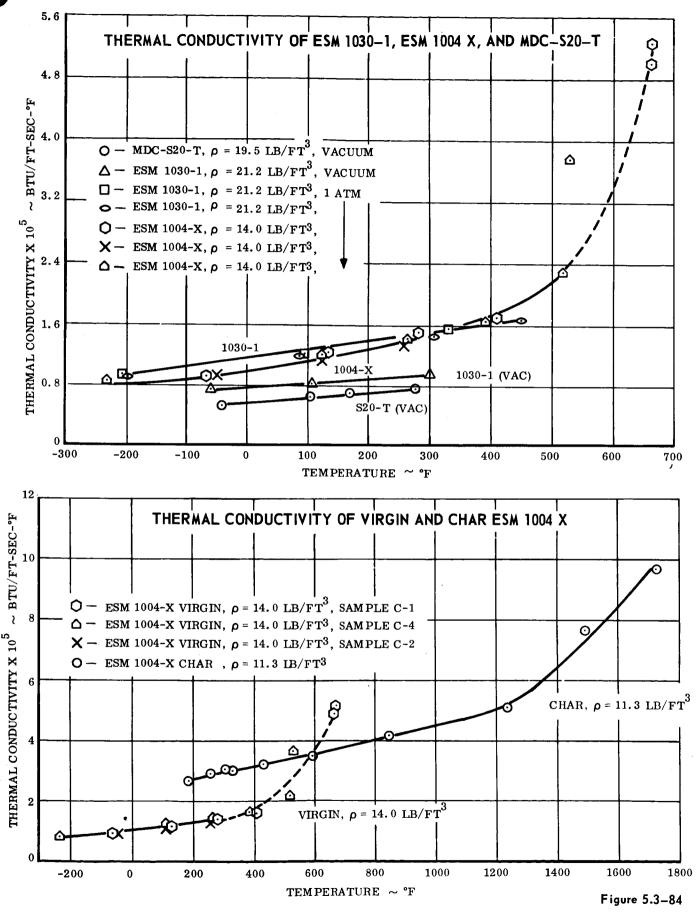
The thermal conductivity of ESM 1004X, char and virgin material is given in Figure 5.3-84. A series of points entering the degradation range of this material were run. The results, sketched in by the dotted line, show a sharp increase in thermal transport. This can be attributed to the onset of some mass (gaseous) transport, and natural convection in the test sample due to the temperature difference imposed across it for this measurement.

Thermogravimetric Analysis - Weight loss versus temperature data were obtained up to a temperature of 1800°F in vacuum (10⁻⁴ torr) to provide a preliminary assessment of thermal stability. The samples were heated in a resistance furnace at a linear heating rate of 20°C/min and their weight continuously monitored by a Cahn RG Electro-balance. The data were in turn displayed on an X-Y plotter as weight versus temperature. Residual weight fraction versus temperature which shows the thermal stability of the four candidate materials, is presented in Figure 5.3-85.

All four materials begin to show a significant weight loss by 800°F. However, the ESM 1030-2(S) material lost weight more slowly, over a wider temperature range, than any of the other materials. The final residual weight fractions at 1700°F of the ESM 1004X, the ESM 1030-2(S), and the S-20T were all about 0.35 whereas the ESM 1030-1 showed a residual weight fraction at 1700°F of 0.15 (a direct result of having a lower content of inorganic reinforcement).







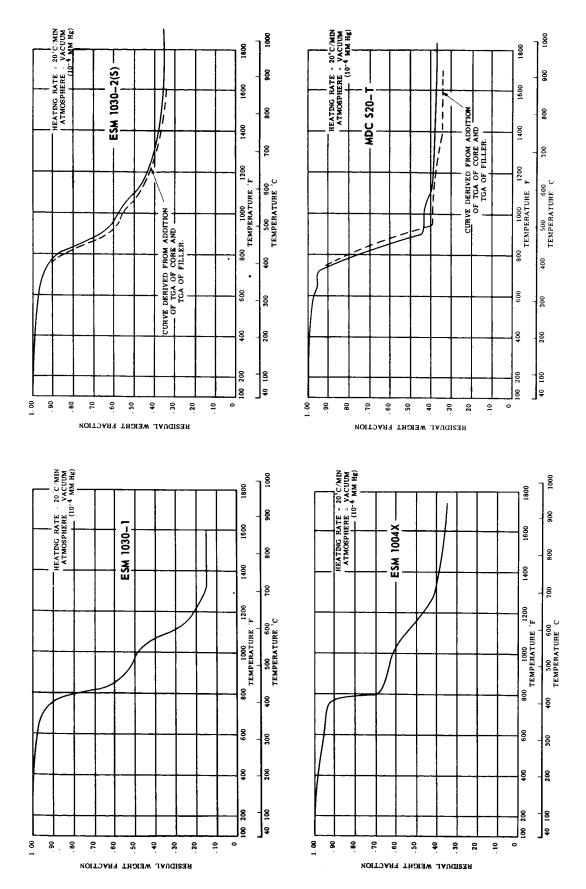


Figure 5.3-85

5.3 - 150

Weight Loss in Vacuum - Specimens of the four candidate materials were exposed to a vacuum of 10^{-5} torr for a period of five days at room temperature, to determine their relative weight loss in a vacuum environment. The measured weight loss of each material is as follows:

Material $(2.5 \times 2.5 \times 0.5 \text{ in.})$	Weight loss gm/gm
*ESM 1030-1	.00624
*ESM 1004X	.00174
S-20T	.00528
ESM 1030-2(S)	.00367
*Bonded ESM 1030-1	.00460
*Bonded ESM 1004X	.00158

* Bonded and unbonded sample tested together.

The weight loss experienced with all samples was less than 1%. Considerable information on higher denisty elastomeric materials tested at pressures less than 10^{-8} torr has indicated the weight loss is greater, and it is therefore pertinent that future evaluation of the selected material(s) include longer exposures at harder vacuums (10^{-8} torr).

Arc Plasma Ablation Tests - To rank the various materials with respect to thermal performance and to permit calibration of computer models for later design calculations, ground tests were performed at both General Electric's and McDonnell's arc facilities. The tests at GE were stagnation splash tests at heat fluxes of 7 and 24 Btu/ft²-sec. with corresponding stagnation enthalpies of 1800 and 5700 Btu lb. The test gas composition was 28% CO₂ - 72% N₂ by volume. These values fairly well cover the expected Martian entry environment as shown in Figure 5.3-86 -87. Each material specimen tested at GE-RSD was instrumented with thermocouples in depth (0.1, 0.2, 0.3, and 0.4 inches below the surface) in addition to a backface thermocouple. At McDonnell, tests were run with a gas composition of 60% CO₂ - 40% N₂ by volume at a heat flux of 12 Btu/ft²-sec and recover enthalpy of 5800 Btu/lb on a wedge type configuration instrumented with three thermocouples at the bondline between ablator and honeycomb structure. A tabulation of the test conditions is shown in Figure 5.3-88.

The criterion for evaluating the various materials is the time required to raise the backface temperature of equivalent unit weight specimens to 600°F. In the MDC test series a nominal surface weight of 0.9 lb/ft² was achieved by allowing the thickness of the specimens to vary with the density of the materials. The time required to raise the backface temperature to 600°F in this series of tests is reported in Figure 5.3-89. A typical backface temperature response from this

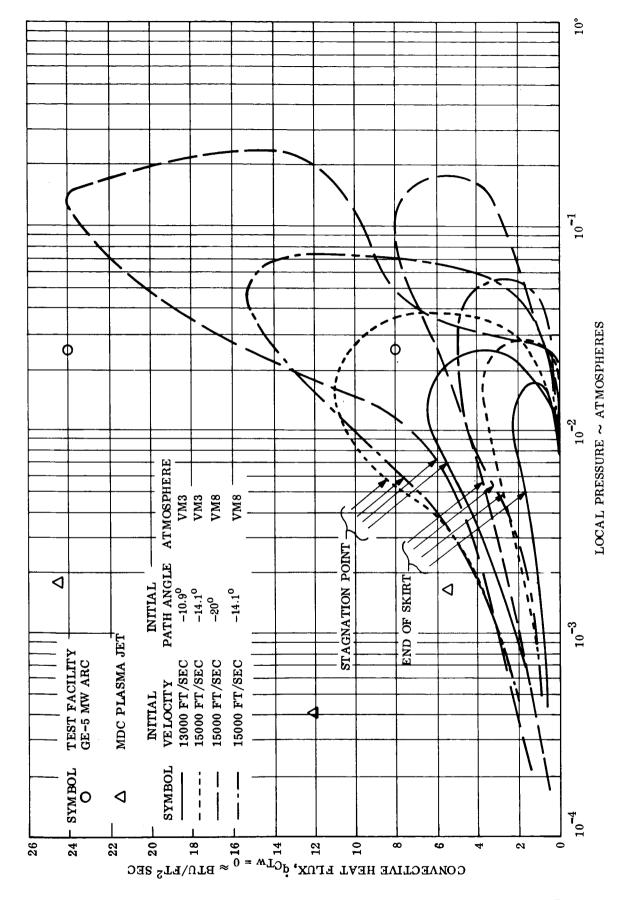
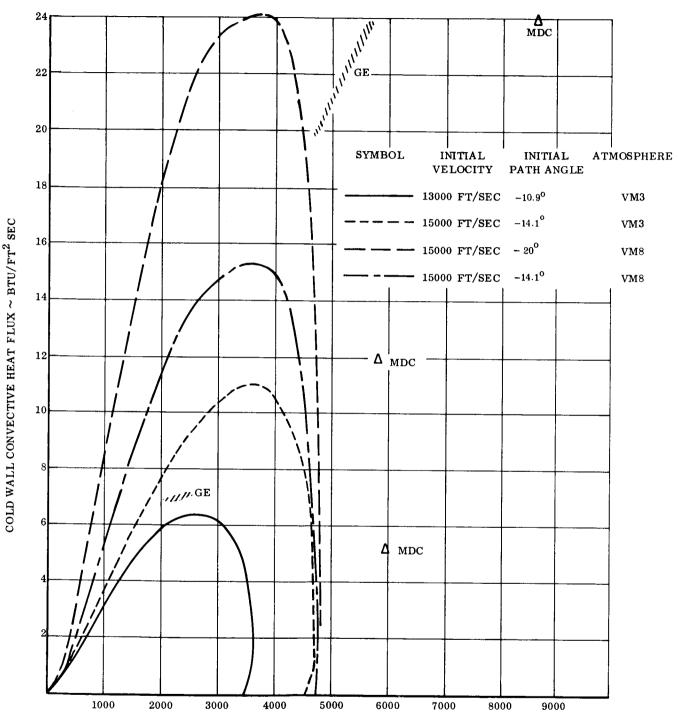


Figure 5.3-86 5.3-152

COMPARISON OF PLASMA JET GROUND TEST CONDITIONS TO FLIGHT ENVIRONMENT



STAGNATION ENTHALPY H_S - BTU/LBM

Figure 5.3-87

ARC FACILITY TEST CONDITIONS

Facility	$q_C (T_W = 0)$ BTU/ft ² - sec.	H _r BTU/lbm	Gas Composition % CO2 - % N2	Ре АТМ	Configuration	Flow
GE 5 MW Arc	7	1700	28 - 72	.026		Laminar
	23	5700	28 - 72	.026		Laminar
McDonnell Arc	12	5800	60 - 40	.00042	→	·Laminar

Figure 5.3-88

SUMMARY OF MCDONNELL TEST DATA

Time Required to Raise Backface Temperature to 500°F and 600°F for Heat Flux of 12 BTU/ft²-sec. and 5800 BTU/Ibm Recovery Enthalpy

Material	Thickness inches	Density Ib/ft ³	Time to Te	mp=Seconds 600°F
ESM 1004X	0.64	16	530	-
			425	550
MDC S-20T	0.53	18.6	400	500
			425	550
ESM 1030-1	0.71	14	405	475
			405	475
ESM 1030-2(S)	0.59	18.4	275	325
			260	300
N-603	0.32	32	225	280
			255	325

Figure 5.3-89

series of test is shown in Figure 5.3-90. In the GE test series a nominal thickness of 0.50 inches was chosen for all specimens except S-20T material which was 0.4 inch thick. Although a variation in surface weight does occur between the various samples, approximate comparisons on a unit weight basis can be made since in-depth temperature response is available on all the specimens as well as the backface temperature response. A typical set of in-depth temperature responses is shown in Figure 5.3-90. As a means of normalizing data with different unit weights the time required to reach 600°F can be plotted versus the product of the in-depth distance and material density. The results of the GE series are shown in Figure 5.3-90 for the heat fluxes of 7 and 24 Btu/ft2-sec.

From a thermal performance standpoint, there appears to be very little difference between the first three materials listed in Figure 5.3-89 of the McDonnell test series (ESM 1004X, S20-T, and ESM 1030-1). A similar comparison can be made between S-20T and 1030-1B in the higher heat flux GE tests and at the lower heat flux between S-20T and ESM 1004X (Figure 5.3-90).

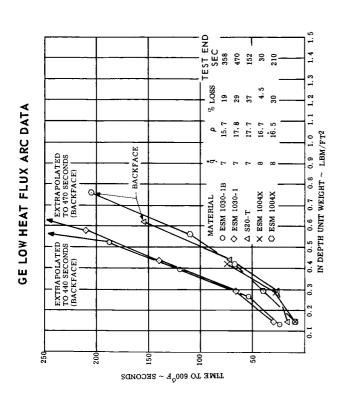
Photographs of the ablated samples from the GE testing at 7 and 24 Btu/ft²-sec and the MDC testing at 12 Btu/ft²-sec are shown in Figure 5.3-91, -92, and -93. At the higher heat flux GE tests the ESM 1030-1 exhibited a rough char surface while the other materials had char surfaces that were smooth and uniform in texture. The samples were sectioned and all candidate materials exhibited sufficient char retention.

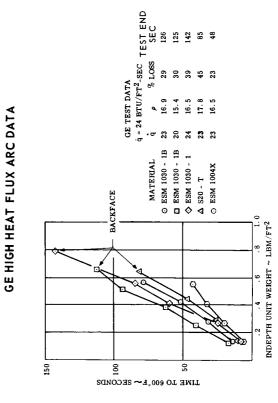
5.3.2.4.5 Optical Properties - The spectral reflectances of ESM 1030-1 and ESM 1004X have been obtained in the wavelength region from 0.3 to 4.0 microns. This region of the spectrum is of primary significance in determining the total solar absorptance of surfaces for heating during orbital descent prior to entry and also lends insight into the infrared characteristics and subsequent total emittance coefficient.

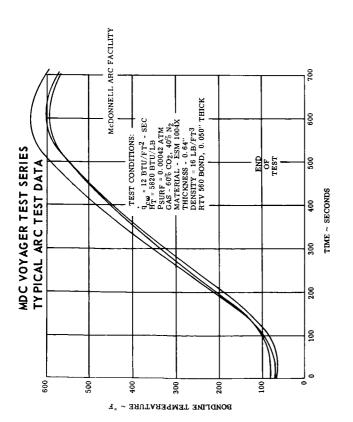
The reflectance functions of the two materials are compared in Figure 5.3-94. These measurements were performed on the Gier-Dunkle Absolute Integrating Sphere which has a proven accuracy of ± 0.01 absolute reflectance units. A significantly higher reflectance (lower absorptance) is observed for the ESM 1030 material up to approximately 1.5 microns. Integration of these spectral data with respect to the energy distribution of the solar spectrum yields a total solar absorptance (α s) of 0.376 for the ESM 1030-1 and 0.755 for the ESM 1004X.

Based on previous experimental reflectance data for ESM 1004AP, it is concluded that the general class of non-supported ESM materials and in particular ESM 1030-1 and ESM 1004X will exhibit a characteristic total hemispherical reflectance ($^{\varepsilon}_{\rm H}$) of 0.85 \pm 0.1.

ABLATION RESULTS FROM ARC FACILITY TESTS







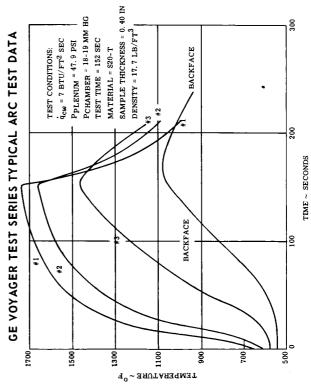
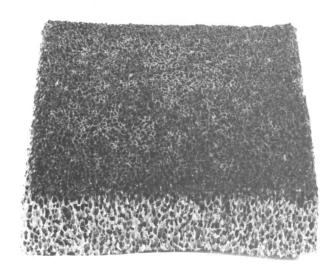
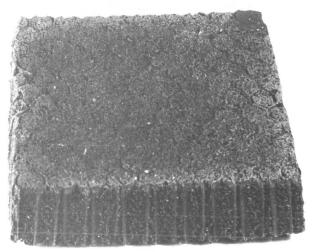


Figure 5.3-90

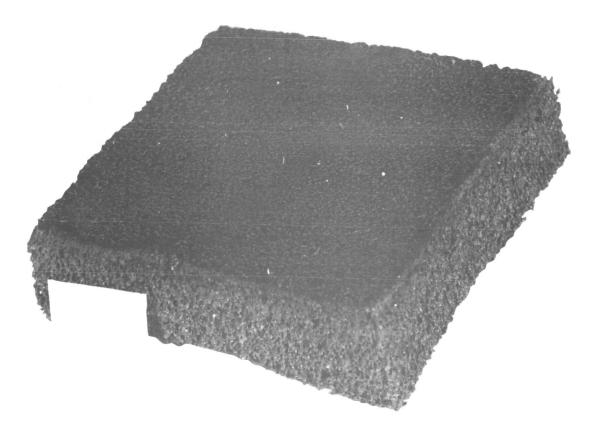
5.3 - 156





Sample V2 ESM 1030-1

Sample V19 MDC S20-T

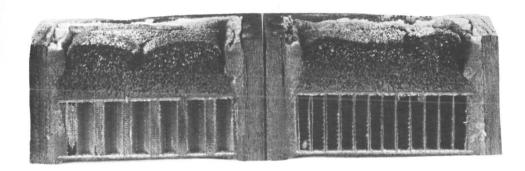


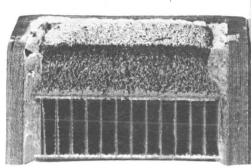
Sample V27 ESM 1004X

Figure 5.3-91

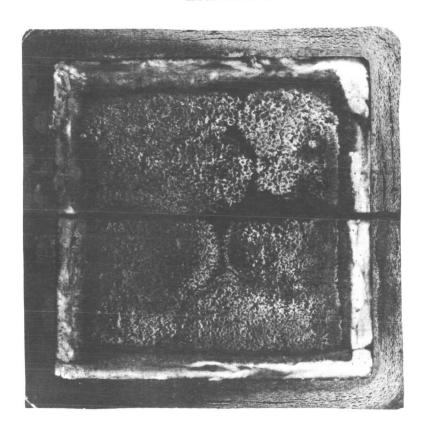
5.3-157

MCDONNELL ABLATION TEST MODELS $q = 12 \text{ BTU/FT}^2\text{-SEC}$





Sample 2B ESM 1030-1



Sample 1B ESM 1004X

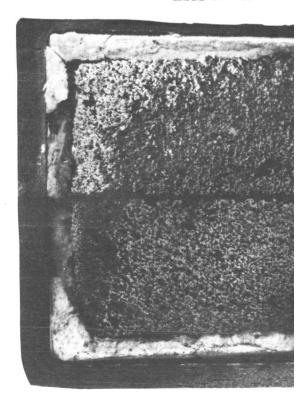
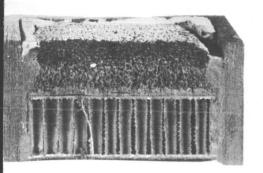
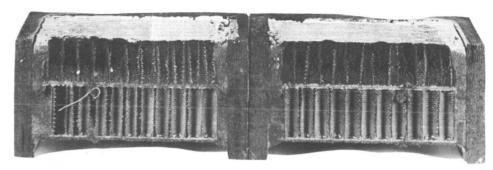


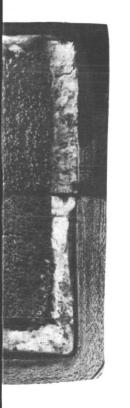
Figure 5.3-92

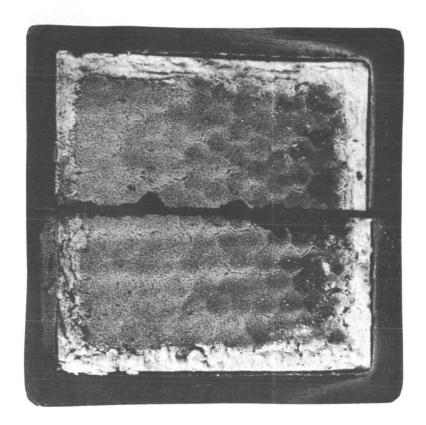
5.3-158 -1





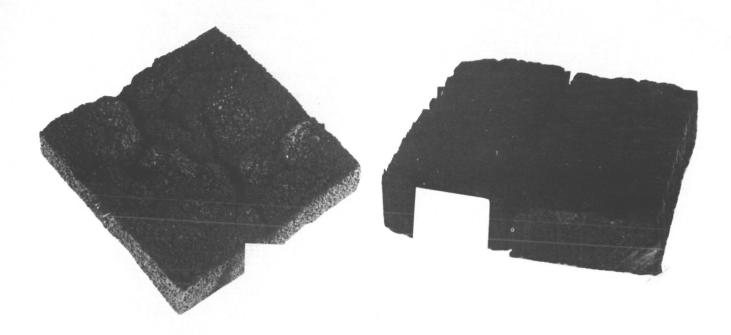
Sample 7B MDC S20-T





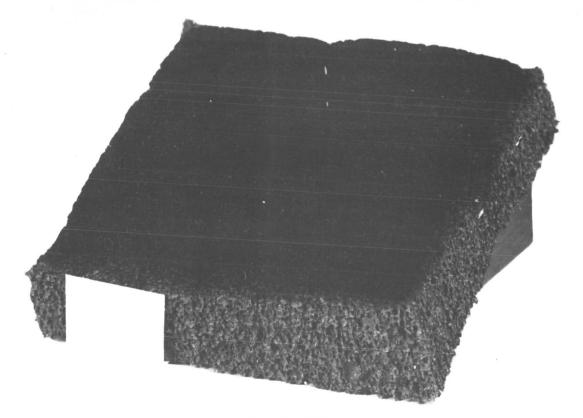
5,3-158-2

GE 5MW ARC TESTS - $q = 24BTU/FT^2$ -SEC



Sample V3 ESM 1030-1

Sample V18 MDC S20-T



Sample V28 ESM 1004X

Figure 5.3-93

5.3-159

REPORT F694 • VOLUME II • PART B • 31 AUGUST 1967

ABLATIVE MATERIAL OPTICAL PROPERTIES

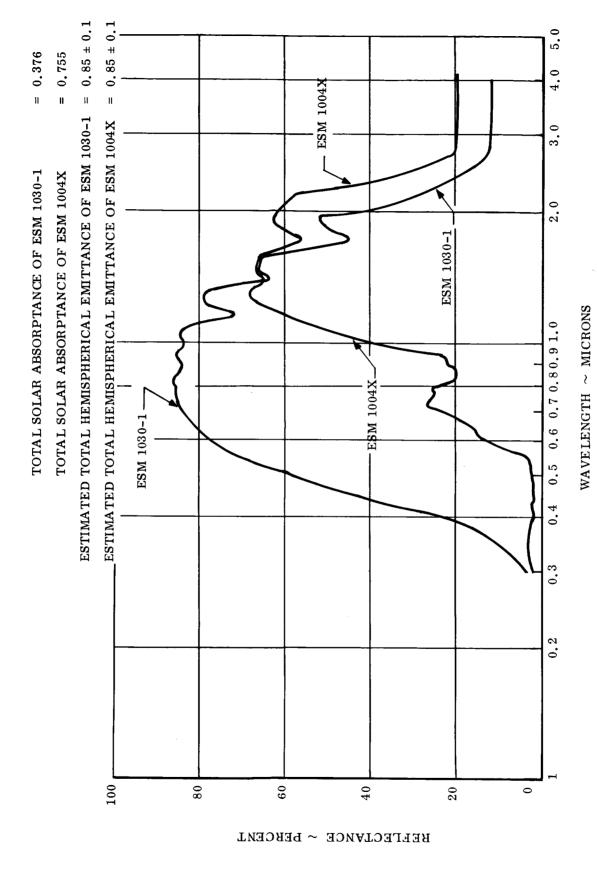


Figure 5.3-94

5.3.2.4.6 <u>Thermo-Structural Compatibility Tests</u> - Hot and cold thermal cycle tests were conducted on 12×12 inch panels and on large curved 34×36 inch panels to demonstrate compatibility of the ablator-bond-structures composite.

Plate Thermal Cycle Tests - Plate thermal cycle tests were conducted to provide experimental verification of the low temperature structural capability of the various candidate materials determined analytically from tensile and thermal expansion characteristics, Figure 5.3-95. A conductive circuit was painted on the 12 x 12 inch specimen surface to aid in crack detection. When this paint cracks, opening the electrical circuit, a sharp discontinuity is produced on the millivolt recorder trace thus giving an indication of failure. All specimens were heated to 300°F for 60 minutes and cooled to room temperature. The specimens were then cooled at 1°F per minute to -300°F to simulate the cold cruise environment. These thermal profiles were accomplished in a standard laboratory convection oven utilizing liquid nitrogen to achieve low temperatures. No cracks developed on the 1004X and S-20T materials down to -300°F. Initial cracks were visible at -75°F for the 1030-1 material and these cracks propagated catastrophically at -280°F.

Large Scale Thermal Cycle Tests - This section presents the results from the thermal cycle testing on panels representing vehicle sections as defined in Test Plan 67SD494 (Reference 5.3-49). They were constructed from 8 mil 6AL4V titanium alloy sheets. The skin and stiffening corrugations were representative of the Aeroshell construction. The panels were 34" x 36.5" and were sections of a right circular cylinder with a radius of 72". The following heat shield structural combinations were studied:

- a. MDC S-20 A higher density syntractically filled precursor of S-20T. Honeycomb is pre-bonded to the structure with HT-424 adhesive prior to being filled with ablator (density = 28 lb/ft^3).
- b. GE ESM 1004AP (unsupported) A higher density precursor of ESM 1004X, soft-bonded to the structure with RTV-560 (density = 36 lb/ft^3).
- c. GE ESM 1001PS (split honeycomb) Soft-bonded to the structure with RTV-560.
- d. N-603 In split honeycomb support, soft-bonded to the structure with RTV-560.

The panels, fabricated primarily to show fabrication and bonding capability were used for evaluating several non-destructive testing techniques to determine bond quality, and in the temperature cycling experiments to provide an indication of the thermo-structural capability of heat shield systems similar to the prime candidate materials.

PLATE THERMAL CYCLE TEST RESULTS FOR VOYAGER CANDIDATE HEAT SHIELD MATERIALS

Material	Temperature at first failure indication ⁽¹⁾	Temperature at catastrophic failure ⁽²⁾	Remarks
ESM 1004X	-195°F	-	Post test examination revealed that circuit had cracked; no cracks were found in the ESM after exposure to -300°F
MDC S20-T	-	-	no failure after cooling to -300°F
N603	+290°F	+290°F	failed at 290°F during heat up to 300°F
ESM 1030-1	-75°F	-280°F	second failure indication at -230°F on opposite side of panel from first indication. These initial cracks propagated catastrophically at -280°F
ESM 1030-2	Not tes	ted	

Notes: (1) as indicated by conductive circuit

(2) as observed visually

The panels were exposed to five thermal cycles as follows:

- o Heat sterilization (2 times) 24 hours at 256°F (125°C).
- o Cold vacuum (3 times) 28 hour total exposure to a pressure below 10^{-5} torr and temperatures down to -100°F, -150°F and -240°F.

The ESM 1004AP and ESM 1001 PS panels survived the thermal cycling visually unchanged. The only measured difference was a slight weight loss during sterilization. The sterilization cycles apparently acted as postcures for the bond material.

During sterilization heat cycling a hairline shrinkage separation developed along the butt joint in the honeycomb segments of the S-20 panels. However, the bond integrity of the pre-bonded S-20 material was uncompromised. Cold vacuum exposures caused the filler material to pull away from the honeycomb cell walls in local areas. The effect was maximized during the third cycle, and at -194°F continuous hairline separations developed to the extent that the detector circuits opened. The nodes of some honeycomb cells were fractured. N-603 suffered excessive cracking during the sterilization cycles and was not subjected to cold vacuum exposure.

X-ray photography provided the best available inspection technique for evaluating bond conditions. With thin (0.016 to 0.020 inch) titanium substructure x-ray absorption balances satisfactorily between shield, bond and structure such that bond voids are readily visible. However, x-rays appear incapable of detecting changes at the bond line since the total density of material remains unchanged along a photon path. By the same mechanism, x-rays cannot detect narrow cracks (less than 0.005 inch wide). Consequently, visual examination and shim stock probing were the only methods available for measuring the cold temperature induced separations observed in the S-20 material. Ultrasonic techniques were developed to the point where inspection results compared favorable to the x-ray methods. This ultrasonic inspection shows promise of additional improvement and will be studied in the next phase.

Bond voids appeared under the N-603 and the ESM 1004AP shield tiles. For the N-603 this was identified as an incompatibility between the wavy surface (Avg. 0.020 inch waves on 3.5 inch centers) of the titanium sheet and the stiff nature of the shield tile. The more significant condition arises from the bond voids under the unsupported ESM 1004AP while none existed under the stiffer ESM 1001PS. For these two panels conformation to the wavy sheet metal is not a problem, and the weights of bond material were not significantly different (estimate 0.040 inch average

thickness). However, some deviations in the actual bonding operation were noted which could have induced this condition. For example, sealing the ESM 1004AP panel during the vacuum bagging step took 4 times longer than with the ESM 1001PS panel. Leakage in this period could have easily induced voids into the bond. 5.3.2.4.7 RF Transmissivity Tests - In the initial phases of the study a requirement existed for the landing radar to transmit through the heat shield during entry. For this reason, each candidate material (or its representative type) was evaluated for the ability to remain RF transparent at $10^{10}Hz$ while being subjected to an average thermal flux of 12 Btu/ft²-sec. This test determined the change in transmissivity with shield material temperature.

A photograph of the test equipment is shown in Figure 5.3-96. The material to be tested is formed into a disk 15 inches in diameter and 0.2 to 0.3 inch thick, and rotated through a pulley by a variable speed electric motor. While the disk is rotating, the flame of an oxyacetylene torch impinges on one sector of the disk front surface. In the area viewed by the RF beam cross-section, the RF beam passes through the non-flame side of the test disk. Because of theoretical considerations and instrument limitations, the current design of this RF/Ablation test equipment does not permit absolute measurements of the RF transmitted and reflected signals. However, the measured changes in transmitted and reflected signal levels during the test are believed to be sufficiently valid to permit ranking of the RF performance of the candidate materials.

The dielectric properties of the VOYAGER/Capsule thermal shield materials were determined by means of standing wave measurements obtained with slotted-line microwave instrumentation. These measurements were made at 9.27 x 10⁹ Hz. The values for complex relative dielectric constant, loss tangent and attenuation coefficient are listed in Figure 5.3-97. These materials are ranked for RF transparency using their calculated values of attenuation coefficient as the criterion. The listed values show that ESM 1004XW, FSM 1030-1B and ESM 1030-1 have the lowest value of attenuation coefficient of the materials tested.

5.3.2.4.8 <u>Titanium Surface Treatments and Bonding Studies for Unsupported Elastomers</u> - Three methods were selected for evaluation for the surface preparation of titanium:

- o Alkaline detergent
- o Conversion coating
- o Acid etch.

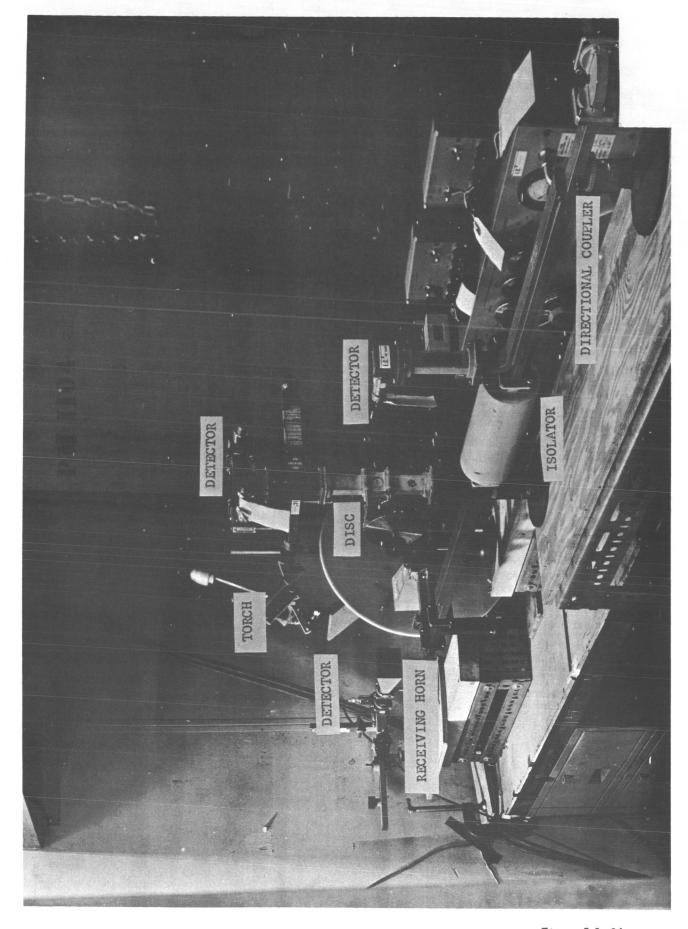


Figure 5.3-96

VOYAGER CAPSULE CANDIDATE MATERIALS DIELECTRIC PROPERTIES/ROOM TEMPERATURE

			3
Material	Complex Relative Dielectric Constant*	Loss Tangent*	Attenuation Coefficient, cm ⁻¹
ESM 1004XW	1.29–j0.006	0.005	0.00595
ESM 1030-1B	1.39~j0.010	0.007	0.00855
ESM 1030-1	1.47-j0.011	0.007	0.00889
ESM 1004HP	1.56-j0.011	0.007	0.00916
ESM 1004AP	1.70–j0.016	6000	0.01229
ESM 1004 HP-S-HC	1.90-j0.022	0.012	0.01732
MDC 5-20	1.69-j0.023	0.014	0.01906
N-602	1.91–j0.026	0.014	0.02026
N-602 S-HC	1.99–j0.029	0.015	0.02216

* Measured at 9.27 x 10⁹ Hz

** Calculated for $10^{10}\ \text{Hz}$ using 9.27 x $10^9\ \text{Hz}$ dielectric values

VOYAGER CAPSULE CANDIDATE MATERIALS RF/ABLATION PERFORMANCE

	Run				
	Time	Trans	Transmission	Reflection	tion
	Sec.	While Heating	During Cool-Down	While Heating	During Cool-Down
ESM 1004XW	30	+0.6	+0.1	-1.3	-0.4
ESM 1030-1B	30	+0.2	0.0	+1.0	9.0-
ESM 1030-1	30	-1.4	-0.3	-3.5	-1.3
ESM 1004 HP	30	-0.4	-0.7	-1.0	-0.06
ESM 1004 AP	30	-0.4	-0.2	-1.7	-0.9
ESM 1004 HP-S-HC	30	+0.2	+0.5	8.0-	+0.5
MDC S-20	30	-1.4	+0.3	-2.4	-3.4
N-602	30	+0.2	+0.1	+0.4	-0.4

NOTE: Each candidate material was bonded to a 1/4 inch thick GE Silicone Resin/glass laminate except ESM 1004AP which was bonded to a JPL phenolic/glass honeycomb

_____ Figure 5.3–97

5.3-166

structure.

The methods were selected primarily because of their ease of application and were evaluated by lap shear tests conducted on specimens bonded with RTV-560. The tests were run at room temperature and 500°F. The bond material failed cohesively in every case showing the adequacy of each surface preparation technique. The detrex alkaline cleaner was selected as the preferred treatment primarily because of ease of operation. This method was used for the surface preparation of all specimens requiring the bonding of heat shield materials to tianium.

Application of an unsupported foam material to a vehicle structure is simplified by the flexibility of the material which conforms to and can be draped over complex curved surfaces. After cleaning and priming the structure, the base elastomer is catalyzed and applied to the structure by roller coating to an approximate thickness of 0.010". The shield material, which has been precut to size and configuration, is draped in place on the structure and rolled to assure wetting of the shield-bond surface and elimination of air entrapped in the bond line. A slight positive pressure is exerted on the shield to assure intimate contact during the room temperature cure of the bond. The bond is postcured during the sterilization cycle.

5.3.2.4.9 Representative Property Data on Other Low Density Ablators - The following sections consist of representative data reported in the literature for the N-603, Apollo, MPN, insulcork and Balsawood heat shield materials.

N-603 - It was assumed that the properties of N-603 would be very similar to those reported for N-602 (Reference 5.3-50).

Thermal Conductivity, (100 to 500°F) (Btu/ft-sec-°F) - 2.05 x 10^{-5} Density - 34 $1b/ft^3$

Specific Heat, $Btu/1b-^{\circ}F$ (0 to 400°F) - 0.40

TGA shows a 5% weight loss at 650 - 700°F

Tensile Properties

Temp. °F	Elastic Modulus(psi)	Ult. Str. (psi)	Strain at Failure (%)
+77	1650	35	4.3
-35	1820	42	7.3
-130	1.21×10^5	720	0.67
-280	3.45×10^5	1580	0.47

Thermal expansion, in/in/°F (0 to 300°F) - 5.6×10^{-5}

Apollo Heat Shield Material (Reference 5.3-50) (5026-39 HCG)

Thermal Conductivity

Direction C	Temp. °F	Thermal Conductivity BTU/ft-hr-°F
(through thickness)	-182	0.0290
	- 92	0.0382
	140	0.0469
	275	0.0532
	513	0.0605

Specific Heat

Temp. °F	Specific Heat (BTU/1b-°F)
-150	0.189
0	0.284
150	0.347
300	0.397
500	0.418

Thermal Expansion - (mils/in)

Temp. °F	A Direction	B Direction	<u>C Direction</u>
-100	-3.47		_
- 82	_	-2.74	-2.81
75	0.00	0.00	0.00
200	1.55	1.53	1.81
500	2.15	2.08	2.14

Density - 33 $1b/ft^3$

Tensile Properties

Direction A	Temp.	Ult. Str. (psi)	Young's Modulus (ksi)	Total Elong. (%)
(parallel to HC ribbon)	-200 0 300	629 485 68	207 130 22	0.30 0.37 0.31
Direction B				
(perpendicular to HC ribbon)	-200 0 300	549 448 52	140 95 13	0.32 0.44 0.42

Microballoon Phenolic Nylon (MPN) (Reference 5.3-50)

Thermal Conductivity, (BTU/ft-sec-°F) - 2.1 x 10^{-5}

Specific Heat, $(BTU/1b - {}^{\circ}R) - 0.40$

Density, 36 lb/ft³

Tensile Properties

Temp. (°F)	Ult. Tensile Strength (psi)	E (tension) (psi x 10 ⁻⁴)	E _{f (%)}
75	435	4.88	0.93
-200	455		0.68

Thermogravimetric Analysis shows that the material begins to lose weight at a significant rate at around $700^{\circ}F$.

Insulcork 2755 (Reference 5.3-51)

Composition

Natural Ground Cork
$$-78 \pm 3$$
 wt. % Plasticized Phenolic Resin -22 ± 3 wt. %

Thermal Conductivity

Temp.
$${}^{\circ}F_{\text{x }10}$$
 $\frac{70}{1.50}$ $\frac{100}{1.18}$ $\frac{150}{1.23}$ $\frac{200}{1.25}$

Specific Heat

0.47 (BTU/1b-°F) - from room temperature to 360°F

Density - $30 \pm 2 \text{ lb/ft}^3$

Tensile Properties

Temp. °F	Ult. Str. (psi)	<pre>% Elongation</pre>
-65	500	2
+75	250	10
200	100	8

Thermal Expansion

(1) As Received
$$-65$$
 to 130 5.1×10^{-5} 130 to 425 1.2×10^{-5} (2) "Bone" dry -65 to 150 4.5×10^{-5} 150 to 450 1.4×10^{-5}

TGA shows a 5% weight loss at 335°F

Balsa Wood (References 5.3-52, -53)

Density - 6 to 16 $1b/ft^3$

Thermal Conductivity

(1) Across Grain (140°F)
$$0.9 \times 10^{-5}$$
 BTU/ft-sec-°F

$$2.2 \times 10^{-5}$$
 BTU/ft-sec-°F

118

156

Specific Heat - (140°F)

0.37 BTU/1b-°F

Tensile Strength (psi)

72

Coefficient of Thermal Expansion - $in/in/^{\circ}F \times 10^{-6}$

$$\frac{6 \text{ lb/ft}^3}{180}$$
(1) Tangential 180

Shear Strength (psi)	6 lb/ft ³	<u>11 lb/ft³</u>	15.5 lb/ft ³
(1) High Strength Value	180	360	522
(2) Low Strength Value	158	298	425

Thermal Conductivity

	6 lb/ft ³	11 1b/ft ³
0°F	0.30	0.41
75°F	0.25	0.35
-100°F	0.20	0.27
-300°F	0.09	0.12

5.3.2.4.10 <u>Materials Performance Summary</u> - The low density charring ablators have been characterized either through literature data or limited laboratory testing. ESM 1004X and S-20T have successfully met or exceeded all the requirements imposed on them to date. Plate thermal cycle tests show that the ESM 1004X and S-20T material, when bonded to titanium with RTV-560 is insensitive to temperatures down to -300°F, the lower limit of the test. Ablation tests show both materials will provide fully satisfactory thermal protection under the most severe conditions anticipated for encounter in the Martian entry.

Studies show the ESM 1030-1 has a uniform structure and has good thermal properties, including endothermic behavior which is reflected in the ablation tests at lower heat fluxes. In the plate thermal cycle tests ESM 1030-1 cracked at -70°F, however this can be overcome by formulation with a phenyl-methyl silicone possessing a lower glass transition temperature than the methyl silicone used in this study. This material also exhibited poor char integrity at higher heat flux ablation tests.

The N-603 material when bonded to titanium failed at elevated temperature in the plate thermal cycle test and for this reason was not exposed to the low temperature. This coupled with a higher density has precluded it from further study.

Of the remaining materials, all of which were evaluated on the basis of literature data, Insulcork holds sufficient promise to merit further consideration. In addition, a continuous survey of low density charring ablators will be maintained to insure that other materials worthy of additional development are given full consideration for the VOYAGER application.

- 5.3.2.5 <u>Heat Shield Material Selection</u> Within the category of low density charring ablators several materials have been considered and evaluated. These materials were ranked to facilitate selection of a preferred, and one or more backup, material. To implement this ranking, an evaluation criterion system was developed and is discussed in the remainder of this section.
- 5.3.2.5.1 <u>Selection Factors</u> An overall evaluation system, including all the various processes, cycles, environments, and requirements for the thermal protection system, were distributed among the five basic selection factors, and were identified along with their relative importance. (See Figure 5.3-98). Under this evaluation system, the dominant factors are thermal efficiency, reliability, and development risk.
- 5.3.2.5.2 <u>Ground Environment</u> In the following paragraphs, each factor and the ratings are fully discussed. The rating is a relative numerical system based on 1 to 10, 10 being the best. No attempt was made to set up a system of weighting the various components under each factor since such a system would have become very cumbersome to establish, and its meaning would be questionable. (See Figure 5.3-99 for specific material ratings).

Sterilization - In general, the silicone-based materials are post-cured at temperatures higher than the sterilization temperatures and do not exhibit degradation due to sterilization. The Apollo and MPN materials are post-cured at temperatures not exceeding the sterilization temperature, and undergo additional cross-linking. This would result in increased stiffness and possible warping. For Insulcork and balsawood, there would be considerable weight loss due to loss of moisture and/or plasticizers, resulting in increased brittleness.

Decontamination - This criterion considers the ability to withstand exposure to the ethylene oxide-Freon mixture at 50°C and 50% relative humidity. There is no evidence of any effect on silicone-based materials. There would also be no effect on the materials containing low concentration of microballoons. MPN contains a large concentration of microballoons and nylon, and may be sensitive to humidity and ethylene oxide exposure. Tests have shown that Insulcork and balsawood lose strength after exposure to the decontamination cycle.

VOYAGER HEAT SHIELD - SELECTION CRITERIA WEIGHTING

GROSS CRITERIA (RECOMMENDED WEIGHTING DETAIL SELECTION CRITERIA	PROBABILITY OF MISSION SUCCESS (0.35)	SYSTEM PERFORMANCE (0.20)	DEVELOPMENT RISK (0.20)	VERSATILITY (0.15)	COST (0.10)	TOTALS (1.00)
GROUND ENVIRONMENT		0.03				0.03
SPACE ENVIRONMENT	0.06					90.0
THERMAL EFFICIENCY	0.03	0.13		0.05		0.21
THERMOSTRUCTURAL COMPATIBILITY	0.06	0.03				0.09
FABRICABILITY	0.03	0.01	0.02			0.06
RELIABILITY	0.12		90.0			0.18
ADAPTABILITY				0.06		0.06
INTERACTION WITH OTHER SUBSYSTEMS	0.05		,			0.05
COST					0.10	0.10
DEVELOPMENT RISK AND LEAD TIME			0.12	0.04		0.16

Figure 5.3-98

SPACE ENVIRONMENT

BASED ON 1 TO 10 - 10 HIGHEST

	т	Γ		г -		т				 -	1	r	
RANKING	9	5	г	1	7	2	4	က	æ	∞	9	9	2
SELECTION FACTORS COMBINED TOTAL	26	29	37	37	25	33	31	32	32	24	26	26	33
SENSITIVITY TO METEORITE DAMAGE	9	9	6	6	5	7	7	7	7	5	8	6	10
ИОТТАПДЯЯП В ЭПОС БЕРЯ В В ЭПО В В В В В В В В В В В В В В В В В В В	8	6	10	10	æ	6	8	6	6	7	7	7	7
HARD VACUUM YTIVITISMES	7	6	8	8	4	8	7	7	7	6	6	7	80
LOW TEMPERATURE SENSITIVITY	5	5	10	10	2	6	6	6	6	3	2	33	8
CANDIDATE SELECTION FACTORS	ESM 1030-1	ESM 1030-1B	ESM 1004X	ESM 1004XW	ESM 1030-1 (S)	ESM 1004X (S)	ESM 1030-2 (S)	MDC S-20T	N-603	APOLLO	MPN	INSULCORK 2755	BALSAWOOD

Figures 5.3-99

Handling and Susceptibility - This is a measure of how readily the material may be damaged after it has been applied to the structure. The unsupported silicone materials are resilient and would exhibit the least damage, the GE ESM 1030-1 having more resistance than ESM 1004X due to its higher tear strength. The split honeycomb in ESM 1030-1 (S) and ESM 1004X (S) would be somewhat more susceptible to damage. ESM 1030-2 (S) and MDC S-20T have low base material strength but good core strength; damage would tend to be localized within individual cells. N-603 has low mechanical strength and is more susceptible to damage. The Apollo material is a filled, honeycomb reinforced system which would be resistant to damage due to handling. MPN is similar but is fabricated in small shield sections with numerous seams and joints. Insulcork is resilient. Balsawood is not as resilient and would be more susceptible to damage (such as dents).

<u>Ease of Repair</u> - Two categories were considered: (a) gouges or surface damage, and (b) damage in depth.

- a. Gouges For the unsupported silicones, a plug of the material can be removed and a new plug bonded. For the honeycomb supported silicone materials, additional material can be applied and cured in place. For the rigid materials, the defect must be removed by machining and new material bonded in the space.
- b. Damage in Depth For all the systems that are soft bonded to the structure, a core is readily removed and a new plug re-inserted. With the hard bonded systems, the adhesive must be removed before a new plug is installed; a more difficult repair procedure.

Sensitivity to Mil Spec Environment (Temperature, Fungus, Humidity) and Ground Storage - In general, the silicones are not sensitive to humidity or storage temperatures and do not support fungus growth. Insulcork and balsawood are limited to specific storage temperatures and humidities. Microballoons are sensitive to moisture and temperature before encapsulation in the elastomer/resin matrix.

5.3.2.5.3 <u>Space Environment</u> - The environmental conditions to which the heat shield will be exposed and the relative ability of the material to withstand them are rated in Figure 5.3-100.

Low Temperature Sensitivity - Tests showed that ESM 1004X and S-20T in 12" x 12" panels bonded to titanium survived temperature cycling from +300°F to -300°F. ESM 1030-1 is predicted to fail at around -100°F, but in test a small crack occurred

GROUND ENVIRONMENT

BASED ON 1 TO 10 - 10 HIGHEST

RANKING		-	1	2	2	3	4	5	S.	7	S	10	&	6
SELECTION FACTORS COMBINED TOTAL		59	59	58	58	55	54	53	53	44	52	33	36	34
S ENVIR- S (TEMPERA- UNGUS,	TURE, FI Tidimuh	10	10	10	10	10	10	10	10	10	10	8	1	J.
EASE OF REPAIR	DAMAGE IN DEPTH	10	01	01	10	8	8	7	4	8	þ	8	7	9
EASE OF	GOUGES	6	6	6	6	8	8	7	10	10	10	3	7	9
GNA ƏNI. YTIJIBIT BAMAGE		10	01	6	6	6	8	6	9	5	10	8	10	9
NOITANIMA	DECONI	10	10	10	10	10	10	10	10	10	10	8	5	5
NOITAZIJ (TAJH		10	10	10	10	10	10	10	10	1	8	8	9	9
ECTION	CANDIDATE MATERIALS	ESM 1030-1	ESM 1030-1B	ESM 1004X	ESM 1004XW	ESM 1030-1 (S)	ESM 1004X (S)	ESM 1030-2 (S)	MDC S-20T	N-603	APOLLO	MPN	INSULCORK 2755	BALSAWOOD

Figure 5.3-100

at -70°F with catastrophic failure occurring at -280°F. ESM 1030-2, which is based on RTV-603, should survive low temperature exposure. The Apollo material, MPN, and Insulcork are expected to fail at temperatures higher than those predicted for ESM 1030-1.

Hard Vacuum Sensitivity - This is a measure of the amount of outgassing of the materials when exposed to hard vacuum. In general, the silicones may outgas, depending on the concentration of unreacted, low-molecular weight constituents. ESM 1030-1 loses more weight than ESM 1004X. ESM 1030-1B is post-cured at 600°F and would lose less weight than ESM 1030-1.

<u>Irradiation - Nuclear and/or Solar - Silicones are among the most resistant</u> materials to nuclear irradiation. Materials with a phenolic honeycomb support would exhibit increased sensitivity. The epoxies and phenolics would be still more sensitive to change in this environment.

Sensitivity to Meteoroid Damage - The heat shield is exposed to potential meteoroid damage for up to six hours after canister release and before entry. A dearth of data exists to evaluate this factor; however, the following judgements were based on past evaluations: (1) balsawood would be the least sensitive followed by unsupported elastomers when above their glass transition point, (2) the presence of microballoons and honeycomb would be harmful with microballoons being less sensitive than honeycomb-supported elastomers above and below their glass transition points. An unsupported elastomer below its glass transition point would be slightly better than the supported version of the same material. Rigid epoxies and phenolics would behave similarly to elastomers below their glass transition temperatures.

5.3.2.5.4 Thermal Efficiency - The thermal efficiency of the candidate materials is evaluated in Figure 5.3-101.

Overall Weight Including Bond - This includes consideration of the thermal efficiency of the heat shield material and the weight of its specific bond systems. Based on times required for a specified backface temperature rise, obtained from plasma arc ablation tests, the following ratings can be made for several silicone elastomer combinations: ESM 1004X is slightly better than S-20T and ESM 1030-1 which are all better than N-603. Under the expected mild entry conditions, the Apollo material and MPN would perform less efficiently than the silicones, Insulcork or balsawood.

THERMAL EFFICIENCY

BASED ON 1 TO 10 - 10 HIGHEST

RANKING	9	9	2	2	5	2	4	1	7	σ	۵	4	7
SELECTION FACTORS COMBINED TOTAL	37	37	45	43	38	45	39	46	37	30	31	38	37
CHAR VTIMRORINU	5	2	б	6	9	6	7	10	10	10	10	10	10
CHAR RETENTION	9	9	8	. 9	8	10	8	10	10	10	10	10	10
TRANSIENT TEMPERATURE TEMPILITY OND FOUD	&	8	8	8	8	8	8	8	8	8	8	8	8
ТНБІЗМ ЯЗЧ ОЗЯІООЗЯ АЗЯА ТІИО	6	6	10	10	8	6	8	6	5	1	2	9	5
OVER-ALL Weight including Bond	6	6	10	10	8	6	8	6	4	1	1	9	4
CANDIDATE MATERIALS FACTORS	ESM 1030-1	ESM 1030-1B	ESM 1004X	ESM 1004XW	ESM 1030-1 (S)	ESM 1004X (S)	ESM 1030-2 (S)	MDC S-20T	N-603	APOLLO	MPN	INSULCORK 2755	BALSAWOOD

Figure 5.3-101

<u>Weight Required Per Unit Area</u> - This is based on the thermal efficiency of the heat shield material for the design range of entry environments, independent of the attachment or bonding requirements.

Transient Temperature Capability of Bond - Laboratory tests show that the RTV-560 and HT-424 bond systems on titanium have adequate strength at 800°F.

<u>Char Retention</u> - For the low shear conditions expected and the internal gas pressures during charring all materials considered have demonstrated adequate char strength and retention. Materials in a honeycomb support have an added safety factor for char retention to resist spalling or external shear. Loss of the char layer during entry has a strong local influence on ablative efficiency and can cause local structural hot spots.

<u>Char Uniformity</u> - Consideration here is given to the final char as to its smoothness, cracks or crazing, shrinkage from honeycomb support, general size of surface pores, etc.

5.3.2.5.5 <u>Thermal-Structural Compatibility</u> - The compatibility of the heat protection material and the structural materials is evaluated in Figure 5.3-102.

System Integrity - This is the overall sensitivity of the system to the complete range of environments. The large panel cycle tests indicated a honeycomb node bond separation for the higher modulus S-20 ablator at -195°F. Although the lower modulus S-20T was not tested in a large panel, no failures occurred on a 12" x 12" panel at -300°F. The presence of honeycomb would be expected to reduce the capability of those systems to the low temperature thermal cycle range, but increase the material capability at the high temperature (ablation) range.

Compatibility with Structure Surface - This means the ability of the materials to conform completely to the surface or to surface imperfections of the structure material. The unsupported elastomeric materials would conform best since they are very flexible sheets of foam rubber. The presence of honeycomb reduces conformity of the system to an uneven surface. The rigid materials which would not conform to an uneven surface would require additional adhesive to fill in the valleys of the structural surface.

Compatibility with Sturcture Materials - Under this category, the thermal expansion of the material is considered in comparison with that of the structure. Also, bond compatibility is evaluated over the entire temperature range. The best performance would be given by the candidate low modulas elastomers soft bonded. These

THERMOSTRUCTURAL COMPATIBILITY

BASED ON 1 TO 10 - 10 HIGHEST

RANKING	4	7	1	1	9	2	5	က	10	8	11	7	6
SELECTION FACTORS COMBINED TOTAL	37	37	48	48	34	44	36	43	21	31	16	33	24
JOINTS, GAPS, INCLUSIONS	6	6	6	6	8	8	8	10	8	10	4	8	9
FLIGHT (MECH.) STATIC AND DYNAMIC ENVIRONMENTS	6	6	10	10	8	6	6	8	6	8	8	8	8
YTIJIBILITY WITH SYNCTURE JAIRJTAM	r.	5	10	10	5	10	6	8	1	3	2	5	9
COMPATIBILITY WITH STRUCTURE STRUCTURE SURPACE	6	6	6	6	8	8	3	8	2	8	1	8	1
SYSTEM INTEGRITY	5	5	10	10	5	6	7	6	1	2	1	4	3
CANDIDATE SELECTION FACTORS FACTORS	ESM 1030-1	ESM 1030-1B	ESM 1004X	ESM 1004XW	ESM 1030-1 (S)	ESM 1004X (S)	ESM 1030-2 (S)	MDC S-20T	N-603	APOLLO	MPN	INSULCORK 2755	BALSAWOOD

Figure 5.3-102

would be followed by the higher modulus elastomers soft bonded. Next would be the non-flexible elastomers which are hard bonded. The ESM 1030 materials are given a low rating at this time because the current formulations would be below their glass transition temperatures during cruise flight conditions.

Flight (Mechanical) Static and Dynamic Environments - This category considers vibrations and acceleration during powered flight, as well as vibration in mid-flight due to course changes, orbit injection, or de-orbit maneuvers. Room temperature vibration tests showed no significant difference in energy abosrbing characteristics of either the supported or unsupported silicone materials. Vibration during the cold cruise environment require additional consideration.

<u>Joints, Gaps, Inclusions</u> - This is a measure of the adaptability, number of separate panels, and ease of sealing joints, gaps, and inclusions. In this respect the S-20T and the Apollo materials would be best because the heat shield is fabricated as one continuous sheet. The unsupported elastomeric materials would be next. MPN is rated low because it must be manufactured in a large number of relatively small sections.

5.3.2.5.6 <u>Fabricability</u> - Ease of fabricability and of handling are examined in Figure 5.3-103.

Handling - This category covers the handling of the heat shield material before and during bonding. The S-20T and the Apollo materials require minimal handling since they are prepared in place. The MPN, Insulcork and balsawood are easy to handle because they are self-supporting. The continuous honeycomb supported elastomeric materials. ESM 1004X has a slightly lower tear resistance than ESM 1030-1. Incorporation of split honeycomb into these materials reduces their strength.

Repairs (Ease and Frequency) - Insulcork and the unsupported elastomers can be repaired with pre-quality controlled materials and bond thickness can be controlled. Elastomers in honeycomb support are more difficult to repair due to the presence of the honeycomb. The continuous honeycomb that is filled prior to bonding, can be repaired more readily than the continuous honeycomb that is pre-bonded to the structure. MPN sections would be difficult to remove and replace.

Special Machining Requirements - The unsupported elastomers require the least special machining. The elastomers in continuous honeycomb are second. The Apollo material and Insulcork also require a minimum of special machining requirements. The split honeycomb is the additional requirement of honeycomb splitting prior to filling with ablator. Balsawood must be machined to conform to the vehicle shape.

		,			r									
знеѕт	RANKING	1	1	2	2	5	4	3	9	10	4	6	2	8
BASED ON 1 TO 10 - 10 HIGHEST	SELECTION FACTORS COMBINED TOTAL	97	97	95	95	98	84	92	85	29	88	75	95	9/
SED (FACILITIES				bəii	itnəbi	rrently	uo səif	ilioe† l	specia	ON			
ВА	КЕГИВВІЗНМЕИТ	10	10	10	10	6	6	80	5	80	9	9	7	9
	FLEXIBILITY IN FABRICATION CYCLE	6	6	6	6	6	6	6	7	8	7	10	10	10
	STORAGE REQUIREMENTS FOR RAW MATERIALS	10	10	8	8	10	8	10	6	6	6	6	8	80
	JOINTS, GAPS, INCLUSIONS	6	6	6	6	9	6	9	8	6	8	5	8	9
	JAINJEN WAR YTIJIBAJIAVA					sm o ti	stock	urrentl)	rials cı	ətem l	ΙĄ			
-	EASE OF FABRICATION	8	8	80	8	9	9	7	9	4	5	5	10	9
	SPECIAL PROCESSING (SUBSTRATE, H/C, ETC.)	10	10	10	10	6	8	6	7	8	6	2	10	10
	TOLERANCE CONTROL	9.	9	9	9	7	7	7	10	3	10	6	6	&
	20AASAH	6	6	10	10	6	10	6	10	10	6	8	5	5
	SPECIAL MACHINING REQUIREMENTS	10	10	10	10	5	2	6	8	5	10	7	10	4
	REPAIRS (EASE AND FREQUENCY)	8	8	∞	∞	7	7	9	5	2	5	1	8	8
	HANDLING	8	ж ж	7	7	9	9	6	10	1	10	10	10	10
	CANDIDATE SELECTION FACTORS FACTORS	ESM 1030-1	ESM 1030-1B	ESM 1004X	ESM 1004XW	ESM 1030-1 (S)	ESM 1004X (S)	ESM 1030-2 (S)	MDC S-20T	N-603	APOLLO	MPN	INSULCORK 2755	BALSAWOOD
						<u> </u>		L	_					

Figure 5.3-103

<u>Hazards</u> - There are no hazards associated with the use of RTV silicone materials. The ESM 1030 materials which are <u>amine</u>-cured epoxies can present a dermatitis hazard.

Tolerance Control - The closest tolerance can be obtained with those configurations in which the honeycomb support is pre-bonded to the structure prior to being filled with the ablative shield materials. These include S-20T and the Apollo material. MPN and Insulcork would give the next best tolerances. This would be followed by balsawood. The supported elastomers would be next, followed by the unsupported elastomers. Poorest tolerance control would be exhibited by the rigid types that are soft bonded.

Special Processing - This category includes any processing required for substrate preparation, honeycomb preparation, etc. The least requirements are necessary for the unsupported elastomers, Insulcork and balsawood. Next in order would be the Apollo material, and then supported ESM 1030 materials. This is due to the fact that the epoxy in the heat shield formulation eliminates the necessity for priming of the honeycomb to obtain good adhesion. The supported silicones require honeycomb priming. MPN is given a low rating because of the special pressure molding equipment required in its manufacturing.

<u>Ease of Fabrication</u> - Insulcork is rated highest because it is purchased in the thicknesses required. The unsupported elastomers are given the next rating. The remainder of the materials require more steps and operations, thus complicating their fabrication.

Raw Material Availability - All raw materials are currently stock items.

<u>Joints, Gaps, Inclusions</u> - This category represents the ease with which these can be made. The soft bonded silicone materials are given the highest rating followed by the S-20T and Apollo. This is due to the use of the base elastomer in sealing these discontinuities versus honeycomb alignment prior to filling.

Storage Requirements for Raw Materials - No special requirements are necessary for the ESM 1030 materials. The base elastomer for the ESM 1004X material and the HT-424 adhesive must be refrigerated. Those materials which contain microballoons are rated lower because the microballoons are sensitive to moisture and temperature. Insulcork and balsawood are also sensitive to temperature and moisture.

Flexibility in Fabrication Cycle - No problems would be expected with MPN Insulcork and balsawood. The ESM materials are manufactured in sheets and do not have to be applied to the structure within any specified time limit. However, the ESM bonding operations with catalyzed RTV is time limited.

Refurbishment - The unsupported soft bonded materials are the easiest to refurbish. Next would be the soft bonded split honeycomb supported materials. The hard bonded systems and especially the honeycomb support hard bonded systems would be the most difficult to refurbish.

<u>Facilities</u> - No special facilities are currently identified.

5.3.2.5.7 <u>Reliability</u> - The reliability aspects of materials and of the shield itself are considered in detail in Figure 5.3-104.

Reproducibility and Uniformity - The Apollo material, MPN, and N-603 are rated high because they are uniform mixes. In bond thickness control, HT-424 is better than RTV-560; hence, Insulcork is rated high. The S-20T material which is foamed in place can lead to some density variations from cell to cell. The unsupported elastomers are more uniform but the bond thickness is not as uniform as with HT-424 film adhesive. The soft bonded supported ESM's are rated the lowest because of both bond variations and possible shield material variations.

Shield Quality Control - Quality control is easiest for the unsupported elastomers MPN, and Insulcork since they can be tested and examined before application. Next are the soft bonded supported elastomers and balsawood, since they are less uniform.

Bond Quality Control - The easiest bond to qualify control is HT-424 where the honeycomb support is pre-bonded to the structure as is the case of S-20T and Apollo material. The hard bond for MPN would be next. Methods for detecting soft bond voids and delaminations are under development.

Raw Materials Quality Control - MPN and Insulcork are purchased materials and would be the easiest to qualify control. The difficulty of quality control increases as the number of raw materials required in the manufacturing of the heat shield increases.

<u>Ground Storage Life</u> - No problems are anticipated for the silicone based materials. Balsawood would be poorest in this respect, since they are nutrients for fungus.

?ELIA3ILITY 。

HIGHENT	
+	
ਟ	
王	
Ξ	
Ξ	
1	
S)
BASED	
a	

ı			0			,					· · · · · · ·				
	RANKING		9	5	1	1	8	4	9	2	5	8	5	7	6
10 - 10 HIGHES 1	SELECTION	COMBINED	72	72	08	80	991	73	72	77	72	92	72	89	61
CASE ON 1 10 10 - 10 HIGHEST	RONMENT 31LITY	ENTRY	ç	S.	80	88	9	6	6	10	6	6	9	9	8
	FLIGHT ENVIRONMENT SUSCEPTIBILITY	TRANSIT	9	7	10	10	9	10	6	6	- ∞	9	9	5	80
	NOITAZIJ YTIJI8IT9		10	91	10	10	10	10	10	10	10	01	80	5	2
	COMPLEXITY	DE2ICN (6	ნ	6	6	∞	∞	7	6	7	6	5	92	7
	GE LIFE		10	10	10	10	10	10	10	10	8	&	∞	22	2
	тевіясь ос	AM WAЯ	9	9	7	7	5	5	5	4	9	9	10	10	&
	ир бс	108	7	7	7	7	9	9	9	10	9	10	6	7	7
	об ос	2HIE	10	10	10	10	6	6	6	8	8	8	10	10	6
	-ORMITY	108938 11 N U	8	8	8	8	9	9	9	7	10	10	10	10	4
	ECTION CTORS	CANDIDATE MATERIALS	ESM 1030-1	ESM 1030-1B	ESM 1004X	ESM 1004XW	ESM 1030-1 (S)	ESM 1004X (S)	ESM 1030-2 (S)	MDC S-20T	N-603	APOLLO	MPN	INSULCORK 2755	BALSAWOOD

Figure 5.3-104

<u>Design Complexity</u> - The best in this respect is Insulcork followed by the hard bonded supported systems and the soft bonded unsupported systems. MPN rates lowest because of the large number of sections required in its application.

Sterilization Susceptibility - Any sensitivity to sterilization, though accountable, will decrease reliability. No problems are expected with the silicone materials or the epoxies. However, MPN would be affected, and Insulcork and balsawood are more severely affected, which makes the thermal performance and reliability of these materials more uncertain after the sterilization exposure.

Flight Environment Susceptibility - This criterion is broken into the two major flight modes: transit and entry. In the former, any degradation, e.g., outgassing, low temperature formation of cracks, etc., will make the material somewhat less reliable. In entry, materials are less reliable if char stability is low or if an exothermic reaction takes place. In the former, the ESM 1004X materials are rated highest because of their better performance to the overall space requirements whereas the ESM 1030-1 or Apollo materials are quite low due to low temperature sensitivity. In the latter, the honeycomb supported elastomers exhibit better control of surface shrinkage and char retention, therefore, they are rated higher than the fiber reinforced elastomers.

5.3.2.5.8 Adaptability - The ability to adapt to change conditions or inputs is desirable in a material. The versatility of these materials discussed in Figure 5.3-105.

Design Requirement Changes - This considers the ability to meet any changes that might be required in the overall design such as added inclusions, change of substrate, addition of coating, etc. The ESM materials, both unsupported and in split honeycomb configurations, the S-20T, the Apollo material, and Insulcork would be among the easiest to meet design changes. MPN, because of the large number of pieces required, and also the necessity for preforming the materials in molds would be the least adaptable to a design change.

Flight Environment Changes - This is the ability to meet any changes that might be induced to increase or decrease the length of the flight, the time in orbit, and entry conditions or atmospheric definition. In this respect, an increase in severity of entry conditions would be more probable. Consequently, the S-20T, the ESM 1004X (S), N-603, Apollo, MPN and Insulcork which have better char integrity, would be more successful in meeting new environments than the fiber reinforced materials, balsawood or ESM 1030.

BASED ON 1 TO 10 - 10 HIGHEST

RANKING	8	9	1	2	7	2	6	2	4	3	8	5	8
SELECTION FACTORS COMBINED TOTAL	47	49	26	55	48	55	46	55	52	53	47	51	47
СНРИ СЕ ЕВ ІМЕ ПТ	7	8	æ	6	7	7	7	7		6	8	7	9
EXTENDED YELL THE CAPABILITY	8	8	10	10	4	6	6	6	6	7	1	1	6
RTG NOITDARETHION	8	6	10	10	8	6	80	6	6	7	7	7	7
екомтн	7	7	6	8	8	10	7	10	10	10	10	10	6
FLIGHT ENVIRONMENT CHANGES	7	7	6	80	∞ .	10	7	10	10	10	10	10	6
CHANGES REQUIREMENT DESIGN	10	10	10	10	10	10	æ	10	9	10	5	10	7
CANDIDATE SELECTION SELECTION FACTORS	ESM 1030-1	ESM 1030-1B	ESM 1004X	ESM 1004XW	ESM 1030-1 (S)	ESM 1004X (S)	ESM 1030-2 (S)	MDC S-20T	N-603	APOLLO	MPN	INSULCORK 2755	BALSAWOOD

5.3-105

<u>Growth</u> - The ability to meet an increase in the ballistic parameter as time progresses or be applicable for later missions is considered.

<u>RTG Integration</u> - Late missions requiring longer life on the planet surface will incorporate nuclear power sources; therefore, the ability of the materials to accommodate radiation is a factor in the material's versatility.

Extended Mission Capability - Here, longer times in transit and in orbit must be considered with the resultant increased sensitivity to the space environment. Most likely to meet this requirement is the ESM 1004X, S-20T, ESM 1004X (S), ESM 1030-2 (S) and the N-603, as well as balsawood.

Experiment Changes - Changes in the experiments could be influenced by out-gassing products, ablation products, and perhaps RF transmissibility of the material. Therefore, the elemental constituents, amount of gasification, and the degree of RF transmissibility have been considered in this ranking.

5.3.2.5.9 <u>Interaction with Other Subsystems</u> - Interactions such as outgassing and ablation constraint selections. The degree of constraint is given in Figure 5.3-106.

<u>Communications</u> - The Apollo and MPN materials are given the highest ratings in this category, and the ESM 1004X is given one of the lowest ratings because of the presence of calcium in the material which would enhance wake ionization levels and aggravate communication problems. Insulcork and balsawood are also rated low because of the high carbon content present in the chars, plus uncontrolled amounts of alkali metals in these natural materials.

Ablation Products - This considers product deposition on windows, radar interference, etc. The ratings is this category are generally fairly equal with the ESM 1030 materials and S-20T being rated the best.

<u>Vacuum Outgassing</u> - The least outgassing would be encountered from the Apollo material, MPN, Insulcork and balsawood. Test results indicated the most outgassing would be expected from silicon-based materials, both supported and unsupported.

Entry Experiments - This considers the effect that the heat shield could have in interfering with various gas sampling entry experiments. Here the Apollo and MPN would be expected to have the least interference followed by Insulcork and balsawood. All the silicone-based materials have been given equal ratings, lowest because their chemical state varies with entry conditions.

INTERACTION WITH OTHER SUBSYSTEMS

BASED ON 1 TO 10 - 10 HIGHEST	RANKING	4	2	4	9	4	4	5	4	3	1	1	3	3
	SELECTION FACTORS COMBINED TOTAL	26	28	26	23	26	26	25	26	27	32	32	27	27
INTERACTION WITH OTHER SUBSYSTEMS	ENTRY EXPERIMENTS	9	9	9	9	9	9	9	9	9	8	8	7	7
TION WITH OTH	MUUDAV ƏNISSAƏTUO	9	7	9	9	9	9	9 .	9	8	6	6	6	6
INTERAC	ABLATION 2TJUQOЯЧ	8	8	7	7	8	7	8	8	7	7	. 7	7	7
	COMMUNICATIONS	9	7	7	4	9	7	5	9	9	80	8	4	4
	CANDIDATE MATERIALS	ESM 1030-1	ESM 1030-1B	ESM 1004X	ESM 1004XW	ESM 1030-1 (S)	ESM 1004X (S)	ESM 1030-2 (S)	MDC S-20T	N-603	APOLLO	MPN	INSULCORK 2755	BALSAWOOD

Figure 5.3-106

5.3.2.5.10 <u>Cost</u> - Cost of facilities and of direct fabrication operations is given in Figure 5.3-107.

Special Equipment Requirements - The most favorable materials in this respect are the S-20T, Apollo, Insulcork and balsawood followed by the unsupported silicone epoxy materials and the supported silicone epoxy materials. Next would be the ESM 1004X type materials, both supported and unsupported, which require a simple vacuum chamber in their fabrication. The most disadvantageous in this respect is the MPN material, because it requires a molding operation in its fabrication.

<u>East of Fabrication</u> - Here the advantage is given to Insulcork since it is a stock item. The unsupported ESM 1004Y and ESM 1030-1 are easier to fabricate than similar supported materials. The poorest in this respect is the Apollo material, since each cell must be individually filled.

<u>Development Tests and Analyses</u> - Materials like the Apollo material have undergone extensive development work, thus rank highest, whereas the very low density silicones, in an earlier stage of development, and never having been flown, require a greater amount of evaluation.

Storage and Special Treatments - Those materials requiring special storage (e.g., refrigeration, etc.) or special treatments (e.g., honeycomb priming, slitting, etc.) will rank lower relative to cost as the number of processes increase. The ESM materials rank highest since they require neither special storage or honeycomb preparation (slitting excepted).

5.3.2.5.11 <u>Development Risk and Lead Time</u> - The risk attached to development and time required to complete design is rated in Figure 5.3-108.

Equipment Requirements - In preparing materials for fabrication, limitations in handling with existing equipment will increase the development risk. Past and present usage of materials like the Apollo material minimize this type risk with these materials. The next best are those systems which are very similar to past systems (S-20T), followed by materials like ESM 1030-2 which is a newly developed system.

Raw Material Availability - All raw materials are currently stock items.

Extent of Test Data Available - For the Apollo, MPN, Insulcork, and balsawood there is a considerable amount of data available in literature. During the Phase B study, a considerable amount of testing at discrete points provided a similar amount of data for all materials considered in this evaluation.

<u>Data Requirements for Design</u> - In this category, the Apollo material will require less additional characterization to define performance at the VOYAGER entry

BASED ON 1 TO 10 - 10 HIGHEST

CANDIDATE MATERIALS	SELECTION FACTORS	SPECIAL EQUIPMENT REQUIREMENTS	EASE OF FABRICATION	DEVELOPMENT TESTS AND ANAL YSES	STORAGE AND SPECIAL TREATMENTS	SELECTION FACTORS Combined Total	RANKING
ESM 1030-1		8	8	6	10	32	2
ESM 1030-1B		8	8	6	10	32	2
ESM 1004X		7	8	6	8	29	5
ESM 1004XW		7	8	6	8	29	5
ESM 1030-1 (S)		8	7	5	10	30	4
ESM 1004X (\$)		7	7	4	8	26	7
ESM 1030-2 (S)		8	7	6	10	31	3
MDC S-20T	-	9	4	6	9	28	6
N-603		5	3	2	9	19	9
APOLLO	-	9	1	10	9	29	5
MPN		2	6	8	9	25	8
INSUL CORK 2755		9	10	10	9	38	1
BALSAWOOD		9	6	8	9	32	2

DEVELOPMENT RISK & LEAD TIME

Figure 5.3-107

BASED	ON	1 TC	10 -	10	HIGHEST
-------	----	------	------	----	---------

								BASED ON 1 10 1	
z	AENTS	ERIAL	OF TEST AILABLE	DATA REQUIREMENTS FOR DESIGN	FLIGHT EXPERIENCE OF SIMILAR SYSTEMS		CTURING NCE WITH SYSTEM	SELECTION FACTORS COMBINED	RANKING
CANDIDATE SELECTION FACTORS	EQUIPMENT REQUIREMENTS	RAW MATERIAL AVAILABILITY	EXTENT OF TEST DATA AVAILABLE	DATA RE(FOR DESI	FLIGHT E OF SIMIL	SHIELD	BOND	TOTAL	
ESM 1030-1	9	10	10	5	5	9	10	58	3
ESM 1030-1B	8.	10	6	5	5	9	10	53	6
ESM 1004X	8	10	10	6	7	10	10	61	1
ESM 1004XW	8	10	3	5	7	10	10	53	6
ESM 1030-1 (S)	8	10	3	4	5	9	10	49	8
ESM 1004X (S)	8	10	5	5	7	10	10	55	5
ESM 1030-2(S)	7	10	8	4	5	9	10	53	6
MDC S-20T	9	10	10	5	7	10	10	61	1
N-603	9	10	6	1	3	1	10	40	9
APOLLO	10	10	9	8	8	1	10	56	4
MPN	8	10	9	8	3	2	10	50	7
INSUL CORK 2755	9	9	9	7	9	8	10	61	1
BALSAWOOD	10	9	9	6	9	6	10	59	2

Figure 5.3-108

environment. The difference in ratings in the remaining materials reflects the amount of currently available data directly applicable to VOYAGER.

Flight Experience of Similar Systems - In this category flight experience available in the country would be utilized. In this respect, there would be most experience for Insulcork and balsawood. This would be followed by the Apollo type material, then the S-20T and ESM 1004X type materials, both supported and unsupported. This arises from the fact that higher density materials similar to ESM 1004X have been flown in the past, and the S-20T material is similar to the more dense material that was flown on the Gemini missions.

Manufacturing Experience with Similar Systems - Two categories are considered:

1) shield, and 2) bond. In both categories, we will be concerned only with

McDonnell and General Electric experience. Considering the shield, experience

with the ESM 1004X type materials is available, both supported and unsupported,

as well as with the S-20T type material. We have, as a team, least experience with

N-603, the Apollo type material, and MPN. There is considerable experience or

related experience with ESM 1030 type materials and Insulcork. For the bond, there

would be considerable team experience split equally between the soft and pre
bonded type systems.

5.3.2.5.12 Overall Rating - Coupling the ratings for each factor with the weighting factors in Figure 5.3-98 yields the overall ratings shown in Figure 5.3-109. be seen from this figure that the numerical spread between the materials is only about 21% based on the total points available. Considering all features of the low density ablators evaluated, each is applicable to the mission in varying degrees of acceptability. In general, the fiber-reinforced silicone elastomers soft bonded to the Aeroshell structure are most applicable, followed by the honeycomb supported silicone elastomers. The one major exception to this is the N-603material. The major experience with this material was in a panel application technique to a large titanium structure in which the inherent weakness resulted in damage to the shield panels and its stiffness precluded compatibility with the wavy substrate. Converting to filling a pre-bonded honeycomb could easily circumvent this problem, making the N-603 material more attractive. However, the material is a syntatic foam, and its inherently higher density and higher modulus will still make it rank low when compared to chemically blown foams. Another interesting feature of the trade off is the high rating of Insulcork. There are several features of this material that make it more attractive than expected. result is not imcompatible with the results of previous studies by other companies.

Figure 5.3-109

Based on the overall results of the study and the ratings in Figure 5.3-109, it is recommended that the fiber reinforced silicone elastomer, GE ESM 1004X, soft bonded with RTV-560 to the Aeroshell structure be the preferred Phase B heat shield material. The recommended backup is the McDonnell S-20T material, a chemically blown silicone elastomer in phenolic glass honeycomb that is pre-bonded to the Aeroshell structure with HT-424 adhesive. The selection of these two different types of heat shield fabrication and attachment methods guarantees having an efficient and reliable heat shield subsystem available on schedule.

5.3.2.6 Ablation Material Design Thickness - The ablative thickness and weight distribution over the conical Aeroshell surface was determined for the selected heat protection materials to satisfy the defined entry heating environment and extreme design trajectory conditions. The arc plasma thermal performance data, defining the overall ablative behavior of the selected low density silicone elastomeric materials, were correlated with computer programs using the thermal-physical data obtained from material property tests. These computer programs analytically describe the ablation material decomposition during exposure to the entry heating environment, and have been calibrated for the selected baseline ablator GE ESM-1004X, and the backup MDC S-20T ablator. Calibration was accomplished by selecting ablative material properties that provide computer temperature predictions which closely match measured arc plasma test temperatures, char depths, and surface recession if any occurs. Valid calibration of the computer program was completed for the span of test heating rate, pressure, and gas enthalpy combinations. program was then available to predict reliably the required ablative thickness that must protect the Aeroshell structure for the most severe design trajectory. 5.3.2.6.1 Thermal Analysis of a Charring Ablator - The thermal response of the heat shield material was calculated using the Reaction Kinetics Ablation Program (REKAP). The convective and radiative heating are provided as inputs to the program along with the material and char properties. This program calculates the transient temperature response of the shield material, including the energy and mass transfer due to material degradation (charring) and gaseous injection into the boundary layer. Chemical reactions in the boundary layer are evaluated using the Ablating Boundary Layer Equilibrium program (ABLE). This computer program for the chemically reacting laminar and turbulent boundary layers calculates heat and mass transfer to the surface of a body subjected to entry heating. The results from this program are provided to the REKAP program for the subsequent transient analysis. A summary is provided in Figure 5.3-61, of the REKAP mathematical model.

Since for most materials all of the required input parameters are not known over the entire range of temperatures and pressures occurring in flight, it is usually necessary to determine some of the parameters by correlating the results of ground and flight tests. When this is completed, a theoretical prediction of the rate of growth of the char layer with time, the variation of the surface and interface temperatures with time, and the removal of the char layer can be made.

5.3.2.6.2 <u>Calibration of Reaction Kinetics Ablation Program</u> - A preliminary calibration of REKAP models was performed for development of models of the ESM 1030-1B and ESM 1004X materials, based on the lower heat flux data obtained at 7 Btu/ft²-sec in the GE facility. This condition is a closer simulation of the heat fluxes expected during entry along the design trajectory. The validity of these models for the lower heat flux condition of the GE tests is indicated in Figures 5.3-110 and -111. The REKAP prediction is within 100°R of most of the measured data. Thermophysical property values used for these two computer models are given in Figure 5.3-112.

The general method for calibrating the REKAP models involves a series of trial and error attempts to predict the measured temperatures. The known thermal conductivity and specific heat of the virgin material, the emissivity of the char, and the Arrhenius constants for the degradation process are initially fixed in the model. Since values of the semi-charred or fully charred conductivities and specific heat are not available, the value of these parameters must be obtained from the best fit between measured and predicted temperatures. In addition to these values, there is also some latitude in the choice of the heat of decomposition and the specific heat of the evolving gases.

A similar approach was followed by MDC to calibrate their (T-687) General Charring Ablation Program model for the S-20T material. Since both the ESM 1004X and S-20T showed similar temperature response in the GE and MDC plasma jet tests, the analyses and performance is interchangeable for these two materials. The remaining discussion will pertain to the ESM 1004X material unless otherwise noted.

After calibrating these REKAP models for the low heat flux data they were used to predict the temperature response of the higher heat flux data obtained in the McDonnell Plasmajet (12 Btu/ft 2 -sec) and GE Hyperthermal Arc (24 Btu/ft 2 -sec).

The predicted temperatures for the high heat flux GE tests were in general lower than the corresponding measured data. Further investigation indicated that the net heat flux to the surface was higher than expected. Boundary layer combustion of the ablation products was shown in our preliminary studies to be a possible factor in increasing the heating rate. True assessment of this phenomena must wait till adequate thermodynamic and transport properties are available for proper boundary layer analysis.

COMPARISON OF PREDICTED TO MEASURED TEMPERATURE RESPONSE

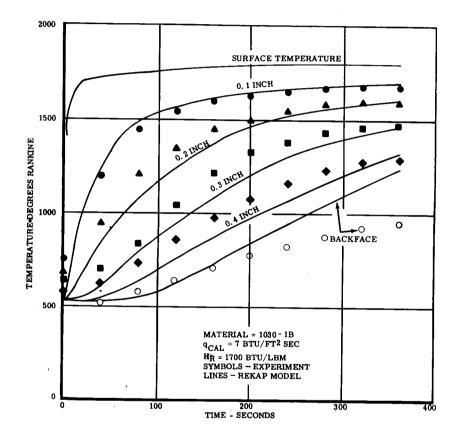


Figure 5.3-110

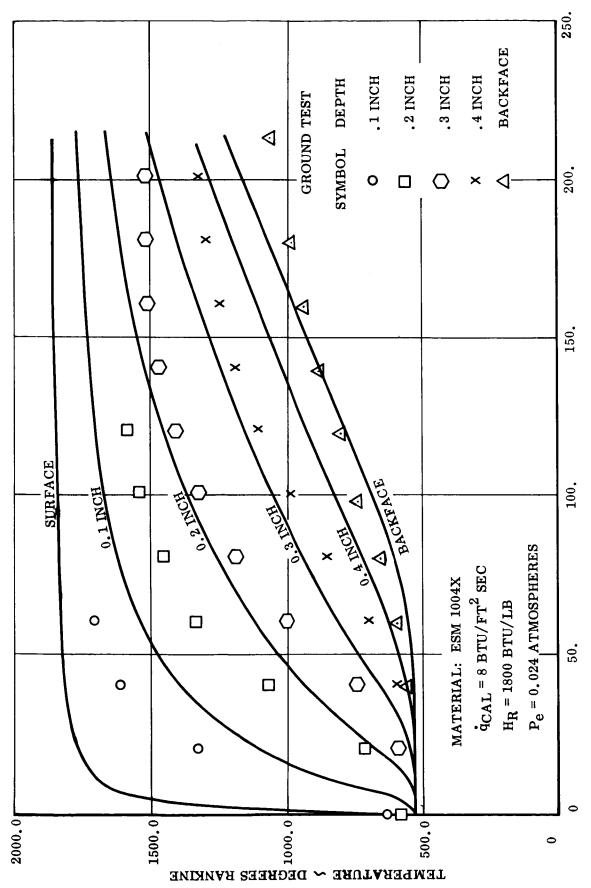


Figure 5.3-111 5.3-198

TIME ~ SECONDS

THERMOPHYSICAL PROPERTIES EMPLOYED IN REKAP

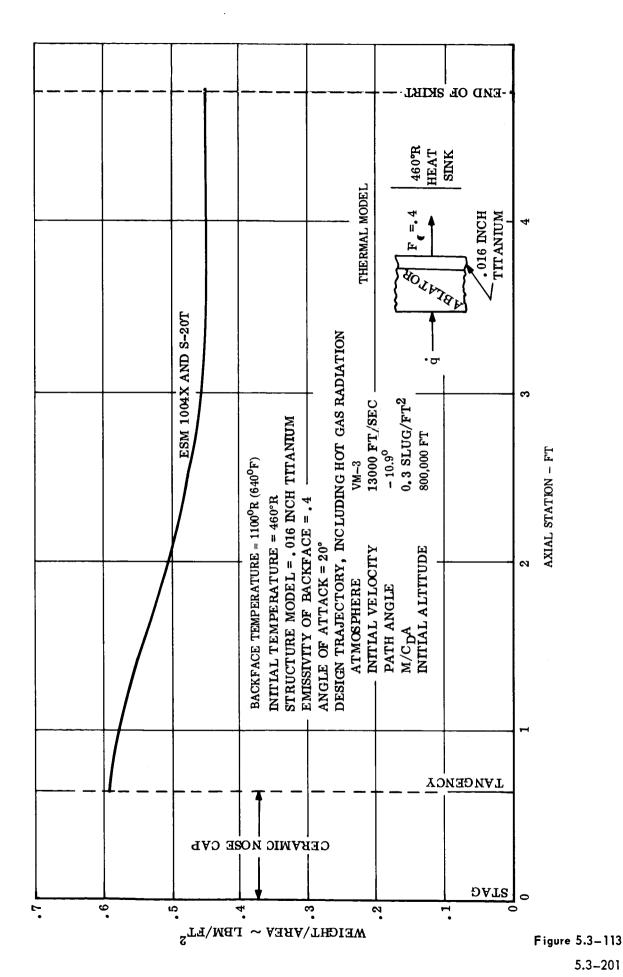
			ESM-1004 X	ESM-1030-1B
Virgin Density, $P_{\rm V}$ lb/ft 3			16.6	16
Char Density, ρ_c lb/ft 3			6.7	4.8
Pyrolysis Gas Specific Heat, C _{pg} BTU/lb°R			0.7	0.7
Molecular Weight of Injected Species, Mg			24.5	24.5
Order of Reaction			2	2
Pre-exponential Factor, Z Sec ⁻¹			15000	30000
Activation Energy, Δ E BTU/Ib mole			44700	44700
Heat of Decomposition, Hgf BTU/Ib Gas Generated			0	1000
Specific Heat, Cp BTU/	b°R	600 °R 710 1210 2075	0.310 0.330 0.440 0.440	0.310 0.360 0.440 0.440
Conductivity, k BTU/ft-sec°R	Virgin,	610 °R 860 1335 1710	.0000115 .0000170 .0000220 .0000260	.000110 .000120 .000145 .000165
	Char,	1335 1710 2210	.0002200 .0000740 .0000850 .0001000	.0000740 .0000850 .0001000

Figure 5.3-112

Assessment of the difference between the REKAP prediction and the MDC data is somewhat more difficult since the data used to calibrate the REKAP model and the MDC data were obtained at different test conditions and in different facilities. A review of the data and test conditions led to the belief that the difference is real and attributable to the difference in test pressure. In evaluating the material properties it was found that the thermal conductivity of these low density formulations is quite sensitive to the local pressure. From these measurements it was determined that the conductivity is 1.13×10^{-5} and 0.86×10^{-5} Btu/ft-sec-°F for the GE and MDC arc test pressures of 0.026 and 0.0004 atmospheres, respectively. By assuming that only the conductivity is pressure sensitive, it was found that the REKAP prediction and the lower pressure MDC data came into reasonable agreement. Based on experience in this program the pressure effect is very real and must be considered. To account for this in the past, analytical low density material perfformance models were capable of considering thermal conductivity as a function of both temperature, pressure, and material density in order to have a fully realistic assessment of the heat shield performance. In the present study, heat shield weights are based on the aforementioned REKAP model. This is felt to be realistic since the test pressure and heat flux for the data used to calibrate the model is approximately a mean value of the entry condition.

5.3.2.6.3 Shield Thickness Requirements - It has been demonstrated in Section 5.3.2.2, that the maximum heat shield thickness requirement is dictated by the shallowest path angle graze entry. Utilizing the heat flux history distribution for the design trajectory, Section 5.3.2.2, assuming that none of the incident radiation is blocked by the products of decomposition in the boundary layer, the design heat shield distribution presented in Figure 5.3-113 was determined. These heat shield thickness requirements are based on a 640°F backface temperature with an initial temperature at entry of 0°F. The thermal mass of the back structure was simulated by including a 16 mils titanium layer with an inside surface emissivity of 0.4 radiating to a 0°F sink. Based on these considerations the structural temperature response was computed for the three critical trajectories. The results shown in Figure 5.3-69 confirm the selection of the design trajectory for thermally sizing the heat shield, in that the backface temperature is less for the other trajectories.

Time histories of the typical thermal energy accommodation modes are illustrated in Figure 5.3-114. Note that the predominate heat protection mode is surface reradiation with blockage of the convective flux by mass injection also providing some relief. Local mass addition rates for the thermal design case are illustrated in



REPORT F694 • VOLUME II • PART B • 31 AUGUST 1967

THERMAL ENERGY ACCOMMODATION DURING ENTRY

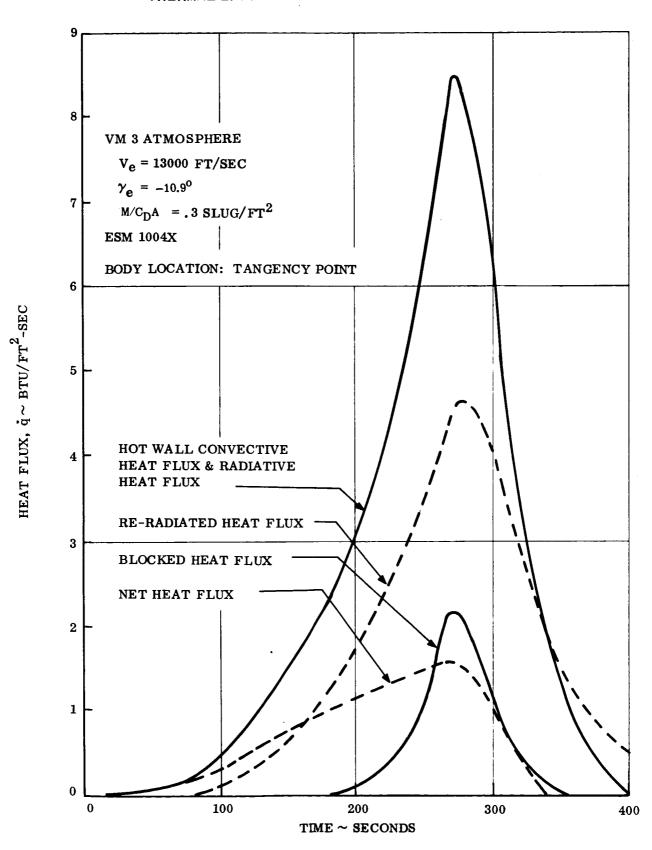


Figure 5.3-114

5.3-202

Figure 5.3-115, and time integrated values in Figure 5.3-116. These figures give an indication of the amount of ablative products that could possibly deposit or interfere with the TV window transmission if the Aeroshell nosecape had ablative heat protection rather than the selected non-ablative low density ceramic material.

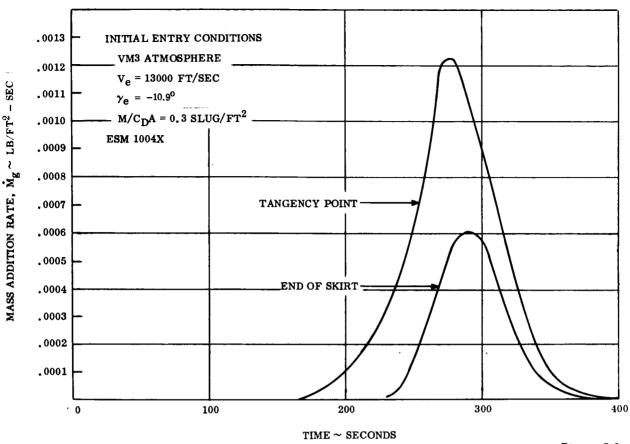
No evidence exists that suggests that the equilibrium convective heating is increased at the corner of a vehicle such as the VOYAGER Capsule. However, it is prosed that the shield thickness on the skirt be continued over the corner. Since the convective heating at the rear of the capsule is extremely small (as discussed in Section 5.3.2.2.5) and the resultant temperature rise is only 520°F, an ablating material is not necessary, and a high emissivity coated tape on the aft structural ring would be adequate protection. Over the remainder of the base a thermal curtain is utilized to protect the backface of the Aeroshell structure, ESP and SLS from the base entry heating, the de-orbit motor rocket plume, and percent excessive cooling during the orbital descent period. Considering the low magnitude of this heat pulse, a fiberglass cloth was selected that has the inner surface facing the Aeroshell covered with a low emissivity gold coating. This material conforms to the required contours and has sufficiently high temperature capability to be compatible with the VOYAGER environment.

5.3.2.6.4 <u>Thermo-Mechanical Performance</u> - Preliminary thermal stress analyses were performed on two of the candidate heat shields, in the cold soak and entry environments. A zero stress state in the shield/bond system exists at the bond curing temperature, +256°F, thus, no thermal stress problems exist for this enironment. The shield materials considered were ESM 1004X with an RTV-560 bond and ESM 1030-1 with an RTV-611 bond. Titanium, magnesism, aluminum, beryllium and fiberglass substrates were investigated.

For the cold soak, -150°F, evaluation, the stresses in the bond, regardless of thickness, are much less than allowables, and the ESM 1004X is not predicted to crack.

A preliminary entry analyses, using temperature gradients for a shallow VM-3 entry at 240,000 feet (representative of the maximum heating conditions), showed thermal stress in the ablator to be negligible.

MASS ADDITION RATE HISTORY



TIME INTEGRATED MASS ADDITION HISTORY

Figure 5.3-115

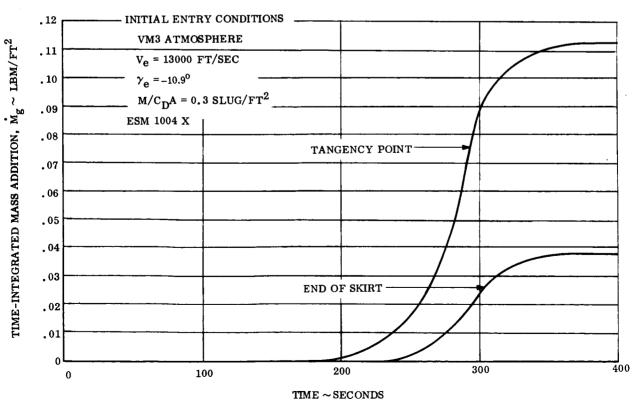


Figure 5.3-116

5.3-204

- 5.3.2.7 Nose Cap Heat Protection The use of a non-ablative heat shield and non-metallic support structure for the nose cap is necessitated by two requirements not imposed on the conical Aeroshell section. These are: (1) RF transparency to the radar altimeter signal, and (2) no outgassed products to interfere with the atmospheric sampling and TV viewing experiments. To completely satisfy this latter requirement precludes the use of ablative materials for the nose cap heat shield. Window contamination from ablative product deposition was shown to occur in the Gemini flights and also in the simulated plasma tests of the candidate ablative heat shield materials.
- 5.3.2.7.1 <u>Candidate Heat Shield and Structural Materials</u> A survey was conducted to select the best heat shield and structural materials for the nose cap assembly. Ceramic materials, in general, were considered most favorable for the heat shield because of their high temperature stability and excellent dielectric properties at elevated temperatures. Certain ceramic materials, including boron nitride, fused silica, and Pyroceram, although possessing excellent elevated temperature dielectric properties, were eliminated from consideration because of their high density and the extensive fabrication development necessary to build a large heat shield. Teflon, although having excellent thermal protection and dielectric properties, was not considered because it sublimes, and the gaseous products would interfere with the atmospheric composition analysis. These gaseous products could also condense on the TV window aft of the nose cap and degrade its optical properties.

A request for technical information (Reference 5.3-54) was issued by McDonnell to obtain recommendations for an RF transparent nose cap. At the time this request was made, the RF transparency requirement was more stringent than at present. However, the thermal and mechanical requirements have not changed. Proposals were received from Brunswick Corporation, (Reference 5.3-55) and Wittaker Corporation, (Reference 5.3-56). Their proposed materials and designs were included in the nose cap selection.

The candidate heat shield materials considered were an alumina foam, an aluminum phosphate bonded fused quartz fabric, and a ceramic bonded aluminosilicate fiber composite (Fiberfrax). These candidate materials all have the required high temperature stability. The aluminum phosphate bonded fused quartz fabric was also considered for use as a structural support material.

The thermophysical, mechanical and electrical properties of the candidate heat shield materials are reported in Figure 5.3-117. The materials considered for use as structural support were phenolic-fiberglass, polybenzimidazole (PBI)-

PROPERTIES OF NOSE CAP HEAT SHIELD MATERIALS

PROPERTY MATERIAL	PHOSPHATE BONDED S-TYPE FIBERGLASS	ALUMINA FOAM	HARDENED FIBERFRAX
Density (lb/ft ³)	112	68	25
Maximum Serviceable Temperature (^o F)	1800 (3000 For Canditate Mat.)	3300	3200
Thermal Conductivity (BTU-ft)/(hr-ft ² -°F)	0.266 at 200°F 0.34 at 800°F	2.0 at 800°F	0.09 at 1200°F
Specific Heat (BTU/Ib-°F)	0.20 at R.T.	0.3 at 800°F	0.25 at R.T.
Modulus of Elasticity (psi)	3.88 × 10 ⁶ at R.T. 2.71 × 10 ⁶ at 800°F	0.5 x 106 at 1000°F	0.3 x 106 at R.T.
Compressive Strength (psi)	5,000 at R.T. 5,500 at 800°F	1400 at R.T.	
Tensile Strength (psi)	30,000 at R.T. 21,200 at 800°F		
Flexural Strength (psi)	21,000 at R.T. 9,500 at 800°F	1050 at R.T.	
Coefficient of Linear Thermal Expansion (in./in./°F)	2.25 x 10 ⁻⁶ at 600°F	4.5 × 10 ⁻⁶ at 1000°F	1.5 x 10 ⁻⁶ ② at 400°F
Dielectric Constant (R.T.)	3.35 at 10k MHz	2.43 at 9.37 MHz	1 at 60 Hz
Loss Tangent (R.Ţ.)	0.0082 at 10k MHz	0.001 at 9.37 MHz	0.1 at 60 Hz

This material was not a candidate but is included as representative background information. Phosphate bonded fused quartz fabric was the candidate. This composite is both structure and heat shield.

Aluminosilicate fibers only.

fiberglass, aluminum phosphate bonded fused quartz fabric, polyimide-fiberglass and silicone-fiberglass. The thermophsical, mechanical and electrical properties of the structural materials are reported in Figure 5.3-118.

Composite Configurations - To optimize the performance of the VOYAGER nose cap, three composite configurations, schematically shown in Figure 5.3-119, were studied in depth from the materials listed in Figures 5.3-117 and -118. The nose cap selection was made on the basis of a composite heat shield/structural viewpoint because of the interaction of the materials when one considers the fabrication aspects. Also, one of the composites studied is an integral shield and structure.

Composite No. 1 - This composite was recommended by the Brunswick Corporation and is a honeycomb sandwich structure fabricated from aluminum phosphate and fused quartz fabric. It serves both as a thermal shield and structural support and is similar to a currently used ceramic composite consisting of aluminum phosphate, S-type fiberglass, and potassium silicate cement.

Processing of the candidate material consists of impregnating fused silica fabric with aluminum phosphate binder to form a prepreg. The honeycomb core and two faceplates are formed from this material. The sandwich structure is fabricated by bonding the faceplates to the honeycomb core using aluminum phosphate as an adhesive.

This composite is not recommended for the nose cap at the present time because the material thermal-physical properties have not been fully determined. At this stage of development, it has yet to be determined if this composite can withstand the combined thermal and pressure loads.

Composite No. II - This composite was recommended by the Whittaker Corporation and is composed of a flame sprayed, dense alumina external skin, a low density alumina foam and a polybenzimidazole (PBI) - fiberglass laminated internal skin. The PBI-fiberglass laminate has high thermal stability with regard to both its electrical and mechanical properties. The material also has a unique feature in that it does not require an adhesive to bond to the core material but can be laminated directly to the ceramic foam.

Fabrication consists of cold pressing, drying, and firing the ceramic slurry, bonding the PBI laminate to the ceramic foam, grinding the outer foam surface, spraying alumina on this surface, and regrinding the outer skin to the proper thickness.

This composite is not recommended for the nose cap because it is heavier than the other composites. The thermal shock resistance of the brittle external skin

PROPERTIES OF STRUCTURAL MATERIALS

MATERIAL PROPERTY	PHENOLIC- FIBERGLASS	SILICONE FIBERGLASS	POLYIMIDE FIBERGLASS	PBI FIBERGLASS	PHOSPHATE BONDED S-TYPE FIBERGLASS (2)
Density (Lb/ft ³)	115	115	901	110	112
Maximum Serviceable (1) Temperature (°F)	°006	750°	1000°	1000°	1800° (3000°F for candidate material)
Thermal Conductivity (BTU-ft)/hr-ft2-°F)	0.056 at R.T. 0.093 at 500°F	0.047 at R.T. 0.091 at 500°F	0.056 at R.T. 0.093 at 500°F	0.26 at 600°F	0.266 at 200°F 0.34 at 800°F
Specific Heat (BTU/1b-ºF)	0.25 at R.T.	0.28 at R.T.	0.25 at R.T.	0.21 at R.T.	0.20 at R.T.
Modulus of Elasticity (psi)	3.0 × 106 at R.T. 2.0 × 106 at 500°F	3.2 × 106 at R.T. 2.1 × 106 at 500°F	2.69 × 10 ⁶ at R.T. 1.95 × 10 ⁶ at 500°F	2.7 × 10 ⁶ at 800°F	3.88 × 10 ⁶ at R.T. 2.71 × 10 ⁶ at 800 ⁶ F
Compressive Strength (psi)	35,000 at R.T.	22,000 at R.T.	38,000 at R.T. 16,000 at 800°F	20,000 at 800°F	5,000 at R.T. 5,500 at 800°F
Tensile Strength (psi)	40,000 at R.T. 25,000 at 500°F	40,600 at R.T. 22,000 at 500°F	39,000 at R.T. 32,000 at 800°F	50,000 at 800°F	30,000 at R.T. 21,200 at 800°F
Flexural Strength (psi)	50,000 at R.T.	43,000 at R.T. 16,000 at 500°F	52,500 at R.T. 22,000 at 800°F	55,000 at R.T.	21,000 at R.T. 9,500 at 800°F
Coefficient of linear Thermal Expansion Parallel to Fabric (in./in./F)	5.0 × 10-6 at R.T.	5.0 × 10 ⁻⁶ at R.T.	5.0 × 10-6 at R.T.	3.0 × 10-6 at 800°F	2.25 × 10 ⁶ at 600°F
Dielectric Constant (R.T.)	4.89 at 8.5 MHz	4.34 at 8.6 MHz	3.74 at 8.5 MHz	4.05 at 9.3 MHz	3.35 at 10 KMHz
Loss Tangent (R.T.)	0.051 at 8.5 KMHz	0.0059 at 8.6 KMHz	0.0044 at 1 MHz	0.0089 at 9.3 MHz	0.0082 at 10 KMHz

For up to 10 minute exposure.
 This material was not a candidate b

This material was not a candidate but is included as representative background information. Phosphate bonded fused quartz fabric was the candidate. This composite is both structure and heat shield.

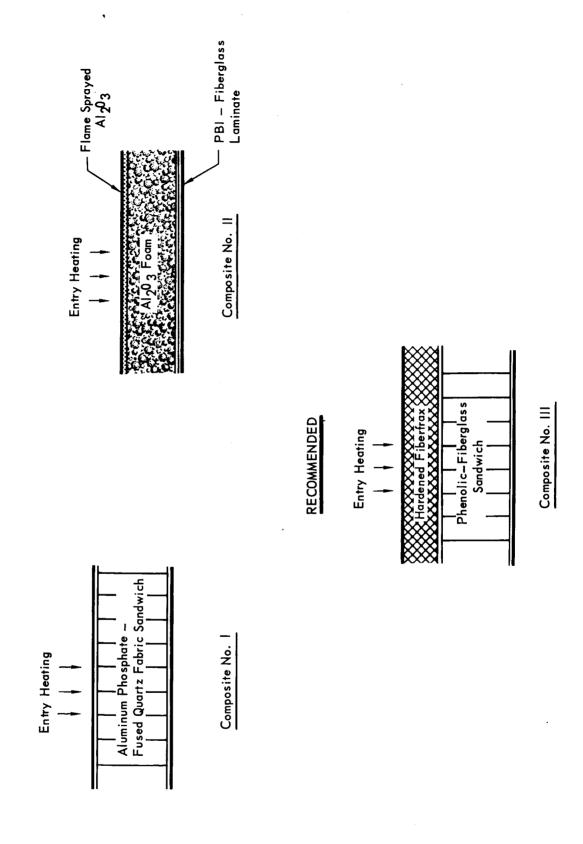


Figure 5.3-119

must be investigated along with the reliability of the bond between the flame sprayed alumina and alumina foam.

Composite No. III - This composite is composed of a low density fibrous composite outer heat shield bonded to a phenolic-fiberglass honeycomb sandwich support structure. The low density fibrous composite (hardened Fiberfrax) provides the required heat protection while the sandwich provides the required support. The hardened Fiberfrax composite is entirely inorganic, consisting of aluminosilicate fibers and a proprietary ceramic binder. It is manufactured by the Carborundum Company and is available in various densities depending upon the amount and type of binder. The density presently recommended is 25 lb/ft although lower densities are feasible. Hardened Fiberfrax is an efficient passive insulator, has a very low modulus of elasticity, and has excellent thermal shock resistance.

HT-435, a modified epoxy adhesive with excellent dielectric properties will be used for all bonding. A similar version of this adhesive, containing aluminum powder, was used on Gemini. the phenolic-fiberglass honeycomb sandwich was also used on Gemini as the heat shield structural support. A high temperature, high emittance overcoating of aluminum phosphate and nickel oxide will be applied to the outer skin. This coating was applied to the silica window and satisfactorily tested to a 2000°F surface temperature and to VHF transmission levels. Processing of the hardened Fiberfrax heat shield consists of vacuum molding it in one piece to the required shape. The support structure will be shaped to the Fiberfrax heat shield using the heat shield as a mold.

This composite is recommended for the VOYAGER nose cap because it is light-weight, is based on state-of-the-art materials, and has excellent versatility in tailoring the material to meet specific requirements. Tests, reported in Section 5.3.2.7.2, show the heat shield material can withstand the entry heat loads efficiently, is not affected by cold soak or vacuum exposure, has negligible outgassing and satisfies the radar altimeter RF transmission requirements. The RF transmission characteristics were checked only at room temperature conditions and must be evaluated at higher temperatures to assure the adequacy of this material. A material such as pure fused silica fiber bonded with colloidal silica may better satisfy the electrical requirements because of the higher purity and lower loss factor. A change from hardened Fiberfrax to a hardened fused silica fibrous composite could readily be accomplished because of the similar characteristics of the two fibers.

Beryllium Nose Tip - A beryllium heat sink is located at the apex of the nose cap to provide an inlet and support for the environmental sensing equipment located inside the nose cap. The beryllium heat sink is bolted to the sandwich structure and is mounted flush with the heat shield. Beryllium is a very efficient heat sink material because of its high melting point and high heat capacity.

A beryllium heat shield was used early in the Mercury Program; cylindrical beryllium shingles were used on Gemini and Mercury; and beryllium heat sinks were also used around the reaction control motors in the ASSET vehicle. Choosing beryllium for the nose tip permits machining the thin wall instrument inlet tubes integrally with the heat shield. This eliminates the problem and questionable reliability of supporting fragile tubes made from high temperature ceramics or coated refractory metals. Complete material property data for design and analysis is available. McDonnell process specifications covering fabrication and quality control for beryllium are established and have been used for some time.

Antenna Cavity Filler - A cavity filler is required to minimize antenna breakdown in the presence of a gaseous atmosphere which can ionize and become conductive. The recommended cavity filler, for use with the radar aft of the heat shield, is Eccofoar FPH. It is a rigid, high temperature resistant polyurethane foam which can be foamed-in-place and has been used for electronic embedments, radome cores, void filling and variety of structural applications where moderately high temperature properties are important. Once cured in place, Eccofoam FPH will withstand continuous exposure to 350°F.

<u>Preferred Nose Cap Fabrication</u> - The hardened aluminosilicate fibrous heat shield (Fiberfrax) will be formed to shape by vacuum molding. To facilitate fabrication and fitting, the sandwich support structure will be constructed using the heat shield as the mold. A black high emittance overcoating will be applied by spraying. Existing procedures and techniques developed for the fabrication and quality control of the Gemini heat shield support structure, are applicable with minor modifications.

5.3.2.7.2 <u>Material Tests</u> - Fiberfrax is a trade name for a family of insulative materials comprised of aluminosilicate fibers bonded with either organic or inorganic binders. By varying the type and amount of binder and the fiber content, a wide range of thermophysical properties can be achieved to meet specific requirements.

The materials having organic binders are designated Series 466; those having inorganic binder are designated Series 61. Testing was conducted with representative

specimens from both series to obtain a comprehensive evaluation of the material versatility. Only those tests needed to evaluate the material performance in the unique VOYAGER conditions, e.g. exposure to cryogenic temperatures, entry heating, weight loss in vacuum and RF transmission, were performed to complement the thermal-physical data obtained from Carborundum Corporation.

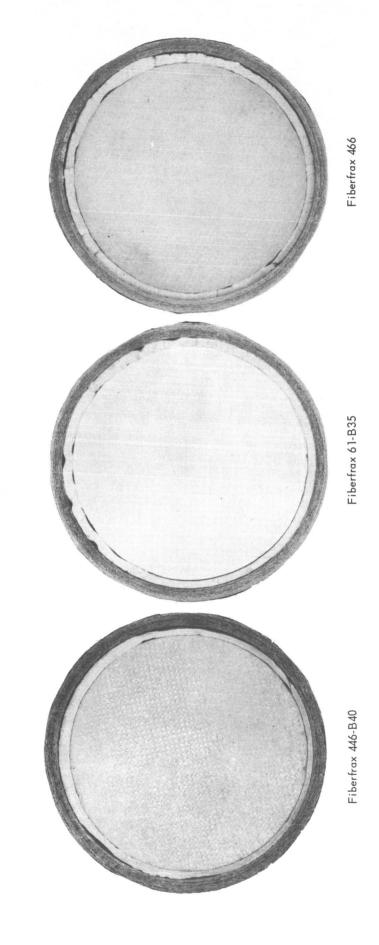
Exposure to Cryogenic Temperatures - Tests were conducted to evaluate the compatibility of the recommended nose cap composite when subjected to cyrogenic temperatures. The hardened Fiberfrax materials were bonded with HT-435 film adhesive to phenolic-fibergalss sandwich support structures.

The test specimens were placed in a cold chamber cooled to $-250\,^{\circ}\mathrm{F}$ and held at this temperature for 30 minutes. The temperature of the specimens was monitored with iron constentan thermocouples. No evidence of cracks in the materials or of the composite structure was visible. These same specimens were later subjected to a cold wall heat flux of 12 BTU/ft²-sec. Figure 5.3-120 shows the test specimens after the simulated entry heating exposure.

Thermal Gravimetric Analysis - TGA was conducted on bulk aluminosilicate fibers in an air atmosphere over the temperature range of 70°F to 2000°F. No significant weight change was observed. TGA of an all inorganic Fiberfrax material also showed no appreciable weight change. However, TGA in vacuum indicated there was a small weight loss (approximately 1.5%) over the 2000°F range. This probably was caused by loss of absorbed moisture which is characteristic of fibrous materials.

RF Transmission Tests - The one-way transmission loss of specimens having 0.1 inch and 0.3 inch thick hardened Fiberfrax (40 $1b/ft^3$) bonded with an elastromeric silicone adhesive (DC-140) to a phenolic-fiberglass honeycomb suport structure was measured at room temperature. The results of the tests are presented in Figure 5.3-121 and show less than 1.5 dB transmission loss up to 6 GH_z , which satisfies the radar altimeter transmission requirements.

Thermal Performance Tests - Both oxy-acetylene torch and plasma-jet tests were performed on representative hardened Fiberfrax materials Oxy-acetylene torch testing is considered adequate for these materials because the heating rate-time parameter, which is of prime interest, was well simulated. Five specimens of hardened Fiberfrax were tested at cold wall heating rates of 12 Btu/ft²-sec and 25 Btu/ft²-sec. The test specimen configuration was representative of the recommended nose cap design with the exception of the phenolic-fiberglass ring used to minimize edge heating effects in the tests.

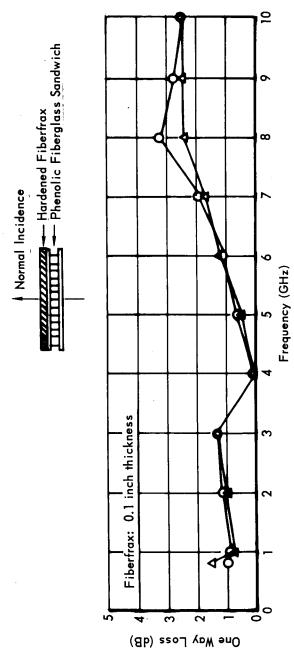


TEST SEQUENCE

30 Minute Exposure at $-250\,^{\circ}$ F (Without Edge Ring) Tested in the Oxy-Acetylene Torch Facility at $q_{cw}=12$ Btu/ft2_sec, for 480 sec

Figure 5.3-120

ONE WAY RF TRANSMISSION LOSS OF HARDENED FIBERFRAX



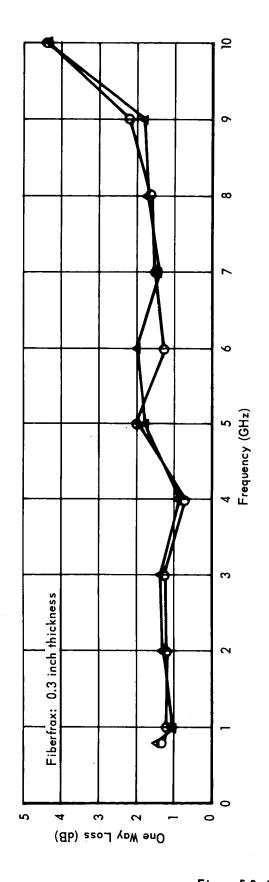


Figure 5.3-121

5.3-214

Each specimen was tested to determine its thermal performance, as measured by the bondline temperature rise. The specimens were allowed to cool to room temperature and then re-tested at the same heating condition. Since no difference in maximum temperature was noted between tests, it was concluded that little if any material degradation occurred during heating. Figures 5.3-122 and 5.3-123 present the temperature response data from these tests.

Tests were conducted in the McDonnell vacuum plasma jet facility at cold wall heating rates of 4.7, 11.6, and 34.7 BTU/ft 2 -sec using a $\mathrm{CO_2-N_2}$ gas stream composition. The specimen configuration was similar to the one described above.

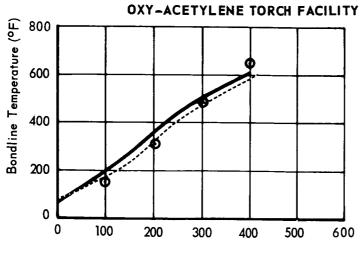
Figure 5.2-124 compares the thermal performance of Fiberfrax with two low density ablative materials. The results indicate that hardened Fiberfrax has better performance at heating rates of 4.7 and 11.6 BTU/ft²-sec but is less efficient at the higher heating rate. The lower heating rate levels corresponds to the heating rates expected for the high total heat design trajectory.

5.3.2.7.3 Nose Cap Heating Shield Design - Having selected the preferred nose cap heat shield material, hardened Fiberfrax, two design tasks remain: First, determination of the passive nose cap area required to prevent outgassed products from interferring with the atmospheric measurements and TV viewing experiments. Second, determination of the heat shield thickness required to limit the backup structure temperature below its design limit.

Two approaches were considered for the first design task: namely, application of hardened Fiberfrax over the entire spherical nose cap, or limited application of hardened Fiberfrax around the atmospheric measurement probe and the upstream region of the TV window by considering a $\pm 20^{\circ}$ variation in angle of attack. Fabricating the entire nose cap with a passive material is an easier manufacturing process and ensures the complete absence of experiment failure from the backwash of ablative products at high angles of attack. Thus, the entire nose cap was chosen to be fabricated with passive insulative material.

The Fiberfrax heat shield was sized to limit the bondline temperature to $640^{\circ} F$ for the spectrum of possible entry heating conditions. As discussed in Section 5.3.1, a maximum design temperature of $735^{\circ} F$ was selected for the backup structure based on the thermal stress consideration. To account for uncertainties in the material properties and heat shield analysis a safety factor of 1.15 is applied to the design temperature rise using $0^{\circ} F$ as a nominal initial temperature $(640^{\circ} \times 1.15 = 735^{\circ} F)$.

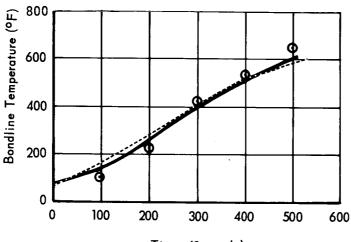
THERMAL PERFORMANCE OF HARDENED FIBERFRAX



First Test Data
Second Test Data
Omputed Results

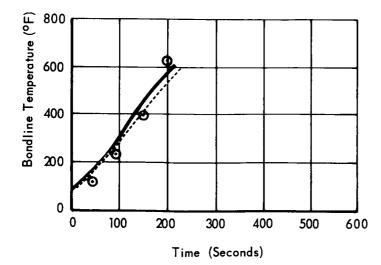
Fiberfrax - 466 Density = 19.0 Lb/Ft³ W/A = 0.604 Lb/Ft² ġcw = 12 Btu/Ft² - Sec





Fiberfrax - 61-B35 Density = 29.0 Lb/Ft3 W/A = 1.26 Lb/Ft2 ġcw = 12 Btu/Ft2 - Sec

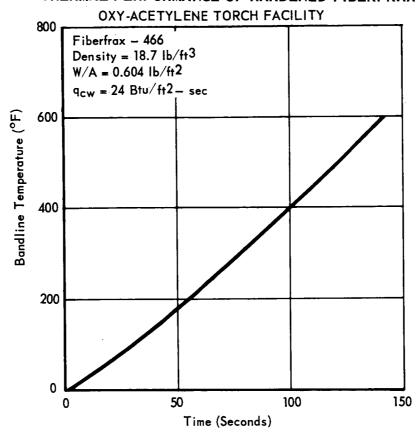
Time (Seconds)



Fiberfrax - 466-B40
Density = 44.0 Lb/Ft3
W/A = 1.11 Lb/Ft2
qcw = 12 Btu/Ft2 - Sec

Figure 5.3-122

THERMAL PERFORMANCE OF HARDENED FIBERFRAX



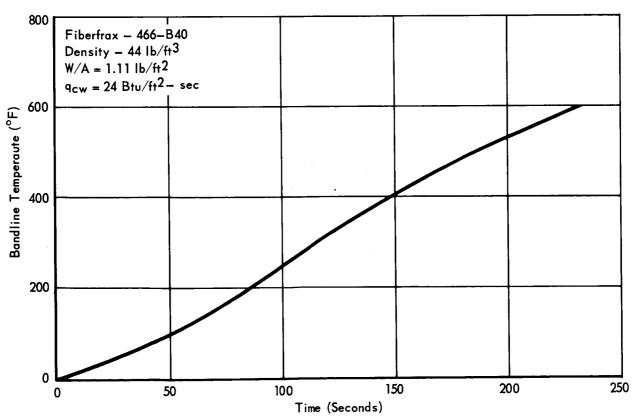


Figure 5.3-123 5.3-217

THERMAL PERFORMANCE OF HARDENED FIBERFRAX, MDC S-6, AND N-P VACUUM PLASMAJET FACILITY

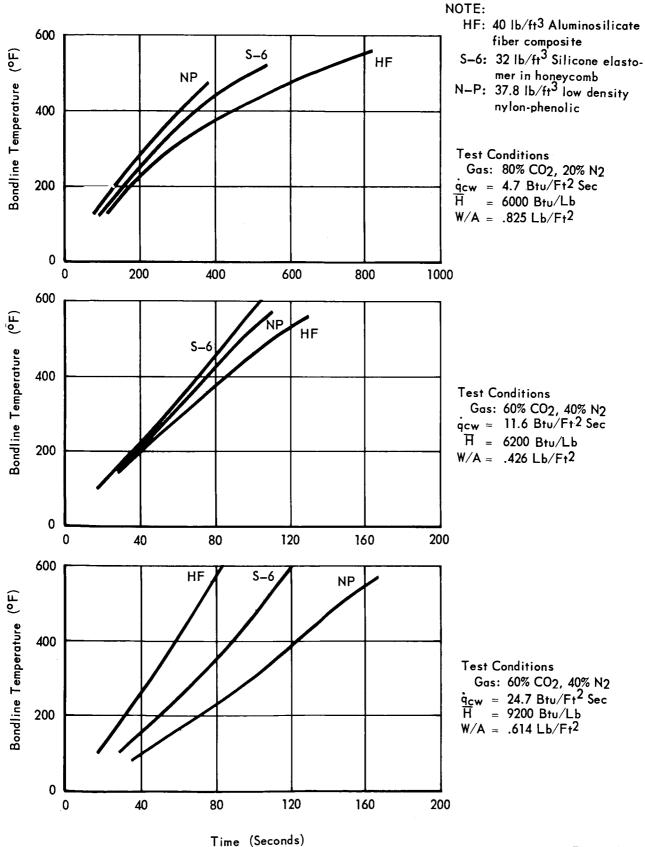


Figure 5.3-124

Heat Shield Thermal Analysis and Material Requirement - Predicting the temperature response of a passive (non-ablating) heat shield, is rather straightforward, especially with the aid of high speed digital computers. The thermal analysis reported herein is based on one-dimensional heat conduction theory for a multiple slab model with radiative and convective heating boundary conditions. Test data correlation using the transient heat transfer program was made, and the results are shown in Figure 5.3-124. The material properties used in the analysis are shown below:

Density	25 lb/ft ³
Specific Heat	0.22 BTU/1b-°F
Thermal Conductivity	0.025 BTU/ft-hr°F at 100°F
	0.080 BTU/ft-hr°F at 1000 °F
	0.140 BTU/ft-hr°F at 2000 °F
Emissivity	0.8

Based on the aforementioned thermal analysis and property data, the trade-off between unit heat shield weight (density x thickness) and maximum bondline temperature is shown in Figure 5.3-125 for the highest heat load entry trajectory. It is shown that to limit the bondline temperature rise to 640°F requires .67 lb/ft² of Fiberfrax material. Considering the range on angle of attack, the entire nose cap area experiences about the same magnitude of heating. Therefore, a uniform thickness nose cap is recommended for ease of fabrication. The surface, mid-point and bondline temperature histories are shown in Figure 5.3-126 for the steep and shallow entry trajectories.

Although the shallow entry provides the highest backface temperature, due to the longer soak period, the steep entry results in the highest surface temperatures. A peak temperature of 2100°F is shown in Figure 5.3-126 for the steep entry condition, but note that the surface temperature is above 1600°F for only 20 seconds. The hardened Fiberfrax material is thermally stable to at least 2300°F for continuous operation.

Because of the rapid change in surface temperature, maximum of 70°F/sec, the steep entry will provide the greatest thermal shock problem. No indications of thermal shock effects, e.g. as surface crazing, were evident in any of the thermal performance tests. In these tests, the material was exposed to an instanteneous square heat pulse which is more severe, with respect to thermal shock, than the sinusoidal entry heat pulse.

MAXIMUM BONDLINE TEMPERATURE VS CERAMIC NOSE CAP WEIGHT

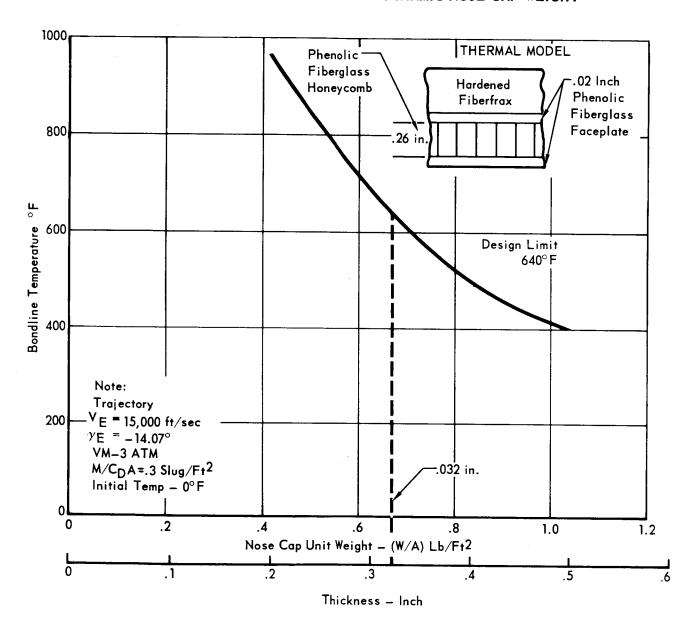
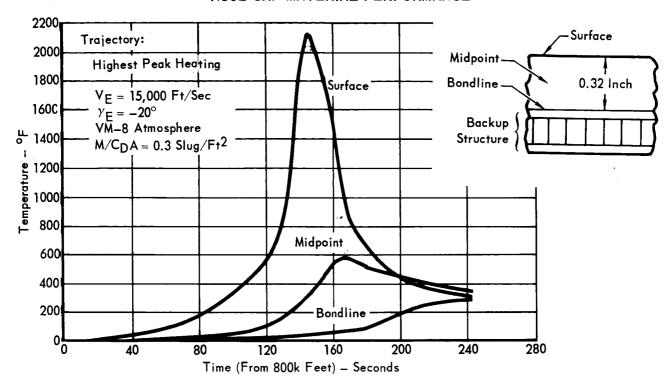


Figure 5.3-125

NOSE CAP MATERIAL PERFORMANCE



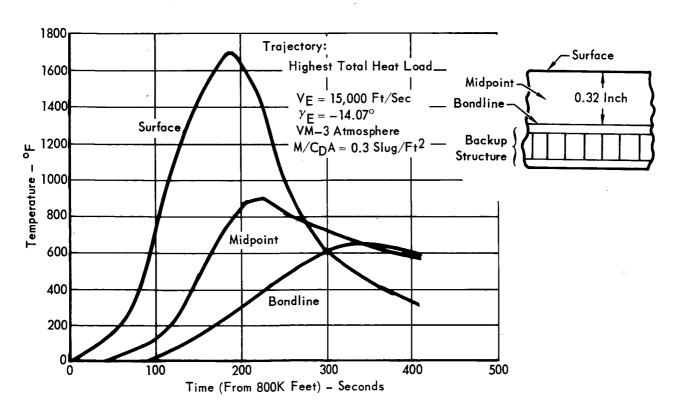


Figure 5.3-126 5.3-221

Berryllium Nose Tip Analysis - The berryllium heat sink was sized to limit its temperature rise to 400°F for the highest total heat trajectory. The low temperature limit, that is much lower than its thermal capability, was chosen primarily to prevent excessive heating of the adjacent pressure transducer and antenna cavity filler material. Approximately 1/2 inch of berryllium (2.0 lbs) is required for the nose tip.

5.3.2.7.4 <u>TV Window</u> - The TV window, located near the sphere cone tangency line, serves an an optical and thermal cover for the TV camera. Thus, it must be capable of withstanding both the entry heating and pressure loads and at the same time minimize backface radiation heating to the TV camera optics.

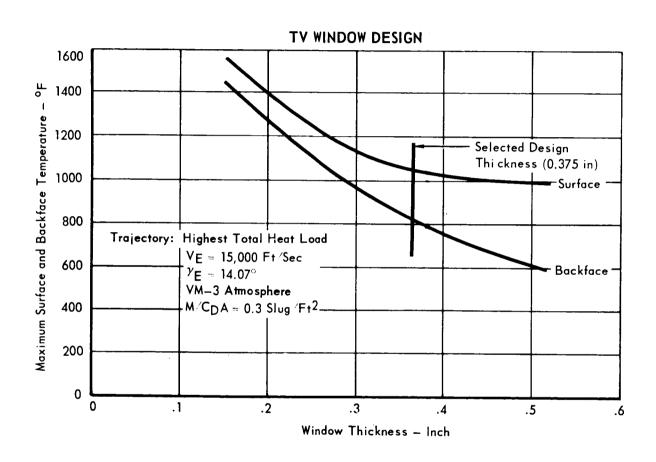
The preferred window material is Corning 7940 fused silica manufactured by Corning Glass Company. It was selected on the basis of adequate temperature capability and good optical properties at high temperature. The window material is optically good to 2000°F and structurally adequate to 1700°F. To reduce radiation heat transfer to the internal optics, the backface is coated with a heat control filter consisting of zinc sulphide and silicon oxide. The filter is optically transparent but reflects a large portion of the infrared radiatior, and it is stable to 2000°F.

Thermal Analysis - A one-dimensional heat conduction analysis, similar to that used on the passive nose cap, was performed to determine the peak temperatures expected during entry and also the window thickness required to minimize backside radiation heating. The following thermal properties of fused silica were used in the analysis.

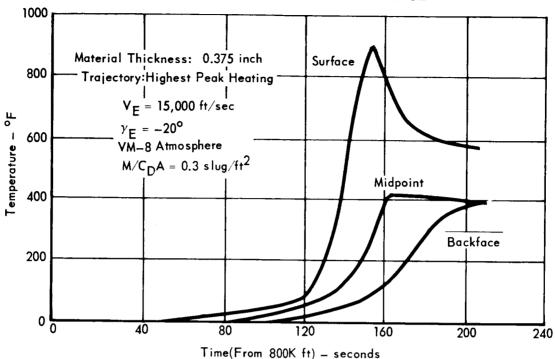
		. 3
0	Density	165 lb/ft ³
0	Specific Heat	0.16 Btu/1b - °F @O°F
		0.25 Btu/lb - °F @ 1000°F
o	Thermal Conductivity	0.765 Btu/ft-hr°F @ 0°F
		1.150 Btu/ft-hr - °F @1000°F
0	Emissivity	0.6

The temperature response for both the peak heating and highest total heat trajectory were investigated.

The variation of peak surface and backface temperatures with window thickness is shown in Figure 5.3-127. A window thickness of .375 inch was selected to provide enough support for the pressure loads and, primarily, to prevent excessive temperature buildup at the backface. In Figures 5.3-128 the temperatures response at the surface, midpoint, and backface is shown for the two limiting trajectories. Note







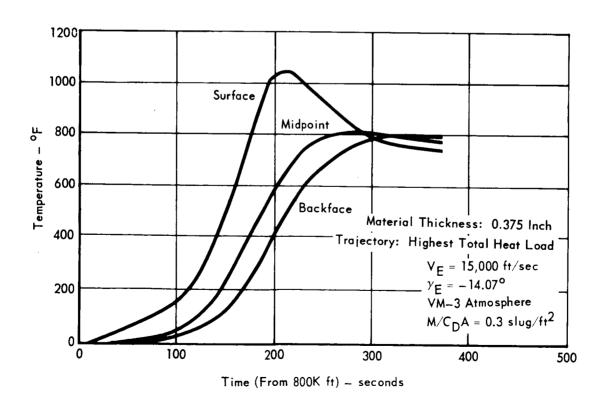


Figure 5.3 – 128 5.3 – 224

that the peak temperature is only 1050°F and occurs for the shallow entry case instead of the peak heating trajectory. This apparent anomally is due to the relatively high thermal conductivity of glass which reduces the surface temperature gradients for the short duration steep entry.

To minimize the radiation heating to the internal TV optics, a heat control filter is applied on both the window backface and the TV camera lens. For the entry heat loads, the estimated heat transfer to the lens is reduced to $60 \, \text{Btu/ft}^2$. This results in a temperature rise of less than $50 \, \text{F}$ which is within the tolerance limit of the lens.

REFERENCES

- 5.3-1 1973 VOYAGER Capsule Systems Constraints and Requirements Document
 Revision 2. Jet Propulsion Laboratory, Pasadena, California (12 June 1967).
- 5.3-2 V. I. Weingarten and P. Seide: <u>Elastic Stability of Thin-Walled Cylindrical</u>
 and Conical Shells under Combined External Pressure and Axial Compression.

 AIAA Journal, Volume 3, p 913 thru 920 (1965).
- 5.3-3 S. B. Batdorf: A Simplified Method of Elastic Stability Analysis for Thin Cylindrical Shells. NACA Report No. 874 (1947).
- 5.3-4 NASA Space Vehicle Design Criteria: <u>Buckling of Thin-Walled Circular</u>

 <u>Cylinders.</u> NASA SP-8007, Vol. III, Part C, Chapter 2 (1965)
- 5.3-5 J. A. Cheney: <u>Buckling of Shell Supported Rings</u>. Journal of Aircraft, Vol. 1, No. 4 (July-August 1964).
- J. H. Percy, T. H. H. Pian, D. R. Navaratna, and S. Klein: Application of the Matrix Displacement Method to the Linear Elastic Analysis of Shells of Revolution. MIT Aerolastic and Structures Laboratory TR 121-7 (January 1967).
- 5.3-7 R. F. Crawford and A.B. Burns: Strength, Efficiency, and Design Data for Beryllium Structures. ASD Technical Report 61-692 (February 1962).
- 5.3-8 E. F. Bruhn: Analysis and Design of Flight Vehicle Structures. Tri-State Offset Company (1965).
- 5.3-9 North American Aviation, Inc., Report SID 66-398. Shell Analysis Manual (1966).
- 5.3-10 H. Becker: <u>Handbook of Structural Stability</u>. Part II Buckling of <u>Composite Elements</u>. NACA TN 3782 (1957).
- 5.3-11 Evaluations of Titanium and Titanium Alloys in Alcohols and Haliginated Hydrocarbons. Compilation of Information Available at DMIC, Columbus, Ohio (1 December 1966).
- 5.3-12 R. E. Johnson: <u>A Case History of Titanium Stress Corrosion in Nitrogen Tetroxide</u>. NASA Manned Spacecraft Center, Houston, Texas (1966).
- 5.3-13 R. Meredith and W. L. Arter: <u>Stress Corrosion of Titanium Weldments.</u>
 Welding Journal, Volume 36 (September 1957).
- 5.3-14 S. Faulkenberry and A. Ianucci: <u>Effects of Sodium Chloride on Stress</u>

 <u>Corrosion Cracking of Titanium Alloy During Stress Relieving</u>. General

 Dynamics/Convair Report MP 59-053 (May 1959).
- 5.3-15 Environmental Specification VOYAGER Capsule Flight Equipment Type Approval and Flight Acceptance Test Procedures for the Heat Sterilization and

- Ethylene Oxide Decontamination Environments. JPL Spec No. Vol 50503-ETS, Jet Propulsion Laboratory, Pasadena, California (12 January 1966).
- 5.3-16 Private Communication between McDonnell and DuPont (25 August 1967).
- 5.3-17 M. Hetenyi: <u>Beams on Elastic Foundation</u>. University of Michigan Press (1946).
- 5.3-18 R. J. Roark: <u>Formulas for Stress and Strain</u>. McGraw-Hill Book Company (1954).
- 5.3-19 S. Timoshenko and J. M. Gere: <u>Theory of Elastic Stability</u>. McGraw-Hill Book Company (1961).
- 5.3-20 R. H. Homewood, A. C. Brine, and A. E. Johnson: Experimental Investigation of the Buckling Instability of Monocoque Shells. Experimental Mechanics, Vol. 1, No. 3, p 88 (March 1961).
- 5.3-21 J. G. Marvin and G. S. Deiwert: <u>Convective Heat Transfer in Planetary</u>
 <u>Gases</u>. NASA TR R-224, July 1965.
- 5.3-22 H. G. Lew: <u>Non-Equilibrium Heat Transfer for Voyager Mars Lander</u>. PIR-2610-15 (May 26, 1967).
- 5.3-23 L. Lees: <u>Laminar Heat Transfer Over Blunt Nosed Bodies</u>. Jet Propulsion Laboratory, Vol. 26, No. 4 (1956).
- 5.3-24 G. K. Walker: A Particular Solution to Turbulent Boundary Layer Equations.

 J.A.S. Vol. 27, No. 9 (1960).
- 5.3-25 J. Gruszczynski and W. Warren: <u>Measurements of Hypervelocity Stagnation</u>

 <u>Point Heat Transfer in Simulated Planetary Atmospheres</u>. General Electric MSD R63SD29 (March 1963).
- 5.3-26 T. Horton and T. Babineaux: <u>Influence of Atmospheric Composition on Hypersonic Stagnation Point Convective Heating</u>. AIAA Journal Vol. 5, No. 1 (January 1967).
- 5.3-27 D. Collins and T. Horton: Experimental Convective Heat Transfer Measurements. AIAA Journal, 2,2046-2047 (1964).
- 5.3-28 R. Rutowski and K. Chan: Shock Tube Experiments Simulating Entry Into
 Planetary Atmospheres. General Research in Flight Sciences, Vol. I,
 Part 2 Fluid Mechanics, Lockheed Aircraft Corp., Technical Report
 LMSD-288139 (January 1960).
- 5.3-29 L. Yee, H. Bailey, and H. Woodward: <u>Ballistic Range Measurements of Stagnation Point Heat Transfer in Air and Carbon Dioxide at Velocities up to 18,000 ft/sec</u>. NASA TN D-777 (March 1961).

- 5.3-30 R. M. Nerem, C. J. Morgan, and B. C. Graber: <u>Hypervelocity Stagnation</u>

 <u>Point Heat Transfer in a Carbon Dioxide Atmosphere</u>. AIAA Journal, Vol. 1,
 No. 9 (September 1963).
- 5.3-31 H. Hoshizaki: <u>Heat Transfer in Planetary Atmospheres at Super Satellite</u>
 <u>Speeds.</u> ARS Journal 32, No. 10 (October 1962).
- 5.3-32 M. L. Finson and N. H. Kemp: <u>Theory of Stagnation Point Heat Transfer in Ionized Monatomic Gases</u>. Physics Fluids 8, 201-207 (1965).
- 5.3-33 J. P. Reilly: <u>Stagnation Point Heating in Ionized Monatomic Gases</u>. Publication 64-1 (AFOSR S4-42) Fluid Mechanics Laboratory, MIT (January 1967).
- 5.3-34 R. W. Rutowski and D. Bershader: Shock Tube Studies of Radiative Transport in an Argon Plasma. Physics Fluids Vol. 7, No. 4 (April 1964).
- 5.3-35 S. M. Scala and L. M. Gilbert: Theory of Hypersonic Laminar Stagnation

 Region Heat Transfer in Dissociating Gases. General Electric Company,

 MSD, Space Science Laboratory, TIS R64SD73 (November 1964).
- 5.3-36 J. S. Gruszczynski, W. R. Warren, and N. S. Diaconis: <u>Laboratory</u>

 <u>Simulation of Hypervelocity Heat Transfer Problem During Planetary Entry</u>.

 General Electric, TIS R64SD73 (1964).
- 5.3-37 J. S. Gruszczynski and D. A. Bradley: <u>Radiative Properties of High</u>

 <u>Temperature 30% CO₂ 70% N₂ Gas Mixture Part 2</u>. EFP-TM-207 (June 1967).
- 5.3-38 F. Wolf and J. M. Spiegel: Status of Basic Shock Layer Radiation Information for Inner-Planet Atmospheric Entry. JPL Report.
- 5.3-39 R. Vaglio-Laurin: <u>Laminar Heat Transfer on Blunt Nosed Bodies in Three-Dimensional Hypersonic Flow</u>. WADC Technical Note 58-147 (May 1958).
- 5.3-40 H. Cheng: The Blunt-Body Problem in Hypersonic Flow at Low Reynolds

 Number. I.A.S. Paper No. 63-92, Presented at IAS 31st Annual Meeting, New York, N. Y. (January 1963).
- 5.3-41 M. H. Bertram, L. Weinstein, A. Cary, and J. Arrington: Effect of Two-Dimensional Multiple-Wave Distortions in the Heat Transfer to a Wall in Hypersonic Flow. AIAA Paper 67-164, 5th Aerospace Sciences Meeting, New York, New York (January 1967).
- 5.3-42 D. L. Schmidt: Ablative Polymers for Hypersonic Atmosphere Flight.

 AGML-TR-66-78 (May 1966).
- 5.3-43 W. E. Welsh, K. E. Starner, D. H. Leeds, and J. I. Slaughter: <u>Low Density</u>
 <u>Ablation Materials Survey</u>. SSD-TR-66-35 (January 1966).

- 5.3-44 P. E. Bauer and D. L. Kummer: <u>Development and Performance of the Gemini Ablative Heat Shield</u>. Journal of Spacecraft and Rockets, Vol. 3, No. 10, p 1495 thru 1500 (October 1966).
- 5.3-45 J. N. Kotanchik and R. B. Erb: <u>Structures and Materials for Manned Re-Entry Vehicles</u>. AIAA Paper No. 66-987, AIAA Third Annual Meeting, Boston, Massachusetts (November-December 1966).
- 5.3-46 R. M. Davis and McCown: Comparison of Radiative versus Ablative Heat
 Shield Concepts for Manned Lifting Entry Vehicles with L/D's of 1.4 and
 2.7. AIAA Paper No. 66-990, AIAA Third Annual Meeting, Boston, Mass.
 (November-December 1966).
- 5.3-47 D. L. Lowe: Effect of Humidity on Tensile Properties of Insulcork 2755.

 General Electric PIR 8155-1305 (November 2, 1966).
- 5.3-48 L. Cohen: ESM 1001 Evaluation: Tensile Properties and Thermal Expansion

 Behavior. General Electric PIR 8.55-176 (January 31, 1963).
- 5.3-49 A. J. Butterfield: A Test Plan for a Preliminary Thermal Environment

 Evaluation of VOYAGER Aeroshell Heat Shield Systems. 67SD494, Revision B

 (April 20, 1967).
- 5.3-50 R. G. Wilson: Thermophysical Properties of Six Charring Ablators from 140° to 700°K and Two Chars from 800° to 3000°K. NASA TND-2991 (October 1965).
- 5.3-51 Armstrong Ablation Material Insulcork 2755. Armstrong Cork Company,
 Defense Division, Lancaster, Pennsylvania.
- 5.3-52 Manufacturers' Literature. Balso Ecaudor Lumber Corporation.
- 5.3-53 A. Lippay: <u>Balsa-Tough Lightweight Challenges Foams</u>. Materials Engineering, page 70 (June 1967).
- 5.3-54 Request for Technical Information for VOYAGER Flight Capsule Radome.

 McDonnell-Douglas Corporation (May 3, 1967).
- 5.3-55 <u>Technical Proposal to McDonnell-Douglas Corporation for a VOYAGER Flight</u>

 <u>Capsule Radome</u> Report No. D-60 26A. Defense Product Division Brunswick

 Corporation, Marion, Virginia (June 23, 1967).
- 5.3-56 <u>Technical Proposal to McDonnell-Douglas Corporation for a VOYAGER Flight</u>

 <u>Capsule Radome</u>, Narmco Proposal No. 100-3059. Narmco Research and

 Development Division, Whittaker Corporation, San Diego, California

 (June 10, 1967).

5.4 LANDER - Our preferred concept, presented in Section A 3.2.1.4, is the Uni-Disc Lander. The concept is simple; a crushable energy absorber is sandwiched between two structural discs. The lower disc is the landing footpad and the upper disc is the base platform which supports the payload. The single circular footpad, equal in diameter to the overall lander, has a continuous lower surface which makes it adaptable to a broad range of landing surface conditions.

Design of the Capsule Lander was challenging due to the design constraints, particularly the 34 degree slope with ridges and cones. Many approaches were studied, including limited directional and omnidirectional landers, mechanical and pneumatic landing systems, and toroidal and spherical shapes. Various legged landers were studied, such as a pendulum payload concept, and others similar to the Lunar Module and Surveyor, as well as flat disc shaped landers. These are pictured and discussed in Section 4.2.

Much of the study effort was directed toward legged lander systems. However, our studies indicate that this approach is not feasible within the constraints. A design having a low c.g., an energy absorber under the center body, and stabilizing outriggers was considered. This concept is workable but heavy and complex. Design of a wider base (platform type) lander eliminates the need for outriggers. This is our preferred concept, the Uni-Disc Lander. It meets all constraints.

The concept of platform landers is not new. For example, they are used for aerial delivery by the Armed Services as shown in References 5.4-1, 5.4-2 and 5.4-3. The Mercury spacecraft is another example; it used an air bag with the heat shield as the footpad for landing shock attenuation. Analytical and experimental evaluations of several landing systems are summarized in Reference 5.4-4 for three velocity regimes - primarily vertical, moderately vertical and horizontal, and primarily horizontal. While the velocities investigated exceed our design velocities, an important (though perhaps obvious) point is borne out. Low values for the geometric parameter, H/R, (c.g. height to base diameter) improve stability. Our concept contains this characteristic.

The Capsule Lander provides the structural support for the Surface Laboratory and Entry Science Package during launch, de-orbit, and entry and insures a soft landing on Mars. Lander design is based on the Structural Design Criteria presented in Section A 2.3. These criteria include the factor of safety requirements, design load factors throughout the mission, combinations of landing velocities and attitudes, and the geometric constraints of the landing surface.

Stability studies show that a four legged lander which is stable on a 34 degree

slope will not clear ridges having slopes greater than 16 degrees or cones having slopes greater than 11 degrees. Additional legs improve stability, but also rapidly add weight. Our preferred concept is stable on slopes up to 40 degrees with the 1973 payload and will tolerate all ridges and cones.

Trade studies were made to optimize the lander structural weight. One study involved trading the stroke of the crushable material for footpad and base platform weight; more stroke results in smaller landing loads and less weight, at a sacrifice in stability. The result of this study was the selection of a maximum landing acceleration of 14 $\rm g_E$. Another trade compared various footpad structural configurations including a beam and ring design, a beam and ring design with a screen-covered hole in the center section and a honeycomb sandwich. We selected the first because it was the lightest. Various materials were considered for the lander structure. Heat treated titanium was selected on the basis of its superior structural efficiency.

The weight of the landing system is 12% of the landed weight which is reasonable when compared to other systems. Aircraft landing gear systems are designed to less severe landing surface constraints and the loads are primarily axial, through the struts, and their weight fraction is about 5%. Platform landers for aerial delivery systems, as discussed in Reference 5.4-3, were found to be 17% of the landed weight. These systems are designed to higher velocity requirements (30 fps vertically and 25 fps horizontally) but less severe landing surface constraints than VOYAGER. The effect of landing on sloping ground is shown in Reference 5.4-5 for a legged lander. Data are presented for ground slopes from 0 to 16 degrees. At 15 degrees the indicated weight fraction is 5.5%. The Surveyor Spacecraft fell in this range. It was designed for a 15 degree landing surface and had a weight fraction of 5.8% (Reference 5.4-6). Extrapolation of the data in Reference 5.4-5 from a 16 degree slope to a 34 degree slope shows that a landing weight fraction of 16% might be expected.

This section is divided into two subsections. In the first we discuss our general stability studies of legged systems and in the second we present stability, strength, and dynamic analyses of our preferred concept. Load factors discussed in these subsections are based on the acceleration of gravity on Earth.

5.4.1 General Stability Studies of Legged Systems - Parametric stability studies of legged landers were conducted using a mathematical simulation of the lander gear system mounted on a rigid body. The landing surface was considered rigid. All of the studies were based on two dimensional analyses. A computer program,

similar to that shown in Reference 5.4-7, was modified to provide the means to perform many landing simulations with the following input variables: lander initial conditions (attitudes and velocities), surface slope, coefficient of friction, load stroke characteristics of gear members, geometry, and mass properties (mass, moment of inertia, c.g.) of the lander.

Three, four, and five legged landers, having single strut gears as shown in Figure 5.4-1, were studied to show the effect of the slope and surface discontinuities on the geometry and stability of legged systems. The results are summarized in that figure. They show the ratio of c.g. height to lander radius (H/R) required to provide stability on various slopes and clearance for various ridge angles. Clearance requirements for cones are more severe than those for ridges; for example, a four legged lander that is stable on a 34 degree slope will not clear ridges with slopes exceeding 16 degrees or cones with slopes exceeding 11 degrees.

Analyses of a four legged gear system were made with each gear constructed as an inverted tripod. This system is more stable than the single strut configuration, however, neither configuration satisfies all of the design requirements.

5.4.2 Preferred Concept - The lander consists of three primary segments, the landing footpad, crushable energy absorber, and base platform as shown in Figure 5.4-2(A).

The landing footpad is a 114-inch diameter disc with a 16-inch diameter hole at the center. The material used is 6Al-4V heat treated titanium. Its structure includes an 0.020 inch thick lower surface skin, three concentric rings with the middle ring attached to the energy absorber, and twenty-two 4-inch deep radial beams. The skin provides the large footprint area required for soft landing surfaces while the rings and beams provide strength for hard landing surfaces.

The footpad design is within the existing manufacturing state-of-the-art. The titanium is obtained in the solution heat treated condition and rough machined. The smallest ring is a one piece forging, while the larger rings are made by welding circular segments. The radial members, channel shaped in cross section, are forgings or built-up weldments. After final machining of all parts the rings and beams are spot welded to the skin. The entire assembly, properly jigged to eliminate warping, is final aged, a process which serves to stress relieve the welds and complete the heat treating process.

The energy absorber is an annular ring of crushable aluminum Trussgrid material, 70 inches in diameter, 13 inches deep and 2.0 inches thick as shown in Figure 5.4-2(A). The Trussgrid material has a density of 3.3 $1b/ft^3$, a crushing strength of 75 psi, and a shear strength of 110 psi. A conference with American Cyanamid Co. indicates

EFFECT OF GROUND SLOPE AND GEOMETRIC PARAMETER (H/R) ON STABILITY AND CLEARANCE OF AN ALTERNATE CONCEPT LEGGED LANDER

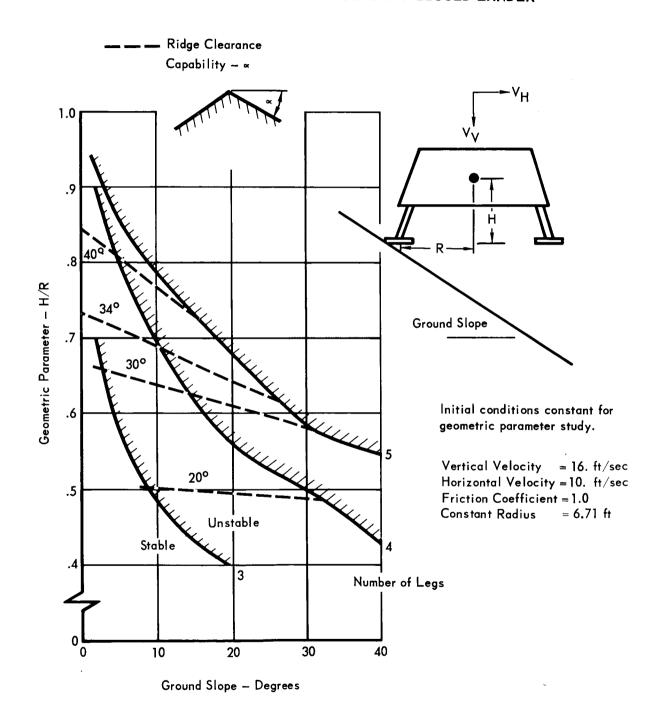


Figure 5.4 -1

PREFERRED CONCEPT - PRIMARY SEGMENTS

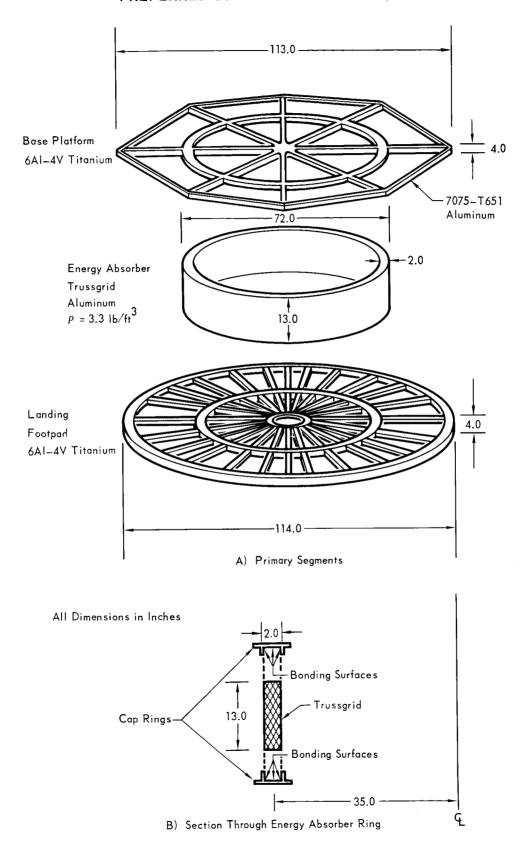


Figure 5.4-2

that there will be no difficulty in designing a Trussgrid with these properties. The function of the energy absorber is to limit the landing load factor to 14, significantly less than the 21.5 encountered during entry, and to transfer shear and compression loads from the footpad to the base platform. The 13-inch Trussgrid attenuates the kinetic and potential energy for the critical landing condition and still has the capability of stroking an additional 3.4 inches. The energy absorber is capped on top and bottom with circular rings which have channel shaped cross sections. The Trussgrid fits into the open end of the channel as shown in Figure 5.4-2(B). The rings are bonded to the Trussgrid with Fpoxylite 810 adhesive.

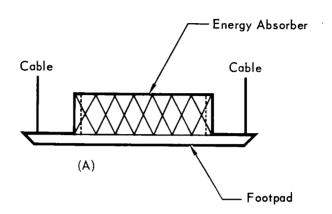
The base platform primary structure, Figure 5.4-2(A), is arranged in spoked-wheel fashion. It includes eight symmetrically spaced radial beams (spokes) joined at the center by a spider fitting (hub). The beams have "I" cross sections, 4-inches deep with 2.6-inch maximum flange widths. A ring spans between the radial beams at a 35-inch radius and attaches to the energy absorber cap ring. The material for the primary structure of the base platform is 6Al-4W heat treated titanium. Secondary framing members span between the ends of the radial beams and support the equipment mounted to the base platform. These members are 7075-T651 aluminum "I" beams and channels. The adapter and Aeroshell structure attach to the base platform at 8 fittings located at the outer ends of the radial beams. The parachute lines and the de-orbit motor support structure tie to the same fittings at four alternate radial beams.

Tension ties are required between the base platform and the footpad to provide balancing tension loads on the landing footpad for unsymmetrical landings. System details are shown in Section A3.2.1.4. They are cable and pulley systems ratcheted and spring loaded. Eight are used, one at each base platform radial beam, extending from the outer end of each beam to the outer ring of the landing footpad. The critical unsymmetrical landing condition occurs when a concentrated load is applied at the edge of the footpad. This condition causes the footpad to rotate about an axis through the cable attachment that is diametrically opposite the applied load. A tension load in the cable results as shown in Figure 5.4-3(B). During symmetrical landings, the Trussgrid is crushed without the need for balancing tension loads in the cable as shown in Figure 5.4-3(C). Since the cables are ratcheted and spring loaded they also insure that the landing footpad is bottomed against the energy absorber throughout the landing sequence.

Assembly of the lander is accomplished by first bonding the Trussgrid to the cap rings. The footpad and platform are mechanically attached to the rings. The

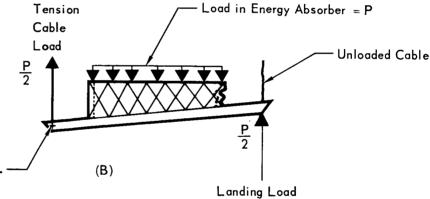
TENSION CABLE FUNCTION

Energy Absorber and Footpad Before Landing



Energy Absorber and Footpad During Unsymmetrical Landing

Footpad pivots about this point.



Energy Absorber and Footpad During Symmetrical Landing

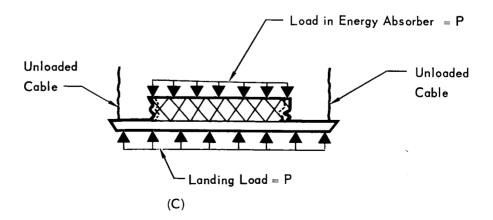


Figure 5.4-3

5.4-7

assembly is completed by installing the cables between the platform and footpad.

5.4.2.1 Trade Studies Related to Preferred Concept - Three studies involving landing load factor, detail footpad design, and material selection were made to optimize the design of the preferred concept.

<u>Landing Load Factor</u> - A study was made which determined the variation in weight of the footpad and base platform with landing load factor. As a result of this study we selected a design landing load factor of 14.

The effect of load factor on footpad and base platform weight is shown in Figure 5.4-4. Separate curves are shown for each structure because the footpad is entirely designed by landing loads, while the base platform is designed by landing loads only if the load factor is above 12. If the landing load factor is less, it is designed primarily by entry and parachute loads. The upper load factor limit on the curves reflects the design constraint that the landing loads shall not exceed the maximum flight load. The stability limit at the low load factor end of the curve results from raising the c.g. to the point of lander instability. However, at load factors less than 13.5, the AR (height to thickness ratio) of the Trussgrid becomes critical. Element test data indicate that at an AR of 7 stability is not critical for compression loading. Considering this to be limiting, the design load factor of 14 was selected. The AR of the Trussgrid in our preferred concept is 6.5

<u>Footpad Design</u> - Three structural configurations were studied to optimize the landing footpad. These were a combination beam and ring design, a beam and ring design with a screen covered center section hole and a honeycomb sandwich. These three structural configurations are shown in Figure 5.4-5.

The first configuration is our preferred concept. It is described in detail in Section 5.4.2. Basically, it consists of 22 radial beams and 3 concentric rings, all 6Al-4V heat treated titanium. Its weight is 270 lb.

The second configuration consists of an outer section of beam and ring structure and an inner section of stainless steel screen. The outer section was a torque box in cross section, 23 inches wide and 4 inches deep. Its inner radius was 34 inches. The structure included machined skins on the upper and lower surface along with machined radial beams. Cap members which ran circumferentially were machined in circular segments and joined by welding. The purpose of the center section screen was to limit the penetration of cone shaped terrain during landing. The screen acted as a membrane, distributing vertical loads to the energy absorber and horizontal loads to the outer torque box structure. Material for the screen was 17-4PH stainless steel because of its excellent ductility and the

THE EFFECT OF LOAD FACTOR ON LANDING FOOTPAD AND BASE PLATFORM WEIGHT

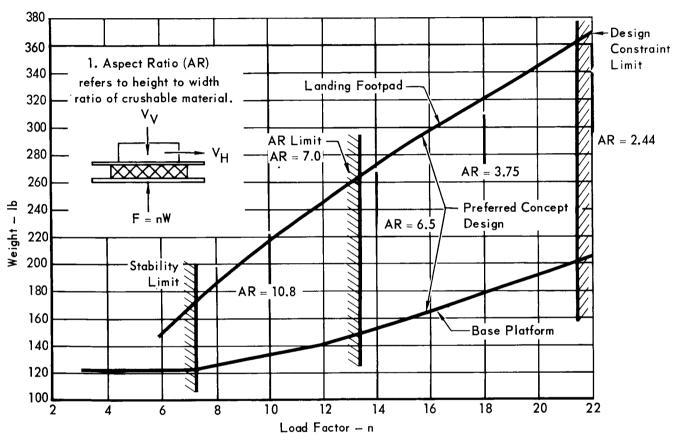


Figure 5.4-5

remaining structure was 6A1-4V heat treated titanium. The weight of this system was 318 lb.

The third configuration, a honeycomb sandwich, included heat treated titanium face plates bonded to an aluminum core. The sandwich thickness was 3.05 inches. The face plates were a constant 0.035 inch thick through the center section (35 inch radius) tapering to 0.020 inch at the edge. An edge ring was required for local horizontal and vertical tip loads. A 6.0 lb/ft 3 aluminum alloy core was used. The weight of this system was 329 lb.

On the basis of this study the minimum weight beam and ring design (270 1b) was chosen for the preferred concept.

<u>Material</u> - Materials considered for the lander structure included aluminum, magnesium, various alloy steels, and titanium. Appropriate mechanical properties and structural efficiencies are compared in Figure 5.4-6. Titanium is ductile and is superior in both ultimate tensile strength efficiency and yield tensile strength efficiency and is, therefore, selected for both the base platform and the footpad.

5.4.2.2 <u>Preferred Concept Stability</u> - The basic computer program for legged landers discussed in Section 5.4.1, was modified to use the forcing functions associated with a Uni-Disc Lander. The combined mass of the lander base platform and payload was represented as a rigid body with the crushable energy absorber located between the footpad and the base platform. The forcing function of the rigid body equations of motion consisted of the forces and moments transmitted to the base platform. The computer program variable inputs were the lander initial conditions, energy absorber load levels, surface slope, coefficient of friction, geometry, and the mass properties of the lander.

The critical stability condition is landing downhill on a 34 degree slope with 16 fps vertical and 10 fps lateral velocity. A pictorial representation of the vehicle motion during this condition is presented in Figure 5.4-7. A time history of the relative vertical, horizontal, and pitching velocity of the vehicle is presented in Figure 5.4-8.

A drop test program using a one-tenth scale model was conducted to verify our computer program. The test results are summarized in Section 4.2.4. The computer program was used to simulate the model characteristics and the test conditions, and good correlation was obtained in terms of stability. Results of the computer program predicted instability at a c.g. height of 3.3 inches for the critical

STRUCTURAL EFFICIENCY COMPARISON FOR VARIOUS MATERIALS

ULTIMATE	YIELD	MODULUS		ULTIMATE	YIELD	SI IIIGON	MOLEVONO
STRENGTH EL/ (psi) F _{ty}	<u> </u>	UF ELASTICITY (psi) E	(lb/in.3)	STRENGTH EFFICIENCY F _{tu} /p	STRENGTH EFFICIENCY F _{ty} /p	MODOLOS EFFICIENCY E/p	(PERCENT)
000'59	≃	10.3 × 10 ⁶	.101	742,000	645,000	10.2 × 10 ⁷	တ
26,000 6	•	6.5 × 10 ⁶	.065	269,000	400,000	10.2 × 10 ⁷	4
130,000	(')	31 × 10 ⁶	.298	570,000	436,000	10.6 × 10 ⁷	01
140,000		26 × 10 ⁶	.286	646,000	489,000	9.09 × 10 ⁷	∞
217,000		29 × 10 ⁶	.283	918,000	266,000	10.25×10^{7}	က
150,000		16 × 10 ⁶	091.	1,000,000	938,000	10 × 10 ⁷	01

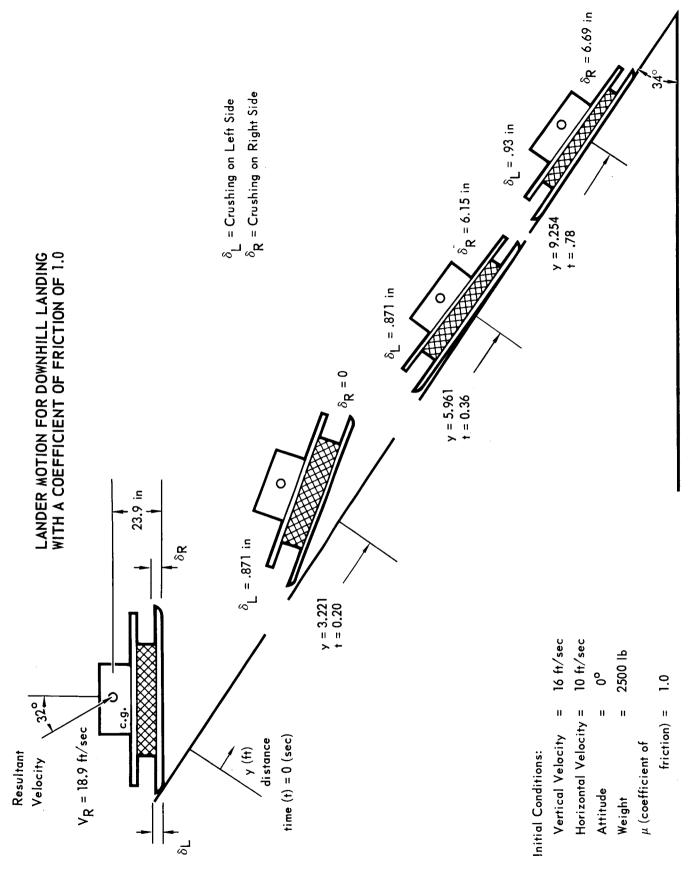
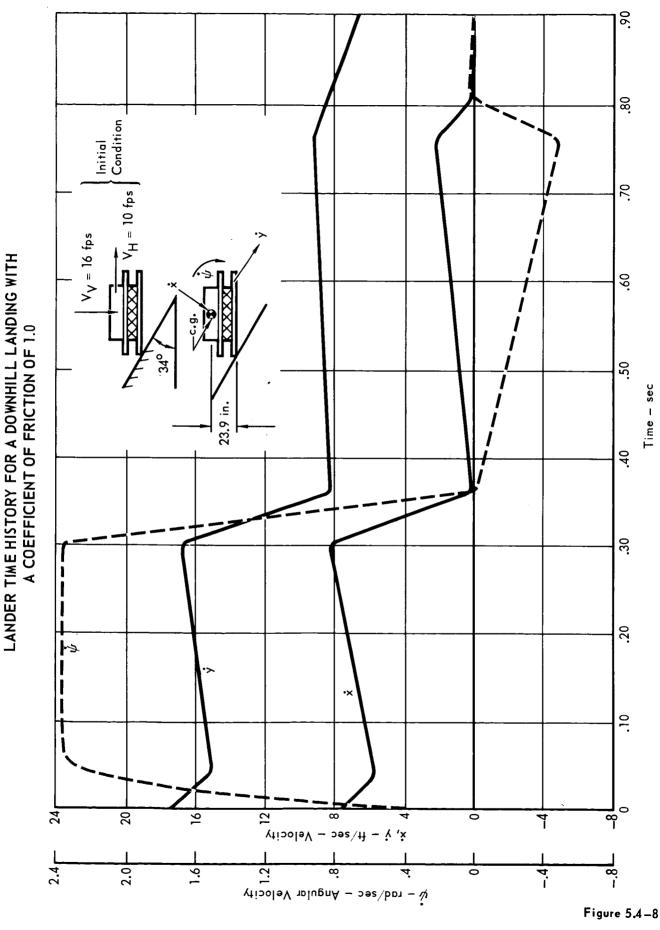


Figure 5.4-7



5.4-14

condition. The drop test model was stable with a 3.2-inch c.g. height (equal to 32 inches full scale) and unstable with a 3.4-inch c.g. height (equal to 34 inches full scale). These test results verify the integrity of the computer program which is used to predict the stability of our preferred concept.

Figure 5.4-9 presents the stability boundary for our preferred concept using a coefficient of friction of 1.0 between the footpad and the ground. This boundary was obtained by increasing the initial condition velocities until the lander became unstable as a result of bottoming out of the energy absorber. Increasing the coefficient of friction to 10 did not significantly alter the stability boundary.

5.4.2.3 Energy and Loads - A summary of the amount of kinetic energy absorbed when the lander first touches the surface is presented in Figure 5.4-10 for various conditions. The data is based on the assumption that the coefficient of friction is 1.0 (Maximum).

Those conditions for which little energy is absorbed during the initial touchdown are generally stability critical. Conditions (and (1)) are examples. Much of the effort relative to stability studies, including computer runs (Section 5.4.2.2) and model drop tests (Section 4.2), was based on condition (1) which was the most critical. This condition absorbs little energy initially and imparts appreciable rotational velocity to the lander. Condition (6) reflects the touchdown which the lander experiences after Condition (1).

The landing load factor is not a function of initially absorbed energy. It varies with the location of the landing load on the footpad and the angle of the applied load. For the unsymmetrical landing the landing load is 1/2 the load in the energy absorber (Figure 5.4-3B). For the symmetrical landing the landing load and the load in the energy absorber are the same (Figure 5.4.3C). Since the energy absorber load is fixed by its crushing strength, the landing load factor is only half as large for the unsymmetrical as for the symmetrical landing. When the landing load is applied at an angle with the vertical, a shear component results. The shear load carried through the energy absorber further alters the load factor.

The maximum vertical load factor of 14 results from a symmetrical landing on a cone, ridge or flat surface as in Condition 4.

The maximum horizontal load occurs from landing Condition where the resultant load factor is 12.8.

LANDING STABILITY BOUNDARY FOR THE UNI-DISC LANDER ON A 34-DEGREE DOWNSLOPE

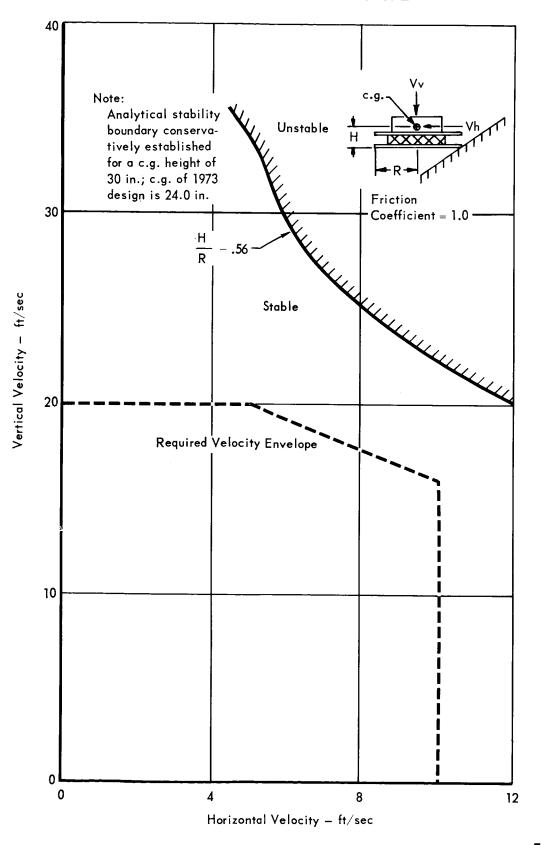


Figure 5.4-9

ENERGY ABSORBED ON INITIAL TOUCHDOWN

LANDING CONDITION AND NUMBER	VERTICAL VELOCITY IN FPS	HORIZONTAL VELOCITY IN ft/sec	FRICTION COEFFICIENT	ENERGY ABSORBED IN FT-LBS
(1) Velocity C.g.	20	5	.25	16610
2 Landing Load	16	10	.625	13860
3 100	16	5	.312	10980
4 777	20	5	0	15500
5	16	10	.65	7090
Rotational Velocity 6	16.32 (Not an initia	9.24 I condition — rota	1.0 tional velocity =	12,100 2.35 rad/sec)
7	20	5	0	6130
810°	16	5	.406	5 6 9 0
9	20	5	0	3100
	16	10	1.0	2600
	16	10	1.0	404

Figure 5.4-10

Two landing conditions, while absorbing little energy initially, are critical design conditions. Condition 9 results in a load factor of only 6.73 but it designs much of the lander footpad and base platform. Condition 10 with a net load factor of 7.8 absorbs even less energy initially but causes the maximum tension load on the Surface Laboratory to base platform interface attachments because of rotational acceleration. Loads for the critical landing conditions 4, 5, 9 and 10 are shown in Figure 5.4-11. The remaining landing conditions have load factors which range between those discussed above.

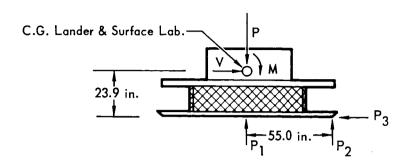
The base platform is designed primarily by landing condition However, that structure performs a multiple function. The adapter and Aeroshell are attached at the ends of the 8 radial beams and the de-orbit engine structure and parachute lines fasten at 4 of these points. Loads for entry and parachute deployment are shown in Figure 5.4-12. These are not critical for the lander but are sufficiently large to warrant consideration. The ascent and de-orbit loads are small and are not included.

The factor of safety (ratio between ultimate and limit load) for structure for launch and entry is 1.25, and for the footpad and the energy absorber in landing; it is 1.00. The lower factor of safety for landing is used because the load is predetermined by the crushing characteristics of the energy absorber. A factor of safety of 1.0 was also used on the Gemini Spacecraft for loads imposed by a water landing. The same philosophy applies to the landing gear design of military aircraft. The radial beams and rings in the footpad are designed to the material yield strength to preclude permanent structural deformation.

5.4.2.4 <u>Structural Analyses</u> - Several representative analyses of primary members of the lander are presented along with internal load distributions and deflection data for the footpad outer ring and radial beams.

The preferred concept for the lander footpad is a multiply redundant structure involving rings and radial beams. The critical condition for the design of the radial beams is landing on one edge of the footpad, condition 9. The load balance of the outer ring and radial beam section of the footpad is shown in Figure 5.4-13. The deflection of the outer ring is presented in Figure 5.4-14. The distribution of load to the radial members was found by considering the ring as a beam on an elastic foundation, the radial members acting as springs to provide the foundation. For this analysis, we used the elastic curve equation for a long beam subjected to a concentrated load, P. (Reference 5.4-8):

CRITICAL DESIGN LOADS FOR LANDING FOOTPAD



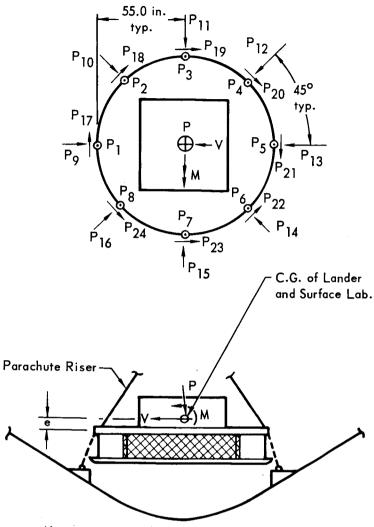
Landing Condition Reference Figure 5.4–10	μ	P (lb.)	V (lb.)	M (inlb.)	P ₁ (lb.)	P ₂ (lb.)	P ₃ (lb.)
4 XXXX	0	35,000	0	0	35,000	0	0
(5) C.G.	0.65	12,800	29,400	0	0	12,800	29,400
9	0	16,900	0	930,000	0	16,900	0
	1.0	13,800	_ 13,800	1,090,000	0	13,800	-13,800

Notes: 1. Loads are limit and positive as shown.

2. Landing weight = 2500 lb.

3. Maximum load factor = 14.

LANDER FLIGHT LOADS



N	A1	۱.	c	
1.4	v		э	

- 1. Loads are ultimate and positive as shown.
- 2. Parachute pulloff angle is 20° with respect to the vertical.
- 3. Capsule Entry Limit Load Factors are 19.4 longitudinal and 2.2 lateral.
- 4 Flight capsule weight minus the weight of the aeroshell structure, heat shield, canister, adapter, and de-orbit engine.
- 5 Entry loads applied to the Lander were calculated by assuming an elastic distribution; plane sections remaining plane.

	Loading Conditions		
	Parachute Deployment	Capsule Entry Maximum Dynamic Pressure	
Weight (lb.)	2750 (4)	2,750 (4)	
e (in.)	5.0	5.0	
P (lb.)	23,500	66,400	
V (lb.)	-8550	8,550	
M (inlb.)	-980,000	586,000	
Pյ (lb.)	0	11,200	
P ₂ (lb.)	0	10,400	
P3 (lb.)	2,190	8,300	
P4 (lb.)	0	6,200	
P5 (lb.)	19,120	5,400	
P6 (lb.)	0	6,200	
P7 (Ib.)	2,190	8,300	
P8 (Ib.)	0	10,400	
P9 (lb.)	0	3,000	
P ₁₀ (lb.)	0	2,780	
Pjj (lb.)	975	2,230	
P ₁₂ (lb.)	0	1,680	
P13 (lb.)	8550	1,470	
P ₁₄ (Ib.)	0	1,680	
P ₁₅ (lb.)	975	2,230	
P ₁₆ (lb.)	0	2,780	
P17 (lb.)	0	0	
P18 (lb.)	0	960	
P19 (lb.)	0	1,360	
P ₂₀ (lb.)	0	960	
P ₂₁ (lb.)	0	0	
P ₂₂ (Ib.)	0	960	
P ₂₃ (lb.)	0	1,360	
P ₂₄ (lb.)	0	960	

LANDER FOOTPAD ULTIMATE LOADS AT OUTER RING - RADIAL BEAM INTERSECTION FOR LANDING CONDITION (9)

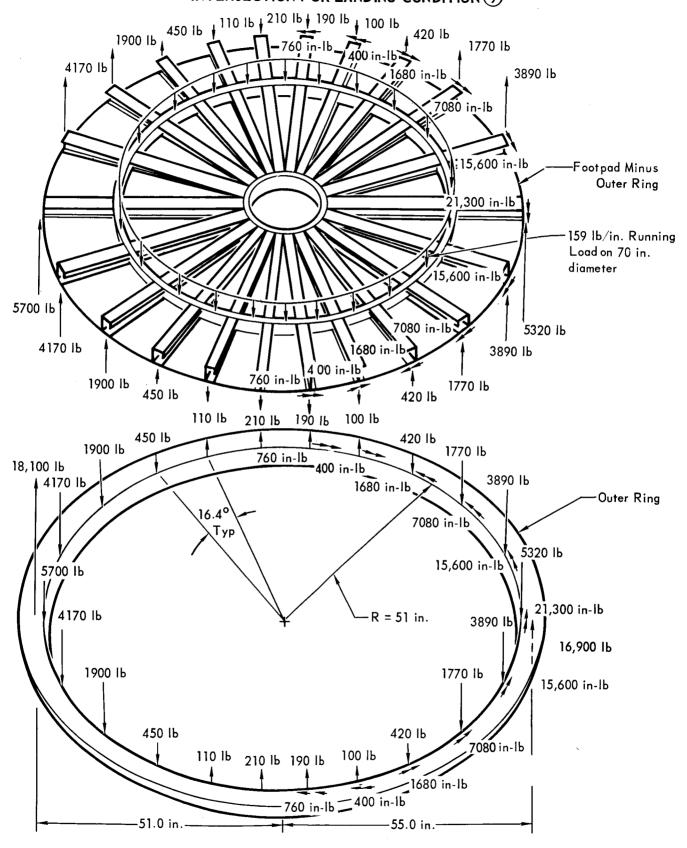
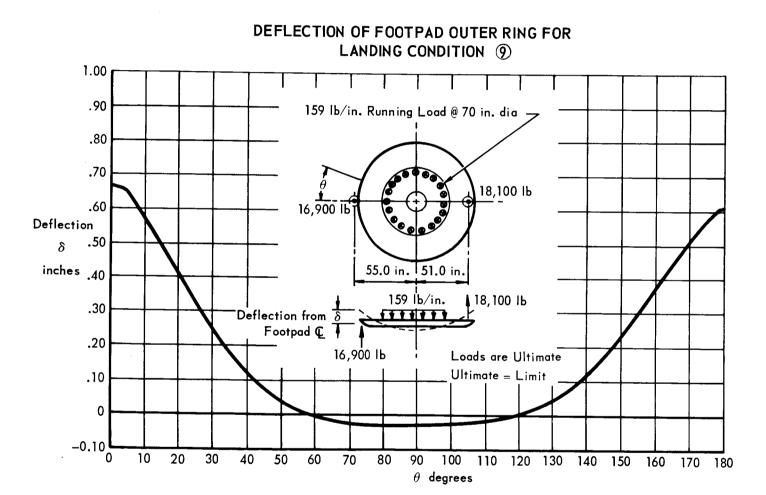


Figure 5.4-13

5.4-21



$$y = \frac{P \beta e^{-\beta x} (\cos \beta x + \sin \beta x)}{2k}$$

where: y = vertical deflection

x = distance along the beam from the applied load

k = spring constant per unit length

 $\beta = \sqrt[4]{k/4EI}$

E = modulus of elasticity

I = beam moment of inertia

An analysis of the radial beams for condition 9 is presented in Figure 5.4-15. Additional conditions which result in landing loads applied between the energy absorber ring and the outer ring or in the center section were also analyzed but are not included.

The outer ring is critical for condition 5 which results in the maximum side load. Its analysis is presented in Figure 5.4-16. For this condition the load was assumed to act over a 10 inch width. Local stiffeners are machined into the ring every 5 inches as shown in Section A 3.2.1.4 to strengthen the ring for concentrated loads.

As discussed in Section 5.4.2.3 the factor of safety (ratio between ultimate and limit load) is 1.0 for the landing footpad. To prevent permanent structural deformation of the primary structure the rings and radial members are designed to the yield strength of the material. The .020 inch thick lower surface skin is not considered primary structure and will be allowed to yield or fail. Its function is to provide a large footprint area for soft surface landings, distributing soil pressure loads to the radial and ring members. It is adequate for a pressure of 27 psi, well above the 6 psi specified. A symmetrical (flat) landing with our system results in a uniform pressure of 4.0 psi over the footpad lower surface. Landing on irregularly shaped, rugged terrain may deform or fail the skin. However its loss will not degrade the landing operation because the rings and radial members are designed to sustain all loads without the aid of the skin.

The base platform provides a common structure for many loads, as discussed in Section 5.4.2.3. The critical loads for its primary members, the radial beams, are obtained from landing condition. The analysis of a radial beam for this condition is shown in Figure 5.4-17. The energy absorber applies a uniform load to the base platform. Loads from the Surface Laboratory, based on an elastic distribution at the interface, are applied at 8 points on the base platform. Like the footpad the base platform is redundant, having 8 radial beams and a circular ring

STRENGTH ANALYSIS OF FOOTPAD RADIAL BEAMS FOR LANDING CONDITION(9)

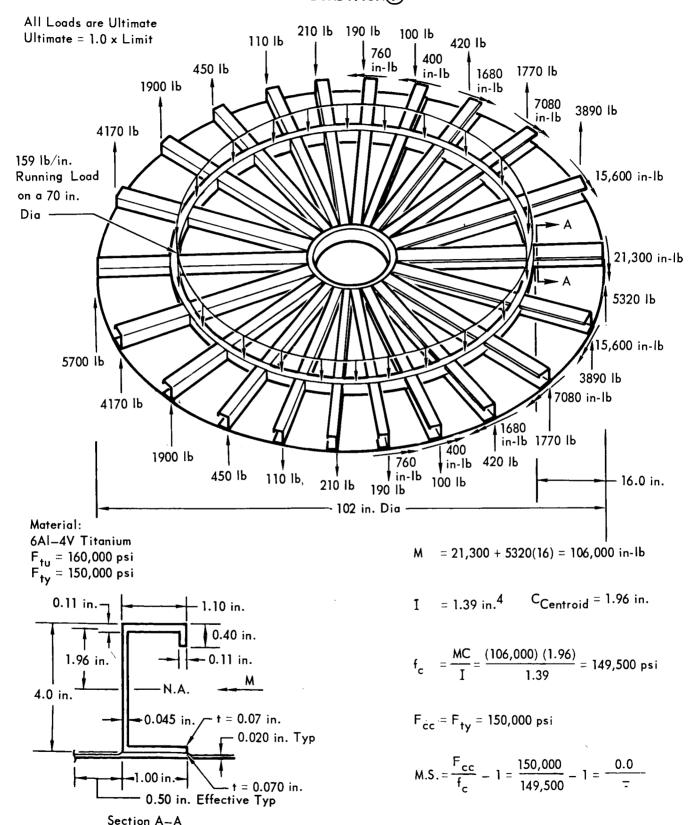


Figure 5.4-15

5.4-24

STRENGTH ANALYSIS OF FOOTPAD OUTER RING FOR LANDING CONDITION (5)

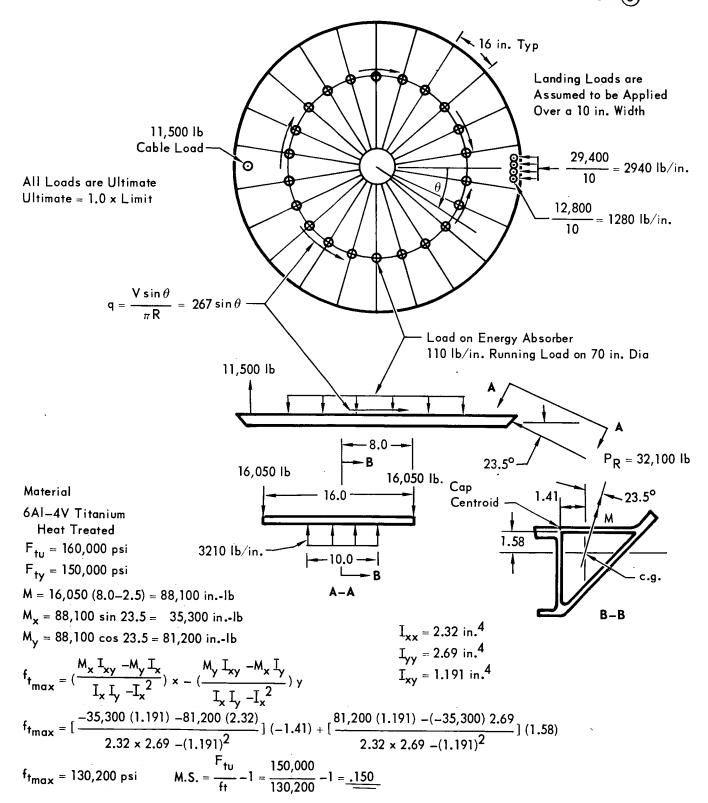


Figure 5.4-16

STRENGTH ANALYSIS OF BASE PLATFORM RADIAL BEAMS FOR LANDING CONDITION(9)

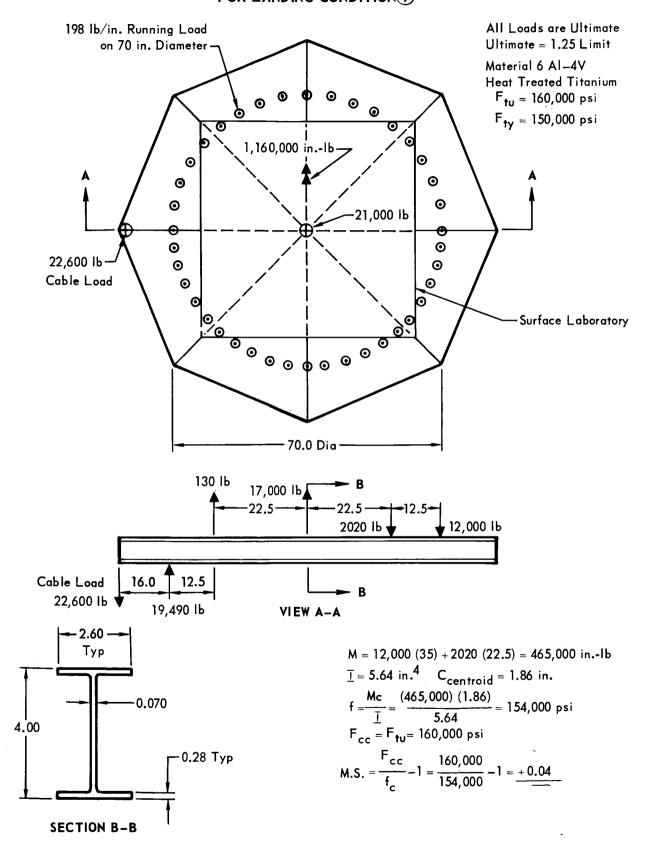


Figure 5.4-17

at the energy absorber diameter. The loads on the beam analyzed in Figure 5.4-17 were derived using both radial beam and ring load paths.

5.4.2.5 <u>Dynamic Analysis</u> - A vibration normal mode analysis was performed for the Lander in the landed configuration. The mass of the Lander less that of the footpad and energy absorber ring was assumed concentrated at 33 points in the plane grid formed by the base platform primary structural members. Eight of these 33 points are over the energy absorber and were considered to be support points. The analysis provided for linear motion perpendicular to the plane of the lander base platform interface; hence, there were 25 degrees of freedom. Flexibilities of all base platform primary structural members were included in the analysis; those of secondary structural members were not included.

The STRESS (STRuctural Engineering System Solver) programming system (Reference 5.4-9) was used to obtain influence coefficients for the base platform. The matrix C of influence coefficients and the matrix M of concentrated masses were then used in the equation

$$CM \ \overline{X}_{j} = \left(\frac{1}{w_{j}^{2}}\right) \left(\overline{X}_{j}\right)$$

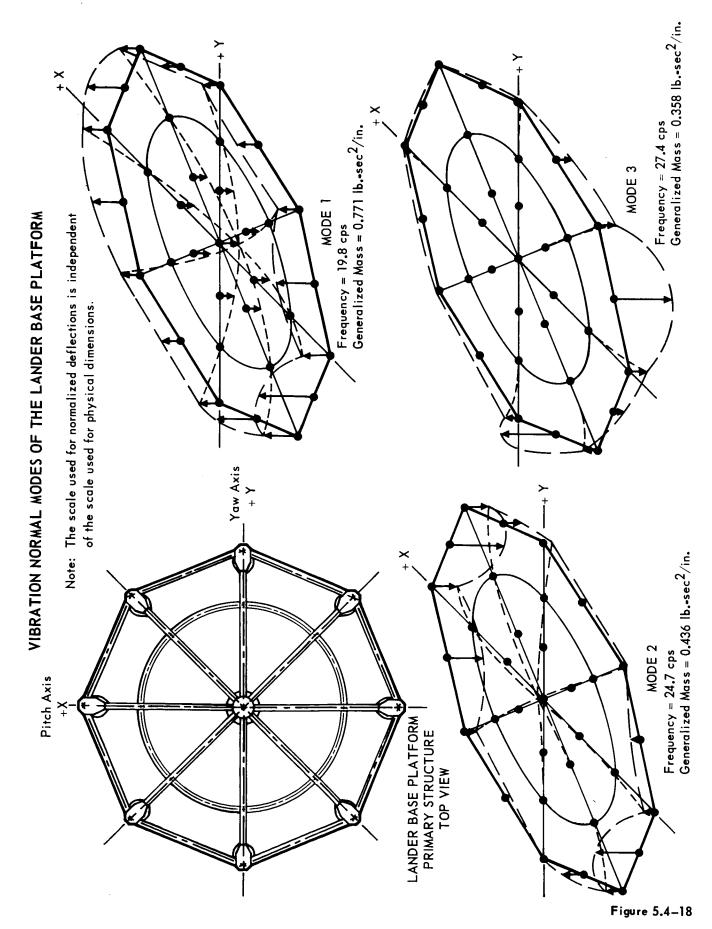
to solve for the natural frequencies w_j and their associated mode shapes \overline{X}_j .

The first three calculated natural frequencies of the base platform are the following:

$$w_1 = 19.8 \text{ cps}$$

 $w_2 = 24.7 \text{ cps}$
 $w_3 = 27.4 \text{ cps}$

The mode shapes corresponding to these natural frequencies are shown in Figure 5.4-18.



REFERENCES

- 5.4-1 E. J. Pulo, R. H. Witting: Static Compression Tests of Honeycombed Paper-board. QMFCI Report No. 24-57, August 1957.
- 5.4-2 E. J. Pulo: Energy Absorbing Characteristics of Honeycombed Paperboard Statically Compressed at Various Angles to the Longitudinal Axis of the Cells. QMFCI Report No. 7-87-03-004B, 16 October 1956.
- 5.4-3 H. W. Bixby: Development of a Paperboard Honeycomb Decelerator for Use with Large Platforms in Aerial Delivery Systems. WADC T.R. 59-776, Radioplane Division of Northrup Corp., Van Nuys, California. May 1959.
- 5.4-4 L. J. Fisher, Jr.: Landing Impact Dissipation Systems. NASA TN D-975. Langley Research Center, Langley Air Force Base, Virginia. December 1961.
- 5.4-5 R. J. Black: Quadrupedal Landing Gear Systems for Spacecraft. Journal of Spacecraft, Volume I, No. 2, March-April 1964.
- 5.4-6 Surveyor Spacecraft Monthly Performance Assessment Report. Hughes Aircraft Company, 21 April 1966.
- 5.4-7 Documentation of Digital Computer Programs for Lunar Landing Dynamics System Investigation. Bendix Products Aerospace Division, Report No. MM-64-9, November 1964.
- 5.4-8 F. B. Seely, J. O. Smith: Advanced Mechanics of Materials. John Wiley and Sons, Inc., New York, July 1962.
- 5.4-9 S. J. Fenves, R. D. Logcher, S. P. Mauch, and K. F. Reinschmidt:

 STRESS: A User's Manual. Massachusetts Institute of Technology, The M.I.T.

 Press, Cambridge, Massachusetts, September 1964.